New Precursors for Direct Writing of Nanostructures using Charged Particle Beams

Dissertation
zur Erlangung des Doktorgrades
der Naturwissenschaften

vorgelegt beim Fachbereich 14

der Johann Wolfang Goethe-Universität
in Frankfurt am Main

von
Dipl.-Ing. Felix Jungwirth, Bsc.

aus Scheibbs

Frankfurt 2022
D 30

Vom Fachbereich 14 (Biochemie, Chemie und Pharmazie) der

Johann Wolfgang Goethe - Universität Frankfurt als Dissertation angenommen.

Dekan: Prof. Dr. Clemens Glaubitz

Gutachter: Dr. habil. Sven Christian Barth,
Prof. Dr. Andreas Terfort

Datum der Disputation:

Parts of this work have been published

- *"Focused Ion Beam vs. Focused Electron Beam Deposition of Cobalt Silcide Nanostructures using Single-Source Precursors: Implications for Nanoelectronic Gates, Interconnects, and Spinntronics "*
  F. Jungwirth, F. Porrati, D. Knez, H. Plank, M. Huth, S. Barth*; *ACS Appl. Nano Mater*. **2022**, accepted.

- *"Nanodruck mit Elektronenstrahlen"*
  S. Barth* and F. Jungwirth; Nachr. Chem. **2022**, 7, 46-48.

- *"Vanadium and Manganese Carbonyls as Precursors in Electron-Induced and Thermal Deposition Processes"*
  F. Jungwirth, D. Knez, F. Porrati, A. G. Schuck, M. Huth, H. Plank, S. Barth*; Nanomaterials **2022**, 12, 1110.

- *"Direct writing of cobalt silicide nanostructures using single-source precursors"*
  F. Jungwirth, F. Porrati, A. G. Schuck, M. Huth, S. Barth*; ACS Appl. Mater. Interf. **2021**, 13, 48252–48259.

- *"Precursors for Direct-Write Nanofabrication with Electrons"*
  S. Barth*, M. Huth, F. Jungwirth; J. Mater. Chem. C **2020**, 8, 15884-15919.

Abstract

Focused electron and ion beam induced deposition (FEBID/FIBID) methods have gained significant attention in recent years because of their unique ability for the maskless fabrication of arbitrary three-dimensional shapes. Both techniques enable material deposition down to the nanoscale for applications in materials science and condensed matter physics. However, the number of suitable precursor molecules, especially for high purity deposits, is usually still very limited to date. Additionally, both the FEBID and FIBID process are very complex when assessed in detailed and the development of process-optimize, tailored precursor molecules is not yet possible.

In the first part of this work hexacarbonyl vanadium ($V(CO)_6$) and dimanganese decacarbonyl ($Mn_2(CO)_{10}$) are investigated for their use in FEBID in order to complement the already existing data on transition metal carbonyl precursors. In addition, chemical vapor deposition (CVD) has been carried out to compare compositional differences for electron induced and purely thermal processes. FEBID using $V(CO)_6$ resulted in the formation of a vanadium (oxy)carbide material with a V:C ratio of approx. 0.6-0.9. The material shows a temperature-dependent normalized electrical conductance typical for granular metals in agreement with TEM analysis. Additionally, characterization of the crystalline fractions reveals a cubic $VC_{1-x}O_x$ phase in agreement with the phase observed in CVD thin films. Thermal decomposition using CVD yielded material of higher purity with V:C ratios of 1.1-1.3. In contrast, an insulating material with approx. 40 at% Mn is obtained for FEBID using $Mn_2(CO)_{10}$ as precursor with very similar compositions being observed for CVD thin films.

The second part of this work deals with the deposition of defined alloy materials by focused charged particle beam deposition. Three silyl substituted transition metal carbonyl complexes have been synthesized and tested for FEBID, FIBID and CVD. The three precursors investigated were: $H_3SiMn(CO)_5$, $H_3SiCo(CO)_4$, and $H_2Si(Co(CO)_4)_2$. FEBID experiments with the manganese derivative show the selective loss of silicon, and metal/metalloid contents of up to 49 at%. Contrary, material derived from both cobalt derivatives did retain the 1:1 and 2:1 Co:Si ratios respectively, resulting in metal/metalloid contents of up to 62 at%. Temperature-dependent normalized electrical conductance measurements of as-grown and post-growth electron beam irradiated samples reveal behavior typical for granular metals except for the as-grown CoSi material which is located on the insulating side of the metal-insulator transition. Ga^+-FIBID revealed $H_2Si(Co(CO)_4)_2$ to be a very suitable precursor, retaining the predefined Co:Si ratio in the deposits, while significant loss of silicon was observed for $H_3SiCo(CO)_4$ derived deposits. Contrary to FEBID high metal/metalloid contents of up to 90 at% are obtained. Additionally, temperature dependent electrical properties of dicobalt silicide and the expected ferromagnetic behavior have been observed for the Co_2Si-FIBID material. Further analysis enables the proposition of different dominating decomposition channels in FEBID and FIBID based on microstructural features such as bubble formation in FIBID materials.

Kurzfassung

Additive Fertigungsmethoden, gemeinhin als 3D Druck bezeichnet, beschreibt eine Reihe von etablierten Verfahren welche Bauteile schichtweise von Grund auf, anhand eines 3D Models, aufbauen. Diese Verfahren sind sehr erfolgreich bei der Herstellung makroskopischer Objekte, aber insbesondere, wenn Dimensionen im Mikrometer- oder Submikrometerbereich benötigt werden, stoßen die Standardverfahren an ihre Grenzen. Um die Auflösungsgrenzen etablierter Verfahren zu überwinden wurden verschiedene neue Methoden entwickelt. Die höchste Auflösung wird dabei durch das direkte Schreiben von Nanomaterialien durch elektronen- oder ioneninduzierte Zersetzung von Vorstufen erreicht. Im englischen als „Focused Electron“ bzw. „Focused Ion Beam Induced Deposition“, kurz FEBID bzw. FIBID, bezeichnet besitzen diese Methoden ein hohes Innovationspotential. Sowohl FEBID als auch FIBID sind maskenlose Verfahren welche die ortsselektive Abscheidung von, üblicherweise anorganischen, Materialien auf der sub-Mikrometer- bzw. Nanometerebene ermöglichen. Die Methoden sind dabei prinzipiell sehr einfach und benötigen nur eine geeignete, gasförmige Vorstufe welcher anschließend lokal durch einen fokussierten Elektronen- oder Ionenstrahl in ein oberflächengebundenes Material umgewandelt wird. Für FEBID werden üblicherweise Rasterelektronenmikroskope (REM) verwendet während für FIBID fokussierte Ionenstrahlen zum Einsatz kommen. Die Form des erhaltenen Deponats wird in beiden Verfahren durch sukzessives abscheiden einzelner Pixel oder Linien auf einer Substratoberfläche definiert. Beide Methoden werden, unter anderem, in der Grundlagenforschung sowie der etablierten Probenpräparation für Transmissionselektronenmikroskopie (TEM) verwendet. Die resultierenden funktionalen Materialien können dabei zum Beispiel in den Bereichen Sensorik, Magnetismus, Supraleitung oder Photonik angewendet werden. Üblicherweise werden metallische oder hableitende Deponate angestrebt und daher metallorganische Vorstufen verwendet. Die Auswahl an geeigneten Vorstufen ist dabei in der Regel zur Zeit noch limitiert, im Speziellen wenn hochreine Deponate angestrebt werden. Außerdem sind die FEBID- und FIBID-Prozesse, wenn sie im Detail betrachtet werden, hoch komplex und diverse Zersetzungspfade und Fragmentierungsmuster können zur finalen Materialzusammensetzung und Mikrostruktur beitragen und dessen Eigenschaften beeinflussen. Daher sind die Abläufe auf molekularer Ebene noch nicht vollständig verstanden und die Entwicklung von prozessoptimierten, maßgeschneiderten Vorläufermolekülen ist bisher nur mit Limitierungen möglich.

Im ersten Teil der Arbeit werden Vanadiumhexacarbonyl, $V(CO)_6$, und Mangandecacarbonyl ,$Mn_2(CO)_{10}$, als Vorstufen für die elektroneninduzierte Zersetzung untersucht, um die bestehenden Daten zu Übergangsmetallcarbonylen zu komplementieren. Ergänzend wurde die rein thermische Zersetzung beider Vorstufen mittels chemischer Gasphasenabscheidung

(engl. chemical vapor deposition (CVD)) untersucht. Sowohl bei FEBID- als auch bei CVD-Deponaten wird für beide Vorstufen ein signifikanter Einbau von Ligand-Atomen in die jeweiligen Deponate beobachtet. FEBID-Deponate welche mit $V(CO)_6$ als Vorstufe geschrieben wurden zeigen ein V:C Verhältnis von ungefähr 0.6-0.9. Die Deponatzusammensetzung ist dabei weitestgehend unabhängig von Depositionsparameter, nur bei einer Erhöhung der Spannung auf 20 kV wird ein signifikanter Abfall des V:C Verhältnisses beobachtet. Etwas höhere V:C Verhältnisse von 1.1 bis 1.3 wurden für CVD-Dünnfilme erhalten, was auf eine effektivere Liganden-Abspaltung im rein thermischen Prozess hindeutet. Mikrostrukturelle Untersuchungen an einem FEBID Deponat zeigen, wie für diesen Prozess üblich, ein granulares Material bestehend aus kleinen Kristalliten welche in einer amorphen Matrix verteilt sind. Die kristalline Phase kann mittels Elektronenbeugung als kubische $VC_{1-x}O_x$ Phase identifiziert werden und die gleiche Phase wird auch in Röntgenbeugungsexperimenten an CVD-Dünnschichten beobachtet. Zudem wurde eine selektive Oxidation der Deponatoberfläche in transmissionselektronenmikroskopischen (TEM) Untersuchungen festgestellt. Da Wasser üblicherweise für einen Großteil des Hintergrunddrucks in der REM-Kammer verantwortlich ist, kann diese Oxidation vermutlich auf elektroneninduzierte Reaktionen mit in der Kammer vorhandenem Restwasser zurückgeführt werden. Zweipol Messungen der FEBID-Deponate zeigen spezifische Widerstände von 0.8×10^{-3} µΩ·cm bis 1.2×10^{-3} µΩ·cm. Dabei wird eine Abnahme des spezifischen Widerstands mit zunehmendem Abscheide-Strom beobachtet. Übereinstimmend mit den TEM-Untersuchungen zeigen temperaturabhängige Widerstandsmessungen der FEBID-Deponate einen Abfall der Leitfähigkeit mit zunehmendem Strom, ein Verhalten welches typisch für granulare Metalle ist die sich auf der metallischen Seite des Metall-Isolator-Übergangs befinden.

Die Verwendung von $Mn_2(CO)_{10}$ als Vorstufe resultiert in Deponate mit etwa 40 at% Mn für FEBID-Experimente als auch für CVD-Abscheidungen. Die FEBID-Deponate zeigen dabei isolierendes Verhalten mit spezifischen Widerständen von 5×10^{10} µΩ·cm bis 1.5×10^{9} µΩ·cm. Die erhaltenen FEBID-Deponate wurden, in einem etablierten Verfahren, durch Nachbestrahlung mittels Elektronenstrahl behandelt um die Leitfähigkeit der Proben zu verbessern. Dies resultierte in einer Zunahme der Leitfähigkeit um etwa eine Größenordnung. Temperaturabhängige Leitfähigkeitsmessungen zeigen aber dennoch für beide Probentypen das Verhalten eines Isolators. Zudem kann bei beiden Materialien ein Phasenübergang bei etwa 15 K beobachtet werden, welcher zu keiner bekannten Mn- oder MnO_x-Phase zugeordnet werden konnte.

Aktuell sind Übergangsmetallcarbonyle die am besten untersuchteste Klasse von Vorstufen für den FEBID Prozess. Zusammen mit den in dieser Arbeit gewonnen Daten können gewisse

Trends in der Reinheit der FEBID Deponate beobachtet werden. Metallgehälter von über 80 at% wurden bisher für den FEBID-Prozess üblicherweise nur für Metallcarbonyl-Vorstufen mit Zentralatomen der Gruppe 8-10, auch als Eisentriade bekannt, berichtet. Im Gegensatz dazu werden für Carbonyle mit Zentralatomen der Gruppe 5-7 maximale Metallgehälter von weniger als 50 at% beobachtet. Die beiden hier untersuchten Vorstufen, $V(CO)_6$ und $Mn_2(CO)_{10}$, folgen diesem Trend mit Metallgehältern von unter 45 at%. Interessanter weise stimmen diese Trends in der Reinheit der Deponate gut mit dem Chemisorptionsverhalten von Kohlenmonoxid auf den korrespondierenden Metalloberflächen überein. CO ist dafür bekannt auf Übergangsmetalloberflächen entweder molekular zu chemisorbieren oder in C und reaktiven O zu dissoziieren. Molekulare Chemisorption wird dabei in erster Linie für Übergangsmetalle der Eisentriade beobachtet, mit einem Übergangsverhalten ungefähr entlang der Fe-Tc-Re-Linie. Dieses Verhalten stimmt gut mit den hochreinen Deponaten in FEBID überein, welche typischerweise für Übergangsmetallcarbonyle der Gruppe 8-10 beobachtet werden, und deutet darauf hin, dass das Zentralatom eine wichtige Rolle in der erzielbaren Reinheit der Deponate spielen kann.

Der zweite Teil der Arbeit beschäftigt sich mit der Abscheidung von Materialien mit vorgegebener Stöchiometrie mittels fokussierter Partikelstrahlen (Elektronen und Ga^+-Ionen) und CVD. Die drei silyl-substituierte Übergangsmetall-Carbonyl Vorstufen welche dafür synthetisiert und verwendet wurden waren: $H_3SiMn(CO)_5$, $H_3SiCo(CO)_4$, und $H_2Si(Co(CO)_4)_2$.

Die rein thermische Zersetzung mittels CVD resultiert in Dünnfilmen mit ungefähr 80 at% Metall/Metalloid-Gehalt für alle drei Vorstufen. In allen thermischen Abscheidungen wurde dabei jedoch ein mehr oder weniger ausgeprägter Verlust von Silizium und somit ein Abweichen der finalen Schichtzusammensetzung von der initial definierten Stöchiometrie beobachtet. Die Ursache für den Si-Verlust könnte dabei durch den Zersetzungsmechanismus bedingt sein, aber auch Nebenreaktionen mit Restgasen, v.a. Wasser, sind denkbar. Unabhängig vom Siliziumverlust werden trotzdem die Phasen, welche der Stöchiometrie der Vorstufe entsprechen, für alle drei Materialien in der Röntgenbeugung beobachtet.

Im Vergleich zur CVD führte die Elektronenstrahl induzierte Abscheidung für alle drei Vorstufen zu einem erhöhten Einbau von Ligandatomen in die jeweiligen Deponate. Für Abscheidungen aus $H_3SiMn(CO)_5$ werden dabei Metall/Metalloid-Gehalte von 45 at% bis 50 at%, in guter Übereinstimmung mit der Literatur, erhalten. Darüber hinaus wird ein ausgeprägter Siliziumverlust beobachtet, der zu einem Mn:Si von etwa 2.5:1 führt. Dies deutet auf eine hocheffiziente, elektronengetriebene Bildung von flüchtigen, siliziumhaltigen Fragmenten hin wobei der genau Mechanismus jedoch noch unklar ist. Alternative könnten auch thermische Effekte oder Reaktionen mit Hintergrundgasen eine Rolle spielen. In einem Versuch die siliziumhaltigen, flüchtigen Bruchstücke im Deponat zurückzuhalten oder thermisch induzierte

Prozesse zu unterdrücken wurden FEBID-Experimente bei Substrattemperaturen von bis zu 250 K durchgeführt, eine signifikante Änderung des Mn:Si - Verhältnis konnte dabei jedoch nicht beobachtet werden.

Im Gegensatz zu $H_3SiMn(CO)_5$ können sowohl $H_3SiCo(CO)_4$ als auch $H_2Si(Co(CO)_4)_2$ als geeignete Vorstufen für den FEBID Prozess angesehen werden. In beiden Fällen werden Metall/Metalloid-Gehälter von 55 at% bis 62 at% erhalten, wobei das vordefinierte Co:Si Verhältnis sehr gut beibehalten wird. Änderungen in den Abscheideparameter, wie beispielsweise Elektronenstrom oder Beschleunigungsspannung, führen dabei nur zu geringfügigen Änderungen in den Deponatzusammensetzungen. Insbesondere die $H_2Si(Co(CO)_4)_2$-Vorstufe zeigt dabei sehr hohe Wachstumsraten im Vergleich zu anderen FEBID-Vorstufen. Für beide cobalthaltigen Deponate werden spezifische Widerstände im Bereich von 4.8×10^4 µΩ·cm bis 0.5×10^4 µΩ·cm beobachtet, welche mit zunehmendem Abscheidestrom abnehmen. Eine Nachbestrahlung der Deponate mit Elektronen führte nicht nur zu einer Abnahme im Widerstand, wie häufig auch für andere FEBID Deponate beobachtet, sondern auch zu einer Änderung des magnetischen Verhaltens. Während für nicht nachbestrahlte Deponate ein negativer Magnetwiderstand beobachtet wurde zeigte das nachbestrahlte Material hingegen einen positiven Magnetwiderstand. Zudem wurden Veränderungen bei temperaturabhängigen Messungen des Widerstands beobachtet. Alle Deponate zeigen dabei ein Verhalten welches typisch für granulare Metalle ist. Der temperaturabhängige Leitfähigkeitsverlauf des CoSi Materials ohne Nachbestrahlung entspricht dabei einem Isolator nahe des Metall-Isolator-Übergangs, während alle anderen Proben ein quasi-metallisches Verhalten zeigen.

Im Gegensatz zu FEBID-Experimenten wurde die vordefinierte Stöchiometrie in Ga^+-FIBID-Experimenten mit $H_3SiCo(CO)_4$ nicht beibehalten. Die langsame Wachstumsrate für Abscheidungen mit dieser Vorstufe, welche bereits bei FEBID-Experimenten beobachtet wurde, führt wahrscheinlich zu einem signifikanten Co-Sputtern von Silizium und dem Einbau von großen Mengen von Ga. Die Gesamtzusammensetzung der Deponate kann dabei als $CoSi_{0.36}C_{0.15}O_{0.09}Ga_{0.72}$ beschrieben werden, was einem gesamt Metall/Metalloid Gehalt von 90 at% entspricht. Im Gegensatz dazu bleibt das vordefinierte Co:Si Verhältnis bei FIBID-Deponate, welche mit $H_2Si(Co(CO)_4)_2$ als Vorstufe abgeschieden wurden, erhalten. Zudem werden, abhängig vom Strahl-Strom, geringe Mengen Ga (unter 15 at%) in die Deponate eingebaut. Der gesamt Metall/Metalloid-Gehalt der Deponate beträgt dabei ebenfalls bis zu 90 at%. Die Materialien welche mittels FIBID erhalten wurden zeigen für beide Vorstufen deutlich niedrigere spezifische Widerstände (720 µΩ·cm bis 300 µΩ·cm) im Vergleich zu den entsprechenden FEBID-Abscheidungen. Auch im Verlauf der temperaturabhängigen Leitfähigkeit können signifikante Unterschiede beobachtet werden. Die FIBID-Deponate

zeigen dabei beiden, anders als die entsprechenden durch FEBID erhaltenen Materialien, nur geringe Änderungen mit sinkender Temperatur. Im Falle des FIBID-CoSi-Deponats wird ein Abfall der Leitfähigkeit mit sinkender Temperatur bis 90 K beobachtet, danach steigt sie wieder leicht an. Dieses Verhalten könnte auf ein Material hindeuten, welches sich nahe am Übergang zwischen metallischem und quasimetallischem Verhalten befindet, da der Temperaturkoeffizient des Leitwerts am Übergangspunkt das Vorzeichen von negativ zu positiv ändert. Das FIBID-Co_2Si Deponat zeigt einen Anstieg der Leitfähigkeit mit sinkender Temperatur, welche auch für Cobaltdislicid beobachtet wurde. Zudem werden Unterschiede im magnetischen Verhalten beobachtet: Das FEBID-Co_2Si-Deponat zeigt (super)paramagnetisches Verhalten während eine Hysterese für das FIBID-Co_2Si-Material beobachtet wird, die auf ferromagnetisches Verhalten hinweist.

Um die Unterschiede in den physikalischen Eigenschaften der mit $H_2Si(Co(CO)_4)_2$ abgeschiedenen Materialien besser zu verstehen wurden mikrostrukturelle Untersuchungen sowohl eines FEBID- als auch eines FIBID-Deponats durchgeführt. TEM-Untersuchungen der FEBID-Co_2Si Probe zeigen ein nanogranulares Material mit cobaltreichen Körnern. Die geringe Größe sowie geringe Abweichungen in der Zusammensetzung der cobaltreichen Körner ließ jedoch keine Phasenidentifikation zu. Im Gegensatz dazu werden bei FIBID-Abscheidungen poröse Deponate beobachtet welche in der lokalen Elementverteilung eine Anreicherung von C und O an den Porenwänden zeigen. Die Porenbildung tritt dabei unabhängig vom Substratmaterial sowie vom Abscheide-Strom auf. Ausgehenden von den mikrostrukturellen Unterschieden, die bei den beiden partikelstrahlbasierten Abscheidemethoden beobachtet werden, können Rückschlüsse auf die unterschiedlichen Zersetzungspfade gezogen werden. Sowohl im FEBID- als auch im FIBID-Prozess werden im ersten Schritt adsorbierte Vorstufenmoleküle unter Freisetzung der meisten CO- und H-Liganden zersetzt und in eine oberflächengebunden Zwischenstufe ($Co_2SiC_xO_y(CO)_z$) überführt, welche zersetzte aber auch intakte CO-Liganden beinhaltet. Die genaue Zusammensetzung hängt dabei vom Prozess, sowie Prozessparametern und der Vorstufe ab. Im Fall von FIBID führt die fortlaufende Abscheidung zu einem kontinuierlichen Ioneneinschlag auf die Probe und zusätzliche Energie wird in die Probe eingebracht. Der Energieübertrag kann dabei als Impulstransfer oder einfach als lokalisierte thermische Effekte verstanden werden. In Folge dessen wird genügend Energie übertragen um die Freisetzung von intakten CO-Liganden sowie die Umstrukturierung der lokalen Mikrostruktur zu ermöglichen. Das dabei freigesetzte, gasförmige Kohlenmonoxid bleibt anschließend in den Poren des Materials eingeschlossen und wird durch sekundäre, elektronenbasierte Prozesse zersetzt. Der daraus resultierende Kohlenstoff scheidet sich and den Porenwänden ab, während der entstehende atomare Sauerstoff das Co_2Si Material oxidiert und so ebenfalls im Deponat erhalten bleibt. Im Gegensatz dazu werden für FEBID dichte Deponate beobachtet welche aber auch, wie zuvor

diskutiert, (anfänglich) intakte Carbonylliganden beinhalten ($Co_2SiC_xO_y(CO)_z$). CO wird in diesem Fall durch die kontinuierliche Elektronenbestrahlung aber nicht freigesetzt, sondern dissoziiert direkt. Zudem ist der Energieeintrag durch den Elektronenstrahl, im Vergleich zum Ionenstrahl, aufgrund der deutlich geringeren Masse, signifikant niedriger. Elektroneninduzierte C-O Bindungsspaltung findet also auch statt, die resultierenden Spezies werden aber deutlich geringere Diffusionslängen besitzen wodurch das Material nur deutlich lokaler beeinflusst wird.

Table of Contents

List of abbreviations XVII

1 Introduction 1

2 Theoretical overview 3

2.1 The FEBID process 3

2.1.1 Fundamental electron-matter interaction processes 3

2.1.2 Modeling the FEBID process 9

2.2 FIBID process 17

2.2.1 Basic principle 17

2.2.2 Modelling of the FIBID process 18

2.3 Chemical vapor deposition 23

2.3.1 CVD process 23

2.4 Precursors for FEBID and FIBID 25

2.4.1 Carbonyls 29

2.4.2 Heterometallic precursor systems 35

2.5 Silicides 38

2.5.1 Mn-Si 39

2.5.2 Co-Si 41

3 Motivation 44

4 Results and Discussion 45

4.1 Homoleptic transition metal carbonyls 45

4.1.1 Vanadium 45

4.1.2 Manganese 54

4.1.3 General considerations for metal carbonyls/conclusion 59

4.2 Single source precursors for FEBID and FIBID 61

4.2.1 $H_3SiMn(CO)_5$ 61

4.2.2 $H_3SiCo(CO)_4$ and $H_2Si(Co(CO)_4)_2$ 66

5 Summary and Conclusion 98

6.1 Precursor synthesis 101

6.2 CVD Process 107

6.3 FEBID and FIBID Process 107

6.4 Analysis 108

7 Appendix 110

7.1 List of references 110

7.2 List of figures and tables 127

List of abbreviations

AE	Auger electron
AES	Auger electron spectroscopy
AFM	atomic force microscopy
AM	additive manufacturing
BF	bright field
BSE	back scattered electron
CMOS	complementary metal oxide semiconductor
CVD	chemical vapor deposition
DD	dipolar dissociation
DEA	dissociative electron attachment
DER	diffusion-enhanced regime
DI	dissociative ionization
EDX	energy-dispersive X-ray spectroscopy
EELS	electron energy loss spectroscopy
ELR	electron limited regime
FEBID	focused electron beam induced deposition
FFT	fast Fourier transform
FIB	focused ion beam
FIBID	focused ion beam induced deposition
GFIS	gas field ion source
GIS	gas injection system
HAADF	high-angle annular dark-field
IR	infrared
LMIS	liquid metal ion source
MIT	metal-insulator transition

MS	mass spectrometry
NBED	nano-beam electron diffraction
NCL	Nowotny chimney ladder
ND	neutral dissociation
PE	primary electron
PLR	precursor limited regime
SAED	selected area electron diffraction
SE	secondary electron
SEM	scanning electron microscope
STEM	scanning transmission electron microscope
TEM	transmission electron microscope
TPD	temperature programmed desorption
UHV	ultra-high vacuum
XPS	X-ray photoelectron spectroscopy
XRD	X-ray diffraction

1 Introduction

The rise of additive manufacturing (AM) processes, commonly referred to as 3D printing, has transformed the way objects can be constructed. Instead of removing material, as in conventional manufacturing methods, components are generated from the bottom up by a defined addition of material according to a 3D model. Initially developed in the 1980s,[1] the techniques have gained significant importance in recent years due to ongoing development, improving not only affordability of the systems but also quality of the prints and range of printable materials.[2] Nowadays AM is especially used for the fabrication of prototypes as well as in small-scale production. The fields of application are broad and range from aviation or automotive industry to medical applications and fundamental research.[2] For example, 3D printing has been used in research laboratories for the fabrication of laboratory hardware, analytical instruments or microfluidic devices.[3] Even though AM is very successful in the generation of macroscopic objects, as soon as the lateral size of the object is decreased various challenges arise. Especially when dimensions in the micron or sub-micron range are required, standard additive manufacturing techniques reach their resolution limit and only a few specialized methods are available, each of which has its advantages and challenges.[4] To address these resolution limits various processes have been developed, all of which rely on either the transfer of preformed material, such as nanoparticles, or the in situ synthesis of the desired material.[4] Among those methods focused electron beam induced deposition (FEBID) and focused ion beam induced deposition (FIBID) achieve the highest resolution. Depending on the experimental parameters, resolutions of below 10 nm,[5] or even below 1 nm have been reported for FEBID.[6]

Both FEBID and FIBID rely on the site-selective decomposition of a volatile precursor molecule by a focused electron or ion beam. The term 3D nano-printing is often used in literature to describe these methods as they allow for the fabrication of nanostructures such as nanodots, nanowires, 2D deposits, as well as complex 3D structures (Figure 1).[7] The shape of the deposit is controlled by scanning the electron or ion beam over a predefined region while controlling the distance (pitch) between each dwell event and the dwell time. Especially the capability of manufacturing 3D nanoscale objects, otherwise not accessible, makes these methods so interesting.[8-9] Various precursor molecules are available for FEBID and FIBID allowing the deposition of materials with interesting superconducting, [10-11] magnetic,[12-13] and/or photonic/plasmonic[14-15] properties. Moreover, deposits have been successfully used as sensing material for various external stimuli including temperature,[16-17] strain,[18] or humidity.[19]

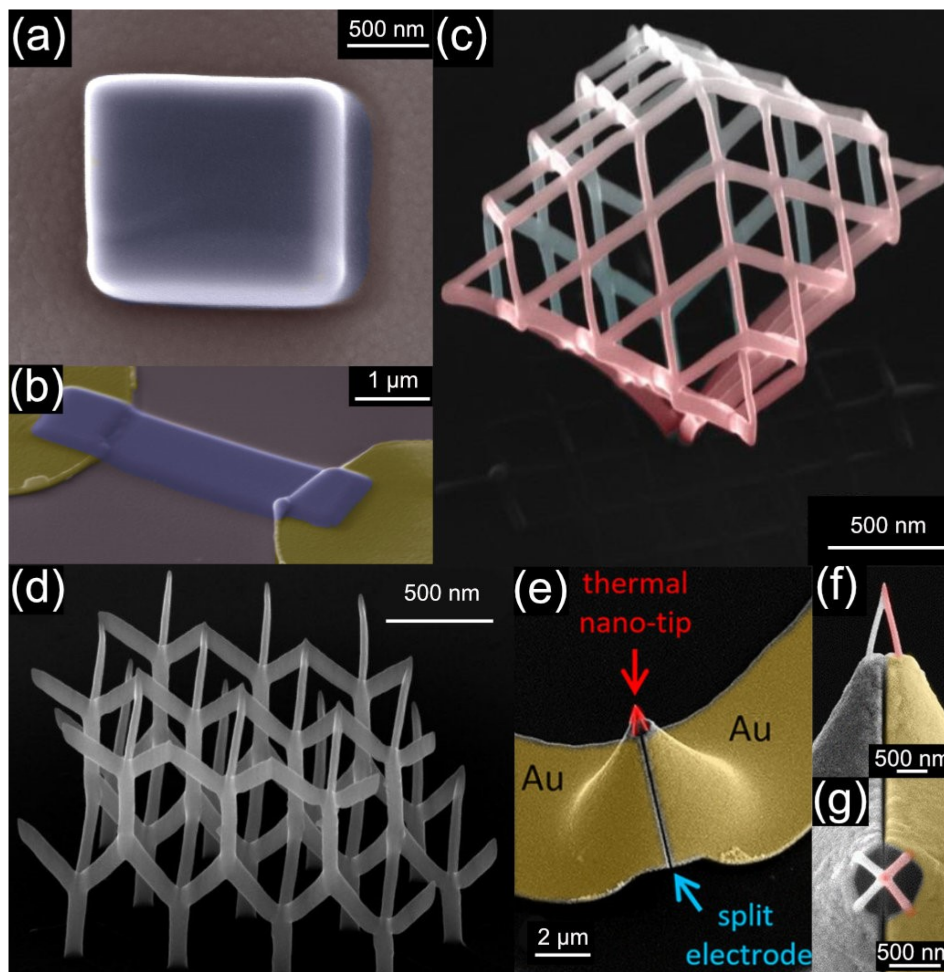

Figure 1: Examples of different FEBID deposits:(a) Square deposit of V:C:O deposited from $V(CO)_6$, (b) tilted view of a bar deposited from $V(CO)_6$ between two gold electrodes for two point conductivity measurements, (c) freestanding PtC nano-cage. Adapted with permission from Ref. 14. Copyright 2017 American Chemical Society. (d) 3D $FeCo_3$ wire-array. Adapted from Ref. 20 by Keller, *et.al.*, licensed under CC BY 4.0 (https://creativecommons.org/licenses/by/4.0/). Published 2018 by Springer Nature. (e) 3D PtC tetrapod acting as thermal nanoprobe deposited across two gold electrodes, (f) side view of the tetrapod, (g) top-view of the tetrapod. Adapted with permission from Ref 17. Copyright 2019 American Chemical Society

2 Theoretical overview

At a first glance, FEBID and FIBID are very similar techniques, both utilizing focused charged particle beams for the local decomposition of adsorbed precursor molecules. The general process is simple and only requires a vacuum chamber equipped with a focused charged particle beam source. Additionally, a suitable precursor is required, which is decomposed by the incident charged particle beam, forming a surface bound material. The desired shape of the deposit is gradually built up by scanning the respective beam over a substrate-surface pixel by pixel according to simple geometric shapes or complex 3D models. However, even though FEBID and FIBID appear to be very similar, distinct differences between both processes exist when viewed in detail. Furthermore, a complex interplay of various reaction pathways has to be considered for each individual process.[21-23]

2.1 The FEBID process

2.1.1 Fundamental electron-matter interaction processes

Focused electron beam-induced deposition typically is carried out in a scanning electron microscope (SEM) at room temperature. Since the actual FEBID process is highly dynamic, complex, and spatially confined, complementary analysis methods are used to gain insights in certain aspects of the process. Interactions of electrons with single molecules or clusters thereof, are investigated in single-collision gas phase experiments (Figure 2(a)). Surface science studies, on the other hand, help to understand electron-molecule interaction of condensed precursor films (Figure 2(b)). Both processes are schematically depicted in Figure 2 and will be discussed in detail below.[23]

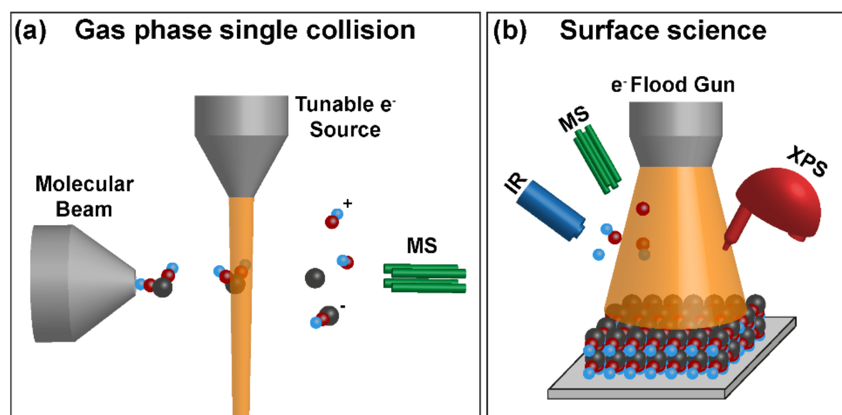

Figure 2: Schematic representation of (a) gas phase single collision experiments and (b) surface science experiments. Reproduced from Ref. 23 with permission from the Royal Society of Chemistry

2.1.1.1 Electron-molecule interactions

The FEBID process fundamentally relies on electron molecule interactions to initiate the decomposition. In principle, two types of interactions can be distinguished: (1) elastic scattering, and (2) inelastic interactions which either lead to excitations (electronic, vibrational, or rotational) or a fragmentation of the molecule. Even though excitations do not necessarily cause a fragmentation directly, they can play an important role in the final composition of the FEBID deposit by taking part in concerted reaction cascades.[24] In general, electron-induced fragmentation of molecules can proceed *via* four different processes:

$e^- + AB \rightarrow A^\bullet + B^-$ dissociative electron attachment (DEA) Eq. (1)

$e^- + AB \rightarrow A^\bullet + B^+ + 2\,e^-$ dissociative ionization (DI) Eq. (2)

$e^- + AB \rightarrow A^\bullet + B^\bullet + e^-$ neutral dissociation (ND) Eq. (3)

$e^- + AB \rightarrow A^- + B^+ + e^-$ dipolar dissociation (DD) Eq. (4)

The effectiveness of each inelastic scattering process can be described by an energy dependent cross section, denoting the probability for the process to occur at a given energy of the incident electron. Actual cross sections span multiple orders of magnitude and depend strongly on the reaction path and the dissociation mechanism. Nevertheless, general trends can be observed for DEA, DI, ND and DD which will be discussed in the following.[25-26]

At the lowest incident electron energies (0-10 eV) dissociative electron attachment typically is the dominating decomposition mechanism. DEA is a resonance process in which the incident electron is captured by the molecule, forming a transient negative ion (TNI). Once formed, the TNI relaxes either by auto detachment of the electron or dissociates, forming an anionic (B^-) and a radical fragment ($A^\bullet$) (Eq. (1)). Both fragments can be either in their ground or in an electronically or vibrationally excited state.[27] The cross section for the overall process is thus the product of the electron capture cross section and the probability for the TNI to survive long enough to induce bond scission. With the probability for electron capture being the highest at 0 eV, the DEA cross sections consequently are typically largest close to 0 eV.[24, 28-30]

For electron energies exceeding 10 eV dissociative ionization becomes increasingly more important. DI is a non-resonant process, in contrast to DEA and can take place if the incident electron exceeds the ionization energy of the parent molecule, causing the liberation of an initially bound electron. This results in the formation of a, potentially excited, cationic parent molecule. If the resulting parent cation is not stable, fragmentation will occur, causing the formation of a cationic fragment and one or more neutral fragments. DI becomes increasingly more efficient with increasing energy, often having a maximum at 50 eV to 70 eV. At higher

energies, a slow decrease in cross-section is observed since the decreased interaction time of the incident electron with the molecule makes a transition less likely.[24-25, 28-30]

Neutral dissociation (ND) is a non-resonant process, similar to DI, that occurs when the parent molecule is electronically excited by an inelastic electron scattering event. The electronically excited parent molecule subsequently dissociates into two (or more) neutral fragments which potentially can be in vibrationally or electronically excited states.[24, 28-30] The threshold for ND is slightly above the bond dissociation energies of the respective bonds broken during the process.[29] For electrons exceeding the threshold energy, the cross-section increases with increasing energy and can be large, even for energies above 100 eV.[28] As the detection of neutral fragments is very challenging only limited data is available.[24, 28-30] However, estimations of ND dissociation cross sections indicate the potential importance of the process in electron-induced decomposition.[31-32] For example, in the case of $Pt(PF_3)_4$ ND is discussed to be the dominant electron induced fragmentation mechanism, with the ND cross section even exceeding the unusually large DEA cross section of the molecule.[33]

Dipolar dissociation (DD) or ion pair formation is very similar to ND but instead of two neutral fragments, a cationic and an anionic fragment are formed. Thus, the Coulomb interaction has to be overcome as well. Consequently, the overall process is considered very inefficient and most likely plays no major role in the electron-induced decomposition.[24, 28-30]

2.1.1.2 Single-collision gas phase experiments

Single-collision gas phase experiments are conducted in order to investigate electron-molecule interactions without any additional intermolecular interactions. The experimental setup consists of a tunable electron source whose beam is crossed with a molecular beam of the precursor of interest. Typically, the experiments are conducted under single collision conditions meaning that the reaction products are detected before any subsequent reactions can occur. As discussed above, cationic, anionic, and neutral fragments can be formed, depending on the electron-molecule interaction mechanism. Charged fragments formed during the electron-molecule collision are extracted from the collision zone by an electric field allowing them to be analyzed by mass spectrometry (MS).[24, 28-29] With this method, energy dependent dissociation cross sections for DEA as well as DI can be determined. The two processes can be distinguished as they are typically active in different energy regions and form anionic and cationic fragments respectively.[26, 28] Moreover, thermodynamic information such as electron affinity, describing the binding energy of an electron to a molecule or a fragment thereof, can be measured.[26, 34] Neutral fragments cannot be distinguished, however, neutral reaction

products of DEA and DI can be derived from theoretically calculated thermodynamics. DD can be investigated as well, however, the cross sections typically are very small.[24, 28-29]

The real FEBID process, however, is considered to be governed by interactions of adsorbed precursor molecules and not free, single molecules in the gas phase.[21, 23] Consequently, additional molecule-molecule and/or molecule-substrate interactions can play a role in electron stimulated reactions. These additional interactions can be investigated, to some degree, in so-called cluster-beam experiments. The setup is very similar to the gas-phase collision experiments described above. However, instead of single molecules, clusters of precursor molecules or aggregates of precursor molecules adsorbed on noble gas clusters are used.[35-36] Considering for example $Fe(CO)_5$, strong influences of the environment on the electron-induced decomposition process were observed when comparing isolated molecules with aggregates adsorbed on argon clusters. For example, a low-energy DEA channel present in single collision experiments was completely suppressed for adsorbed $Fe(CO)_5$. Additionally self-scavenging was observed at higher energies (5-25 eV), resulting in the formation of complex fragments.[37] Thereby self-scavenging denotes a reaction in which the incident electron is slowed down by one cluster constituent and subsequently attaches to a different one, a process not possible for isolated molecules.[37]

Gas phase studies are an important tool for understanding the fundamental mechanisms of electron-molecule interactions. However, molecule-molecule and molecule-substrate interactions present in the FEBID-process cannot be modeled well. As a consequence, dissociation mechanisms dominant for isolated molecules can be suppressed for condensed precursor molecules, as indicated in gas-phase cluster experiments.[28]

2.1.1.3 Surface science studies

The gas-phase studies are complemented by so-called surface science experiments. Instead of single molecules or clusters, few monolayers of precursor molecules are condensed onto a chilled (below 200 K), typically very defined, substrate. The resulting precursor film is subsequently irradiated by an electron flood gun with low energy electrons (typically 200-500 eV).[38] Changes in the film are monitored by various analytical methods during and after the irradiation. Typically Auger electron spectroscopy (AES) or X-ray photoelectron spectroscopy (XPS) are used for monitoring changes in composition and chemical nature of the surface-bound species.[38-40] Additionally, infrared spectroscopy (IR) can be used, providing information on the presence of certain bond types.[39, 41] Upon irradiation of precursor films volatile fragments are formed, which subsequently are analyzed by MS.[42-43] Often temperature programmed desorption (TPD) experiments are performed in which the irradiated films are heated to room temperature (or above) and the evolving volatile species are monitored by

MS.[38, 44-45] Thermal effects during the decomposition process can be investigated by comparing TPD experiments with and without electron beam irradiation. For example, significant contributions of thermal fragmentation have been observed in surface science experiments for $HFeCo_3(CO)_{12}$,[42] $Ni(CO)_4$[46] and $Fe(CO)_5$,[47] all showing the evolution of CO after heating of electron irradiated precursor films. However, this approach is limited as the origin of the detected ligand or ligand fragment is typically unclear. In the simplest case the desorbing species is caused by temperature-induced desorption of ligands, already cleaved from the central atom by electron irradiation. Yet, the electron-induced formation of thermally labile intermediates which decompose upon heating could also be possible.

Based on surface science studies conducted with various FEBID precursors a two-step process for the electron induced decomposition is very likely.[39, 42-43, 48-52] Initially, physisorbed precursor molecules are converted into a surface-bound species by a stepwise loss of ligands. In very few cases heating of this intermediate results in the liberation of all remaining ligands and pure deposits can be obtained, indicating that retained ligands stay intact.[46-47] Most of the time, however, the remaining ligands will be incorporated into the deposit and undergo fragmentation upon further irradiation of the deposit.[44, 53]

Surface science investigations only provide partial information on the real FEBID process, similar to the gas phase studies. Contrary to the very controlled conditions during these types of experiments, the local pressure, as well as the substrate temperature are much higher during FEBID. This causes a complex interplay of adsorption and desorption of intact precursor molecules and fragments thereof. Additionally, kinetic effects such as deposition dynamics cannot be modelled in surface science studies. In the real FEBID process fragment desorption also has to be considered. Because even if all ligands can be removed by electron beam irradiation the resulting fragments also need to desorb fast enough in order to not be buried by subsequently deposited material. Furthermore, surface science experiments typically use very defined, single crystalline substrates whereas FEBID materials usually are either granular materials exposing various crystal facets or amorphous.[38] The different surfaces could impact the decomposition mechanism or the adsorption/desorption behavior, thus altering the final deposit.[23] For example, crystallographic orientation plays a major role in heterogenous catalysis with typically high-indexed faces showing higher catalytic activity.[54] Furthermore, an influence of different crystal facets on adsorption and desorption behavior of molecules has been demonstrated.[55]

2.1.1.1 Electron-specimen interaction processes

In surface science studies low electron energies of typically 500 eV or less are used,[38] while the actual FEBID process uses much higher acceleration voltages of typically 5 kV to 30 kV.[21, 23] As a consequence, various interactions of the electrons with the substrate material have to be considered. Similar to the interaction of electrons with molecules, two fundamental processes can be distinguished: (1) Elastic interactions in which the electrons only change their trajectory conserving their kinetic energy and (2) inelastic collisions where some energy is transferred to the sample causing various secondary processes.[56] The interaction volume is not confined to the irradiated area but electron-substrate interactions will take place in a pear shaped volume since electrons can undergo multiple scattering events. The exact shape and size of this interaction volume are determined by the energy of the primary electrons (PE) E_0 and the substrate material. Electrons can be emitted from this volume resulting in a spatial distribution, as well as an energy distribution, both also depending on the substrate material and E_0.[22] The emitted electrons are typically categorized into low energy secondary electrons (SE), and higher energy backscattered electrons (BSE), as described in detail below.[56] Additionally, inelastic collisions can cause the generation of photons in the form of characteristic X-rays, Bremsstrahlung X-rays, and cathodoluminescence, as well as heat.[56] Figure 3 shows a schematic representation of the energy distribution of electrons emitted from a metallic surface, being irradiated with an electron beam with energy E_0. The low energy region is dominated by secondary electrons formed by inelastic collisions of primary electrons (PE) with, typically weakly bound, electrons of the substrate material. Commonly SE are defined as electrons with energies below 50 eV with their maximum well below 10 eV.[56] Secondary electrons are the dominating species since each primary electron typically generates multiple secondary electrons. The exact amount, as well as, the shape of the SE energy distribution is dependent on the nature of the substrate and E_0.[57-58] SE are considered to be the main cause of electron-stimulated decomposition during FEBID processes, due to their large abundance at the surface and their high interaction probability with molecules.[59] However, also electrons above 50 eV, commonly referred to as backscattered electrons, will contribute in the decomposition process.[60-61] The broad energy range of BSE from 50 eV up to the primary electron energy is caused by electrons suffering multiple energy losses, as well as, undergoing multiple scattering events. Additionally, minor contributions of Auger electrons (AE) can be observed. Similar to X-ray photons Auger electrons are generated when a core electron is removed by an elastic collision and the vacancy is filled with an electron of higher energy. The energy difference is either released as an X-ray photon or transferred to another electron, which then is ejected from the atom as AE. Similar to X-ray photons Auger electrons can be used for spectroscopy. The upper end of the electron energy distribution is dominated by the elastically scattered primary electron beam. Additionally, peaks related to plasmonic

losses can be visible close to E_0 for metallic substrates. Plasmons can be described as collective oscillations of the electron gas. Consequently, plasmonic losses are observed for inelastic collisions which cause the excitation of such oscillations.

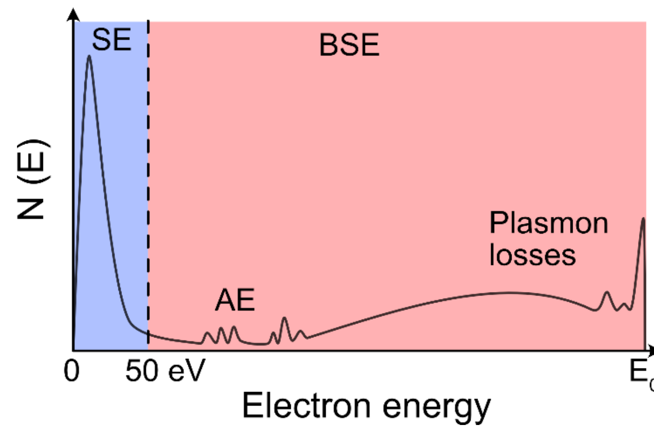

Figure 3: Schematic representation of electron energy distribution emitted from a metallic surface upon electron irradiation with an electron beam of energy E_0. Electrons below 50 eV are defined as secondary electrons (SE) while electrons exceeding 50 eV are called backscattered electrons (BSE). Additionally, Auger electron (AE) peaks and signals corresponding to plasmon losses are visible. Redrawn following Reimer.[56]

2.1.2 Modeling the FEBID process

Based on the fundamental understanding of electron-matter interactions models describing different aspects of the FEBID process have been developed.

2.1.2.1 Continuum model of FEBID

A schematic representation of the FEBID process is depicted in Figure 4. In a first step precursor molecules are fed into the high vacuum environment of the deposition chamber and subsequently physisorb on the substrate surface. Typically, a gas injection system (GIS), equipped with a thin needle (typically about 500 µm diameter), is used to provide the precursor molecules in close proximity to the deposition site (usually few 100 µm laterally and vertically). Physisorption is a reversible, dynamic process in equilibrium with desorption for the suitable precursors at room temperature. Consequently, an equilibrium coverage of the surface will result which is characterized by an average residence time τ. When the electron beam is scanned over the surface, adsorbed precursor molecules are decomposed in the focus of the beam, forming the deposit and volatile by-products, which subsequently desorb. This causes a local depletion of precursor which is replenished either by surface diffusion or by adsorption from the gas phase. The shape of the deposit is controlled by the lateral distance between each deposition event (pitch) and the time the beam remains at a certain position (dwell time).

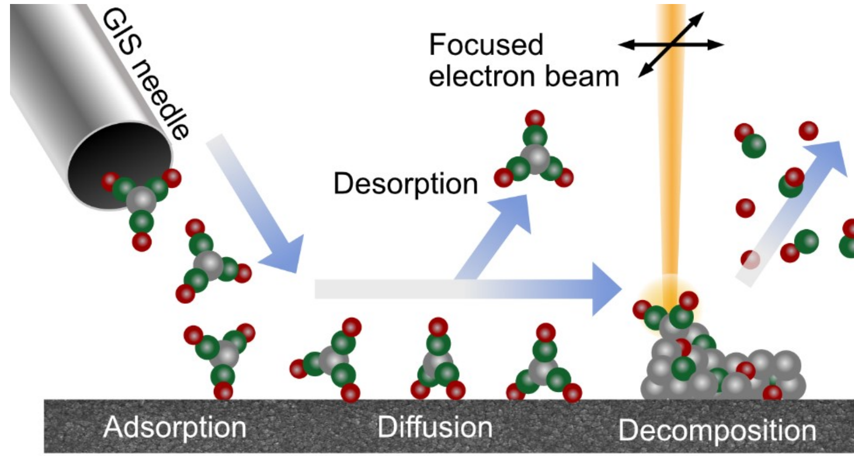

Figure 4: Schematic representation of the FEBID process.

Ideally the growth-rate and shape evolution can be described by a mathematical model as function of the experimental parameters, thus helping in the understanding of the underlying growth mechanisms. One model to describe the FEBID process is the so called continuum model. This model is comprised of equations describing the local growth rates in dependence on the deposition parameters as well as the local availability of precursor molecules.[62] The local, electron-induced growth rate $R_e(r)$ per unit time can be described as:[21]

$$R_e(r) = Vn(r) \int_0^{E_0} \sigma_e(E) f_e(r, E) dE \qquad \text{Eq. (5)}$$

Where V is the volume deposited per precursor molecule, $n(r)$ is the local precursor density, $\sigma_e(E)$ is the energy dependent decomposition cross section and $f_e(r, E)$ is the energy dependent electron flux distribution (including secondary and backscattered electrons).[21] The subscript e is used to indicate electron beam related terms. The energy dependent dissociation cross section is typically not known accurately and thus usually is approximated by an effective, energy-integrated cross section σ_e.[21, 59] As a consequence, the integral term in Eq (5) can be replaced by the product $\sigma_e f_e(r)$. Thus, the growth rate per unit time can be approximated as: [21]

$$R_e(r) = Vn(r)\sigma_e f_e(r) \qquad \text{Eq. (6)}$$

The effective local electron flux distribution $f_e(r)$ can be measured independently or simulated by Monte Carlo methods.[21, 59] For the description of the local evolution of precursor coverage four general processes have to be considered: (1) Adsorption and (2) desorption of precursor molecules from the gas phase, (3) diffusion of adsorbed precursor on the surface, and (4) precursor depletion, due to electron induced decomposition.[21, 59, 62] Assuming a Langmuir

adsorption behavior, a surface-reaction diffusion equation can be established, for simplicity the location dependency of n is not stated explicitly:[21, 59, 62]

$$\frac{\partial n}{\partial t} = \underbrace{sJ\left(1-\frac{n}{n_0}\right)}_{Adsorption} - \underbrace{\frac{n}{\tau}}_{Desorption} + \underbrace{D\left(\frac{\partial^2 n}{\partial r^2}+\frac{1}{r}\frac{\partial n}{\partial t}\right)}_{Diffusion} - \underbrace{\sigma_e f_e n}_{Decomposition} \qquad \text{Eq. (7)}$$

In the Langmuir model adsorption is governed by the sticking probability s, (local) precursor flux J, and surface coverage n/n_0. Desorption is only governed by the amount of adsorbed precursor molecules n and the average residence time τ. Diffusion is described by the diffusion coefficient D and the local concentration gradient of the precursor. Removal of precursor by electron induced decomposition is given by the product $\sigma_e f_e n$ similar to Eq. (6). If all these parameters are known, Eq. (7) can be solved for the local precursor coverage $n(r)$ at each time step.[21, 63] Many of the parameters required are, however, precursor specific and have to be either estimated or extracted from experimental data. For example, dissociation cross sections can be estimated reasonably well from gas phase and surface science studies.[64-65] Temperature dependent diffusion and desorption behavior can be deduced, for instance, from specially designed FEBID experiments.[64, 66-67] In conjunction with Monte Carlo simulations, describing the local electron flux, the equations can be solved for each time step, thus allowing to effectively simulate FEBID growth.[59]

2.1.2.2 Growth regimes

Based on the continuum model described above three different growth regimes can be distinguished. (1) The precursor limited regime (PLR) which is characterized by a quick depletion of precursor in the beam region. Additionally, surface diffusion is negligible and precursor replenishment is governed by adsorption from the gas phase. (2) The diffusion-enhanced regime (DER), a subset of PLR. Precursor molecules are still depleted rapidly in the focus of the electron beam and replenishment now proceeds predominantly by surface diffusion. (3) The electron limited regime (ELR), in which precursor is replenished much faster than it is decomposed and thus the growth is limited only by the amount of available electrons.[21] Morphological changes can be expected in dependence on the growth regime and patterning strategy. Assuming a Gaussian-shaped, stationary electron beam four distinct cases are predicted by the continuum model (Figure 5(a)), matching well with experimentally observed shapes.[68]

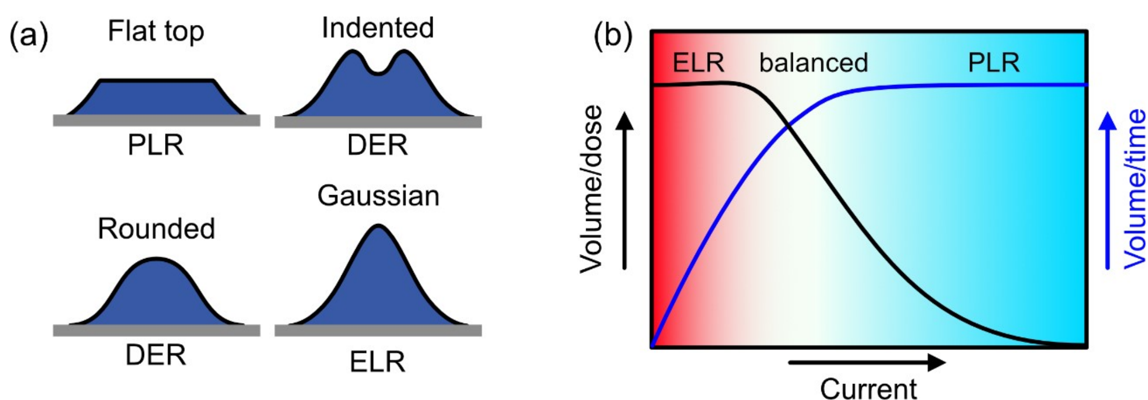

Figure 5: (a) Shapes observed for a Gaussion electron beam dependent on the different growth regimes, based on.[68] (b) Development of growth rate as a function of electron supply (current). With increasing current, a transition from electron limited growth to precursor limited growth is observed.

For the PLR a flattop deposit is expected.[68] Precursor molecules are depleted rapidly in the irradiated region while precursor replenishment is dominated by gas phase adsorption which, in first approximation, is isotropic.[68] In the case of diffusion enhanced growth two different shapes are observed (Figure 5(a)).[68] If diffusive replenishment is slow compared to the electron induced decomposition the precursor molecules will already be decomposed by the tails of the electron beam resulting in an indented shape.[68] If however, the decomposition is slow or, *vice versa*, surface diffusion is fast, a rounded deposit will be observed.[68] In electron limited growth, precursor molecules are replenished faster than they are decomposed and the deposit will reproduce the Gaussian shape of the electron beam profile.[68] For 2D and 3D deposits similar effects can be observed as well.[69] However, clever choice of patterning strategy can reduce or eliminate the effects.[69] Additionally, the directionality of the precursor supply has to be taken into account. Since the precursor molecules are typically supplied by a needle, positioned in close proximity to the growing deposit, shadowing effects can drastically alter the local precursor concentration.[70-71] These effects can become especially pronounced for 3D deposits.[70-71]

Growth regimes can also be distinguished using laterally extended deposits by considering normalized volume growth rates as schematically depicted in Figure 5(b). In the ELR the growth rate only depends on the number of available electrons. Consequently, the same volume will be deposited per charge, independent of the electron beam current (black line in Figure 5(b)). However, if the deposited volume per time is considered, an increase will be observed since by increasing the current more electrons are supplied in a shorter time frame (blue line in Figure 5(b)). In PLR the growth rate depends only on precursor supply, thus the faster the electrons are provided (*i.e.* the higher the current) the less time is available for precursor replenishment, causing a decrease in growth rate normalized to the dose. In the

most extreme case, the complete dose is provided instantaneously and only the initially adsorbed precursor molecules are decomposed, resulting in a quasi-zero growth. No change with increasing electron current is expected considering the time-dependent growth rate, as already enough electrons are available. Diffusion-enhanced growth can be distinguished by the morphological features of the deposits, depending on the patterning strategy. In this work, for example, a serpentine scanning routine was chosen. If the diffusive replenishment is slow compared to the time required for one pass, decomposition of diffusing precursor molecules will be concentrated to the sides of the deposit resulting in elevated edges.[69, 71] It should be noted, however, that all volumetric growth rates will only be exact for one deposition shape and size and of course precursor and deposition parameters. For example, doubling the irradiated area while keeping pitch and dwell time constant will also double the time required for one pass. As a consequence, much more time for replenishment is available, potentially causing an increase of the local precursor concentration (depending on equilibrium coverage and diffusion constants at the given temperature).

2.1.2.3 FEBID process on a molecular level

The overall FEBID process is dependent on many different parameters (pressure, substrate temperature, electron beam-related parameters, …) and thus a universal understanding of the process is still missing. And even though continuum models of the FEBID process can be used to accurately describe the shape evolution, processes taking place at a molecular level are not considered. These are however important in understanding for example the purity of the deposit and if and how deposition processes could be optimized. Based on the fundamental understanding of electron-matter interactions described in chapter 2.1.1, a schematic representation of the FEBID process on a molecular level can be provided (Figure 6).

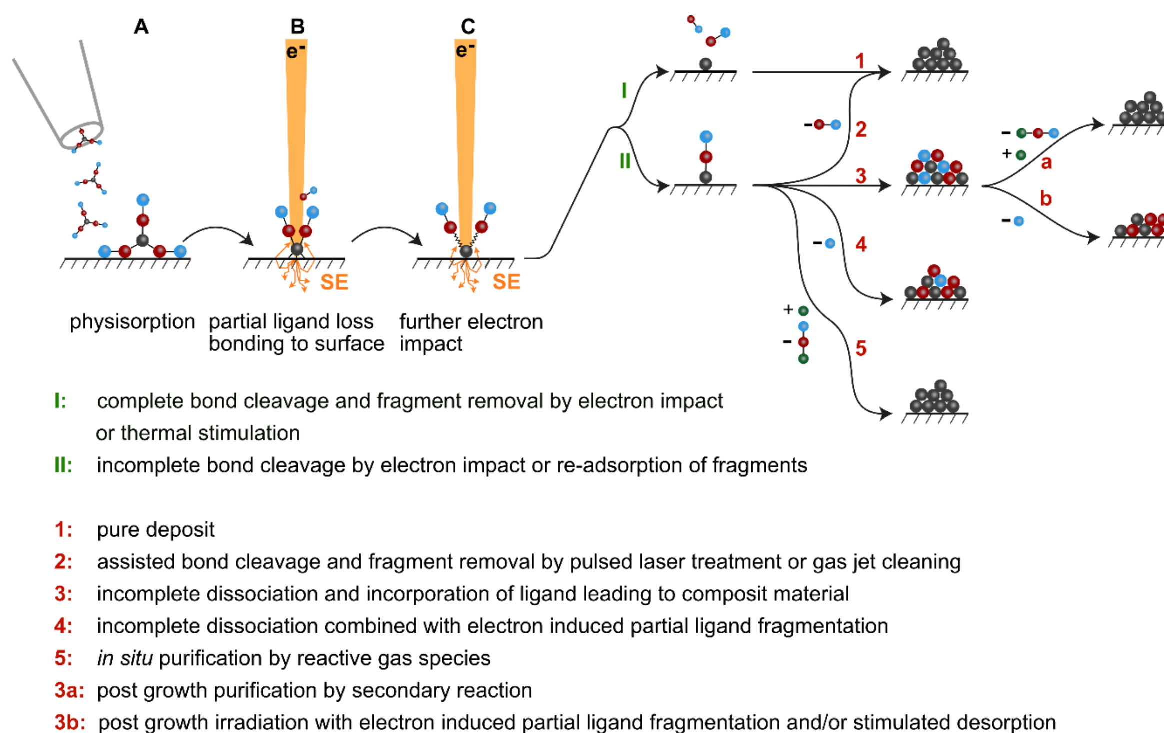

Figure 6: Schematic representation of the FEBID process. Adapted from Ref. 23 with permission from the Royal Society of Chemistry.

In the first step, precursor molecules are leaked into the SEM chamber in close proximity to the deposition area. This allows for high local precursor pressures, and thus an increased surface coverage, while the pressure in the SEM chamber typically remains below 1×10^{-5} mbar. The precursor pressure is adjusted according to the volatility of the molecules by either heating or cooling of the reservoir and regulated by the use of needle valves. The incident precursor molecules then physisorb on the substrate (Figure 6 A). Physisorption arises from van der Waals forces, *i.e.* the interaction of two dipoles, the interaction of a dipole with an induced dipole, or two fluctuating dipoles interacting with each other. Since physisorption is caused by intermolecular forces and no chemical bond is formed it is considered weak (typically 10-100 meV).[72] Consequently, physisorption as well as its inverse process, desorption, is fast for substrates at room temperature. A dynamic exchange of surface-bound and gas phase species will take place, resulting in an equilibrium coverage that is characterized by an average residence time of the adsorbed species. This residence time is dependent on the strength of molecule-substrate interactions as well as substrate temperature and local partial pressure of the adsorbing molecules. For the FEBID process to be efficient, the average residence time of intact precursor molecules must be sufficiently long to allow for an interaction of the incident electrons with the molecules. Additionally, cleaved ligands and fragments thereof should interact very little with the surface and desorb quickly, in order to not be incorporated in the growing deposit and compete with intact precursor molecules for

adsorption sites. As already mentioned above, the electron-stimulated decomposition processes are likely dominated by interactions with SE and BSE. In most setups, a high abundance of SE is observed near the surface, as each PE can create many SE. The electron-molecule interaction can, in theory, lead to a complete or partial decomposition. According to surface science studies a partial loss of ligand(s) and the transition to a chemisorbed species is often observed (Figure 6 B).[42, 44, 48, 52] Successive electron irradiation or, more likely, thermally induced processes can support the cleavage of remaining metal-ligand bonds (Figure 6C) resulting in their liberation and the formation of pure deposits (Figure 2 C-I).[23] However, only very few precursors, namely $Ni(CO)_4$[73], $Fe(CO)_5$,[74] $Co_2(CO)_8$,[75-76] and $HFeCo_3(CO)_{12}$[20] have been reported to yield basically pure deposits. More often only partial ligand loss (Figure 6 C-II) or re-adsorption of initially removed ligands or ligand fragments is observed, resulting in impure composites.[23, 44, 48, 77] For re-adsorption, the diffusion layer close to the surface, as well as the by-products of the decomposition, have to be considered. In both cases, a composite material will be obtained and the elemental composition will reflect the relative elemental distribution of the ligands (Figure 6 C-II-3). Additionally, intra-ligand bond scissions can be observed, resulting in the partial liberation of ligand fragment(s) thus altering the overall composition (Figure 6 C-II-4).[78] For example, in the case of $Pt(PF_3)_4$ selective loss of fluorine has been observed, indicating an effective P-F bond scission.[79] Similar effects were described for transition metal carbonyls. For instance, deposits derived from $Co_2(CO)_8$ show a selective loss of oxygen when compared to carbon.[80] Even though this indicates a C-O bond scission additional effects have to be considered as well. Fragmentation of the carbonyl ligand will form highly reactive oxygen species which can form oxides, thus potentially retaining O in the sample. In this case a selective loss of oxygen could be observed nevertheless since some transition metal oxides can be reduced by prolonged electron beam irradiation under vacuum conditions.[81]

Pure deposits can be obtained from partially decomposed/re-adsorbed intermediates (Figure 6 C-II) if additional energy for the desorption of ligands/ligand fragments is supplied (Figure 6 C-II-1). Two approaches have been discussed in the literature, both using $W(CO)_6$ as the precursor which typically yields deposits with up to 50 at% tungsten under standard conditions.[75, 82] The first method relies on the combination of laser-assisted chemical vapor deposition (CVD) with FEBID. Initially, a thin layer was deposited by FEBID which then was purified by a pulsed laser treatment, resulting in an efficient (thermally induced) removal of remaining CO ligands. By alternating FEBID with laser irradiation, high purity deposits were obtained.[83] In an alternative method the precursor molecules were delivered to the substrate in a supersonic carrier gas jet.[84] The high purity of the material, in this case, is very likely related to a momentum transfer of the incident gas molecules to the partially fragmented precursor species causing the liberation of CO.[23]

Alternatively, unwanted contaminations can be removed by co-dosing of additional reactive gas species during the deposition process (Figure 6 C-II-5). In most cases oxidizing process gases are used, typically O_2[85] or H_2O.[85-86] For example, $Me_2Autfac$ yields deposits with approximately 15 at% to 30 at% gold using standard conditions[87-88], however by co-dosing of water during the deposition material with up to 92 at% gold has been obtained.[89] In the case of non-precious metals their high oxygen affinity typically leads to the formation of the respective oxides such as SiO_2,[90-91], MoO_x,[92] and Fe_3O_4.[93]

A different approach is the purification of the deposit after the FEBID process, either by physical or chemical means (Figure 6 C-II-3a+b). Chemical post-growth purification methods rely on thermally or electron-induced reactions with either oxidizing or reducing process gases (Figure 6 C-II-3a). Oxidizing conditions, typically using oxygen[94-95] or water[96], are used for noble metal containing deposits such as Pt[97] and Au[89]. For example, pure Pt deposits have been obtained by electron irradiation of $MeCpPtMe_3$-derived material in the presence of water.[96] Moreover, also deposits containing less noble metals such as ruthenium can be purified by electron stimulated reactions with water. However, fine-tuning of electron dose is required to prevent oxidation of the metal.[98] Alternatively, reducing conditions can be applied, using atomic hydrogen, formed by passing hydrogen gas over a hot tungsten filament.[99] On the other hand, physical post-growth purification can be achieved by either thermal annealing of the samples at elevated temperatures[100-101] or post-growth electron irradiation of the deposit, each under vacuum (Figure 6 C-II-3b).[102-104] Both physical post-growth purification methods can alter the chemical composition of the deposit by liberation of incorporated ligands or fragments thereof. The chemical nature of the carbon matrix, present in most FEBID deposits, will change as well, due to perpetual C-H cleavage and/or graphitization/carbonization.[100, 102] Moreover, changes in microstructure can be observed as energy for diffusion and/or grain growth is provided during the treatment. In the case of granular PtC_x deposits, for example, prolonged post-growth electron irradiation was reported to cause a decrease in resistivity by more than two orders of magnitude while also changing the temperature dependent conduction behavior of the samples.[102] Microstructural analysis related these changes to a reduction of Pt inter-grain distance as well as graphitization of the carbonaceous matrix.[102] The observed grain growth implies the presence of “free” platinum in the deposit, most likely in the form of incompletely dissociated precursor. Upon continuous electron beam irradiation, these platinum reservoirs release metal species that subsequently diffuse to already formed grains. This causes an increase in Pt particle size, consequently altering the electronic behavior of the deposit.[23]

2.2 FIBID process

Since their development in the 1970s and 1980s focused ion beams (FIBs) have found widespread application as nanofabrication tools.[26, 105] Typically, ion beams are used for localized etching, for example in the preparation of TEM lamella.[106] However, similar to FEBID, they can also be used for the localized decomposition of precursor molecules. Analogous to FEBID this process is called focused ion beam induced deposition or FIBID.[105] The working principle of a focused ion beam is very similar to the focused electron beam in an SEM. A beam of ions is generated from a source which is then focused on the sample using electronic and magnetic lenses.[106] Similar to the electron beam in an SEM the FIB can be scanned over the surface using deflector coils, thus irradiating only a defined region of the sample.[105, 107]

2.2.1 Basic principle

Various ion sources are available for focused ion beam methods, however, Ga^+ is the most common one and is typically used in dual beam electron microscopes.[108] In the case of gallium, the ion beam is generated from a liquid metal ion source (LMIS). Besides Ga, this type of ion sources can be used for various other metals and low melting eutectic alloys.[108] The ion beam is generated by feeding the molten metal or alloy to a sharp tungsten needle. Subsequently, a Taylor cone is formed by applying a strong electrical field and ions are ejected from the tip of the cone by field evaporation.[109] Furthermore, gas field ion sources (GFISs), typically providing noble gas ions, are also available.[105] In these sources the ion beam is formed by field ionization of a gas in close proximity to a cooled, sharp needle held at a high voltage.[108] The best known application of a GFIS is helium ion microscopy,[110] which also has been used successfully for FIBID applications.[111-112]

When a material is irradiated by an ion beam various elastic and inelastic interactions can take place. In the simplest case an elastic interaction with the substrate occurs and the ion is reflected, forming a backscattered ion. However, if energy is transferred to the substrate distinct reactions can take place. If the kinetic energy of the incident ion exceeds the binding energy of a surface atom it can be ejected as a sputtered particle (either as a neutral atom or a charged ion). The sputtered species will be, depending on their trajectory, redeposited on any nearby surface, resulting in the buildup of material around the sputtered area. Displacement of surface atoms can occur if less than the binding energy is transferred, effecting the crystallinity very locally and leading to amorphization. Additionally, the incident ions can be implanted in the material, often causing swelling. Whenever an inelastic collision occurs, energy is transferred from the incident ion to substrate atoms. In turn, this additional energy is dissipated by the formation of secondary electrons and secondary ions or causes

the emission of photons of various energies (ranging from X-rays to IR). Furthermore, the collisions of high-energy ions with the substrate leads to a local heating.[26, 105]

All the secondary particles generated by ion impact can be used for image generation as well as for spectroscopy techniques, analogous to the scanning electron microscope.[105] Compared to SEM, ion beam microscopy has one big advantage. With their significantly higher mass the corresponding wave length is considerably shorter for ions and thus much higher resolutions become physically possible.[113] Plus the shorter wave lengths allow to reduce the convergence angle, therefore increasing the depth of view.[113] However, sputtering and ion implantation during the imaging process will alter the sample, making ion beam microscopy a destructive technique.[113]

2.2.2 Modelling of the FIBID process

The general process and instrumentation for FIBID are very similar to FEBID, with the main difference being that a focused ion beam instead of a focused electron beam is used to initiate the decomposition reaction. This implies different decomposition mechanisms and, due to the higher mass of ions compared to electrons, physical sputtering has to be considered as well. Nevertheless, the volume dependent growth rate can be described analogous to Eq. (5).[21] Similar to FEBID the energy dependent cross section is not known and approximated by an effective dissociation cross section σ_i.[21] The growth rate can then be described as:

$$R_i(r) = Vn(r)\sigma_i f_i(r) \qquad \text{Eq. (8)}$$

Where V is the volume deposited per molecule, $n(r)$ the local precursor concentration and $f_i(r)$ describes an effective local ion beam flux.[21] Additionally, sputtering has to be taken into account decreasing the total growth rate. For FIBID the sputtering rate is assumed to be independent of the number of adsorbed precursor molecules and can be described as: [21]

$$R_s(r) = Y_s V f_i(r) \qquad \text{Eq. (9)}$$

With Y_s being the physical sputtering yield and V the corresponding volume.[21] A net growth of a deposit is only observed if the growth rate supersedes the sputtering rate ($R_i > R_s$). The overall growth rate then becomes:[21]

$$R_{net} = R_i(r) - R_s(r) \qquad \text{Eq. (10)}$$

Similar to FEBID the local precursor concentration can be described by a surface-reaction equation and knowing all the parameters, the local growth rate for each timestep could be

calculated.[21] Up to date, however, the main focus for modelling focused particle beam growth is on FEBID processes as they are simpler and better understood. To the best of my knowledge no simulation packages for FIBID are currently available.

2.2.2.1 Towards a molecular understanding of the FIBID process

Similar to FEBID, fundamental processes in the decomposition of molecules by ion beams can be investigated by gas phase or surface science studies. However, FIBID is significantly less well investigated when compared to FEBID. Additionally, in FIBID, interactions of electrons as well as ions have to be considered.

In single collision experiments of ions with molecules two interaction mechanisms can be distinguished: (1) interaction of the ion with the electron cloud of the molecule and, (2) interaction by elastic collision with the nucleus. The contribution of these two mechanisms depends on the energy of the ion, its charge state, as well as, its mass. Studies with FIBID precursors are very rare and to the best of my knowledge only $Fe(CO)_5$ has been investigated to date. When $Fe(CO)_5$ was irradiated with noble gas ions of different charges and energies, differences in the fragmentation pattern were observed. In all cases, stepwise loss of CO groups is observed as the main decomposition pathway. Interactions of light ions, such as He^+, are dominated by electronic interactions and thus the formed fragments have low kinetic energies and *vice versa*. Extensive fragmentation was observed for singly charged ions with He^+ and Ar^+ resulting in, on average, one CO group remaining on the iron atom. In the case of higher charged ions (He^{2+}, Ne^{4+}, Ar^{3+}, Kr^{3+}, Kr^{17+}) on average two CO groups were retained. The highest efficiency was reported for Ne^+ at 6 kV with only 0.3 CO groups on average remaining on the Fe.[114]

Surface science studies for irradiation with ions are conducted very similar to surface science studies for irradiation with electrons. Instead of an electron flood gun a low energy ion source is used (typically argon).[38] The precursor of interest is condensed onto a cooled substrate, which is positioned inside an ultra-high vacuum (UHV) setup, and subsequently irradiated. The film is analyzed prior to and after the irradiation, typically using XPS, AES, and/or IR allowing for investigation of not only composition but also the chemical nature of the respective atoms.[38, 48, 115] Additionally, volatile fragments formed during the irradiation are investigated by MS.[38, 48, 115] The available studies indicate that, similar to FEBID, the process proceeds in two steps. Initially, the physisorbed molecules are transformed to surface-bound species by metal-ligand bond scission. Typically, more ligand atoms are removed in this initial step when compared to electron beam irradiation, however a strong dependence on ligand type is observed. For example, carbonyl ligands are removed very effectively while Cp or iodine are retained in the deposit.[115-116] Additionally, some of the ligands potentially undergo decomposition. In the

second step, ion-induced sputtering becomes dominant causing a purification of the material because light atoms and atoms with lower binding energy are sputtered more efficiently.[117] However, as sputtering is a statistical process, also some of the heavier metal atoms are removed by subsequent ion beam irradiation.[48, 115-116]

Surface science studies, as well as, gas phase investigations only provide a piece of the complete picture. Nevertheless, they are important tools in building a deeper understanding of how the FIBID process works.

2.2.1.2 FIBID process on a molecular level

Even though the FIBID process is not as well investigated as FEBID some general conclusions can be drawn based on surface science and gas phase studies. In FIBID not only (secondary) electrons can play an important role for decomposition, contrary to FEBID. Additionally, energy transfer *via* direct collisions, causing decomposition or sputtering, has to be taken into account as well. The contribution of each individual process, however, will depend on the ion type and incident energy.[118-121]

A schematic depicting the potential process on a molecular level is shown in Figure 7. In the first step (Figure 7-A) precursor molecules are leaked into the chamber and physisorb on the substrate surface. Experiments are typically conducted at room temperature and a dynamic equilibrium of adsorption and desorption will be established, similar to FEBID. The decomposition is then initiated by scanning an ion beam over the desired deposition area (Figure 7-B). The interaction of the FIB with the substrate, or later the deposit, results in the formation of secondary electrons, which, similar to FEBID, contribute to the decomposition of adsorbed precursor molecules. Additionally, the momentum transfer of the incident ions to the substrate has to be considered as well. The energy transfer is often described as a series of binary collisions, resulting in the displacement of atoms.[21, 119] The term collision cascade is used to describe this process.[119] If the collision occurs near the surface and the transferred energy exceeds the surface binding energy the recoil atom will be sputtered from the surface.[122] A net deposition of material thus is only obtained if the growth rate exceeds the sputtering rate. However, also if no sputtering takes place energy will be transferred to the substrate resulting in localized heating.[123-124] Alternatively, the localized heating is described as excited surface atoms which interact with adsorbed precursor molecules *via* binary collisions.[119] Independent of the model, energy will be transferred to adsorbed precursor molecules causing desorption, (partial) ligand loss, or excitation of adsorbed precursor molecules (Figure 7-B). Further ion beam irradiation (Figure 7-C) will result in either partial (Figure 7-C-II) or complete (Figure 7-C-III) dissociation. In the ideal case, complete removal of all ligands is observed and a pure deposit is obtained (Figure 7-C-I-1). However, reports of

clean FIBID deposits are rare.[111] During the deposition process, sputtering and material deposition will take place simultaneously. Sputter rates are, however, dependent on bond strength as well as the mass of the atom.[117] With lighter elements being typically sputtered preferentially a complete (Figure 7-C-II-2) or partial (Figure 7-C-II-4) removal of ligand atoms can be observed. On the other hand, if the growth rates and/or the ligand binding energies are very high, sputtering effects will be limited and all initially remaining ligands will be incorporated into the deposit (Figure 7-C-II-3). Finally, interactions of ions with molecules in the gas phase can potentially contribute to material deposition as well.[125]

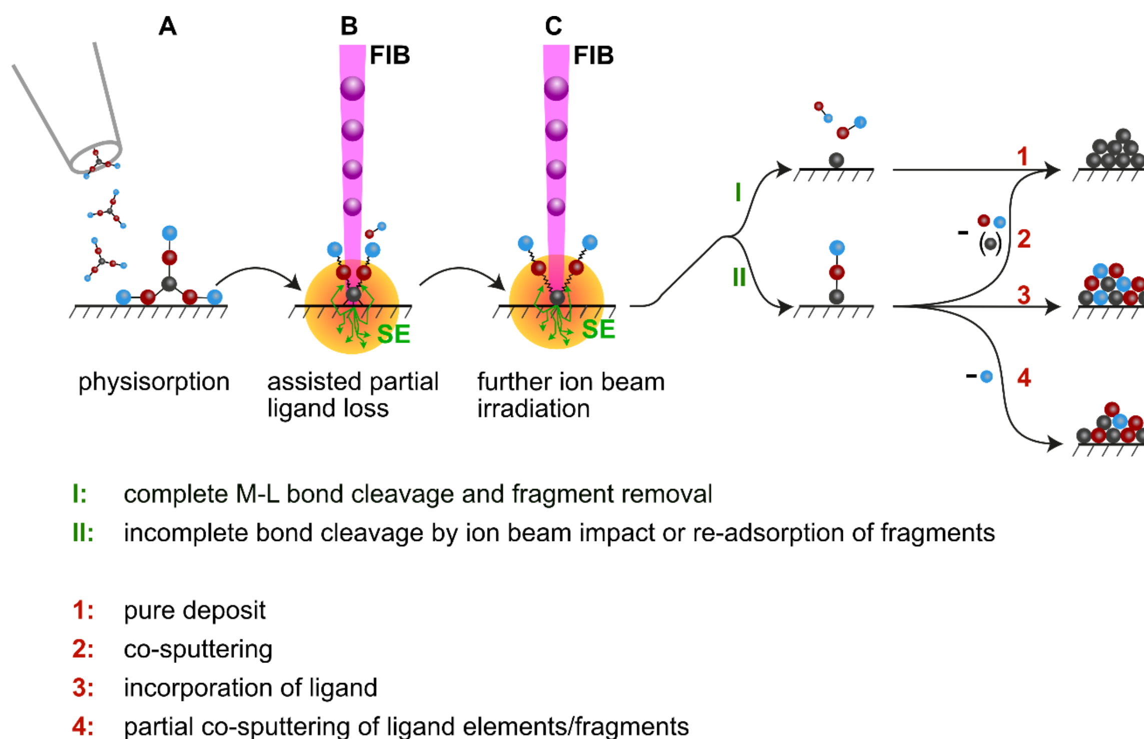

Figure 7: Schematic representation of the FIBID process.

Different aspects will be more pronounced during the deposition, depending on the type of ion. Usually, He^{+}[126-128] or Ga^{+} ion beams[11, 129-130] are used for FIBID, both of which show very similar deposition yields per ion which typically are one to two orders of magnitude higher than in FEBID.[125, 131] The increased growth rate indicates a much more efficient decomposition mechanism by ion impact. Additionally, the higher secondary electron yield generated from ion irradiation when compared to electron irradiation could play a role.[125] For example, when a silicon substrate is irradiated with Ga^{+} ions a 5-50 times higher SE yield is observed when compared to electron irradiation.[21] However, He^{+} and Ga^{+} are drastically different in other regards. He^{+} ion beams, on the one hand, are very similar to electrons and their energy loss is dominated by electronic effects. Consequently, penetration depths similar to electrons are observed (Figure 8). In the case of Ga^{+} ions, on the other hand, interactions are dominated by nuclear collisions resulting in significantly lower penetration depths (Figure 8) as well as

10- to 50-fold higher sputtering rates relative to He due to the much more localized energy input.[132] As a consequence, FEBID and He^+-FIBID derived material is very similar in composition (not considering implanted He) while material deposited with Ga^+ ions typically has higher purity.[125] Additionally, the incorporation of ion beam atoms in the deposits has to be considered. For example, when using the very popular gallium source, typically 5 at% to 15 at% gallium are incorporated in the deposit,[11, 133-136] potentially altering the electronic properties of the material drastically.[137-138] Even though He^+ ions should not have a significant effect on electronic properties they are implanted in the material nevertheless where they can cause swelling, bubble formation or even cracking of the substrate.[139]

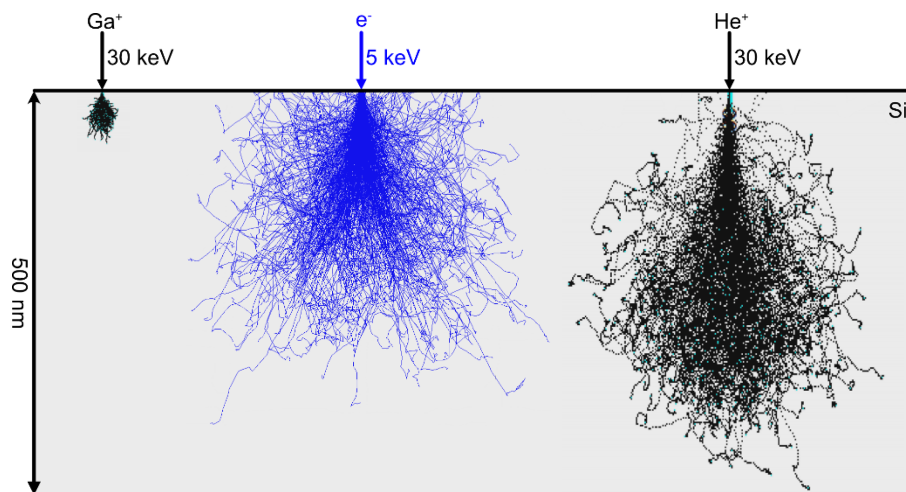

Figure 8: Comparison of penetration depth for electrons and ions at typical acceleration voltages used in FIBID and FEBID. The substrate material is silicon. While Ga^+ ions are already stopped within approximately 50 nm He^+ ions of the same energy will penetrate much deeper into the substrate. Both electron and ion trajectories were calculated using Monte Carlo simulations. Ion trajectories were calculated using SRIM,[140] electron trajectories were calculated using CASINO.[141]

2.3 Chemical vapor deposition

Chemical vapor deposition (CVD) is an exclusively thermal-driven process, contrary to FEBID and FIBID, that relies on the thermal decomposition of precursor molecules on a heated substrate surface. CVD is a very mature technique and finds widespread application in industry as well as research. The first use of CVD dates back to 1890 where pure Ni deposits were formed from $Ni(CO)_4$ in the so called Mond-process.[142]

Several types of CVD equipment and process controls are known to date. They can be distinguished, for example, based on pressure (atmospheric or low pressure) or heating of the substrate (cold wall or hot wall).[143] Additionally, aerosol-assisted, plasma-assisted, and laser-enhanced CVD are known.[143] CVD can yield high purity materials depending on the precursor molecules as well as the process conditions.[143] The process is widely used in industry and research, typically for covering large surface areas with (thin) films.[143] However, various methods for localized deposition are also available. For example, CVD on heated micromembranes[144-145] or laser assisted CVD[146-147] have been successfully used to locally confine the deposition area. Many of the precursors initially used for FEBID and FIBID were primarily used for CVD, because of their commercial availability. However, only because a precursor yields high purity films in CVD, it is not necessarily well suited for charged particle beam-induced deposition processes.

2.3.1 CVD process

In comparison to FEBID and FIBID chemical vapor deposition has been studied for much longer and thus the fundamental processes are understood significantly better. A general schematic for the CVD process is depicted in Figure 9.

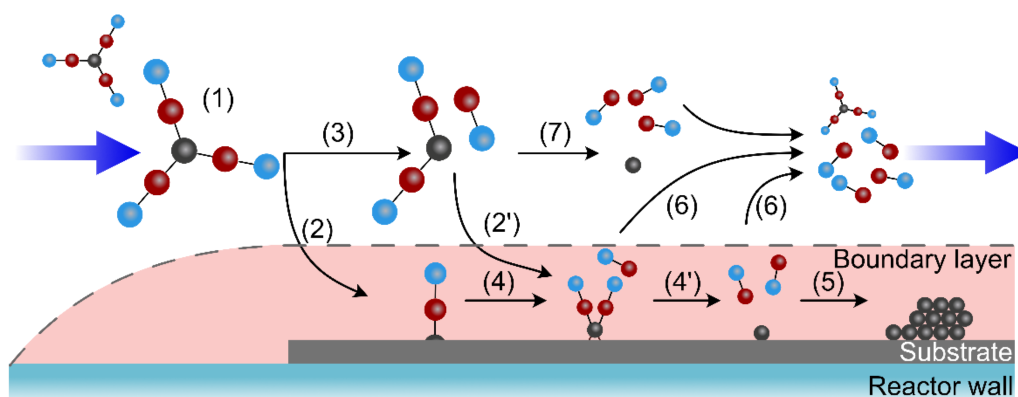

Figure 9: Schematic representation of the CVD process.

In an initial step, the precursor molecules are transported into the reactor *via* the gas phase (Figure 9-1) either using a pressure gradient or a carrier gas. The precursor molecules subsequently diffuse through a hydrodynamic boundary layer and adsorb onto the substrate

surface (Figure 9-2). Additionally, partial fragmentation or reactions in the gas phase can occur (Figure 9-3), depending on precursor stability and temperature in the reaction chamber. Depending on their stability the resulting intermediates can also cross the boundary layer and adsorb on the substrate (Figure 9-2’). The adsorbed species will undergo thermal decomposition (Figure 9-4 and 4’) and diffuse along the substrate surface until film growth is initiated (Figure 9-5). Volatile byproducts formed during the decomposition desorb from the surface and diffuse through the boundary layer (Figure 9-6) where they are removed from the chamber, together with unreacted precursor molecules. Alternatively, decomposition can already occur in the gas phase forming a powder and volatile byproducts (Figure 9-7). The powder will subsequently be deposited on the substrate surfaces where it can act as a nucleation site for film growth.[143]

2.4 Precursors for FEBID and FIBID

Various molecules, typically metalorganic complexes, have been studied as precursors for FEBID and FIBID. The initial choice of precursors for charged particle beam induced deposition was mainly driven by commercial availability, as indicated above. Therefore, many of the early FEBID and FIBID precursors were metalorganic molecules originally used for CVD. However, the purity obtained for a certain precursor in CVD can typically not be translated to charged particle beam induced deposition processes due to the very different decomposition mechanisms. In general, the choice of suitable precursor molecules for FEBID and FIBID is not trivial and several parameters have to be considered.[23] (1) The molecule has to be sufficiently volatile at temperatures below 70 °C (the typical limit for commercial GISs). (2) The precursor has to be stable in the employed temperature and pressure range to avoid undesired decomposition. (3) Ideally, all ligands are cleaved readily by electron/ion irradiation, and only the desired atom(s) are incorporated in the deposit, while cleaved ligands and ligand fragments are readily removed by the vacuum system.[23] In most cases described to date metallic or metalloid deposits are desired, however, also insulating materials are of interest. Currently, almost all transition metals, as well as all group 4 elements have been deposited *via* FEBID resulting in materials with a broad range of purity.[77] In most cases significant incorporation of ligands or fragments thereof is observed, even though some precursors will yield high purity deposits of up to 100 at% of the targeted element.[23, 77, 148] Typically the same precursor molecules are used for FEBID and FIBID, however, significantly fewer of the known precursor molecules have been studied for ion beam-induced deposition.[105, 149]

From a chemist's perspective metalorganic precursor molecules can be categorized into two major classes, namely homoleptic (only identical ligands) and heteroleptic (various different ligands) compounds. These precursor molecules can be further categorized based on the type of ligand. One of the simplest ligands possible is hydrogen, however, only a few metal hydrides are suitable and have been used for FEBID. The homoleptic group 14 hydrides, mono- and disilane,[150] as well as digermane,[151] have been successfully used in FEBID. In all three cases the deposition of basically pure metalloid material has been reported.[150-151] Another simple class of ligands are homoleptic alkyl, usually methyl or ethyl, compounds. Precursors of this class investigated for FEBID include $Si(CH_3)_4$,[152] $Sn(CH_3)_4$,[153] and $Pb(C_2H_5)_4$[154] all of which typically form carbon-rich deposits. In the case of $Si(CH_3)_4$ approximately 15 at% Si have been observed in the deposit, however a peculiar contribution of oxygen has been reported as well.[152] The tin analogue $Sn(CH_3)_4$ has also been employed as precursor in FEBID, but no compositional analysis has been provided.[153] The highest metal content in this group of precursor molecules has been reported for $Pb(C_2H_5)_4$ with 46 at% Pb.[154] However, large amounts of oxygen, not present in the precursor molecule, have been noted as well, indicating

potential contributions from background gases.[155] Another group of ligands successfully used for FEBID are homoleptic phosphines (PR_3). Typically, trifluorophosphine (PF_3) complexes including $Pt(PF_3)_4$[79, 156-158] and $Ni(PF_3)_4$,[159] are employed. A wide range of compositional variations, ranging from 15 at% to 83 at%, has been reported for the Pt-based precursor.[79, 156-158] The large variation in Pt content cannot be explained by beam currents alone and (electron-stimulated) side reactions with residual gases are very likely the reason.[156] The main disadvantage of the PF_3 ligand is the release of fluorine gas during its decomposition causing etching of the sample and substrate as well as potential damage to the equipment.[75] Even though low amounts of fluorine are typically reported, [79, 156-159] the deposits will deteriorate upon exposure to ambient conditions due to oxidation and hydrolysis of the retained phosphorous, leading to the formation of phosphorous-based acids.[23] Similar problems are encountered when transition metal halides are used as precursor. A broad range of homoleptic halides, including $AuCl_3$[160], $AlCl_3$[160], AlF_3[161], $SnCl_2$[162] $SnCl_4$[153], $TiCl_4$[163], and WF_6[164], has been studied for FEBID. Typically, a complete fragmentation is not observed and halide atoms are incorporated into the deposit. Homometallic, homoleptic transition metal carbonyls are the best-investigated class of molecules among all precursors investigated for FEBID and FIBID allowing for the deposition of material with up to 95 at% or higher purity.[74, 76] This type of precursors have also been used in this work and will be discussed in detail in chapter 2.4.1 below.

Various homoleptic, polyhapto-hydrocarbon complexes have been investigated as candidates for FEBID, including anionic as well as neutral ligands. Cyclopentadienyl $(C_5H_5)^-$ (Cp) and its methylated analogue $(C_5H_5CH_3)^-$ (MeCp), as well as allyl $(C_3H_5)^-$ are among the best known anionic polyhapto ligands. Precursors with these ligands investigated for FEBID include ferrocene and 1,1'-dimethyl nickelocene, both transition metal sandwich complexes.[159, 165-166] In the case of $Ni(C_5H_4CH_3)_2$ low metal contents of approximately 10 at% have been reported[159] This value is close to the amount of metal present in the intact precursor molecule and thus indicates a very good retention of the MeCp ligand in the deposit.[23] For ferrocene no composition has been reported, but low metal contents are expected as well, based on the very similar ligand.[165-166] In general removal of the η^5-C_5H_5 ligand is already challenging in solution and proceeds via η^3-C_5H_5 and η^1-C_5H_5 binding modes.[167] The various possible binding modes, η^5, η^3, and η^1 could explain the good retention of the ligand during FEBID and consequently the low metal amounts observed.[23] Additionally, the homoleptic sandwich complex $Cr(C_6H_6)_2$ has been considered for FEBID. Contrary to the anionic Cp or MeCp ligands two neutral benzene rings coordinate the chromium atom. Material deposited with this precursor did contain 16 at% Cr, additionally 22 at% O were observed as well, indicating a significant contribution from background gases.[168] A possible removal of the neutral benzene ring by electron stimulated reactions is suggested by gas phase studies.[169-170] Additionally, the

liberation of benzene was observed in surface science studies after heating of an electron irradiated $Cr(C_6H_6)_2$ film.[171] However, evolution of CO was also reported indicating the potential presence of water. Polyhapto allyl ligands also have been studied as ligands for FEBID precursors, however only heteroleptic molecules, such as $(\eta^3\text{-}C_3H_5)Ru(CO)_3Br$, have been reported to date.[172] In agreement with surface science studies[51] the removal of about four carbon atoms was observed during the FEBID deposition, corresponding to the loss of all CO groups and one in three allyl groups.[172] Similar to Cp the good retention of the allyl group is very likely related to its polyhapto bonding nature.[51]

Furthermore, bidentate β-diketonates,[43, 173-174] as well as carboxylates[175-176] are discussed as potential ligands. In the case of β-diketonates the volatility of the corresponding transition metal complexes can be adjusted by (partial) fluorination of the ligands.[177] Similar to other polyhapto-hydrocarbon complexes low purity deposits (11-14 at%) were obtained, as has been demonstrated for Cu,[178] Pt,[43, 157] and Pd[179-180] based precursors. The chemically closely related carboxylates have currently been reported only for the deposition of Ag and Cu.[175, 181-182] The FEBID deposition of $Cu_2(\mu\text{-}O_2CC_2F_5)_4$ did result in films with a metal content of approximately 25 at% Cu.[181] Similar Ag precursors, $Ag_2(\mu\text{-}O_2CC(CH_3)_2CH_2CH_3)_2$ and the perfluorinated $Ag_2(\mu\text{-}O_2CC_2F_5)_2$, have been reported to yield metal contents of up to 67 at% and 74 at% respectively.[175, 182] A very likely explanation for the high metal contents is given by surface science studies showing an efficient formation of CO_2 and a volatile alkene species, as a result of atomic hydrogen loss, during electron irradiation.[183] Additionally, the evolution of volatile fluorocarbons has been observed by MS when pieces of solid precursor of both $Cu_2(\mu\text{-}O_2CC_2F_5)_4$ and $Ag_2(\mu\text{-}O_2CC_2F_5)_2$ were irradiated with electrons.[184]

An overview summarizing the different homometallic precursor classes is presented in Figure 10. Based on the experimental data available up to date carbonyls and hydrides are still the best classes of ligands when targeting high metal content in FEBID. However, carboxylates are also promising candidates as ligands for new molecules.[23]

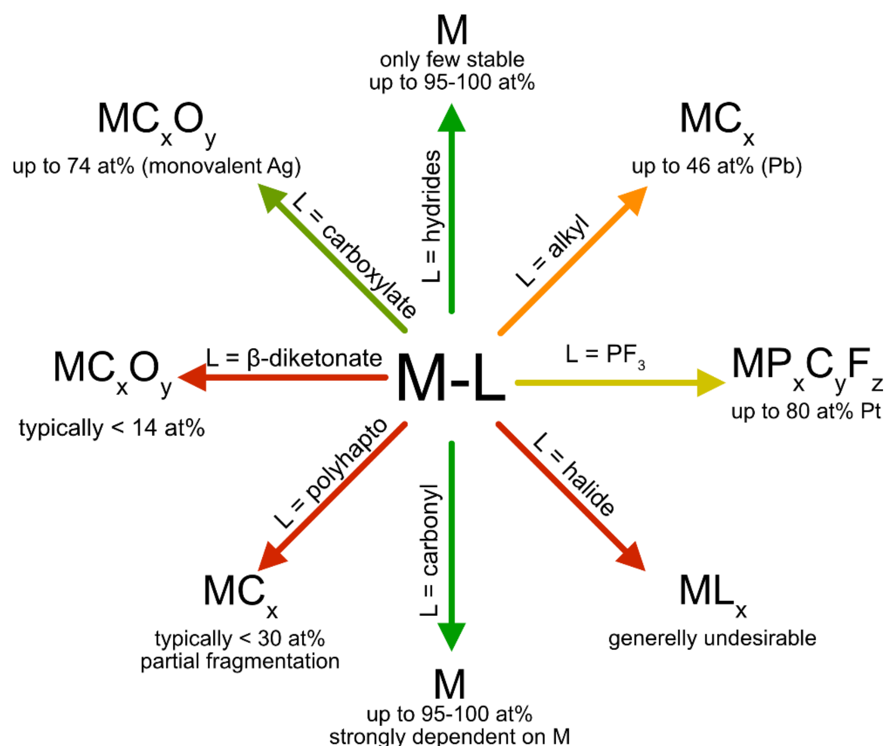

Figure 10: Overview of different ligand classes and their potential for providing metallic deposits. Arrow colors range from green (almost ideal) to red (bad) indicating the suitability for obtaining pure metallic deposits. Adapted from Ref. 23 with permission from the Royal Society of Chemistry.

In addition, various heteroleptic compounds are known. The most important precursor of this class is $(CH_3C_5H_4)Pt(CH_3)_3$ ($MeCpPtMe_3$). It is not only used routinely in TEM lamella preparation but also is the most popular precursor for studying electron-molecule effects in FEBID.[70-71, 185-186] $MeCpPtMe_3$ can thus, most likely, be considered the best investigated FEBID precursor. Deposits obtained from this precursor typically contain 10 at% to 24 at% Pt[102, 187-190] with higher purities most likely being the result of *in-situ* purification due to residual water in the deposition chamber. Additionally, high purity (up to basically pure Pt) deposits can be obtained by using post-growth purification protocols.[94-97, 191] Moreover, this precursor is used routinely for FIBID deposition, for example for electrical contacting,[192] protection of samples during TEM lamella preparation[106, 193] or the formation of specialized AFM tips.[194] Typically compositions of 20 at% to 30 at% Pt are observed in the FIBID processing.[195]

Besides homometallic molecules, some heteronuclear compounds have been investigated as potential precursors for beam induced deposition, even though only very few have been actually used for FEBID and, to the best of my knowledge, none for FIBID, prior to this work.[40, 49, 52, 115, 196-198] Not only can they be used for the deposition of alloys with defined stoichiometry they also allow for the investigation of differences in electron-induced decomposition depending on the central atoms of the precursor. Heteronuclear precursors will be discussed in detail in chapter 2.5.2 below.

2.4.1 Carbonyls

Homoleptic, homometallic transition metal carbonyls are the largest class of precursors investigated for focused beam induced deposition, as well as, in complementary studies. This is most likely due to their ease of use as well as their commercial availability. Furthermore, carbonyl compounds of a large number of transition metals are known. Figure 11 shows all known transition metal carbonyls, with those already used for FEBID and/or FIBID marked in bold. $V(CO)_6$ and $Mn_2(CO)_{10}$ were investigated in this work and the results are discussed in detail in chapter 4.1 below.

5	6	7	8	9	10
$V(CO)_6$*	**$Cr(CO)_6$**	**$Mn_2(CO)_{10}$***	**$Fe(CO)_5$** **$Fe_2(CO)_9$** $Fe_3(CO)_{12}$	**$Co_2(CO)_8$** $Co_4(CO)_{12}$ $Co_6(CO)_{16}$	**$Ni(CO)_4$**
	$Mo(CO)_6$	$Tc_2(CO)_{10}$ $Tc_3(CO)_{12}$	$Ru(CO)_5$ **$Ru_3(CO)_{12}$**	$Rh_4(CO)_{12}$ $Rh_6(CO)_{16}$	
	$W(CO)_6$	**$Re_2(CO)_{10}$**	$Os(CO)_5$ **$Os_3(CO)_{12}$** $Os_6(CO)_{18}$	$Ir_4(CO)_{12}$ $Ir_6(CO)_{16}$	

Figure 11: List of all known homometallic, homoleptic transition metal carbonyls. Carbonyls already investigated for FEBID/FIBID are marked in bold and have a green background. The orange background denotes carbonyls not yet used. * indicates precursors that have been investigated in this work. Exact composition and sources are provided in Table 1.

The metal content obtained in FEBID deposits of the various carbonyls shows a strong dependence on the central metal atom. Transition metal carbonyls of group 5 to 7 elements generally yield less pure (typically below 50 at% metal) deposits (Table 1). Contrary, transition metal carbonyls with a central metal atom of group 8 to 10, also known as iron triad, typically yield deposits of about 80 at% for 2D deposits.[199-201] Higher metal contents, above 90 at%, are typically only reported for 3D deposits.[76] The data available for FIBID deposits is much more limited. Typically Ga^+ ion beams are used, resulting in the incorporation of usually 5 at% to 30 at% Ga, thus increasing the overall amount of metal in the deposits.[134-136, 154, 202-203] Compared to FEBID a decrease in carbon and oxygen is typically observed due to preferential sputtering of lighter ligand elements and altered fragmentation channels.[117] However, the relative amount of precursor derived metal incorporated in the deposits is often very similar to FEBID experiments. Additionally, some studies using He^+[111] as well as Ar^+ ions[30] have been conducted resulting in compositions also very similar to FEBID. Metal contents above 90 at% have only been reported for the 3D deposition of $Co_2(CO)_8$ using a He^+ ion beam.[111]

Table 1: Comparison of metal carbonyl IR-data and amount of metal obtained in FEBID and FIBID. The metal content given for FIBID is the sum of the respective metal and Ga except: † indicates noble gas FIB (Ar^+ or He^+) where no additional Ga is incorporated. Values for $V(CO)_6$ and $Mn_2(CO)_{10}$, marked by *, are taken from this work and will be discussed in detail in chapter 4.1.

Precursor	CO-stretch (cm^{-1})	Metal in FEBID (at %)	Metal + Ga in FIBID (at %)
$V(CO)_6$	1972[204]	30 – 40*	n.a.
$Cr(CO)_6$	2000[205]	20 - 40[206]	n.a.
$Mo(CO)_6$	1989[207]	8[208]-20[92], 41[209]	36 + 30 - 45 + 31[154]
$W(CO)_6$	1997[210]	37 - 58[75], 50[82]	36 + 12[135], 39 + 20[202], 40 + 10[203]
$Mn_2(CO)_{10}$	1983, 2014, 2045[207]	41 – 45*	n.a.
$Fe(CO)_5$	2000, 2023[207]	>80[199], 82[211], 95[74]	85[30] (Ar^+)†
$Fe_2(CO)_9$	1826b, 2018, 2085[212, a]	80 - 85[201], 93[76]	n.a.
$Co_2(CO)_8$	2023, 2030, 2069[213]	73[200], 80[214], 82[215], 97[76]	46 + 9 - 53 + 18[134], >95[111] (He^+)†
$Ni(CO)_4$	2045[207]	95[73]	n.a.

The trend of iron triade carbonyls yielding high purity deposits in FEBID matches well with the chemisorption behavior of carbon monoxide on transition metal surfaces or clusters. After the initial physisorption of the carbon monoxide from the gas phase a conversion to a chemisorbed species is observed. Depending on the nature of the transition metal the CO molecule either chemisorbs intact (molecular) or dissociates into carbon and reactive oxygen.[216-217] Molecular adsorption is very likely required for high purity deposits, allowing the CO ligands to be removed intact. Contrary in dissociative adsorption the C-O bond is broken and two new bonds are formed (M-O and M-C) increasing the likeliness of carbon and oxygen incorporation into the deposits. Molecular adsorption at room temperature is only reported for transition metals of groups 8-10. A transition to dissociative adsorption is observed approximately along the Fe-Tc-Re/W line[216-217] matching well with the high purity FEBID deposits. This CO adsorption behavior is not only observed on clean metal surfaces but also reported for metal atom clusters, indicating that CO bonding to transition metals is dominated by processes at the atomic scale.[218] Considering the bonding situation, CO molecules adsorbed at on-top sites of

transition metal surfaces are very similar to transition metal carbonyl complexes. In both cases, the σ^* orbitals of the CO interact with metal $d_z{}^2$ and s states forming a σ bond, while the metal $d_{xy, yz}$ interact with the π^* orbitals of the CO forming a π back bond. This back bonding is very important in determining the chemisorption behavior of the CO molecule. With the Fermi energy of the transition metal elements increasing from Ni to Ti the d orbitals become more diffuse.[219] As a consequence, more electron density is transferred to the antibonding π^* orbital of CO weakening the C-O bond while simultaneously increasing the M-C bond strength.[219] At a certain threshold, the dissociation and reformation of a new M-O bond will be energetically favorable and dissociative chemisorption is observed.[219] Similar considerations can be applied to the single precursor molecule. For a strong M-CO bond, a significant back bonding into the antibonding π^* orbital of CO can be observed resulting in a decrease of the C-O bond strength and *vice versa*. In the case of FEBID or FIBID, a weak M-CO bond is desirable since it should increase the likeliness of a metal-ligand bond scission. At the same time, the ligand itself is kept intact, thus facilitating its removal. This potentially explains the increased tendency of early transition metal carbonyls to yield less pure FEBID (and FIBID) deposits.

A simple tool to investigate C-O bond strengths in transition metal carbonyls is IR spectroscopy. A stronger C-O bond, and consequently weaker M-CO bond, is observed as hypsochromic shift of the characteristic C-O stretching band, allowing for a qualitative discussion of bond strengths in transition metal carbonyls.[220] At a first glance, the expectations of high energy C-O stretch vibrations corresponding to high metal contents in FEBID and FIBID deposits hold true (Table 1).[23] Low to intermediate metal contents (>58 at%) are reported for carbonyls with CO stretching vibration wave numbers below 2000 cm^{-1}. High metal contents of above 80 at% are only reported for Co, Fe, and Ni carbonyls all of which show CO stretching modes above 2020 cm^{-1}. Even though IR data can be correlated with the reported metal contents one has to keep in mind that surface adsorption and potential cluster formation will change the bonding situation. Additionally, electron-initiated fragmentation will also alter the chemical nature of the surface species and thus the IR spectrum, as was demonstrated for $W(CO)_6$.[39] Consequently, IR data is a questionable tool for the general prediction of precursor feasibility for FEBID or FIBID.[23] Bond energies can also be measured directly in the form of bond dissociation energies. The available data, however, is not very reliable as broad ranges of actual values are published for the same molecule.[23] Additionally, not only first bond dissociation energies but also subsequent ones have to be considered as they can drastically change upon ligand abstraction. Therefore, bond dissociation energies also do not provide a predictive tool for precursor selection.[23]

In general, high metal contents are desired for FEBID or FIBID and carbonyl precursors are well suited to illustrate the extreme requirements necessary for high metal contents. Figure 12

illustrates the correlation of deposit purity with the actual percentage of removed CO ligands for $M(CO)_x$ with x = 4 - 6. Especially deposits with metal contents above 80 at% are of interest for applications, however, this already requires the loss of more than 95 % of CO ligands. Considering for example $Fe(CO)_5$: In order to obtain a deposit with metal concentrations of approximately 90 at% 17 out of 18 molecules have to be decomposed completely while one CO group may remain on the 18th molecule. Even for purities of only 50 at%, as for example observed for $W(CO)_6$ derived deposits,[75, 82] one CO group may remain per every two precursor molecules. With six carbonyl groups attached to each tungsten atom in the precursor this equates to a removal of 92 % of the initial ligands. Similar results will be obtained for other carbonyl complexes as well, showcasing the high efficiency in ligand abstraction necessary for high purity deposits. The overall composition will be the consequence of a statistical process and the kinetics of the deposition will play a major role. High metal contents not only require a very efficient bond cleavage but also a fast removal of resulting fragments. Otherwise, impurities can be buried in the growing deposit and low metal contents are achieved.

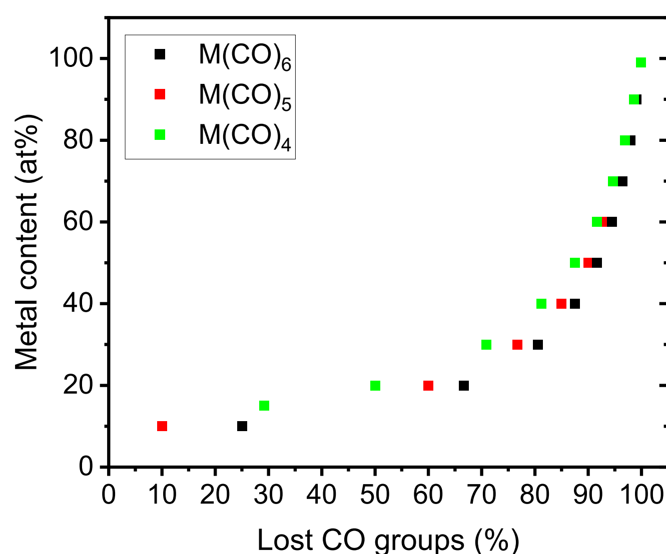

Figure 12: Correlation of abstracted CO groups with the corresponding metal content illustrating the extreme requirements for “pure” metallic deposits. Values were calculated for generic $M(CO)_x$ x = 4, 5, 6 with equal amounts of C and O in the deposit. Reprinted from Ref. 23 with permission from the Royal Society of Chemistry.

The large body of data available for transition metal carbonyls, including surface and gas phase studies, allows to draw some overarching conclusions considering FEBID. Gas phase studies indicate the stepwise release of CO by M-CO bond scission. In some cases, the complete removal of all ligands is observed, resulting in the formation of significant amounts of atomic metal ions.[34, 221-222] In surface science studies, at low temperatures, a complete ligand abstraction is not observed and, typically, more ligands remain in the deposit than would be

expected from gas phase investigations.[42, 48-49] Thus, an initial transformation of the adsorbed precursor molecules to a surface-bound species by electron-molecule interactions as illustrated in Figure 6-B is very likely. Also, the formation of bigger clusters is plausible considering electron-molecule interactions observed in cluster studies.[35-37] In some cases, for $Ni(CO)_4$[46] and $Fe(CO)_5$,[47] surface science studies show that initially retained CO ligands can be removed by thermal effects (at temperatures of approximately 330 K). In the case of $Co_2(CO)_8$ similar studies are missing, however, planar FEBID deposits at elevated substrate temperatures (below the decomposition temperature) were reported to yield 80-100 % pure deposits indicating a similar mechanism.[223] Interestingly, exactly these precursors are reported to yield metal contents of more than 80 at% probably related to the molecular chemisorption behavior of CO on the corresponding transition metals or the thermal lability of the clusters potentially formed during electron irradiation. For precursors yielding low to intermediate metal contents, thermal annealing most likely is not efficient in the removal of remaining CO ligands, as demonstrated, for example, with $W(CO)_6$.[39] In these cases, surface-bound clusters containing CO ligands are obtained (Figure 6-C-II). The remaining ligands will be very likely incorporated in the growing deposit (Figure 6-C-II-3) where they will undergo electron-stimulated C-O bond cleavage.[115] The resulting reactive oxygen species will oxidize the transition metal atom and will thus be incorporated in the deposit, as well as the carbon atom (Figure 6-C-II-3). However, oxygen could be (partially) liberated from these deposits if the oxide can be reduced by electron irradiation.[81]

For high purity FEBID deposits, the energy input has to be balanced. Enough energy for the M-CO bond fragmentation has to be provided while ideally suppressing C-O bond cleavage. The C:O ratio can be an indicator for various processes. A C:O ratio of larger than one indicates a C-O bond scission and liberation of oxygen. However, additional effects such as electron beam induced reduction of a potentially formed oxide species have to be considered as well.[81] Moreover, co-deposition of carbon from hydrocarbon background gases can potentially impact the C:O ratio. In the case of C:O ratios smaller than one a substantial contribution of water from background gases can be assumed.[23] Water typically is omnipresent inside an SEM chamber and is considered the main contributor to the SEMs base pressure, based on MS investigations.[224-226] Even though the vapor pressure of water is 32 mbar at room temperature, water films of approximately 0.7 nm, corresponding to two double-layers of water molecules, are observed down to a critical pressure of 2×10^{-7} mbar on SiO_2/Si(100) substrates.[227-228] In most FEBID studies the background pressure is higher than the aforementioned critical pressure, thus potential reactions with water have to be always considered. Additionally, water has a very high diffusion constant of about 2×10^{8} nm²/s which is one order of magnitude larger than typical precursor diffusion constants (for example 1×10^{7} nm²/s for

$MeCpPtMe_3$[62]).[229] As a consequence, the replenishment of water can be very efficient and play an important role in the FEBID deposits' composition.[23]

Significantly less data is available concerning FIBID of transition metal carbonyls. However, based on the available data, FIBID derived material appears to be very similar to FEBID. To the best of my knowledge gas phase studies are limited to $Fe(CO)_5$ using various noble gas ions of different charges and energies.[114] In all cases, a stepwise loss of CO by M-CO bond scission is observed with the degree of fragmentation depending on the mass and charge of the projectile. The highest efficiency was reported for Ne^+ with on average 0.3 CO groups remaining on the Fe.[114] In the case of He^+ and Ar^+ 1 and 1.1 CO groups were retained in the fragments while ions with higher charges were less efficient in decomposition.[114] For condensed precursor films a two-step process similar to FEBID is reported for the irradiation with low-energy ions. For example, $Fe(CO)_5$ films irradiated with low energy Ar^+ ions did release approximately 80 % of CO during the initial irradiation.[48] The remaining carbonyl ligands did undergo C-O bond scission and oxygen was removed. Pure iron deposits could be obtained by prolonged irradiation causing preferential sputtering of the remaining carbon.[48] Electron irradiation of the same $Fe(CO)_5$ films did only cause a removal of approximately 50 % of CO ligands during the initial irradiation, while the remaining ligands stayed intact.[48] Additionally, surface science studies with the heteroleptic, CO containing precursors, $Ru(CO)_4I_2$[116] and $(\eta^5\text{-Cp})Fe(CO)_2Re(CO)_5$,[115] did show a preferential removal of carbonyl ligands during the initial ion beam irradiation. In Ga^+-FIBID typically higher purity deposits are reported.[125] This is related to the increase sputtering rate of lighter atoms and atoms with lower binding energy. Since the sputtering rate not only depends on the mass but also on the bond strength, preferential sputtering of light atoms could be (partially) suppressed if strong chemical bonds are formed. Deposits derived from $W(CO)_6$ by Ga^+-FIBID for example, have a very low (0 at%[135, 202] to 8 at%[203]) oxygen content while the C:W ratio is close to one. This indicates the effective formation of tungsten carbide, which was also confirmed by atom probe tomography showing only signals corresponding to WC while no atomic tungsten ions were observed.[135] A potential explanation is that carbon will be bound strongly to tungsten, drastically reducing its sputtering rate while oxygen is still removed preferentially due to its lower mass. A similar trend is observed in the case of $Mo(CO)_6$. For this precursor selective loss of oxygen during FIBID deposition was observed as well while the carbon content remained very high and close to a Mo:C ratio of 2:1, in this case potentially related to Mo_2C formation.[154] Contrary, for $Co_2(CO)_8$ derived deposition using Ga^+ ions, no preferential removal of oxygen was observed for currents of 9.7 pA, indicated by C:O ratios of 0.8 to 1.4 depending on the deposit region.[134] However, at low currents a significant increase of carbon relative to oxygen was reported

(C:O = 2.4 – 4.9), which could be related to increased deposition times and more significant contributions of hydrocarbons from the background.[134]

2.4.2 Heterometallic precursor systems

The deposition of alloys or materials with predefined composition is still very challenging for FEBID, even though various precursor molecules are available. In the case of FIBID the deposition of binary alloys has not been reported prior to this work, to the best of my knowledge. A potential approach is the simultaneous injection of two different precursors during the writing process. This process has been demonstrated for FEBID with a variety of materials including $PtSi_x$,[230] $CoPt_x$,[12, 231] $CoSi_x$,[232] and $FeSi_x$.[233] However, targeting specific stoichiometries is difficult and requires fine-tuning of local precursor pressures depending on their respective decomposition efficiency and surface residence time. Even though broad ranges of compositions can be achieved the overall process is tedious and requires a fine adjustment of various parameters such as precursor feed rate and relative GIS needle positioning.[230, 232] Furthermore, slight variations in the parameters (such as changes in local pressure) could lead to local compositional variations in the deposits.

A potential solution is the use of heterometallic precursor molecules with pre-defined stoichiometries within one molecule (single source precursor) thus gaining compositional control. Up to date, only a few heterometallic precursors have been reported in the literature including $HFeCo_3(CO)_{12}$,[20, 196, 234] $H_2FeRu_3(CO)_{13}$[49] as well as $CpFe(CO)_2Mn(CO)_5$,[40, 52] and $CpFe(CO)_2Re(CO)_5$.[115] Additionally, the heteronuclear/heterometallic (metal/metalloid) precursors synthesized and tested in this thesis include: $H_3SiMn(CO)_5$,[197] $H_3SiCo(CO)_4$,[198] and $H_2Si(Co(CO)_4)_2$[198]. These systems will be discussed in detail in their respective chapters below.

$HFeCo_3(CO)_{12}$ works very well as FEBID precursor and yields deposits of approximately 80 at% metal content for in-plane deposition.[196] On the other hand, basically pure deposits are obtained for 3D geometries.[20] In both cases, the initial metal stoichiometry is retained in the deposits. In single collision experiments, DEA was observed up to approximately 20 eV, which is unusually high as it is approximately 11 eV above the ionization threshold for $HFeCo_3(CO)_{12}$.[235] This behavior has been attributed to the high density of metal-based HOMOs in combination with low-lying anti-bonding CO π^* orbitals. As a result, quasi-continuous electron attachment from 1 eV up to 20 eV is possible, resulting in all $[HFeCo_3(CO)_n]^-$ fragments with n = 12 - 0 being observed.[49, 235] Additionally, a secondary reaction channel was described in the gas phase resulting in the liberation of $[Fe(CO)_4]^-$ and $[Fe(CO)_3]^-$.[49, 235] However this secondary reaction path apparently has no significant impact in the FEBID process as the ideal $FeCo_3$ composition is retained in the final deposit.[20, 49] In the case of $H_2FeRu_3(CO)_{13}$ a similar, band-like, structure at the HOMO-LUMO gap is observed,

nevertheless only low purity deposits with about 26 at% metal have been obtained.[49] Therefore, the similarity in band-like structures is not sufficient to explain the extraordinary performance of $HFeCo_3(CO)_{12}$ in electron-induced decomposition processes. A potential explanation is provided by surface science studies. In the case of $HFeCo_3(CO)_{12}$ initial immobilization by electron stimulated partial decarbonylation leads to the formation of a thermally labile surface-bound species "$HFeCo_3(CO)_3$".[42] Subsequent heating to room temperature results in the desorption of the remaining ligands and high purity metallic deposits are obtained.[42] In the case of $H_2FeRu_3(CO)_{13}$ a similar amount of eight to nine CO ligands is removed during the initial transformation. However, the resulting chemisorbed species $H_2FeRu_3(CO)_x$ ($x = 4.5$) is thermally stable and will not release the remaining CO ligands, thus resulting in an overall low metal concentration.[49] No FIBID experiments have been reported for both $HFeCo_3(CO)_{12}$ or $H_2FeRu_3(CO)_x$.

A second set of hetero-bimetallic precursors are the heteroleptic allyl carbonyl compounds $CpFe(CO)_2Mn(CO)_5$[40, 52], and $CpFe(CO)_2Re(CO)_5$[115]. Gas phase single collision experiments with $CpFe(CO)_2Mn(CO)_5$ revealed that single CO loss and Fe-Mn bond cleavage are the dominating channels for DEA. DI on the other hand resulted in the loss of five to six CO ligands as well as metal-metal bond scission.[40] Furthermore, the bare metal cations Fe^+ and Mn^+ have been observed as well.[40] Surface science investigations revealed the initial removal of five out of seven CO ligands, while the Cp ring remained in the deposit, likely related to the multimodal binding situation.[52] Subsequent electron beam irradiation resulted in the decomposition of the remaining CO and cyclopentadienyl ligands forming a carbonaceous matrix and reactive oxygen species which selectively oxidized the Mn atoms according to XPS studies.[52] FEBID using the same precursor resulted in deposits retaining the initial 1:1 metal ratio, as expected for the irradiation of condensed precursor films.[52] The overall composition of films created by electron beam irradiation at room temperature can be described as $FeMnC_{2.8}O_{0.72}$, corresponding to 36 at% metal content.[52] The low amount of carbon observed in the FEBID deposits either indicates the effective removal of Cp ligand or, more likely, (electron-stimulated) side reactions with residual water. The amount of hydrogen was not determined. It can be assumed, however, that prolonged electron irradiation of the deposit will result in efficient C-H bond cleavage.[45, 236-237] The homologous Fe-Re precursor $CpFe(CO)_2Re(CO)_5$ has only been investigated in a surface science study, however both electron and ion beam irradiation have been discussed.[115] At low electron doses, three to four carbonyl ligands were removed under the retention of the metal-to-metal ratio. Subsequent electron beam irradiation resulted in the formation of reactive oxygen species followed by selective oxidation of iron. The preferential oxidation of certain metals should be related to oxophilicity and metal-oxygen bond strength, which in this case would be Re > Fe > Mn (M-O bond strength).[23, 238-239] A deviation from this thermodynamically expected tendency, as observed for $CpFe(CO)_2Re(CO)_5$ derived deposits,

could be related to the highly complex nature of electron induced fragmentation processes.[23] The decomposition of condensed precursor films with Ar^+ ions also proceeds in two steps.[115] During the initial irradiation, all CO ligands are removed, additionally, dehydrogenation of the Cp ring is very likely.[240] Furthermore, some sputter removal of intact precursor molecules is observed.[115] Prolonged irradiation of the metal-carbon composite material results in physical sputtering with light elements being removed preferentially, consequently obtaining pure metallic deposits.[115] However, since sputtering is a statistical process also some Re atoms are removed by prolonged irradiation. Preferential sputtering of Fe relative to Re is very likely because of their significant difference in mass, the data is however not presented in the paper.

2.5 Silicides

One focus of this work was the preparation of silicon-containing transition metal carbonyls and their subsequent application for FEBID and FIBID processes. Ideally, deposits containing silicides should be formed and consequently, this type of material will be discussed in more detail in the following.

Silicides are, typically binary, compounds of silicon with other elements of lower electronegativity, typically metals.[241] Depending on the partnering element three main groups can be defined: (i) saline silicides forming with alkali and earth alkali metals, (ii) covalent compounds forming with elements of similar electronegativity, and (iii) metallic silicides forming with basically all transition metal elements expect Ag, Au, Zn, Cd, and Hg. The vast amount of transition metal silicides is illustrated in Figure 13. Metallic silicides are not only of fundamental interest due to their diverse structural and physical properties, but are also of technological relevance. The field of application is based on their electronic,[242-243] magnetic,[244] optical,[245] and mechanical,[246] as well as, catalytical[247] properties. Especially their low resistivity, high-temperature stability, and compatibility with silicon integrated circuits (SICs) makes them a very important and well-investigated class of materials.[243] Metallic silicides, especially silicon-rich ones, find broad application as ohmic contacts, interconnects, or as gate material in silicon based CMOS technology.[242] Semiconducting silicides on the other hand are investigated for optoelectronic applications such as LEDs[248] or IR detectors.[245, 249]

Metallic Compounds
Eutectic/Peritectic
Unknown /not examined

Sc_5Si_3 $ScSi$ Sc_3Si_5	Ti_3Si Ti_5Si_3 Ti_5Si_4 Ti_6Si_5 $TiSi$ $TiSi_2$	V_3Si V_5Si_3 V_6Si_5 VSi_2	Cr_3Si Cr_5Si_3 $CrSi$ $CrSi_2$	Mn_3Si Mn_5Si2 Mn_5Si_3 $MnSi$ $Mn_{11}Si_{19}$	Fe_2Si Fe_5Si_3 $FeSi$ $FeSi_2$	Co_3Si Co_2Si $CoSi$ $CoSi_2$	Ni_4Si Ni_3Si $Ni_{31}Si_{12}$ Ni_2Si Ni_3Si_2 $NiSi$ $NiSi_2$	$\sim Cu_{8\text{-}3}Si$	Zn-Si
Y_5Si_3 Y_5Si_4 YSi Y_3Si_5 YSi_2	Zr_3Si Zr_2Si Zr_5Si_3 Zr_3Si_2 Zr_5Si_4 $ZrSi$ $ZrSi_2$	Nb_3Si Nb_5Si_3 $NbSi_2$	Mo_3Si Mo_5Si_3 $MoSi_2$		Ru_4Si_3 $RuSi$ Ru_2Si_3 $RuSi_2$	Rh_2Si Rh_5Si_3 $Rh_{20}Si_{13}$ Rh_3Si_2 $RhSi$ Rh_4Si_5 Rh_3Si_4	Pd_5Si Pd_9Si_2 Pd_3Si Pd_2Si $PdSi$	Ag-Si	Cd-Si
	Hf_2Si Hf_3Si_2 Hf_5Si_4 $HfSi$ $HfSi_2$	Ta_3Si Ta_2Si Ta_5S_3 $TaSi_2$	W_5Si_3 WSi_2	Re_2Si $ReSi$ $ReSi_{1.8}$	$OsSi$ Os_2Si_3 $OsSi_2$	Ir_3Si Ir_3Si_2 $IrSi$ Ir_4Si_5 Ir_3Si_4 Ir_3Si_5 $IrSi_3$	Pt_3Si $Pt_{12}Si_5$ Pt_2Si Pt_6Si_5 $PtSi$	Au-Si	Hg-Si

Figure 13: Periodic table of transition metal silicides, adapted from Kieffer and Benesovsky,[246] with revised and updated data.[250-258]

In the following sections, the transition metal silicon systems relevant for this work will be discussed in more detail.

2.5.1 Mn-Si

The manganese-silicon phase diagram depicted in Figure 14 is highly complex. Seven intermetallic phases are observed in addition to the pure elements. At the manganese-rich extreme, four different allotropes with cubic crystal structure are known, all of which can form solid solutions with silicon. At room temperature α-Mn is the thermodynamic stable phase which has a maximum solubility for Si of 6 at%. At 635 °C a eutectoidal transformation to β-Mn and R phase is observed. β-Mn has the highest solid solubility of Si of all Mn phases with 14.7 at%. Silicon free β-Mn shows an allotropic transformation to γ-Mn at 1100 °C while a peritectic reaction at 1155 °C is observed if Si is present. γ-Mn crystallizes in a cubic structure belonging to the F*m-3m* space group and has a solubility limit for Si of 2.8 at%. An allotropic, or peritectic if Si is present, transformation to cubic δ-Mn is observed at 1137 °C or 1205 °C respectively. The high temperature δ-Mn has a very low solubility of Si and melts at 1246 °C. [259]

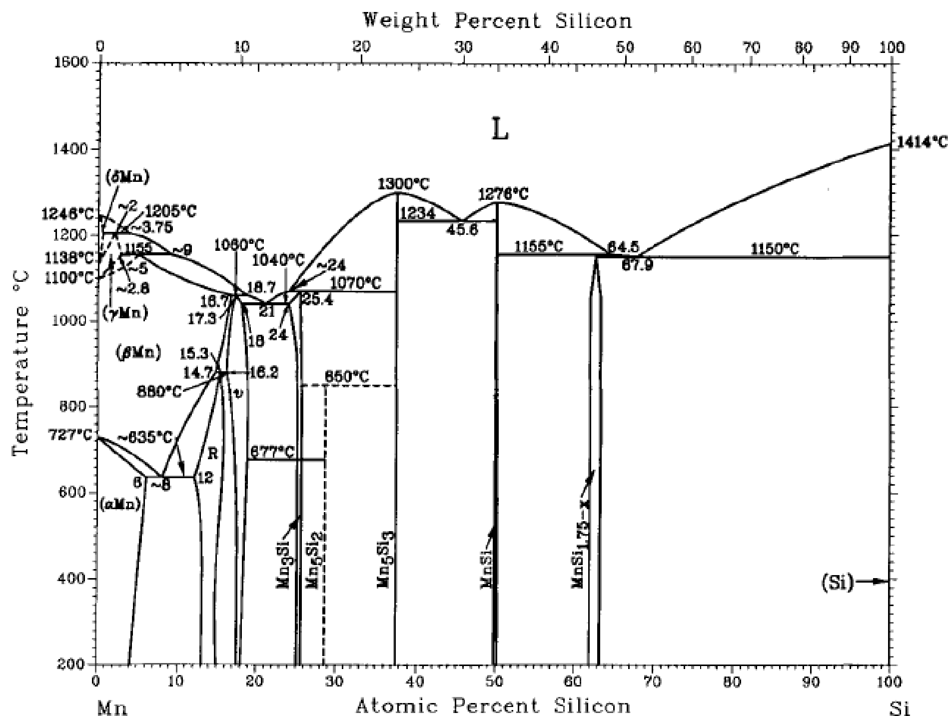

Figure 14: Binary phase diagram of Mn-Si. Reprinted by permission from Springer Nature Customer Service Centre GmbH: Springer Nature, Journal of Phase Equilibria[259], Copyright 1990.

Coming from the manganese-rich side, the first binary compound encountered is the trigonal R phase. The R phase has a broad homogeneity range from about 12 at% to 15 at% Si corresponding to approximately Mn_6Si.[259] At 880 °C a peritectoid transition to β-Mn and ν phase is observed. The orthorhombic ν phase is stable up to 1060 °C and corresponds to approximately Mn_9Si_2, also exhibiting a broad homogeneity range.[259] The next phase is Mn_3Si with a narrow phase region. Two modifications of Mn_3Si are known: The low-temperature disordered cubic B2 α-phase shows an allotropic transformation to the cubic β-phase at 677 °C.[259] For the tetragonal Mn_5Si_2 conclusive evidence is missing, however it has been reported to form peritectoidally at 850 °C.[259] When increasing the silicon content, the line compound Mn_5Si_3 is observed. Mn_5Si_3 crystallizes in a hexagonal structure and has the highest melting point of the binary Mn-Si system, congruently melting at 1263.2 °C[250] or 1300 °C.[259] The next phase is MnSi which has a narrow homogeneity range of 49.5 at% to 50.2 at% Si. MnSi crystallizes in a cubic structure and congruently melts at 1269.6°C.[250] For $MnSi_x$ with x = 1.72-1.75 a series of silicon rich, distinct crystallographic phases, also known as higher manganese silicides (HMS), has been reported. Four different HMS phases have been observed according to literature: Mn_4Si_7,[260] $Mn_{11}Si_{19}$,[261] $Mn_{15}Si_{26}$,[262] and $Mn_{27}Si_{47}$,[263] all forming so called Nowotny chimney ladder (NCL) crystal structures. NCL phases are commonly found for intermetallic compounds of transition metals of group 4 to 9 and main group elements of group 13 to 15.[264] Their crystal structure can be considered as two overlaid sublattices: a β-Sn type sublattice comprised of transition metal atoms (here Mn) overlaid by a nearly face-centered cubic one, formed by the main group element (here Si). Alternatively, the structure can be described as chimneys of transition metal atoms containing spiraling ladders of main group elements.[265-266] All of them are highly anisotropic along the c-axis.[265-266] In the phase diagram all HMS phases are subsumed as $MnSi_{1.75-x}$. Recent investigations on the stability of the HMS phases indicate that $Mn_{27}Si_{47}$ is the only stable phase at room temperature up to at least 800 °C.[266] $Mn_{15}Si_{26}$ and $Mn_{11}Si_{19}$ were only observed at temperatures exceeding 820 °C, while Mn_4Si_7 was never observed.[266] The formation of Mn_4Si_7 is mainly reported for thin films but the material can also be obtained by rapid thermal annealing of a mixture of $Mn_{27}Si_{47}$ and Si.[267] The phase diagram is bordered by silicon in which the solid solubility of Mn is very low.[259]

Among the binary manganese silicides, MnSi is one of the most investigated materials due to its interesting physical properties. MnSi crystallizes in a cubic B20 lattice which has no inversion symmetry, therefore, resulting in a helical crystal structure.[268] At temperatures below 29.5 K, a helimagnetically ordered state emerges due to chiral spin-orbit interactions.[268] Applying a magnetic field to the material at temperatures well below the critical temperature results in a depinning of the helical state and a conical phase emerges.[269] If a critical field strength (0.6 T) is exceeded chiral spin-orbit interactions are suppressed leading to a

ferromagnetic state.[269] At temperatures near the transition temperature and intermediate fields an additional phase, the so-called A-phase exists.[269] It is described as a hexagonal lattice of magnetic vortex lines (so-called skyrmions) parallel to a magnetic field.[269] Skyrmions are not only interesting from a fundamental point of view but they also have great potential for the application in spintronic devices.[270] Higher manganese silicides have gained attention because of their unusual, highly anisotropic, crystal structure. All four phases (Mn_4Si_7, $Mn_{11}Si_{19}$, $Mn_{15}Si_{26}$, and $Mn_{27}Si_{47}$) show direct or indirect semiconducting behavior with varying bandgaps ranging from 0.4 eV to 0.9 eV.[265] Additionally, as a consequence of their complex crystal structure, the HMS phases show a low thermal conductivity (2-4 W/mK at 300-700 K) making them interesting candidates for thermoelectric applications.[271]

2.5.2 Co-Si

The cobalt silicon binary phase diagram (Figure 15) shows four distinct intermetallic phases, all of which have a relatively narrow phase region. Cobalt is described in two allotropic forms, α and ε, both of which can form solid solutions with silicon. The low temperature ε-Co is stable up to a temperature of 1204 °C where a peritectic transformation to α-Co and melt is observed. ε-Co crystalizes in a hexagonal structure and has a maximum solubility of Si of 18.4 at%. α-Co has a cubic structure and can form solid solutions with up to 16.4 at% Si. α-Co melts at 1495 °C. Beginning on the cobalt-rich side the first binary compound is the line compound Co_3Si. Co_3Si is formed in a peritectic reaction at 1214 °C from the melt and is only stable down to 1193 °C where it undergoes a eutectoid reaction forming ε-Co and α-Co_2Si. Co_3Si crystallizes in the hexagonal $CdMg_3$ structure.[272] For Co_2Si two modifications are known. The low-temperature orthorhombic α-Co_2Si phase is stable up to 1320 °C where it undergoes a peritectic transition to β-Co_2Si and CoSi. Both α-Co_2Si and β-Co_2Si have homogeneity ranges of approximately 2 % and 4 % respectively. The remaining two binary phases crystallize in a cubic structure: CoSi is stable at 49 at% to 51 at% Si and melts congruently at 1460 °C and Co_2Si, a line compound, which congruently melts at 1326 °C.[250] Finally the phase diagram is completed by Si in which the solubility of Co is very low.

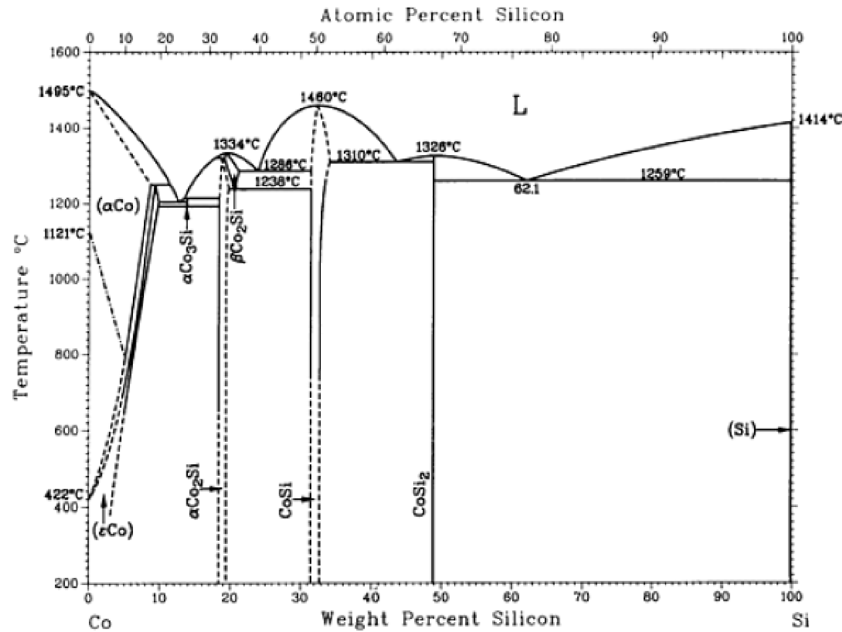

Figure 15: Binary phase diagram of Co-Si. Reprinted by permission from Springer Nature Customer Service Centre GmbH: Springer Nature, Journal of Phase Equilibria[273], Copyright 1991.

The physical properties of bulk Co_3Si are not well investigated due to its narrow stability range. However, a non-equilibrium cluster-deposition method was successfully used for the deposition of crystalline Co_3Si nanoparticles.[274] Ferromagnetic behavior with large coercivities and saturation polarization was reported when the material was deposited while applying a magnetic field.[274] Additionally, a significant anisotropy was observed, explained by an easy axis alignment during the deposition process.[275] The other three thermodynamically stable phases have been characterized more extensively. Bulk Co_2Si shows metallic behavior with a room temperature resistivity of 190 $\mu\Omega\cdot$cm, while being paramagnetic.[276-277] However a very small magnetization of 0.04 μ_B per Co atom has been observed at 4 K.[277] Interestingly when the lateral dimensions of the material are decreased, low-temperature ferromagnetic behavior was observed in nanomaterials.[278-279] Especially Co_2Si nanobelts did show large magnetoresistances of more than -10 % at low temperatures.[279] In the case of 0 D nanoscale objects, an increase of room temperature magnetic moment by two orders of magnitude compared to the bulk material, up to 0.49 μ_B per Co atom, was observed.[274] The significant size dependence of the magnetization was explained by a strong spin-polarization of the surface Co atoms.[274] Bulk CoSi exhibits a low resistivity of approximately 125 $\mu\Omega\cdot$cm and shows metallic behavior.[280] Layers of CoSi were successfully used for reducing contact resistances in ohmic contacts for Si-based MOSFETs, outperforming the more popular NiSi and $CoSi_2$.[281] Furthermore, nanowires of the material have been demonstrated to be ferromagnetic, thus making it a potential candidate for spintronic applications.[282-283] The silicon-rich $CoSi_2$ is the most relevant binary Co-Si phase as it played an important role in the

semiconductor industry where it was used as a contact material in complementary metal-oxide semiconductor (CMOS) devices.[284] Initially, aluminum was used as electrode material, however, the tendency of it to diffuse into the silicon required the implementation of diffusion barriers. Transition metal silicides were the material of choice as they not only fulfill the required physical properties (low resistivity, good thermal stability) but also can be formed in a self-aligned silicide (SALICIDE) process. In this process, the desired metal is deposited on the silicon and transformed into the silicide by a thermal annealing step. The process is called self-aligned as the silicide will only form on exposed silicon while silicon dioxide will not react, consequently, additional masking steps are not required. The silicide not only prevents the diffusion of Al but also reduces contact resistance. $CoSi_2$ replaced the initially used $TiSi_2$ and PtSi as both of them imposed problems with decreasing feature sizes. With the advent of FinFET technology requirements for silicide contacts changed and the industry returned to TiSi.[284]

3 Motivation

Currently the number of available precursors for FEBID and FIBID is quite limited, especially for the deposition of high purity materials. Additionally, the body of data on different ligand systems and especially hetero-metallic systems is also sparse. Consequently, a highly reliable prediction of process-optimized, tailored precursor molecules is not possible. With the most extensive body of data being available for homometallic metal carbonyls it is surprising that not all of them have been studied for FEBID. First-row transition metal carbonyls of group 5 to 10 are known, however dimanganese decacarbonyl $Mn_2(CO)_{10}$ and vanadium hexacarbonyl $V(CO)_6$ were not investigated for focused beam induced deposition yet. This is especially interesting for $Mn_2(CO)_{10}$ as it is commercially available and easy to handle. In order to provide a more comprehensive overview and to fill the gap in the first-row transition metal carbonyls both $Mn_2(CO)_{10}$ and $V(CO)_6$ have been investigated as precursor for focused beam induced deposition. Furthermore, low pressure CVD experiments have been performed in order to compare electron driven processes with exclusively thermal decomposition.

The deposition of alloys or materials with predefined composition has gained increased interest in recent years. Most of the binary FEBID deposits have been achieved by co-injecting two different precursors during the deposition. [12, 230-231] This process however is challenging and requires fine tuning of deposition parameters, especially if defined stoichiometries are targeted.[230, 232] The alternative approach is the use of single-source precursor molecules with predefined stoichiometries. However, only very few heterometallic precursors have been used for FEBID and only for one of them, $HFeCo_3(CO)_{12}$, metal contents above 80 at% have been reported.[20, 40, 49, 52, 196, 234] To the best of my knowledge no heterometallic precursors have been investigated for FIBID prior to this work. In this work silyl substituted transition metal carbonyl complexes have been synthesized and tested for focused beam induced decomposition, based on the high efficiency reported for homometallic precursors using the same ligand classes. The precursors investigated here are: $H_3SiMn(CO)_5$, $H_3SiCo(CO)_4$, and $H_2Si(Co(CO)_4)_2$. Focused charged particle beam induced deposition experiments have been performed to investigate effects of deposition parameters on composition, microstructure, as well as, electronic and magnetic properties of the deposited materials.

4 Results and Discussion

4.1 Homoleptic transition metal carbonyls

Homometallic, homoleptic transition metal carbonyls $M_x(CO)_y$ are the largest and best investigated class of precursor molecules used for FEBID. This is most likely related to their broad commercial availability and general ease of handling. Furthermore, the CO ligand has been proven to be well suited for FEBID as it is often cleaved easily and effectively leading to deposits containing high amounts of metal.[23] Nevertheless some of the neutral carbonyls have not yet been described in FEBID literature. In order to give a more comprehensive overview and to reveal potential tendencies $Mn_2(CO)_{10}$ and $V(CO)_6$ have been investigated as precursors for focused electron beam induced deposition. Additionally, CVD experiments were performed to investigate their thermal decomposition behavior and compare it to the FEBID experiments.

4.1.1 Vanadium

Vanadium hexacarbonyl is the only homoleptic transition metal carbonyl complex not obeying the 18-electron rule. $V(CO)_6$ is not commercially available, contrary to most other neutral homoleptic carbonyls, and was prepared similar to a procedure reported in literature.[285] Due to negligible intermolecular interactions and its low molecular weight, $V(CO)_6$ has a high vapor pressure making it a suitable precursor for gas phase deposition methods such as FEBID or CVD.

4.1.1.1 CVD

Low pressure cold wall CVD was performed at substrate temperatures of T_s = 473 K - 673 K using Si (911) and sapphire (0001) single crystal substrates. The resulting dark bronze films were analyzed using EDX as well as XRD. The compositional analysis via EDX was complicated by an overlap of V_L and O_K signal (Figure 16(a)). As a consequence, the quantitative discussion is limited to the V_K:C_K ratio. The EDX spectra of thin films deposited at 573 K and 673 K (Figure 16(a)) suggest that the thermal decomposition is incomplete and significant amounts of carbon and oxygen were incorporated in the deposits, evidenced by the large signals in the C_K and O_K/V_L region. With increasing substrate temperature, a decrease in V:C ratio from 1.3 to 1.1 is observed, indicating a switch in growth kinetics or different decomposition channels become active at higher substrate temperatures. The obtained thin films typically show columnar growth with well-defined facets, as illustrated by the representative SEM image in Figure 16(b). XRD analysis of the films revealed an oriented

growth, especially pronounced for samples deposited at lower growth rates (precursor reservoir at T_P = 263 K). Faster growth rates (precursor reservoir at T_P = 273 K) resulted in lesser oriented films thus facilitating a clear phase identification. A cubic F*m-3m* symmetry can be assigned based on references for the isostructural VC (PDF-01-073-0476) and VO (PDF-01-075-0048). The exact phase identification however, is difficult as the reflections are located in between both references, consequently, either a solid solution of $VC_{1-x}O_x$ or a highly sub-stoichiometric VC_{1-x} can be assumed. Decreasing the growth rate does not result in different composition or phase, but an oriented growth along the ⟨111⟩-axis is observed. This results in a reduction of the XRD pattern to reflexes at 2θ values of 37.5° and 80.0° corresponding to the {111} and the {222} planes respectively.

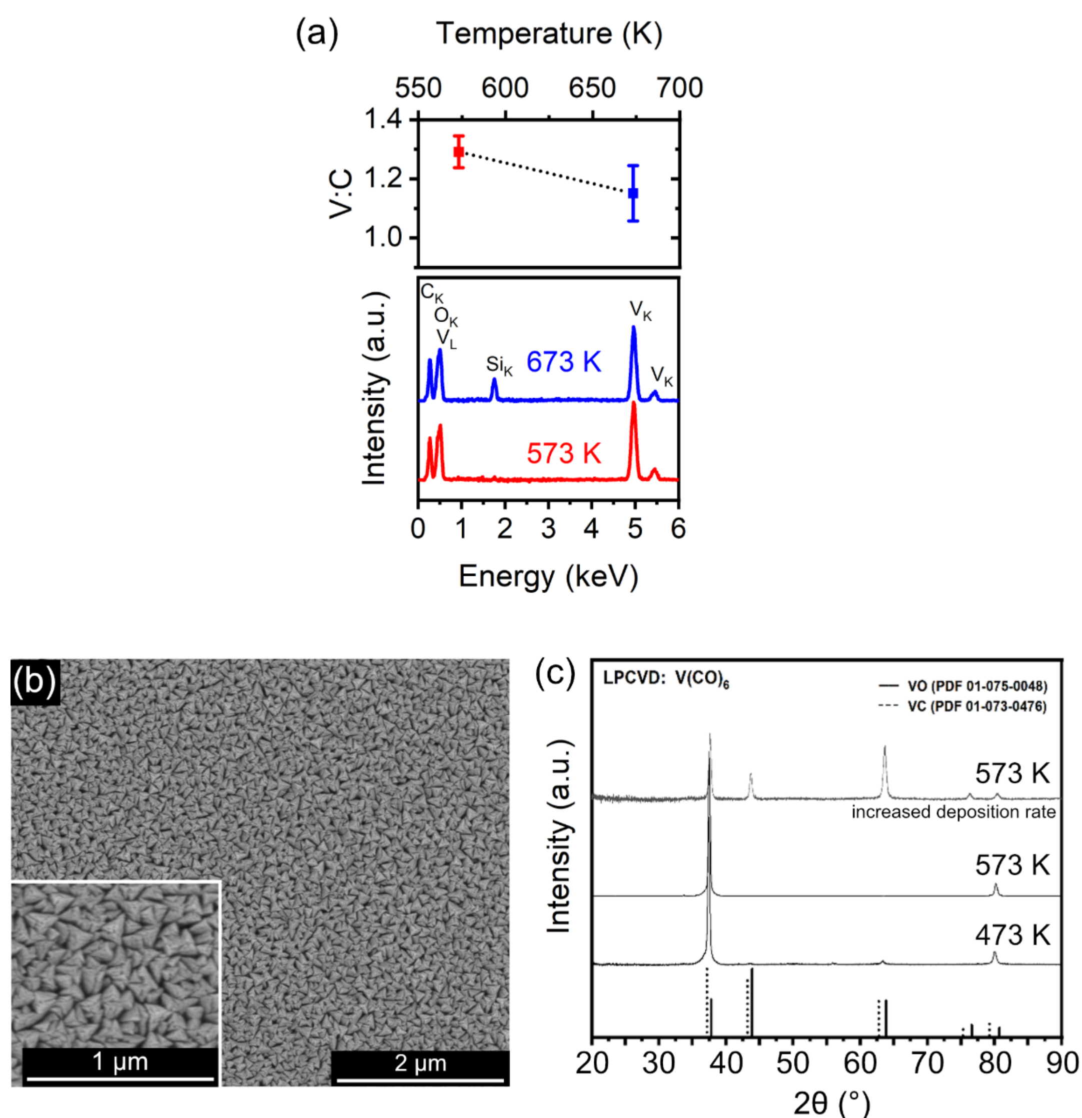

Figure 16. (a) V:C ratio and representative EDX spectra determined for the CVD films at different temperatures. (b) SEM image of a homogeneous CVD film deposited at 573 K on Si (911). (c) XRD patterns recorded at room temperature for films grown at T_S = 473–573 K showing oriented growth. With increased deposition rate less oriented films are obtained facilitating the phase identification. Adapted from Ref. 286 by Jungwirth, *et.al.*, licensed under CC BY 4.0 (https://creativecommons.org/licenses/by/4.0/). Published 2022 by MDPI.

4.1.1.2 FEBID

The electron-induced decomposition process was studied by varying deposition parameters such as beam current and voltage, as well as, precursor pressure. Other FEBID writing parameters (dwell time, pitch, scan strategy, *etc.*) were kept constant. Investigations on the effect of beam current and voltage have been carried out at overall chamber pressures of 0.85×10^{-6} mbar to 1.03×10^{-6} mbar. The influence of the precursor supply was studied in the pressure range of 0.5×10^{-6} mbar to 1.8×10^{-6} mbar. All pressures are recorded as total chamber pressure and the local precursor pressure in the deposition zone will be much higher due to the directionality of the GIS needle. Prior to deposition experiments plasma cleaning of the system was performed. Subsequently, the chamber was pumped for at least 48 h and a Meissner trap was used for 4 h reducing the amount of residual water. Total background pressures of below 3.6×10^{-7} mbar were achieved by using this procedure.

In Figure 17 the effects of electron beam current, electron beam voltage and precursor supply (denoted as total system pressure) are shown. Similar to the CVD samples an overlap of V_L and O_K is observed limiting the analysis to the V_K:C_K ratio. Representative EDX spectra are included, indicating incomplete bond scission and O and C incorporation similar to the CVD thin films. Variation in electron beam current between 0.4 nA and 6.3 nA did not cause variations in the composition as evidenced by a constant V:C ratio, as well as, the very similar EDX spectra (Figure 17). Similarly, variations in precursor flux did only cause minor variations in composition. Only at very low precursor pressures (close to the background pressure of the system) a decrease in vanadium content was observed. This could be related to either contributions from background gasses or a more pronounced fragmentation and subsequent incorporation of carbonyl ligands in the growing deposit. The latter appears to be more likely based on the relatively constant C_K to O_K/V_L peak ratio observed over the whole pressure range investigated. Material deposited with 1 kV and 5 kV acceleration voltage did show only minor compositional variations, however increasing the acceleration voltage to 20 kV did cause a drastic decrease in V:C ratio. In combination with the C_K to O_K/V_L peak ratio remaining relatively constant, this indicates a more pronounced incorporation of ligand or ligand fragments in the deposit. The cause of this are most likely changes in the growth kinetics, as indicated by a decrease in volume growth rate for high currents (Figure 18(b)). With increasing acceleration voltages less secondary electrons will be able to reach the surface and contribute to the growth, shifting the system towards electron limited growth.[58] Consequently, incomplete decomposition and subsequent incorporation of ligands or ligand fragments in the deposit will become more likely, causing a decrease in vanadium content. In all cases EDX spectra indicate the significant incorporation of oxygen in the deposits which appears to be largely independent of deposition parameters. EDX spectra also show the presence of Au_M signals

corresponding to the substrate material, but interference with any signals of interest can be excluded.

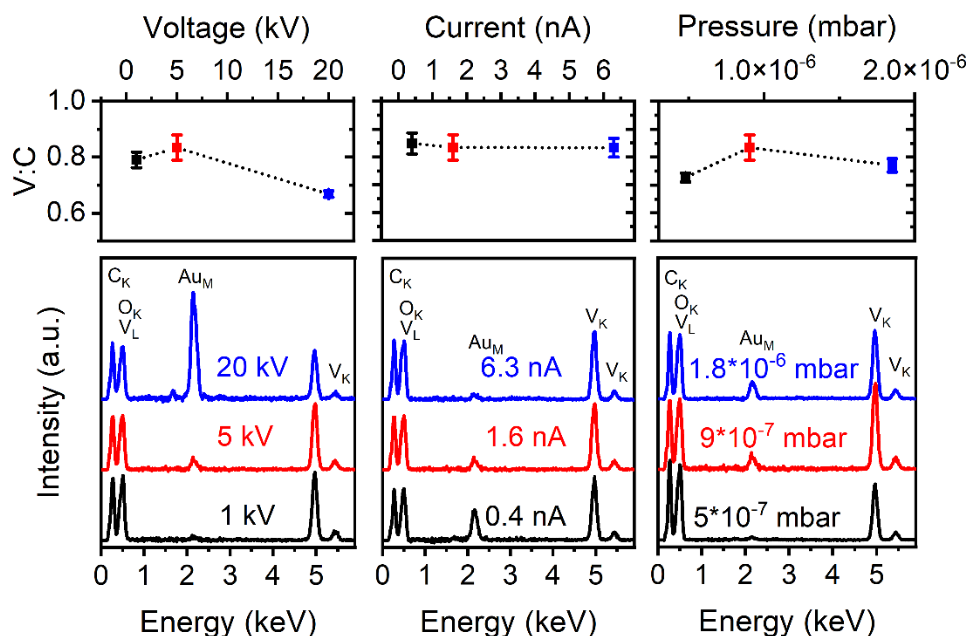

Figure 17: Dependence of V:C ratio for the variation of different deposition parameters as well as representative EDX spectra. Variation in current was carried out at 5 kV, the beam parameters for pressure variation are 5 kV and 1.6 nA. Further deposition parameters include deposition area of 1.4 µm × 1.4 µm, pitch of 20 nm × 20 nm and a dwell time of 1 µs. Sapphire single crystals with 200 nm Au and 8 nm Cr as adhesion layer were used as substrates. EDX spectra were recorded at 11 kV acceleration voltage.

Based on AFM measurements of samples deposited at different electron beam currents and voltages, volume-based growth rates were calculated (Figure 18). With increasing beam current a decrease in growth rate from 4.0×10^{-3} µm³/nC to 1.6×10^{-3} µm³/nC is observed (Figure 18(a)). Similar trends have been reported for other FEBID precursors as well and are indicative of a precursor-limited growth regime.[71] By increasing the beam current more electrons are available in a shorter time frame. As a consequence, the growth rate will become limited by precursor supply and less volume is deposited per electron. The inset in Figure 18(a) shows representative AFM line scans of samples deposited at 5 kV with varying currents. In all three cases a broadening at the base is observed, which can be related to side-edge effects. A broadening of deposits in FEBID is expected and is caused by more secondary electrons being able to reach the surface at edges.[287] This is also the reason why curved surfaces appear brighter in the secondary electron image of an SEM.[56] Additionally, morphological artefacts due to deposition conditions, such as elevated edges, are observed in the cross sections (inset Figure 18(a)) and the AFM image shown as inset in Figure 18(b). In conjunction with the serpentine scanning strategy this behavior can be ascribed to diffusion-enhanced precursor limited growth.[69, 71] In the diffusion-enhanced growth regime (DER) precursor replenishment is dominated by surface diffusion. If the diffusion is slow compared to the time required for one

pass (loop time) a complete replenishment of the surface is not ensured and precursor decomposition will be concentrated at the edges of the deposit.[69, 71] The effect is observed especially at low beam currents as the process has to be repeated more often to obtain the same dose. As a consequence, the relatively minor effect is more pronounced for small current values.[69, 71] A detailed discussion of growth regimes is provided in chapter 2.1.2.2. When increasing the deposition voltage while using similar currents, a decrease in growth rate from 8.30×10^{-3} µm³/nC to 1.1×10^{-3} µm³/nC is observed as well (Figure 18(b)). This effect can be explained with the increase of penetration depth of the primary electrons causing less SE and BSE to reach the surface where they can contribute to precursor decomposition.[57-58]

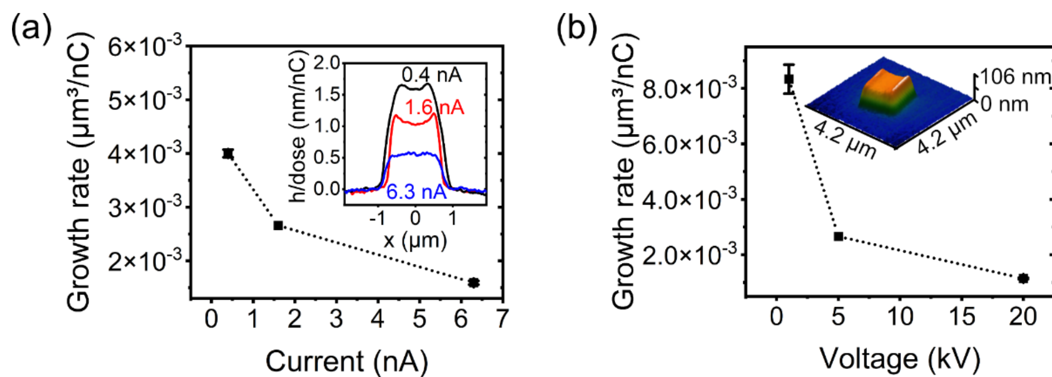

Figure 18: (a) Volume-based growth rates determined for V-based FEBID material in dependence on beam current at constant voltage of 5 kV. The inset shows corresponding, representative height profiles normalized to the dose at different currents. (b) Volume-based growth rates in dependence on deposition voltage. The inset shows an AFM image of a sample deposited at 5 kV and 1.6 nA. Further deposition parameters include deposition area of 1.4 µm × 1.4 µm, pitch of 20 nm × 20 nm and a dwell time of 1 µs. Sapphire single crystals with 200 nm Au and 8 nm Cr as adhesion layer were used as substrates.

4.1.1.2.1 Microstructural characterization of a Vanadium based FEBID deposit

The microstructure of a FEBID-V sample, deposited with an acceleration voltage of 5 kV and an electron current of 6.3 nA, has been investigated using TEM. In the high angle annular dark field (HAADF) image a dense deposit is observed, additionally the polycrystalline gold substrate can be seen as bright feature to the right of the image (Figure 19(b)). The high-resolution bright-field (BF) image (Figure 19(a)) provides more information and reveals small features of approximately 2 nm to 5 nm in size based on phase/diffraction contrast. Fast Fourier transform (FFT) of the BF image (Figure 19(c)) reveals concentric rings, indicating the presence of polycrystalline material. A similar diffraction pattern is obtained for nanobeam electron diffraction (NBED) recorded in the same region (Figure 19(d)). Based on the averaged rotational brightness profile of the FFT as well as the NBED image (Figure 19(e)) lattice plane spacings can be determined. However, the identification of a distinct crystalline phase is not

possible since the signals could be assigned to either the isostructural VC, VO or a solid solution of $VC_{1-x}O_x$, all of which having very similar lattice spacings. The reference of the cubic VC is thus chosen as representation for all the aforementioned possible phases. The observed diffraction pattern is in good agreement with thin films prepared by CVD, as discussed before.

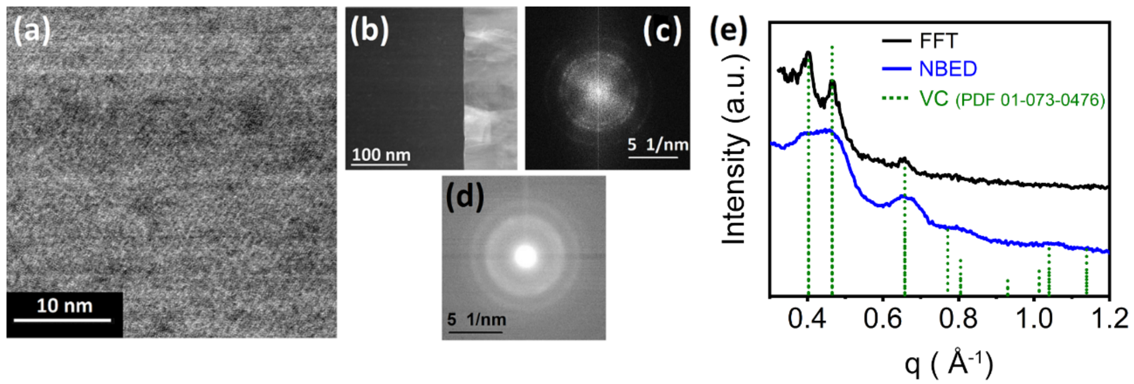

Figure 19: TEM investigation of a sample deposited at 5 kV, 6.3 nA. (a) high resolution brightfield image of the V-based FEBID material with diffraction/phase contrast suggesting particles of 2-5 nm. (b) High angle annular dark field image (HAADF) of the lamella showing the ~200 nm thick deposit with the gold substrate layer (bright). (c) Fast Fourier transform (FFT) of image (a) showing distinct rings indicating a poly-crystalline nature which is further supported by the (d) nanobeam electron diffraction both of which provide information on the crystalline fraction of the FEBID material. (e) Rotational brightness profile of (c) and (d) allowing the assignment of a crystalline phase such as VC or VO, which can be described as generalized solid-solution of type $VC_{1-x}O_x$. Reprinted from ref. 286 by Jungwirth, *et.al.*, licensed under CC BY 4.0 (https://creativecommons.org/licenses/by/4.0/). Published 2022 by MDPI.

The EDX spectrum recorded for the bulk of the TEM lamella shows distinct differences in the V_L/O_K region when compared to that recorded in the SEM (Figure 20(a)). A significant decrease in oxygen is observed in the TEM bulk EDX spectrum when related to the V_L signal. This behavior can be explained by a post-growth electron-stimulated oxidation of the sample surface by residual water during SEM investigations. In this process the carbon content at the surface is reduced by the formation of volatile compounds, while the oxophilic metal is oxidized. A potential surface oxidation is further indicated by a darker top layer of about 25 nm thickness visible in the HAADF image (inset Figure 20(b)) as well as a slight dip of the brightness trace signal at the corresponding position. HAADF imaging is based on scattered electrons and is thus very sensitive to Z-contrast with darker areas corresponding to regions where lighter atoms are present. Furthermore, an EDX spectrum of the surface region, recorded in the TEM, reveals a significant increase of the V_L/O_K signal while the C_K signal drastically decreases. Consequently, the different layers observed in the HAADF image (shown in the inset of Figure 20(b)) can be described as following. Starting at the left, the protective FEBID-PtC_x deposit is visible as bright, granular material followed by a dark oxidized VC_yO_z layer. Subsequently, the slightly brighter bulk FEBID-$VC_{1-x}O_x$ material and finally the very bright Au

substrate layer are observed. In the electron energy loss spectrum (EELS) (Figure 20(b)) a decrease in C and V signal at the surface region is observed in accordance with the EDX data. Furthermore, the V:C ratio remains constant throughout the bulk of the material, indicating a homogeneous deposition process. A quantitative measurement of oxygen was also not possible by EELS due to overlaps with the V_L signal, similar to the problems encountered for EDX. The slope observed for the EELS line scan signal is a consequence of the wedge shape of the TEM lamella.

Microstructural investigations, especially the electron diffraction results, match well with a cubic vanadium (oxy)carbide phase. This is interesting since the only other transition metal carbonyl precursor known to form a metal(oxy)carbide phase in FEBID is $W(CO)_6$.[23] The overall composition of FEBID deposits derived from $W(CO)_6$ is typically described as $WCO_{0.7}$.[75, 83, 288-289] But the assumption of a carbide formation for the tungsten deposits is mainly based on their composition and electrical transport characteristics.[23] However, recent *in situ* MS experiments during the FEBID deposition of $W(CO)_6$ did show significant amounts of carbide-type WC_x^+/$WC(CO)^+$ signals,[184] in good agreement with single collision experiments.[290] Furthermore, freestanding 3D rods deposited with FEBID showed SAED patterns corresponding to pure W as well as W_2C and W_3O.[291] Contrary to $W(CO)_6$ no carbide-type fragments were observed in single collision gas-phase studies with $V(CO)_6$.[292] Nevertheless, microstructural analysis reveals nanoparticles owing a cubic phase, matching very well with the VC reference. In conjunction with the oxygen content being below that of vanadium and carbon and the isostructural nature of VO with VC the formation of a vanadium (oxy)carbide species is very likely.

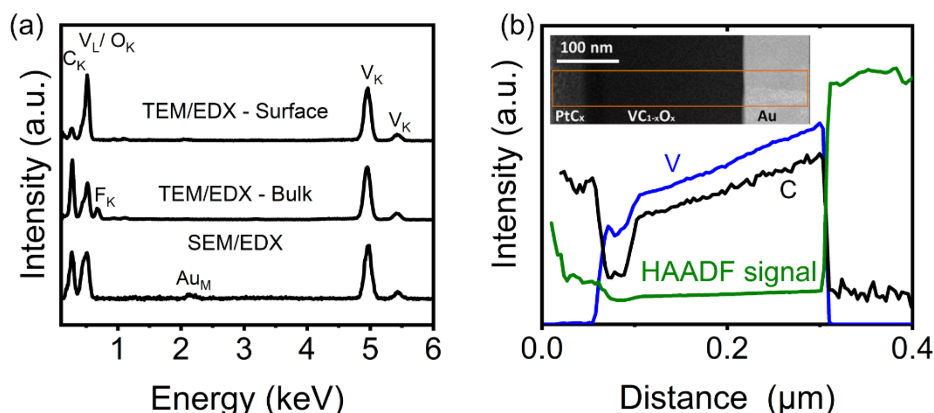

Figure 20: (a) EDX spectra recorded in the SEM as well as TEM. F observed in the TEM sample is a residue of the lamella preparation. (b) EELS line scan of the region indicated by the orange square. For the bulk material a constant V:C is observed. (b) Reprinted from ref. 286 by Jungwirth, *et.al.*, licensed under CC BY 4.0 (https://creativecommons.org/licenses/by/4.0/). Published 2022 by MDPI.

Comparing the composition for FEBID and CVD deposits lower amounts of carbon were incorporated in the CVD thin films. This indicates that the exclusively thermal decomposition

process is more efficient in V-CO bond cleavage. However, additional side reactions with residual water could also cause a slight reduction of carbon content and cannot be excluded at this point. As a consequence, heating of the substrate during the FEBID process could potentially increase the purity of the deposit slightly. However, in both cases no metallic vanadium was obtained. Despite the variation in composition, diffraction patterns observed for both materials indicate the formation of a crystalline phase corresponding to a cubic solid solution of $VC_{1-x}O_x$.

An alternative application of the $V(CO)_6$ precursor would be the deposition of vanadium oxides. Among the various vanadium oxide phases VO_2 would be especially interesting as it shows a metal to insulator transition (MIT) close to room temperature accompanied by drastic changes in resistivity and optical properties.[293] Post-growth electron irradiation of samples in an oxygen atmosphere, however, did not cause any changes in electrical behavior or composition. Alternatively, co-deposition of the precursor with water as reactive gas could be a feasible method for the deposition of vanadium oxides. $V(CO)_6$ would be ideal for this procedure as the molecule is stable against hydrolysis but readily oxidizes in contact with molecular oxygen.

4.1.1.2.1 Electrical transport measurements of FEBID deposits

Room temperature electrical transport measurements were carried out in the SEM after the deposition. The samples were deposited across Au electrodes on SiO_2 (200 nm)/Si substrates and I-V curves were recorded in two-probe geometry. The exact geometries of the samples were determined by AFM and resistivities for each individual deposit were calculated. The inset in Figure 21(a) shows an AFM image of a typical two-probe device used for the electrical characterization. The two-probe resistivity values in dependence of the deposition current are shown in Figure 21(a). Only minor changes in resistivity are observed when the deposition current is altered in the range of 0.4 nA to 6.3 nA at acceleration voltages of 5 kV. Resistivities of 1.2×10^3 μΩ·cm to 0.8×10^3 μΩ·cm were observed, with the lowest value corresponding to the highest beam current. Additionally, four probe measurements have been performed (typical device shown in inset of Figure 21(c)) indicating negligible contact resistances for the FEBID material deposited across Au microelectrodes. Post-growth irradiation of the samples led to a slight increase in resistivity (Figure 21(b)), in contrast to the often-reported electron curing induced decrease for other materials.[102, 198] Significant oxidation of the deposited material during the post-growth irradiation can be excluded as no changes in composition were observed. A deliberate electron assisted post-growth oxidation in an oxygen atmosphere (2×10^{-6} mbar) was not successful and composition as well as resistivity remained unaltered.

Temperature dependent electronic conductivity measurements in the range of 2 K to 300 K were recorded in a variable-temperature insert mounted in a ^{4}He cryostat (Figure 21(c)).

Samples deposited with 6.3 nA and 1.6 nA at 5 kV acceleration voltage were investigated. Both samples showed a behavior indicative of a granular metal on the quasi-metallic side of the metal-insulator transition.[189] Similar trends have been reported for other FEBID materials such as PtC_x,[189] Co_3Fe,[20] and W.[289]

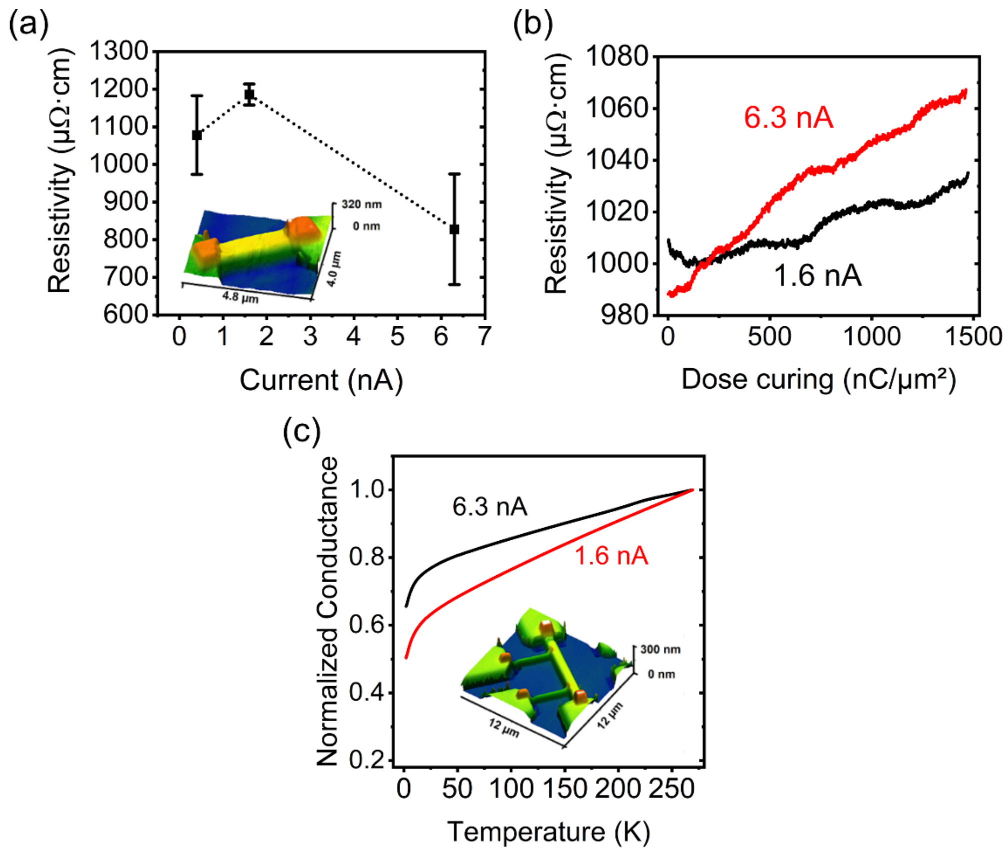

Figure 21: (a) Resistivity measured in two-probe configuration for material deposited at 5 kV and varying current. The inset shows an AFM image of a typical device geometry. (b) Effect of post growth electron beam irradiation on samples deposited at 5 kV and 1.6 nA and 6.3 nA respectively. (c) Temperature dependence of the conductance normalized to the conductance at 285 K for deposits prepared at 5 kV and beam currents of 6.3 nA and 1.6 nA. The inset shows again the geometry of a typical four-probe device as measured by AFM. (c) Reprinted from ref. 286 by Jungwirth, *et.al.*, licensed under CC BY 4.0 (https://creativecommons.org/licenses/by/4.0/). Published 2022 by MDPI.

4.1.2 Manganese

Even though dimanganese decacarbonyl $Mn_2(CO)_{12}$ is commercially available and relatively easy to handle it has not been investigated as FEBID precursor so far. $Mn_2(CO)_{10}$ was purified by sublimation under reduced pressure prior to use since commercially available manganese decacarbonyl typically contains 5 % to 10 % hexane. $Mn_2(CO)_{10}$ has a significantly lower vapor pressure than $V(CO)_6$ or other monomeric transition metal carbonyls due to its dimeric nature and associated higher molecular mass. However, the volatility of manganese carbonyl is still sufficient for CVD and FEBID experiments when kept at room temperature and no additional heating is required to evaporate the precursor.

4.1.2.1 CVD

Thin films with a metallic appearance were obtained for low pressure cold wall CVD performed at substrate temperatures T_S = 573K to 673 K using sapphire (0001) and Si (911) single crystal substrates. When exposed to ambient an oxidation of the films was observed, often resulting in delamination after storage. To keep the oxidation to a minimum, films were either transferred to the SEM chamber directly or stored under an inert atmosphere prior to EDX characterization. EDX analysis revealed a Mn content of 45 at% to 50 at%, decreasing with increasing deposition temperature (Figure 22(a)). At low temperatures a significant intra-ligand bond scission with subsequent desorption of oxygen is observed, indicated by a C:O ratio larger than one. When increasing the deposition temperature, more oxygen is retained in the thin films likely related to a more efficient oxidation of Mn, also indicated by a decrease in Mn:O ratio. These results are in agreement with earlier studies reporting an *in-situ* oxidation as well as indications of carbide formation, observed by XPS, for thermal decompositions at 623 K.[294] The large amount of carbon and oxygen present in the thin films imply an inefficient thermal fragmentation or pronounced chemisorption of carbon monoxide. Even tough dissociative chemisorption of carbon monoxide on transition metals is known, it is typically not as evident in thermal decomposition reactions.[216] XRD analysis of the thin films is very challenging due to the high oxidation tendency. Mainly signals corresponding to cubic MnO have been observed. Other, not identified, reflexes were observed as well which typically were changing during the measurement due to the ongoing oxidation. SEM images revealed porous structures (Figure 22(b)). In conjunction with the high oxygen affinity of Mn the large surface area of the thin films is likely responsible for the oxidation observed during XRD measurements.[295]

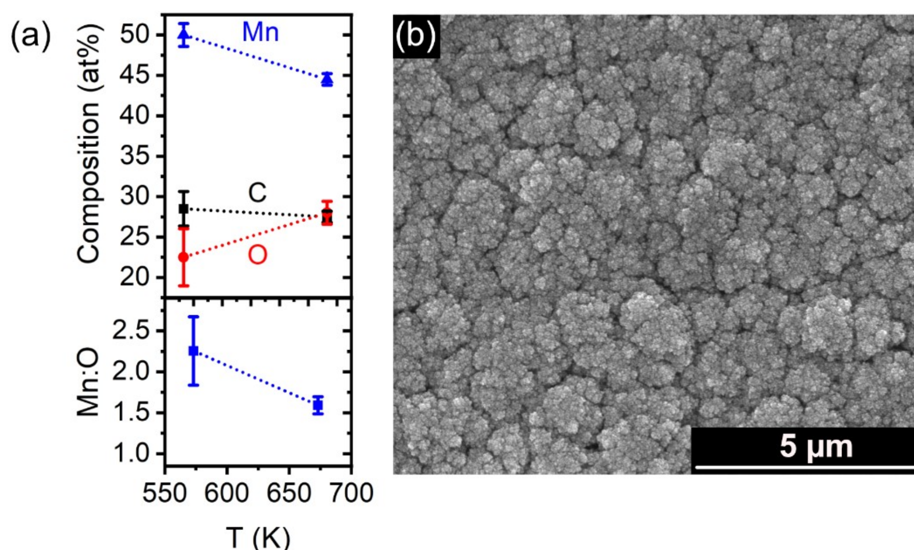

Figure 22: (a) EDX analysis of CVD grown thin films at different temperatures, as well as ratios of Mn:O and C:O. (b) SEM image of a representative film grown at 673 K showing a highly porous nanostructure.

4.1.2.2 FEBID

Similar to $V(CO)_6$, the electron beam associated parameters such as acceleration voltage and beam current were varied, while dwell time, pitch and scanning strategy were kept constant. A variation in deposition pressure was not possible due to the low vapor pressure of the dimeric $Mn_2(CO)_{10}$. Only a slight increase in total pressure was observed (typically below 4×10^{-7} mbar) when the precursor was leaked into the SEM chamber. Local pressures are, however, much higher and electron beam induced deposition was possible nevertheless. In order to ensure a low amount of background gases the chamber was plasma cleaned and subsequently pumped 48 h prior to deposition and a Meissner trap was used for 4 h. This resulted in background pressures of below 3.73×10^{-7} mbar.

The composition in dependence of beam parameters was analyzed by EDX and is presented in Figure 23(a). Only minor variations with electron current were observed for a beam energy of 5 kV, resulting in Mn contents of approximately 43 at%. With the C:O ratio remaining constant at about 1:1 it can be assumed that approximately one intact CO ligand remains in the deposit per 1.5 Mn atoms. The overall composition can be described as $MnC_{0.65}O_{0.65}$. This composition is very close to the results obtained for CVD thin films, indicating that thermal effects, such as heating of the substrate or 3D growth, will most probably not increase the purity. A slight decrease in Mn content is observed for depositions performed at low currents (0.4 nA) and at low voltages (1 kV). Similar trends have also been observed for other precursors and can be related to slight changes in growth regime causing an increased incorporation of ligand atoms and/or contributions of residual gases.[71, 198] The increase of

oxygen relative to carbon for increasing deposition voltages is very likely related to an increased impact of residual water (Figure 23(a)).[23] Increasing the acceleration voltage will decrease the amount of available secondary electrons and change their energy distribution.[58] As a consequence, the growth rate decreases and an increased impact from residual gases, typically water, could be expected potentially causing a removal of carbon in the deposits. The Mn:O ratio remains relatively constant at 1.4:1 for all beam parameters, indicating the formation of a manganese sub-oxide or a mixture of manganese metal and some manganese oxide(s). The importance of using a Meissner trap prior to FEBID deposition experiments is demonstrated especially well with this precursor. Control experiments performed without using the Meissner trap prior to deposition revealed a significant increase in oxygen, accompanied by a drastic decrease in carbon (Figure 23(b)). In these experiments a nominal composition of $MnC_{0.19}O_{0.90}$ was observed for samples deposited at 5 kV and 1.6 nA. This points towards an efficient, electron-induced oxidation and carbon removal by residual water. Consequently, intentional co-dosing of water could potentially be used for the deposition of defined manganese oxides, similar to methods already demonstrated for SiO_2,[90-91], MoO_x,[92] and Fe_3O_4.[93]

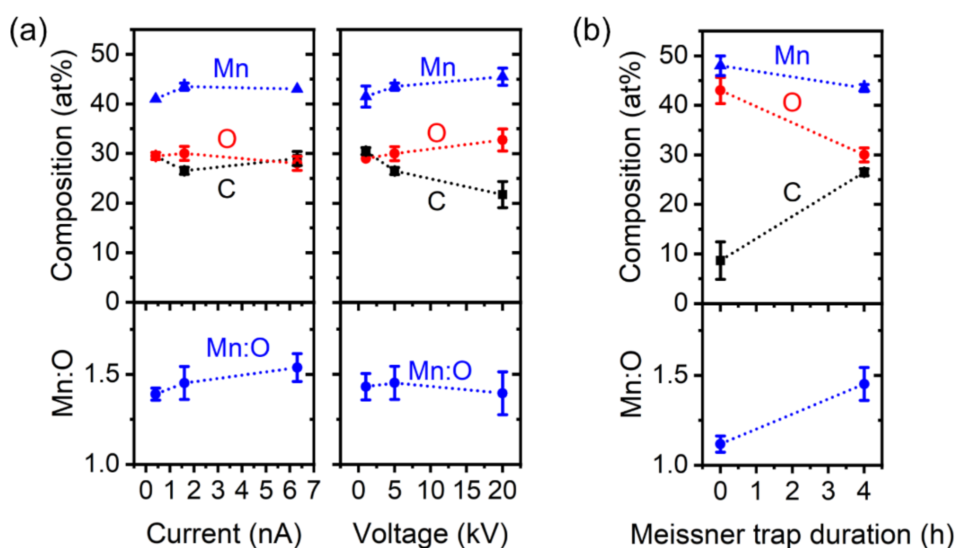

Figure 23: (a) Compositional analysis of the deposits via EDX as well as elemental ratios for varying current and voltage. For the variation of current the voltage was set to 5 kV. (b) Influence of Meissner trap usage on the composition of samples deposited at 5 kV and 1.6 nA. Further deposition parameters: sample size 1.4 µm × 1.4 µm, 20 nm × 20 nm pitch and a dwell time of 1 µs was used. Sapphire single crystals with 200 nm Au and 8 nm Cr as adhesion layer were used as substrates.

AFM investigations of the deposits show moderate growth rates of 1.8×10^{-3} µm³/nC to 0.4×10^{-3} µm³/nC, decreasing with increasing deposition current (0.4 nA to 6.3 nA). Similar effects have been observed for $V(CO)_6$ (discussed above) as well as other FEBID precursors reported in literature.[71, 198] A decrease in growth rate with increasing current is indicative of the

precursor limited growth regime. With increasing current, the same dose is applied in a shorter time and thus less time for diffusive replenishment of precursor is available. As a consequence, less volume is deposited per electron and a decrease in growth rate is observed. A more detailed discussion of growth regimes is provided in chapter 2.1.2.2. Cross sections of representative samples, depicted in the inset of Figure 24, show no elevated side edges indicating no diffusion-enhanced growth for this set of deposition parameters.

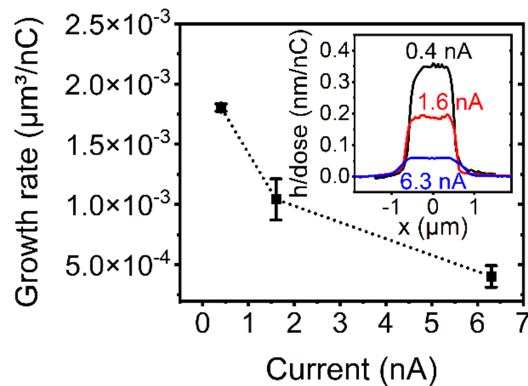

Figure 24: Volume based growth-rate determined by AFM. The insert shows representative height profiles for each current normalized to the total dose. Parameters used for the deposition were 5 kV, 0.4 nA to 6.3 nA, 20 nm × 20 nm pitch, 1 μs dwell time, typically 1.0 μm × 5.0 μm deposit size.

4.1.2.2.1 Electronic characterization

Room temperature electronic transport measurements were performed inside the SEM after deposition. I-V curves have been recorded in two-probe configuration on samples deposited across gold microelectrodes located on SiO_2 (200 nm) coated Si. The shapes of the samples were determined by AFM measurements. Typical sample dimensions were 1.0 μm × 5.0 μm with heights of 120 nm to 180 nm. Two-probe resistivity values, neglecting lead and contact resistances, for samples deposited with 5 kV acceleration voltage and varying electron beam current are shown in Figure 25(a). All samples show very high room temperature resistivities of 5×10^{10} μΩ·cm to 1.5×10^{9} μΩ·cm, decreasing with increasing current. Additional four-probe measurements revealed no significant contact resistances at room temperature.

Post-growth irradiation of the sample deposited at 5 kV and 6.3 nA with the same beam parameters and a dose of 1350 nC/μm² leads to a decrease in resistivity by about one order of magnitude (Figure 25(b)), similar to other FEBID deposits reported in literature.[102, 198] Nevertheless, the resistivity remains very high with values larger than 1×10^{8} μΩ·cm.

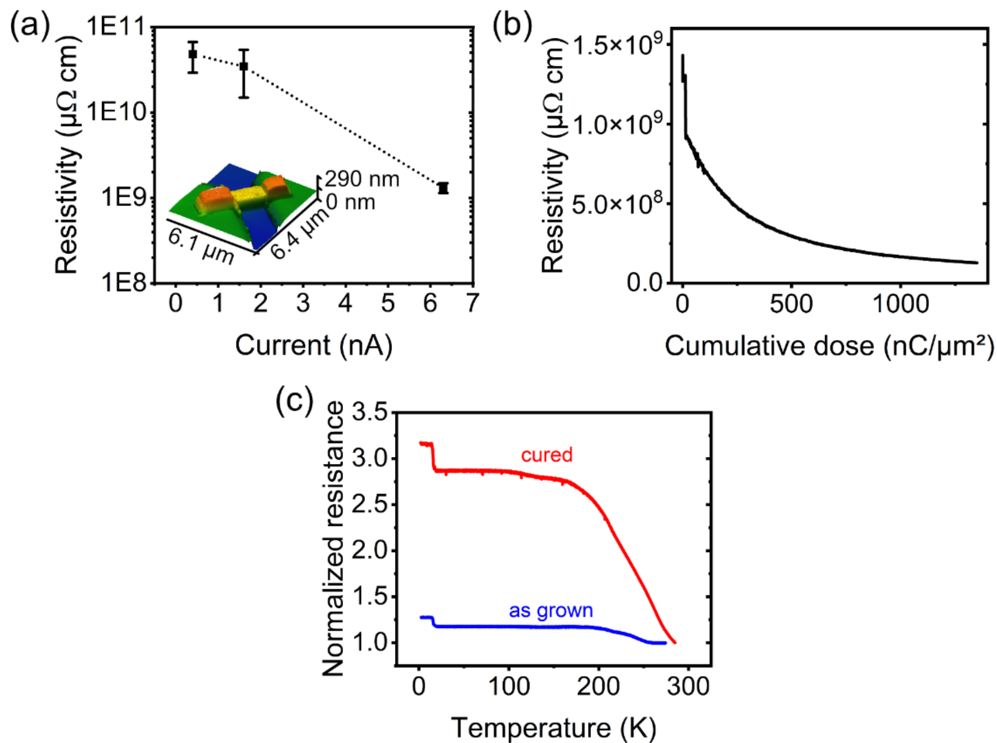

Figure 25: (a) Two-probe resistivity measurements of samples deposited with 5 kV and varying current; the geometry of the samples has been determined by AFM. (b) Change in resistivity during post growth curing of a sample deposited at 5 kV and 6.3 nA using the same beam parameters and a dose of 1350 nC/µm². (c) Temperature dependence of normalized resistance normalized at 285 K for samples deposited with 6.3 nA and 5 kV. The cured sample was irradiated with 6.3 nA and 5 kV for a dose of 1000 µC/µm². Adapted from ref. 286 by Jungwirth, *et.al.*, licensed under CC BY 4.0 (https://creativecommons.org/licenses/by/4.0/). Published 2022 by MDPI.

Temperature dependent electrical transport characteristics were investigated in a temperature range of 2 K to 275 K for an as grown and an electron beam cured sample (Figure 25(c)). The measurements were performed in two-probe configuration, because of the high resistivities of the samples. Both materials showed insulating behavior, however the increase in resistance was significantly less pronounced for the as grown sample. For both samples a distinct phase transition with an abrupt onset at approximately 15 K was observed. To the best of my knowledge neither metallic nor oxidic manganese phases known in literature show a phase transition in this temperature region. However, reliable statements are not possible since microstructural investigations have not been performed because of the high oxidation sensitivity of the material. Nevertheless, the formation of a nano-granular or amorphous material is very likely based on FEBID deposits with similar carbonyl precursors, also potentially forming metastable and/or unknown phases.[197, 291, 296] Additionally, different metastable oxides of manganese are known to form at room temperature, often leading to multivalent mixtures of manganese-oxides.[297] In conjunction with a well-known size effect for transition temperatures, only a qualitative discussion of the temperature dependent behavior is therefore possible.[298] Beginning from room temperature a monotonic increase of resistance

is observed for both samples, being more pronounced in the cured material. In the region of 170 K to 25 K negligible variation in resistance is observed for both samples until a distinct phase transition occurs at about 15 K. Below 15 K both samples show virtually no variation in resistance. Due to the high oxidation sensitivity of the sample a slight variation in electrical properties is already observed when transferring between experimental setups.

4.1.3 General considerations for metal carbonyls/conclusion

Transition metal carbonyls are the largest class of precursors discussed for FEBID in literature up to date. When considering the maximum metal contents reported in literature for homometallic, homoleptic transition metal carbonyls a general trend can be observed (Figure 26). Carbonyls of elements located in the so-called iron triad (group 8-10) are reported to typically yield metal contents above 80 at% for 2D deposits,[199-201, 214] while metal contents of 90 at% or larger are typically reported for 3D structures.[73-74, 76] On the contrary, carbonyls with central atoms of group 5-7 typically only yield materials with less than 50 at%. $V(CO)_6$ and $Mn_2(CO)_{10}$ are following this trend with intermediate metal contents of less than 50 at%.

5	6	7	8	9	10
$V(CO)_6$* 30-40 at%	$Cr(CO)_6$ 25-30 at%	$Mn_2(CO)_{10}$* 41-44 at%	$Fe(CO)_5$ $Fe_2(CO)_9$ 80-95 at%	$Co_2(CO)_8$ 73-100 at%	$Ni(CO)_4$ 95 at%
	$Mo(CO)_6$ 20-41 at%		$Ru_3(CO)_{12}$‡ ? at%		
	$W(CO)_6$ 37-58 at%	$Re_2(CO)_{10}$+ ? at%	$Os_3(CO)_{12}$‡ ? at%		

Figure 26: Slice of the periodic table showing homoleptic homometallic transition metal carbonyls described in FEBID literature[49, 73-76, 82, 92, 199, 201, 209, 211, 215] with their associated metal contents. The values for $Cr(CO)_6$ are unpublished results by P. Gruszka and M. Huth. *Precursors discussed in this work, +SAED shows only pure Re, but no compositional analysis was performed[291], ‡ no compositional analysis provided[299]

Furthermore, when considering compositions reported for CVD a similar trend becomes visible. Only transition metal carbonyls with a central metal of group 8, 9 or 10 yield thin films of high purity and *vice versa* (Figure 27). The trends observed in both FEBID and CVD match well with the chemisorption behavior of carbon monoxide on the corresponding transition metal surfaces. As discussed in chapter 2.4.1 the nature of the metal influences the C-O bond and the tendency of CO molecules to chemisorb molecular or dissociate into carbon and reactive oxygen.[216-217] Molecular adsorption is primarily observed for elements to the right in the periodic table with a transition behavior approximately along the Fe-Tc-Re line.[216-217]

This matches well with high purity deposits in FEBID and CVD being typically observed for carbonyls of transition metals of group 8-10. For both deposition methods the tendency of CO to either dissociate or to adsorb molecular will have similar effects on the purity of the deposit, thus similar trends could be expected. The overall slightly higher purities observed for CVD thin films are likely caused by an increased desorption probability of ligands or fragments thereof due to much higher deposition temperatures.

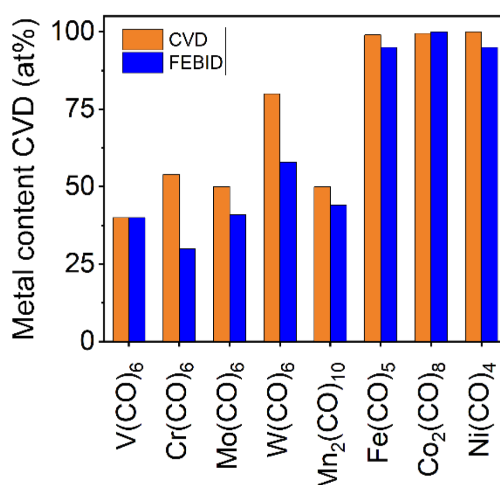

Figure 27: Comparison of maximum metal contents obtained in CVD with those obtained in FEBID. FEBID[49, 73-76, 82, 92, 199, 201, 209, 211, 215] and CVD[142, 300-306] compositions have been deduced from literature. The FEBID values for $Cr(CO)_6$ are unpublished results by P. Gruszka and M. Huth.

In general, homoleptic transition metal carbonyls are precursors well suited for the FEBID process due to their typically sufficient vapor pressure, ease of availability, and simple handling. The purity of the resulting deposits strongly depends on the precursor molecule and high purity deposits are currently only reported for elements belonging to the iron triad. High purity deposits of group 5-7 elements are most likely not accessible *via* simple FEBID experiments using carbonyl precursors and will require post-growth purification strategies. However, the precursors evaluated in this work, i.e. $V(CO)_6$ and $Mn_2(CO)_{10}$, are potentially good candidates for the formation of defined oxide phases as both are not susceptible to hydrolysis but will easily oxidize upon contact with molecular oxygen.

4.2 Single source precursors for FEBID and FIBID

Single-source precursors are of great interest for direct-write deposition methods such as FEBID and FIBID, as already discussed above. In this chapter three new single source precursors for focused beam induced deposition of transition metal silicides are presented.

4.2.1 $H_3SiMn(CO)_5$

$H_3SiMn(CO)_5$ was the first silyl substituted carbonyl precursor investigated for FEBID.[197] A high vapor pressure is observed due to its small molecular mass and weak intermolecular forces. As a consequence, the precursor reservoir had to be cooled to approximately T_P = 233 K, using an ethanol cooling bath, during FEBID and CVD deposition experiments.

4.2.1.1 CVD

Low pressure cold wall CVD was performed at substrate temperatures of T_S = 573 K to 673 K using sintered Al_2O_3 as well as Si (911) and Si (111) single crystals as substrate. The composition of the resulting dark-grey films was analyzed by EDX and the results are shown in Figure 28(a). Very significant amounts of oxygen are observed and, with the oxygen concentration surpassing that of carbon, post-growth oxidation during transfer between measurement setups is very likely. Similar effects have been observed for samples derived from $Mn_2(CO)_{10}$, discussed above. As a consequence, total metal/metalloid contents of 47 at% to 56 at% are observed. When compared to CVD thin films deposited by other metal carbonyls a C:O ratio close to or smaller than one is usually observed.[300-302] Thus, total metal/metalloid contents of approximately 70 at% to 80 at% are much more likely, assuming a C:O ratio of 1:1. This would also agree well with results reported for the thermal decomposition of $H_3SiMn(CO)_5$ at T_S = 444 K inside an SEM.[197] Interestingly, selective loss of silicon containing fragments is observed, resulting in a Mn:Si ratio of about 1.5:1, also in good agreement with CVD experiments and FEBID deposition.[197] A potential reaction that could cause the Si loss is thermally activated dimerization of two $H_3SiMn(CO)_5$ molecules, forming $H_2Si(Mn(CO)_5)_2$ and SiH_4, indicated in thermal stability experiments.[307] However side reactions with residual gases, such as water, have to be considered as well. Additionally, the CVD process is highly dynamic and various other reactions could also be responsible. Furthermore, an increase of carbon signal with increasing temperature is observed, indicating a more pronounced incorporation of carbonyl ligand fragments in the growing deposit. SEM analysis of the thin films revealed a network of nanowires (Figure 28(b)) for both deposition temperatures. The highly porous nature of the thin films could also explain the high oxidation tendency of the deposits. XRD analysis of thin films deposited at 673 K indicate a cubic crystal symmetry in accordance with a MnSi phase (PDF 00-042-1487). Additionally, very weak, broad reflexes in agreement with a cubic MnO phase (PDF 01-072-1533) were observed. Films deposited at 573 K did not show

a crystalline phase according to XRD measurements, even though the morphology revealed by SEM was very similar. In contrast, pyrolysis of $H_3SiMn(CO)_5$ at 773 K reportedly did yield a material with a Mn:Si ratio of approximately 1.1, additionally crystalline MnSi and significant amounts of Mn_5Si_3 were observed.[308]

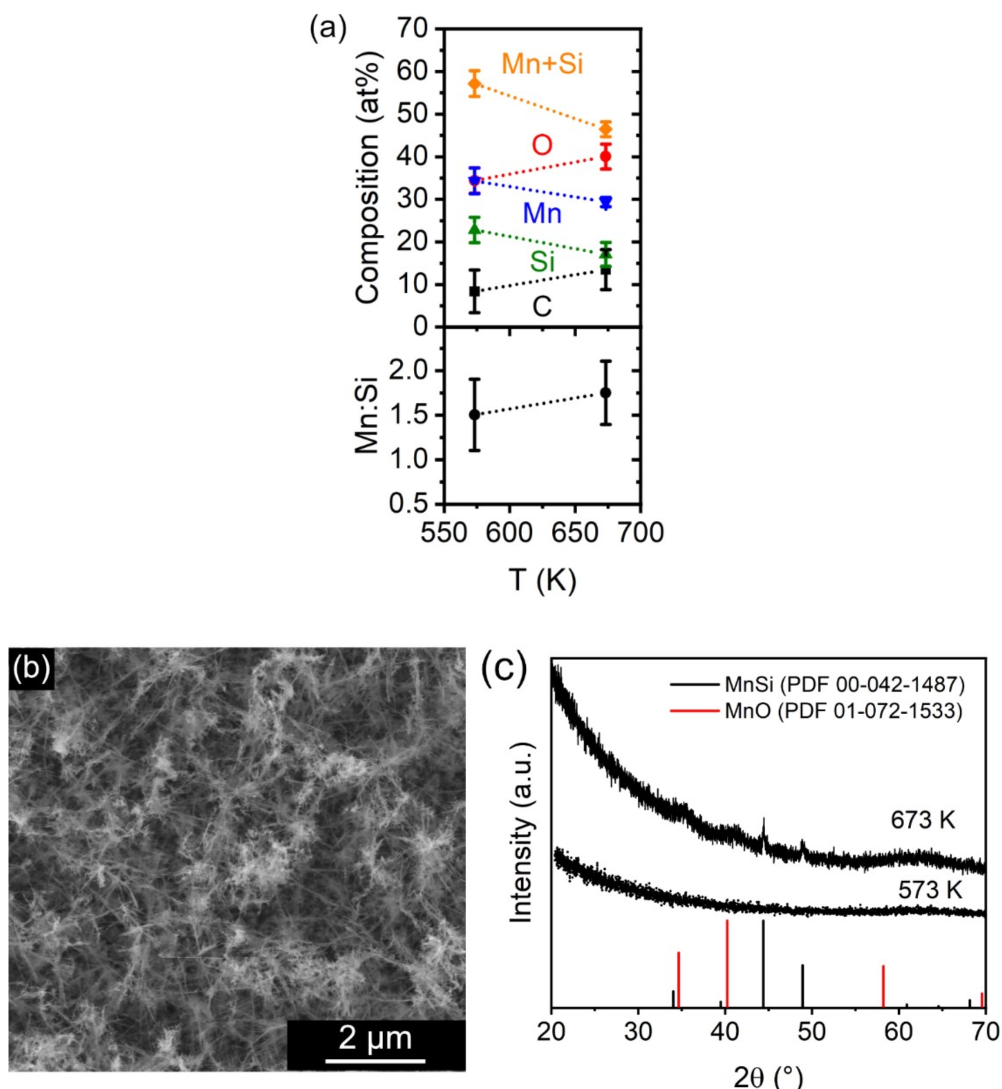

Figure 28: (a) EDX analysis of the thin films as well as elemental ratio of Mn:Si and C:O. (b) Representative SEM image of a film grown at 673 K showing a network of interconnected nanowires. (c) Diffractogram of thin films deposited at 573 K and 673 K.

4.2.1.2 FEBID

The influence of various deposition parameters, such as electron current and voltage, on the properties of the deposited material were investigated in FEBID experiments. Other writing parameters, such as pitch, precursor pressure and scan strategy, were kept constant. The deposition pressure typically was kept at 2×10^{-6} mbar.

Figure 29(a) shows the compositional variation of deposits for varying electron beam currents and a constant acceleration voltage of 5 kV. The overall metal/metalloid content of 45 at% to

49 at% is in good agreement with data reported in literature (40-55 at%).[197] Only minor variations in composition are observed for beam currents of 98 pA to 6.3 nA. The average composition at 6.3 nA can be described as $MnSi_{0.4}C_{0.9}O_{0.7}$ indicating the loss of about 82 % of carbonyl ligands as well as approximately 60 % of silyl ligands. Very similar compositions are obtained if an acceleration voltage of 20 kV is used (Figure 29(b)). Contrary to the results reported in literature,[197] a significant amount of oxygen is incorporated into the deposits, especially at low currents. Since the amount of oxygen surpasses that of carbon, influences from residual water are very likely.[23] Additionally, volatilization of carbon by electron stimulated oxidation with water is possible and could cause a reduction of C content, as has been demonstrated for RuC_x deposits.[98] A selective loss of silicon, much more pronounced than in CVD experiments, is observed, resulting in Mn:Si ratios of approximately 2.5:1. In comparison, lower Mn:Si ratios of about 2:1 have been reported in literature.[197] Two, potentially electron-stimulated, reactions can be considered for the formation of volatile, silicon containing fragments: (1) dimerization of two precursor molecules, or (2) reactions with residual water.[307] The distinct silicon loss observed in this work, when compared to literature, could be caused by a more pronounced contribution of water during the deposition, as evidenced by the larger amount of oxygen incorporation. However, FEBID is a highly dynamic, statistical process and a combination of various reaction pathways will be responsible for the final composition.

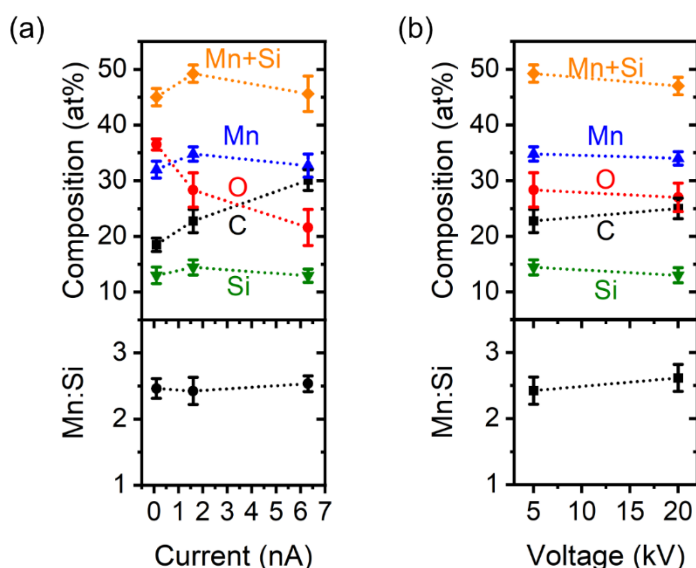

Figure 29: (a) Compositional analysis of deposits at varying current and 5 kV acceleration voltage. (b) Composition of samples deposited at varying deposition voltage. Further deposition parameters: sample size 1.4 µm × 1.4 µm, 20 nm × 20 nm pitch and a dwell time of 1 µs was used. Sapphire single crystals with 200 nm Au and 8 nm Cr as adhesion layer were used as substrates.

If volatile silicon-containing fragments are formed during the initial electron beam irradiation, cooling of the substrate should increase their surface residence time and thus increase the probability of their incorporation in the deposit. To study the influence of temperature on the

decomposition process a home-built cooling stage was used. The cooling stage consisted of a substrate holder which was thermally coupled to a Meissner trap, cooled by liquid nitrogen. Temperature control was achieved by heating the substrate using resistive heating. The setup allowed temperatures as low as 250 K with a control accuracy and thermal stability of approximately 1 K. The compositions for samples deposited at varying temperature with varying electron beam currents are shown in Figure 30. For all currents negligible variations in Mn:Si ratio have been observed, indicating that the side reaction causing the selective loss of silicon can also proceed at low temperatures. Additionally, the volatile silicon-containing products are apparently not retained on the surface long enough for them to be incorporated in the growing deposit. Furthermore, the amount of O incorporated in the deposits decreases with temperature, while at the same time the C increases. At low temperatures the precursor coverage of the substrate will increase and higher growth rates will be observed. Consequently, contributions of residual gases should decrease. At the same time a transition in growth regime towards a more electron limited growth will be observed and increasingly more ligand and ligand fragments can be incorporated in the growing deposit (depending on the desorption kinetics). Furthermore, prolonged use of the cooling stage will remove water from the background gasses in the same way a Meissner trap does, potentially also contributing to a decreased of oxygen in the deposits. The contribution of residual water to the composition is especially pronounced for the lowest deposition current of 98 pA. This is a consequence of longer deposition times being required to achieve the same height as for other currents.

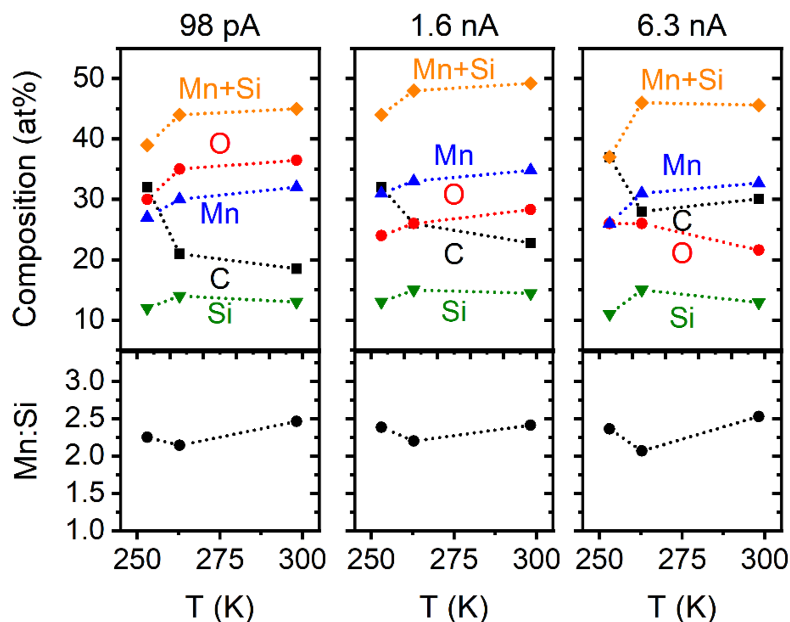

Figure 30: Composition of samples deposited at different substrate temperatures and beam currents using a constant acceleration voltage of 5 kV. Further deposition parameters: sample size 1.4 µm × 1.4 µm, 20 nm × 20 nm pitch, dwell time of 1 µs. Sapphire single crystals with 200 nm Au and 8 nm Cr as adhesion layer were used as substrates.

Volume-based growth rates were determined based on AFM measurements of the samples deposited at room temperature (Figure 31). An intermediate growth rate of 3.2×10^{-3} µm³/nC decreasing to 6×10^{-4} µm³/nC with increasing current was observed, very similar to that of $V(CO)_6$. A decrease in volume-based growth rate with increasing current is indicative of precursor limited growth, as discussed in chapter 2.1.2.2 above. Additionally, the presence of higher edges (inset Figure 31), in conjunction with a serpentine scanning strategy, indicates diffusion-enhanced growth. The effects are more pronounced at low beam currents due to increased deposition times and thus are especially visible for samples deposited at 98 pA and 1.6 nA. Contrary, no morphological artifacts related to the deposition strategy were observed for samples deposited with 6.3 nA.[69, 71] In contrast, diffusion enhanced growth is not observed for the AFM images shown in literature, very likely related to the different size of the deposit and the associated increase in refresh time.[197]

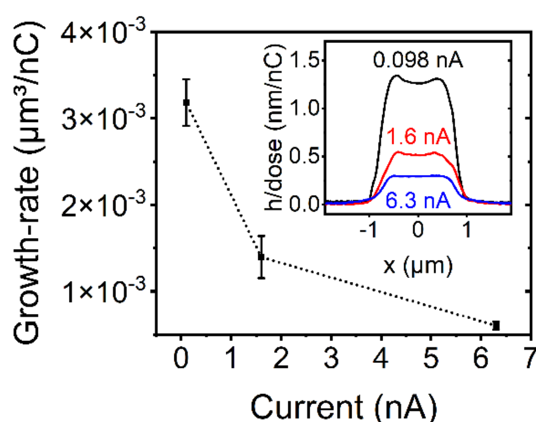

Figure 31: Volume based growth rates for samples deposited at room temperature with varying currents and an acceleration voltage of 5 kV. The inset shows representative cross sections normalized to the supplied electron dose. Further deposition parameters: sample size 1.4 µm × 1.4 µm, 20 nm × 20 nm pitch, dwell time 1 µs. Sapphire single crystals with 200 nm Au and 8 nm Cr as adhesion layer were used as substrates.

A detailed analysis of electronic transport behavior as well as microstructural investigations of the $H_3SiMn(CO)_5$ derived material have been provided in literature.[197] Temperature dependent conduction measurements did show quasi-metallic behavior, very similar to other FEBID materials. Post growth irradiation of the samples not only reduced their conductivity but also a change from electron to hole dominated transport was observed. Microstructural investigations did show amorphous Mn_2Si grains embedded in a carbon-rich matrix. Additionally, post-growth electron beam irradiation did cause the formation of a new crystalline spinel phase, potentially being Mn_2SiO_4.[197]

4.2.2 $H_3SiCo(CO)_4$ and $H_2Si(Co(CO)_4)_2$

In this chapter, a comparison of two different single source precursors for cobalt silicides with nominal compositions of Co:Si = 1:1 and 2:1 is presented. The precursors $H_3SiCo(CO)_4$ and $H_2Si(Co(CO)_4)_2$ were prepared in a salt elimination reaction from $NaCo(CO)_4$ and H_3SiI or H_2SiI_2 respectively, similar to literature.[309] Both precursors have been investigated for FEBID and FIBID. Additionally, their thermal decomposition behavior was examined in CVD experiments. Materials derived from these precursors will be denoted as CoSi and Co_2Si for simplicity, but the specific composition will be discussed in each subsection. For clarity, the deposition method will be specified as prefix, for example FEBID-CoSi denotes samples deposited by FEBID using $H_3SiCo(CO)_4$ as precursor.

4.2.2.1 CVD

Low-pressure cold-wall CVD was performed at substrate temperatures in the range of T_S = 573 K to 773 K using sapphire (0001) and Si (911) single crystal substrates. For both precursors, dark deposits with a metallic appearance were obtained. The composition of the obtained thin films was investigated by EDX and revealed significant incorporation of ligand atoms in the films for both CVD-CoSi (Figure 32(a)) and CVD-Co_2Si (Figure 32(b)). Using $SiH_3Co(CO)_4$ as the precursor, thin films with a total metal/metalloid content of approximately 80 at% were obtained, independent of the deposition temperature. The initial precursor stoichiometry was not retained and a selective loss of silicon has been observed. A Co:Si ratio of approximately 1.2:1 is obtained for both temperatures studied. The selective loss of silicon indicates the presence of a secondary reaction path leading to the formation of volatile silicon-containing fragments. A potential reaction would be the dimerization of two precursor molecules forming $H_2Si(Co(CO)_4)_2$ and SiH_4.[309] Alternatively, reactions with residual water have to be considered as well. SEM analysis shows facetted crystals for thin films deposited at 773 K (Figure 32(c)). When the temperature was decreased to 553 K a granular coating was deposited and no defined crystal facets were observed. XRD analysis of thin films deposited at low temperatures only shows few, broad reflexes indicating low crystallinity/crystal size. For thin films deposited at 773 K a cubic CoSi phase (PDF-00-050-1337) can be identified (Figure 32(e)).

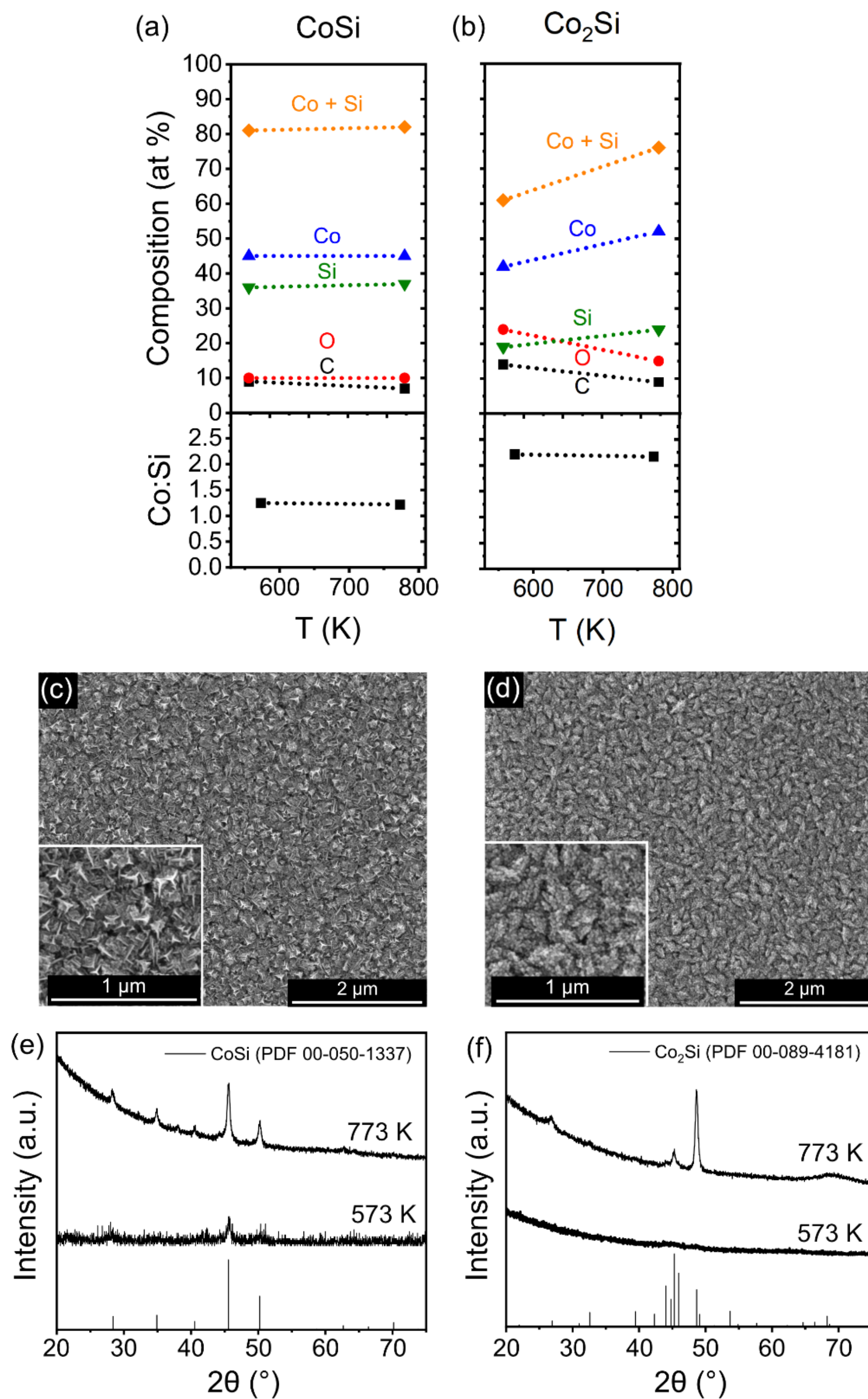

Figure 32: EDX analysis of thin films deposited at different temperatures for both (a) CVD-CoSi and (b) CVD-Co_2Si. SEM image of a representative CVD-CoSi (b) and CVD-Co_2Si (c) thin film deposited at 773 K. (d), (e) XRD patterns recorded at room temperature for thin films deposited at 573-773 K for CVD-CoSi and CVD-Co_2Si respectively.

In the case of $SiH_2(Co(CO)_4)_2$-derived thin films, EDX revealed a similar, yet slightly lower, total metal/metalloid content of up to 76 at% when deposited at 773 K (Figure32(b)). A decrease of metal/metalloid content to 61 at% was observed for lower substrate temperatures (573 K). Additionally, significant oxidation of the material is observed, as evidenced by a C:O ratio

smaller than one. The oxidation, most likely, is related to post-growth oxidation during transfer between measurement setups. Even though CVD-CoSi samples were treated similar no/minor signs of post-growth oxidation are present. This could be related to differences in morphology or oxidation resistances of both samples. Hence, the actual metal/metalloid content will likely be higher at about 72 at% and 82 at% respectively, assuming a C:O ratio of 1:1 as typically observed for other carbonyl-derived CVD thin films.[300-302] Thermal decomposition inside the SEM using a micro hotplate revealed even higher metal contents of up to 95 at% with a C:O close to 1:1. The hotplate was set to a temperature of 573 K, however the actual temperature in the SEM chamber will be significantly higher as the hotplates are calibrated at ambient pressures. A selective loss of silicon-containing fragments was observed for CVD-Co_2Si resulting in Co:Si ratios of approximately 2.2:1. Figure 32(d) depicts a typical SEM image of a Co_2Si thin film deposited at 773 K showing facetted crystals. Deposition at lower temperatures did yield a granular material. XRD analysis shows no crystalline phases for samples deposited at 573 K. Distinct reflexes were only observed if the deposition temperature was increased to 773 K. An orthorhombic crystal symmetry can be assigned in accordance with a Co_2Si reference (PDF-00-089-4181) (Figure 32 (f)). When compared to the reference spectrum different intensities are observed, indicating an anisotropic growth of the crystallites. Even though significant amounts of oxygen are present in the EDX spectra a crystalline oxide phase has not been observed in the diffractograms.

Micro-Raman analysis of thin films deposited by CVD at 773 K is shown in Figure 33. Raman shifts around 200 cm^{-1} to 240 cm^{-1}, observed for the CVD-CoSi deposit, can be assigned to a CoSi phase according to literature.[310-311] The band observed at 303 cm^{-1} could stem from the lattice vibrations of silicon however the first order Si Raman band, typically observed at 520 cm^{-1}, is not present.[311] CVD-Co_2Si thin films also show the formation of the desired silicide phase with the peak at 148 cm^{-1} belonging to Co_2Si, while signals at 198 cm^{-1} and 218 cm^{-1} could correspond to CoSi.[312] For both CVD thin films two signals are observed at around 1350 cm^{-1} and 1550 cm^{-1} corresponding to carbon.[313] The two bands are typically called D for disordered and G for graphitic respectively.[314] These two peaks typically dominate the Raman spectra of a various carbon materials ranging from highly ordered graphite to nanocrystalline and even amorphous carbons.[315] Analysis of position and intensity of the D and G band allows to draw conclusions regarding the chemical nature of the carbon incorporated in the deposit.[315] Deconvolution of the D and G band was performed using two Gaussian profiles, providing peak positions, areas and intensities. Both CVD-CoSi and CVD-Co_2Si deposits show very similar G band positions of 1586 cm^{-1} and 1590 cm^{-1} as well as similar intensity ratios I_D/I_G of 1.23 and 0.92 respectively. This corresponds to carbon being mostly present as nanocrystalline graphite according to the model of Ferrari and Robertson.[315]

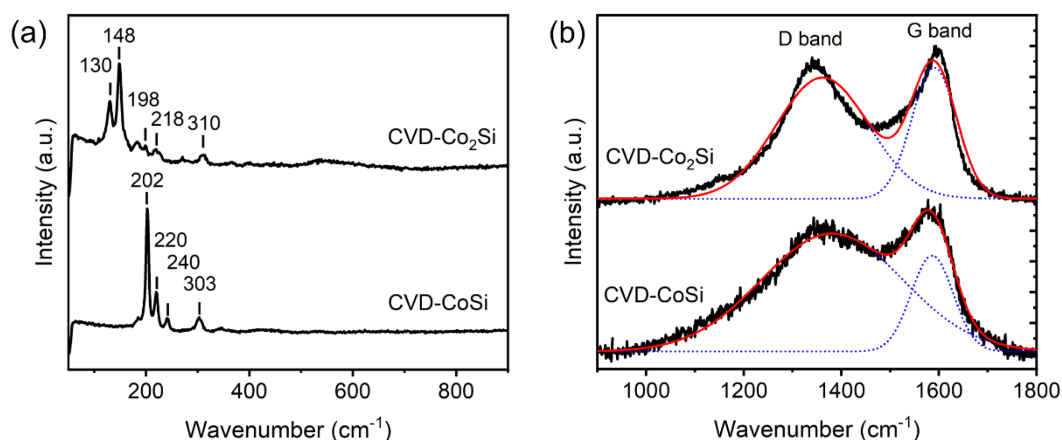

Figure 33: Raman spectra of thin films deposited at 773 K for both CVD-CoSi and CVD-Co_2Si normalized to the respective maximum intensity. (a) Low energy region of the spectrum showing peaks corresponding to a CoSi- and Co_2Si-phase respectively. (b) Carbon region of the Raman spectra (background subtracted). The red curve shows the fit to the data using two Gaussian curves (blue).

4.2.2.2 FEBID

Electron beam induced decomposition was studied similar to other precursors discussed in this work. Beam parameters such as acceleration voltage and current, as well as precursor pressure were varied while other writing parameters (dwell time, pitch, scan strategy, etc.) were kept constant. The chamber pressure during depositions was typically kept below 2×10^{-6} mbar. All pressures presented here are total system pressures, the local pressure at the deposition site is much higher. After initial plasma cleaning, the system was pumped for at least 48 h prior to deposition and a Meissner trap was used for 4 h to reduce the amount of residual water. This procedure guaranteed a background pressure of below 3.6×10^{-7} mbar.

Deposits of typically 1.4 µm × 1.4 µm with a height of at least 100 nm were used for compositional analysis. The analysis was carried out using EDX with an acceleration voltage of 3.5 kV in order to reduce contributions from the substrate material to a minimum. Figure 34 illustrates the change in composition with varying beam currents at a constant acceleration voltage of 5 kV. Both FEBID-CoSi and FEBID-Co_2Si show very similar total metal/metalloid contents of approximately 60 at%. For both precursors, the pre-defined Co:Si ratios of 1:1 and 2:1 were retained well within the deposits over the whole range of beam parameters investigated. The overall composition of $H_3SiCo(CO)_4$ derived materials can be described as $CoSi_{0.9}C_{0.5}O_{0.8}$. This composition indicates that approximately 0.5 carbon atoms remain in the deposit and accordingly 88 % of the initial carbonyl ligands are removed during the decomposition. The retention of 0.9 Si atoms per Co atom indicates the loss of approximately 10 % of Si. A slight decrease in silicon (and thus an increase in the associated Co:Si ratio) is observed with increasing current, indicating the contribution of an electron-stimulated reaction.

Interestingly, for the very similar precursor $H_3SiMn(CO)_5$ Mn:Si ratios of approximately two or larger were observed, pointing towards a very efficient (electron-stimulated) selective loss of silicon-containing fragments.[197] The increased silicon retention in $H_3SiCo(CO)_4$ could be associated with a stronger metal silicon bond implied by a hypsochromic shift in the infrared absorption band of the M-Si vibration and the trans-located CO ligand.[307, 309] A decrease in oxygen content from 28 at% to 21 at% is observed when the current is increased from 98 pA to 6.3 nA. Since the amount of oxygen surpasses that of carbon it is very likely caused by water, present in the residual atmosphere.[23] Water typically is the main constituent of the residual gas and can undergo electron stimulated reactions, causing the oxidation of the deposit, as well as, the reduction of carbon.[23] With increasing current, the total deposition time required for the same dose decreases. As a consequence, less time is available for the contribution of residual gases during the deposition process and thus less oxidation is observed. Consequently, a C:O ratio of approximately 1:1 is observed for 6.3 nA.

Slightly lower total metal/metalloid contents are obtained for $H_2Si(Co(CO)_4)_2$ derived material with a maximum of 60 at%, corresponding to an overall composition of $CoSi_{0.5}C_{0.4}O_{0.6}$. The Co:Si stoichiometry of the precursor molecule is retained very well in the deposit and only minor fluctuations are observed within the parameters investigated. Similar to FEBID-CoSi about 0.4 carbon atoms remain, however, due to the larger amount of CO ligands in the Co_2Si precursor this equates to the loss of 95 % of initial carbonyl ligands. A contribution of residual water is also observed, indicated by a C:O ratio of smaller than one. However, the contribution of water is much less pronounced for Co_2Si when compared to CoSi. This can be attributed to the overall higher growth rate of FEBID-Co_2Si when compared to FEBID-CoSi (Figure 35). A more detailed discussion of growth rates is provided below.

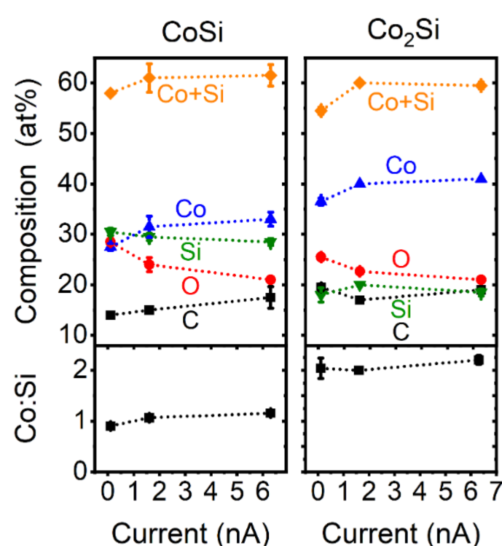

Figure 34: Compositional analysis of CoSi and Co_2Si FEBID deposits for varying current with a fixed acceleration voltage of 5 kV. The sample size was 1.4 µm × 1.4 µm, further deposition parameters were: 20 nm × 20 nm pitch and 1 µs dwell time. Sapphire single crystal substrates with 200 nm Au and 8 nm Cr as adhesion layer were used.

The composition of both precursors shows only minor dependence on deposition pressure and acceleration voltage (Figure 35). If pressures very close to the background pressure of the system are used FEBID-CoSi shows a drastic decrease in metal/metalloid content to about 27 at% (Figure 35(a)). This is very likely related to the considerable decrease in growth rate at low pressures discussed below (Figure 38). As a consequence, a significant contribution from background gases, especially water, is observed, evidenced by the large amount of oxygen in the deposit. The composition of $H_2Si(Co(CO)_4$ derived materials shows only marginal variation with pressure which can be partially related to the significantly higher growth rates discussed in the following. Variations in acceleration voltage between 1 kV and 20 kV did only cause minor compositional variation for both precursors (Figure 35(b)).

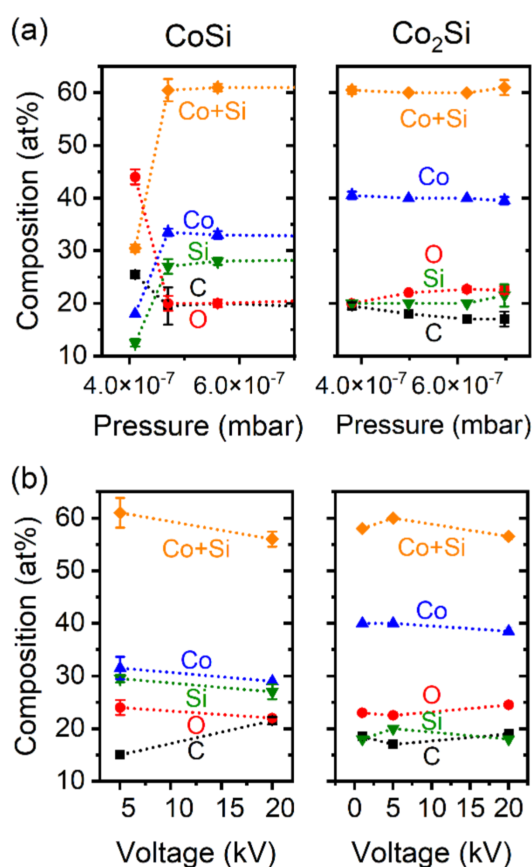

Figure 35: (a) Compositional variation of FEBID CoSi and Co_2Si deposits with varying deposition pressure and acceleration voltage. Deposition pressure was varied for 5 kV and 1.6 nA. (b) Influence of changes in acceleration voltage on the composition of FEBID-CoSi and FEBID-Co_2Si. For (a) and (b) deposit size was 1.4 µm × 1.4 µm, 20 nm × 20 nm pitch and a dwell time of 1 µs was used. Sapphire single crystals with 200 nm Au and 8 nm Cr as adhesion layer were used as substrates.

Compared to the compositions obtained in CVD, FEBID-CoSi shows significantly larger amounts of oxygen and carbon. Similarly, FEBID-Co_2Si also shows larger amounts of ligand incorporation when compared to CVD. This indicates that heating of the substrate stage or 3D

growth could improve the purity of the deposits. However, for the very similar precursor $H_3SiMn(CO)_5$ only minor effects were observed when the substrate temperature was increased during FEBID.[197] Additionally, neither CVD-CoSi nor CVD-Co_2Si thin films are completely pure indicating that 3D growth or additional heating during deposition will most likely not drastically increase the deposit's purity.

Micro-Raman spectroscopy was performed on FEBID-CoSi and FEBID-Co_2Si samples deposited with varying currents and an acceleration voltage of 5 kV, providing additional information about the bonding situation of the residual carbon (Figure 36(a)). Two signals characteristic for carbon are observed at approximately 1300 cm^{-1} and 1500 cm^{-1} for both FEBID-CoSi and FEBID-Co_2Si.[313] The contributions of D and G band were deconvoluted using two Gaussian profiles, providing peak positions, peak areas and intensities. Peak intensity ratios I_D/I_G and G band position in dependence of deposition current are depicted in Figure 35(b). For both FEBID-CoSi and FEBID-Co_2Si deposits their G band positions of 1516-1486 cm^{-1} and 1545-1517 cm^{-1} in conjunction with I_D/I_G ratios of 0.7-0.5 and 1.9-1.1 respectively, suggest that mostly amorphous carbon is deposited.[315] However, the G band positions of the FEBID-CoSi deposits are unusually low (below 1520 cm^{-1}), making the application of the model questionable.[315-316] The shift to lower values could be related to bond disorder,[315] or the presence of predominantly sp^3 carbon, also known as tetrahedral amorphous ta-C.[316] However, Raman spectroscopy of carbon materials is highly complex and a systematic study would be required for a better understanding of the exact bonding situation. Nevertheless, the overall Raman spectra are comparable to those of other carbonyl derived FEBID materials such as $FeCo_3$[317] and Co[100] suggesting that similar carbon species are present.

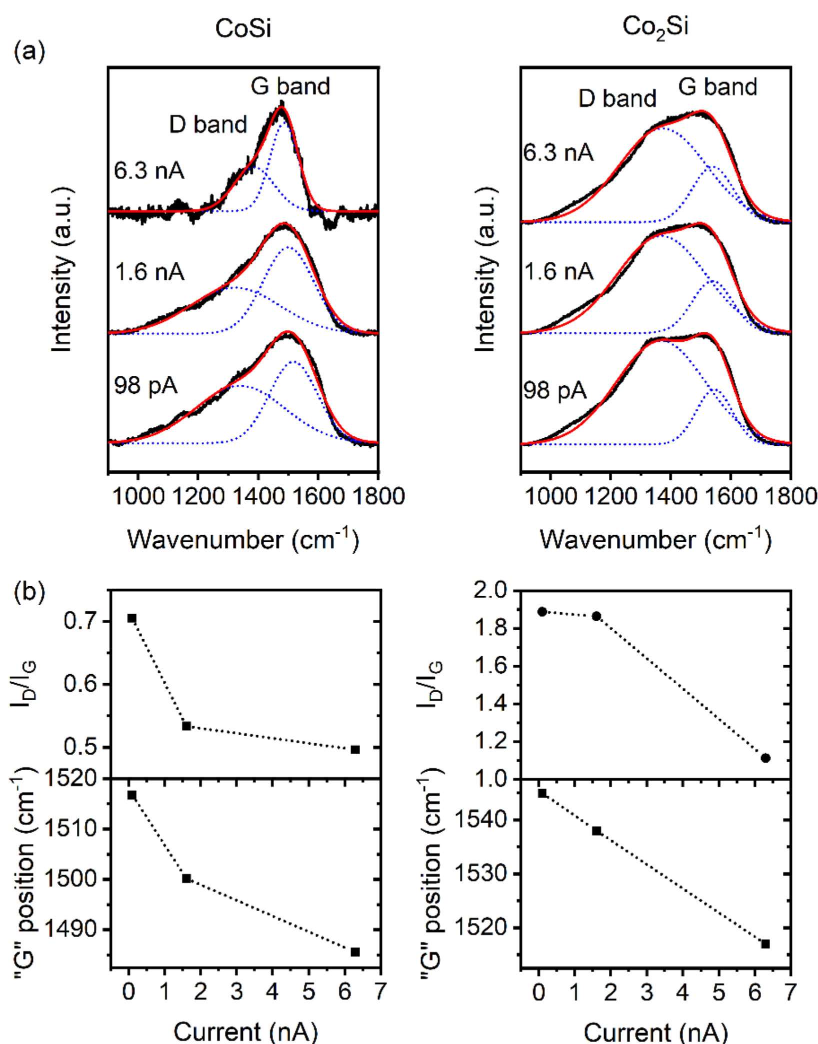

Figure 36: (a) Raman spectra of the carbon region for FEBID-CoSi and FEBID-Co_2Si normalized to their respective maximum (background subtracted). The red curve shows the fit to the data using two Gaussian curves (blue). (b) Corresponding Intensity ratios I_D/I_G and position of the G band maximum in dependence of the deposition current. All samples have been deposited with 5 kV and varying current of 98 pA to 6.3 nA.

The volume growth rates for different decomposition conditions have been calculated based on AFM measurements of the respective samples (Figure 37). Representative cross sections of samples deposited with 5 kV and varying electron beam current are shown in the insets in Figure 37. The sample heights have been normalized to the supplied dose for better comparability. Interestingly, the growth rate for FEBID-Co_2Si deposits is significantly higher than that of FEBID-CoSi. This could either be related to different adsorption kinetics or significantly different dissociation cross-sections. The volume growth per dose for CoSi is 1.7×10^{-3} to 4×10^{-4} µm³/nC while growth rates of 7.9×10^{-3} to 1.4×10^{-3} µm³/nC were observed for Co_2Si for currents of 98 pA to 6.3 nA. For both precursors the deposition efficiency decreases with increasing electron beam current, indicative of precursor-limited growth, as

discussed above.[69] Additionally, for FEBID-CoSi as well as FEBID-Co_2Si deposits the formation of side edges can be observed in the line scans shown in the insets of Figure 37. In conjunction with the serpentine pattering strategy, this points towards a diffusion-enhanced precursor-limited growth.[69, 71] A more detailed discussion of growth regimes is provided in chapter 2.1.2.2.

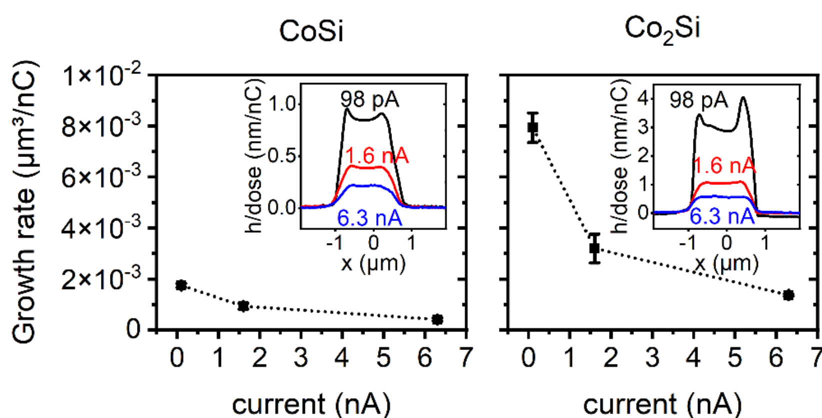

Figure 37: Volume-based growth rates of FEBID CoSi and Co_2Si deposits for varying currents with a constant acceleration voltage of 5 kV. Insets show line scans of representative deposits at varying currents with height normalized to dose for better comparability. Parameters used for the deposition were 5 kV, 98 pA to 6.3 nA, 20 nm × 20 nm pitch, 1 µs dwell time, and a deposit size of 1.4 µm × 1.4 µm.

Pressure-dependent growth rates for samples deposited at 5 kV and 1.6 nA have also been recorded and are shown in Figure 38. The lowest growth rates are observed for the lowest pressures, as can be expected. In the case of FEBID-CoSi, the growth rate starts to level off at a pressure of approximately 6×10^{-7} mbar. In contrast, FEBID-Co_2Si shows a monotonic increase with pressure. Even at the lowest pressure investigated in this study FEBID-Co_2Si has a significantly higher growth rate than FEBID-CoSi at the conditions typically used. For FEBID-Co_2Si even larger growth rates would very likely be possible if higher precursor pressures are used. In this study, however, the maximal pressure was limited by the volatility of the precursor at 296 K. The AFM height profiles (depicted in the insets of Figure 38) show that the shapes of the deposits are very similar for each precursor and largely independent of deposition pressure.

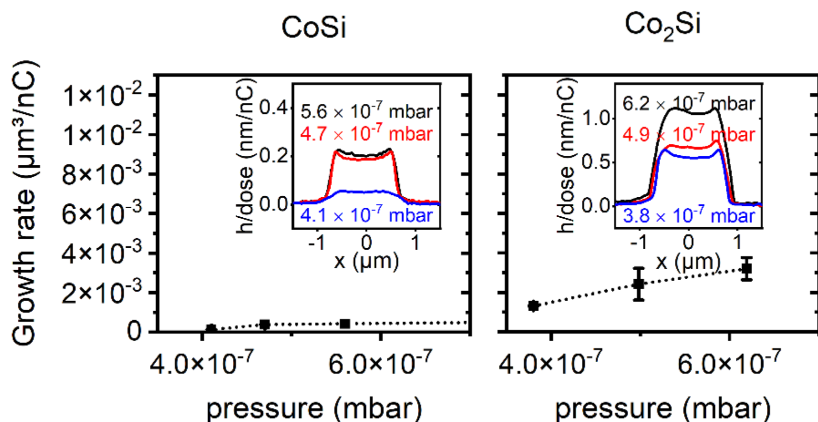

Figure 38: Volume-based growth rate of FEBID deposits of CoSi and Co_2Si in dependence of deposition pressure. The insets show line scans at the respective pressures normalized to the total dose. Parameters used for the deposition were 5 kV, 98 pA to 6.3 nA, 20 nm × 20 nm pitch, 1 µs dwell time, and typically sample size 1.4 µm × 1.4 µm.

4.2.2.2.1 Electrical transport

Initial room temperature electrical transport measurements have been carried out in the SEM directly after the deposition. I-V curves have been recorded in two-probe configuration for samples deposited across two Au microelectrodes located on a SiO_2 (200 nm) coated Si substrate. The exact dimensions of all samples were determined by AFM allowing to calculate resistivities for each individual deposit. The typical sample dimensions were approximately 1.0 µm × 4.0 µm, with heights of 90 nm to 250 nm. Both precursors were deposited with 5 kV and varying currents. The resulting two-probe resistivities are shown in Figure 39.

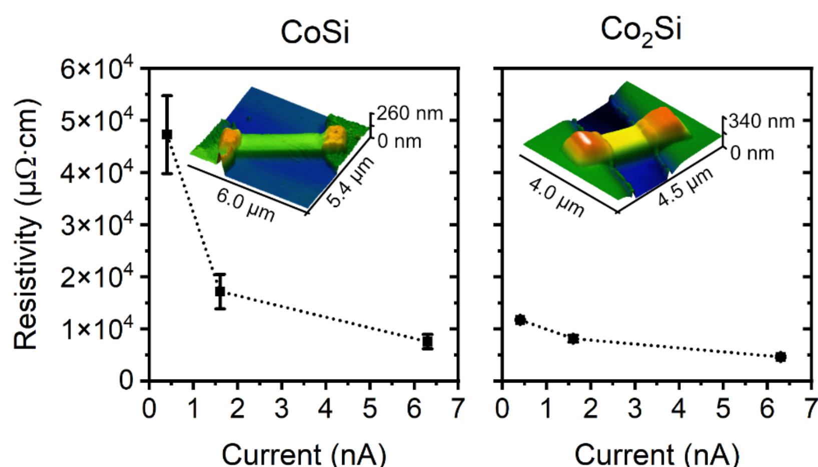

Figure 39: Comparison of room temperature resistivity measured in two-probe configuration for FEBID-CoSi and FEBID-Co_2Si. The samples were deposited at 5 kV and the beam currents were varied from 0.4 nA to 6.3 nA. The insets show AFM images of representative devices used for the measurement. Adapted with permission from Ref. 198. Copyright 2021 American Chemical Society.

FEBID-CoSi deposits did show a decrease in resistivity from 48 mΩ·cm down to 7.5 mΩ·cm with increasing current. The resistivity observed for deposits with the highest current (6.3 nA) is very similar to material prepared by a co-deposition approach using $Co_2(CO)_8$ and Si_5H_{12} as precursors.[232] However, a detailed discussion of both materials is not possible since their microstructures are not known and very likely different, as revealed by temperature dependent conductance measurements discussed below. The cobalt-rich FEBID-Co_2Si deposits, on the other hand, had overall lower resistivities of 12 mΩ·cm to 4.8 mΩ·cm, also decreasing with increasing current. In principle, higher purity deposits with larger amounts of metal could be an explanation for the observed decrease in resistivity. However, according to EDX analysis, no significant changes in composition have been observed when increasing the current from 1.6 nA to 6.3 nA. Thus, a more likely explanation for the increased conductivity are changes in microstructure as well as grain growth due to an increased electron flux, as often reported for FEBID deposits.[231]

A significant decrease in resistivity is observed for post-growth electron beam irradiation of both sample types. Figure 40(a) shows the evolution of resistivity with increasing electron dose for both materials, measured in two-probe configuration. The effect of the post-growth irradiation is thereby independent of beam current but rather depends on the total dose, as demonstrated in Figure 40(b) for FEBID-Co_2Si deposits. According to EDX analysis no changes in composition were observed for post-growth irradiation. This indicates that microstructural changes and/or grain growth are very likely the cause for the decrease in resistivity, similar to what has been reported for other FEBID deposits.[102] Electron beam curing of FEBID-CoSi samples deposited with 5 kV and 6.3 nA using the same beam parameters and a dose of 1200 nC/µm² did result in a decrease of resistivity from initially 6.6 mΩ·cm to 2.1 mΩ·cm. For FEBID-Co_2Si samples a decrease of resistivity from 4.6 mΩ·cm to 2.1 mΩ·cm was recorded, also using 5kV/6.3nA and a dose of 1200 nC/µm². The same samples have been used for temperature dependent electrical characterizations (Figure 41). Comparison of resistivity values measured in two- and four-probe geometry showed only minor contributions from lead or contact resistances for all four material types. Typically, differences below 10 % were recorded throughout all samples.

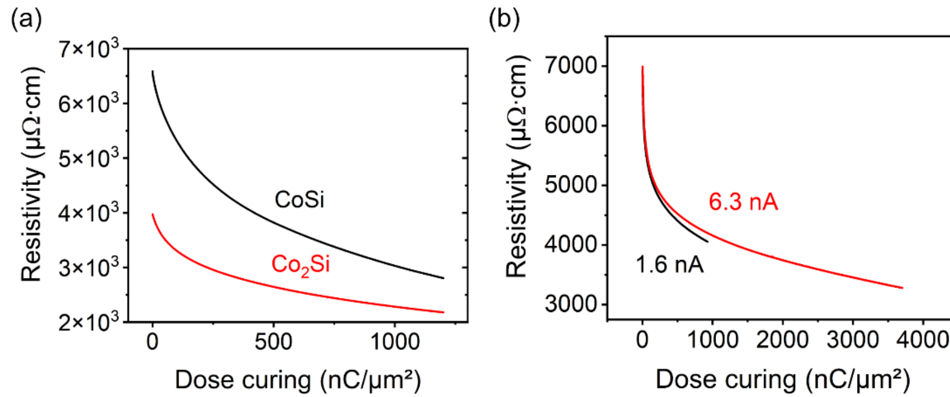

Figure 40: (a) Effect of post-growth electron beam irradiation of CoSi and Co_2Si samples deposited at 5 kV and 6.3 nA and irradiated with the same beam parameters. Irradiation was performed for a total dose of 1200 nC/µm². (b) Comparison of different beam currents for post growth irradiation of FEBID-Co_2Si deposits. The resistivity decrease appears to be dependent on electron dose but not beam current. (b) Adapted with permission from Ref. 198. Copyright 2021 American Chemical Society.

Figure 41 shows the temperature dependent normalized conductance of all four samples measured in the temperature range of 2 K to 285 K. An AFM image of a typical device is depicted as inset in Figure 41. All samples showed a decrease of conductance with decreasing temperature, typical for granular metals.[189] The logarithmic derivative $\omega = dln\, \sigma / dln\, T$ is extrapolated for $T \rightarrow 0$ to distinguish between metallic or insulating behavior (Figure 42).[318] If the sample is on the metallic side of the metal-insulator transition, ω is expected to approach zero.[318] Based on this analysis, all samples, except the as-grown FEBID-CoSi, are in the quasi-metallic regime of granular metals. The only sample on the insulating side of the metal-insulator transition is as-grown FEBID-CoSi as evidenced by finite ω values for $T \rightarrow 0$. This contradicts results reported for FEBID-Co_xSi materials prepared by co-deposition of two precursors. In this case, metallic behavior was reported for Co_xSi with x = 0.6-1.[232] The variations in temperature dependent conductance are likely related to different microstructures, as already mentioned above but for both materials no microstructural characterizations have been performed. Post-growth electron beam curing not only increased the conductivity of the samples but also affected their temperature dependence, resulting in a much smaller reduction of normalized conductance at low temperatures. Very similar behavior of normalized conductance values and changes associated with electron beam curing have been reported for several other FEBID materials.[189, 230]

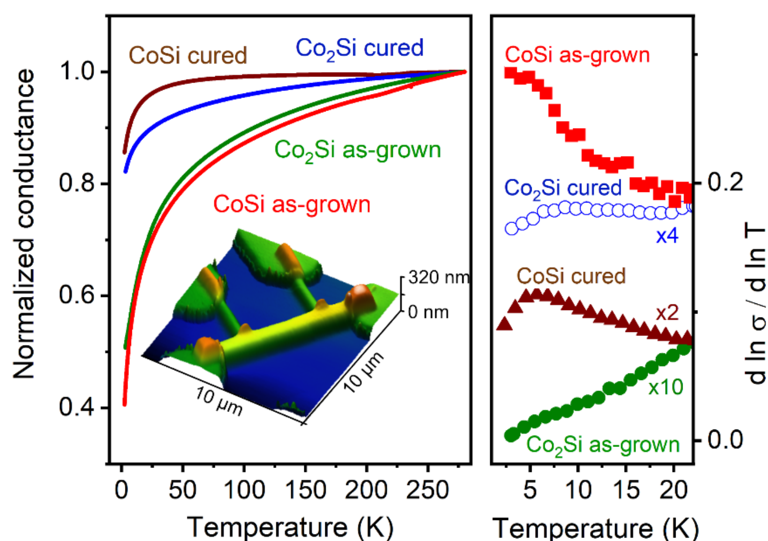

Figure 41: Temperature dependence of conductivity normalized at 285 K for FEBID samples of CoSi and Co_2Si deposited with 5 kV and 6.3 nA. Cured samples were irradiated with 5 kV and 6.3 nA for a total dose of 1200 nC/µm². The inset shows the AFM image of a typical deposit used in these studies. Adapted with permission from Ref. 198. Copyright 2021 American Chemical Society.

Additionally, changes in magnetoresistance (MR) were observed between irradiated and as-grown deposits (Figure 42). Generally, the magnetoresistance in all samples is negative. In the case of as-grown samples, both FEBID-CoSi as well as FEBID-Co_2Si show a saturation at 1.5 T with a maximum MR of -1 % and -0.7 % respectively. Negative magneto-resistance is typically observed for ferromagnetic metals, because spin misalignment causes scattering of charge carriers. When a magnetic field is applied the spins align, reducing scattering and thus the overall resistance of the material. The values reported here are similar to other ferromagnetic FEBID deposits such as Co_3Fe[196] and Fe:C:O from $Fe(CO)_5$.[226] Interestingly, upon irradiation of the samples a suppression of the negative MR is observed and the background (with a positive MR) becomes more pronounced. This causes a deviation from the expected saturation behavior. The general shapes recorded in all samples can be associated to a tunnel magnetoresistance effect (TMR) with a positive background magnetoresistance, most pronounced in the cured samples. TMR can be expected, among other materials, for ferromagnetic granular metals and is caused by spin dependent tunneling effects.[319] Considering two ferromagnetic islands separated by an insulator, tunneling of electrons between these particles is more likely for electrons with parallel spin.[319] When applying an external magnetic field, the spins will begin to align, causing a decrease in electrical resistance when compared to randomly oriented spins.[319]

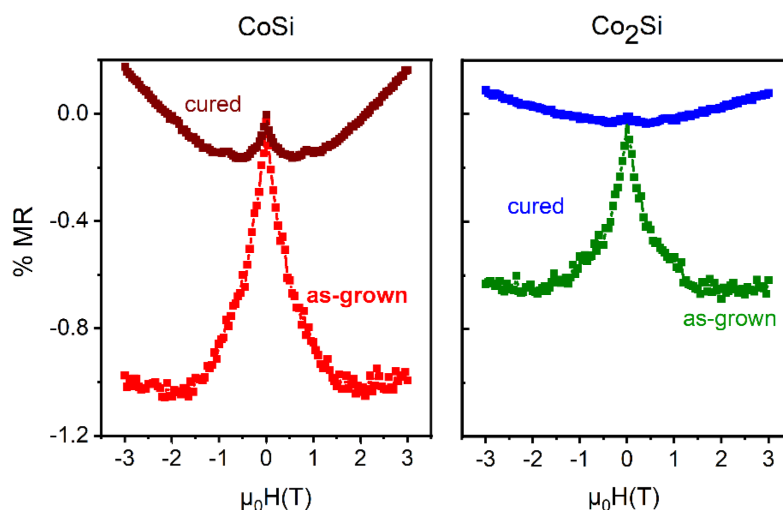

Figure 42: Magnetoresistance measurement of as-grown and beam cured FEBID material. Samples were deposited at 5 kV and 6.3 nA, post growth curing was performed using the same beam parameters and a total dose of 1200 nC/µm². Adapted with permission from Ref. 198. Copyright 2021 American Chemical Society.

Various effects can contribute to the overall different behavior observed in cured samples: (1) Prolonged electron beam irradiation may liberate metal species from incompletely dissociated ligand fragments causing grain growth[102] and changes in microstructure[320] (2) Additional energy is provided, potentially assisting in the completion of phase formation or crystallization.[230] (3) Initially intact bonds of incorporated ligand/ligand fragments may be broken, forming reactive species. For example, reactive oxygen could be formed from initially intact CO, which, in turn, could oxidize the material altering the electronic and magnetic properties of the metallic grains.[48] (4) Alternatively, initially retained Si-H bonds can be broken, liberating Si which in could form more cobalt silicides or react with oxygen forming SiO_2.[52] (5) Changes of the carbon matrix, for example graphitization, have also been reported.[102] Very likely all these effects will contribute to some degree causing the changes in the overall electronic and magnetic behavior of the samples.

4.2.2.3 FIBID

FIBID investigations were carried out similar to FEBID by varying current as well as voltage of the Ga^+ ion beam. Due to the different decomposition efficiency as well as sputtering, significantly lower beam currents of 1 pA to 30 pA were used while the acceleration voltage was varied from 15 kV to 30 kV. Scanning strategy, pitch (30 nm × 30 nm) and dwell time (0.2 µs) were kept constant throughout the experiments. Additionally, different substrate materials have been investigated. Similar to FEBID experiments the chamber was pumped for at least 48 h after plasma cleaning and the water level was reduced to a minimum using a Meissner trap prior to deposition resulting in background pressures of below 3.6 × 10^{-7} mbar.

4.2.2.3.1 Precursor characteristics in FIBID

The dependence of composition on beam current variation was investigated with EDX. Typically, 1.4 µm x 1.4 µm sized deposits of at least 100 nm thickness were analyzed with an acceleration voltage of 3.5 kV reducing substrate contributions to a minimum. Initially Au coated (250 nm) sapphire single crystal substrates were used. However, a combination of high sputter efficiency and low growth rate did cause the deposits to be (partially) embedded in the gold substrate layers, as depicted in Figure 43(a). These effects were already observed for the second lowest current of 9 pA. As alternative, Au was replaced by Cu as substrate material due to its significantly lower sputtering yield.[117] Nevertheless, EDX spectra of samples deposited on Au did only show minor contributions of substrate peaks, indicating deposits of approximately 100 nm thickness. In conjunction with AFM measurements showing significant etching (for example Figure 43(a)) this implies a (partial) embedding of the material in the gold substrate. This potentially is caused by a complex interplay of growth and sputtering rate of the deposit as well as the sputtering rate of the substrate material. For example, deposits in plane with the surface of the substrate, as shown in Figure 43(a), will be obtained if sputtering and growth rate are very similar. These embedding effects have also been reported for the deposition of NbC_x by Ga^+-FIBID.[130] Comparing samples deposited on Au and Cu using identical deposition parameters only minor differences in composition were observed (Figure 43(b)). For Cu however, no significant embedding of the deposit in the substrate material was evident (Figure 43(c)), thus both precursors were analyzed predominantly using Cu or SiO_2 as substrate material.

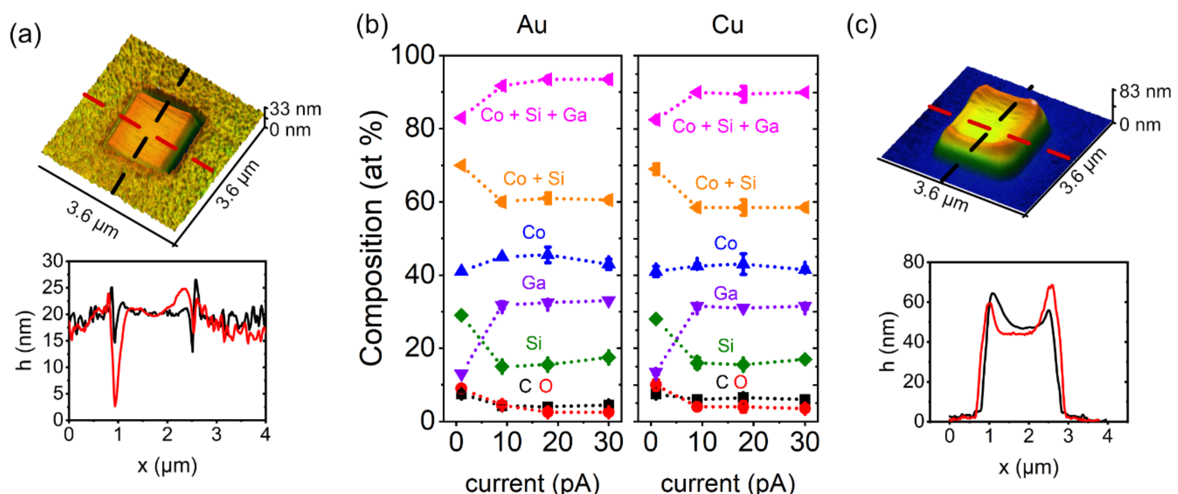

Figure 43: (a) AFM image and line scans of FIBID-CoSi having been deposited on a Au substrate showing the problematic embedding of the sample in the substrate material. Beam parameters: 30 kV, 9 pA, 0.2 µs dwell time, and 30 nm × 30 nm pitch. (b) Comparison of composition in dependence of beam current for Au and Cu as substrate material. (c) AFM image and corresponding line scans of a FIBID-CoSi deposit on Cu. Parameters and duration were the same as in (a).

Figure 44 compares the composition of FIBID materials to the FEBID deposits discussed above. In the case of FEBID a voltage of 5 kV was used, while for FIBID 30 kV acceleration voltage were employed. Similar deposition currents for FEBID and FIBID have not been used because of the very different growth rates associated with each process. FEBID would take very long for currents in the pA range and *vice versa* etching would be dominating in FIBID for currents in the range of nA. For CoSi the overall Co + Si concentration varies very little when comparing FIBID and FEBID. Contrary to FEBID, in the case of FIBID the initial Co:Si ratio is not retained causing an enrichment of Co up to a Co:Si ratio of approximately 2.6:1 for beam currents of 9 pA to 30 pA. The drastic reduction in Si can be very likely attributed to co-sputtering competing with the ion beam induced growth, causing preferential removal of lighter atoms as well as atoms with lower binding energies. Especially when comparing to exclusively electron stimulated or thermal reactions where most of the silicon was retained in the deposits, sputtering effects are very likely the cause. The drastic decrease of C and O could also be explained by co-sputtering, however additional effects such as a more efficient Co-CO bond scission when compared to FEBID have to be considered as well. Additionally, large amounts of Ga from the ion beam are incorporated in the deposits, thus the overall metal/metalloid content is very high with up to 90 at%. The average composition of material deposited at 9 pA to 30 pA can be described as $CoSi_{0.36}C_{0.15}O_{0.09}Ga_{0.72}$. The large amount of Ga together with the selective loss of Si make this precursor inferior for FIBID deposition.

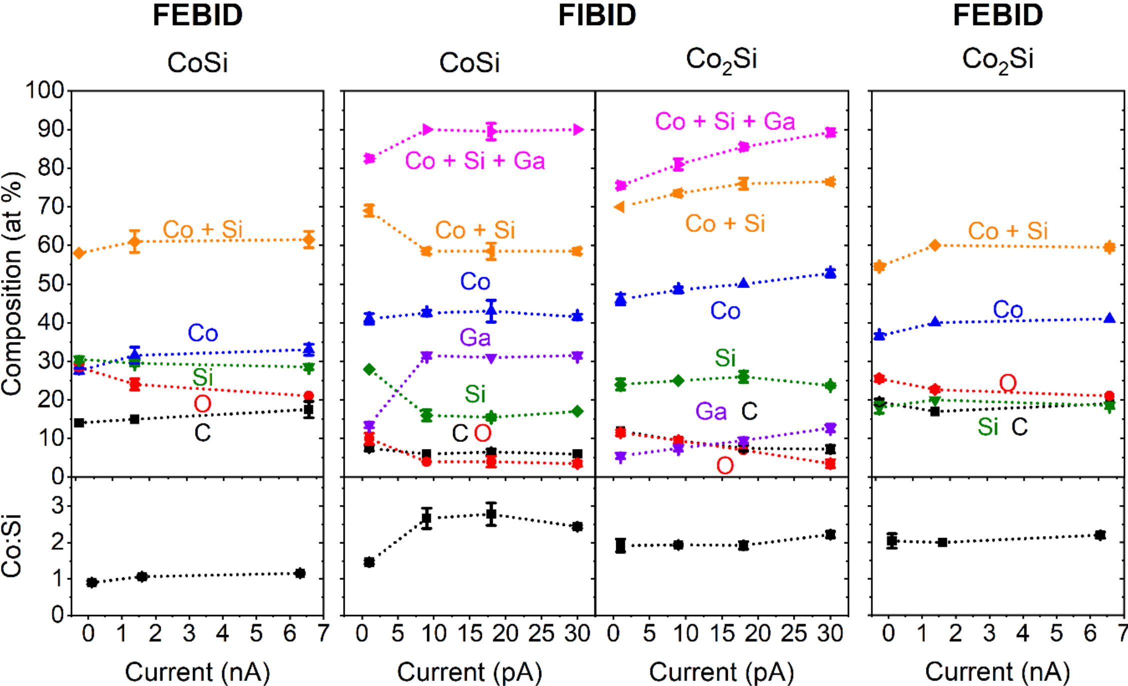

Figure 44: Comparison of composition for FEBID and FIBID deposits of CoSi and Co_2Si at varying currents using 5 kV and 30 kV as acceleration voltage respectively. Additionally, the Co:Si elemental ratio is plotted showing the retention of the initial ratio in all cases but FIBID-CoSi.

In contrast, material derived from $SiH_2(Co(CO)_4)_2$ retained the initial Co:Si ratio very well over the whole range of ion beam currents investigated (Figure 44). The deposits contained only 6 at% to 12 at% Ga with larger amounts of Ga being related to higher currents. Consequently, metal/metalloid contents of 75 at% to 90 at% with Co + Si contents of approximately 70 at% to 76 at% are achieved, corresponding to an increase of about 25 % relative to FEBID. The increased metal/metalloid content is mainly related to the significantly lower C and O incorporation related to the co-sputtering of lighter atoms and/or more efficient Co-CO bond cleavage during the deposition process. A variation of acceleration voltage between 15 kV to 30 kV did only cause slight variations in composition (Figure 45). For FIBID-Co_2Si a minor increase in overall metal content is observed for 30 kV, likely related to a slightly increased sputtering of C and O accompanied by more Ga being incorporated

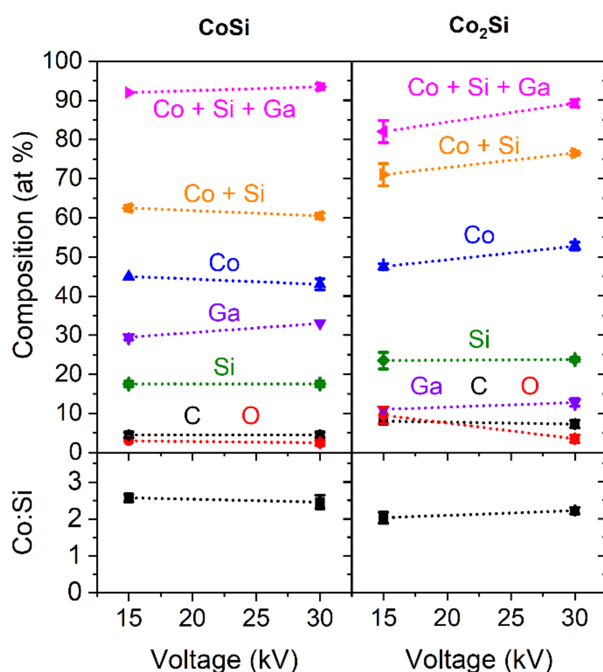

Figure 45: Comparison of composition for FIBID deposits of CoSi and Co_2Si at varying voltages with a current corresponding to 30 pA. The high current was chosen to facilitate focusing for 15 kV. Additionally, the Co:Si elemental ratio is plotted.

Raman spectroscopy was performed on FIBID samples of both precursors, providing additional information on the bonding situation (Figure 46). For FIBID-CoSi only two samples, deposited at 1 pA and 30 pA were investigated. Very low amounts of carbon related signals were observed for the sample deposited at 1 pA, consequently no peak deconvolution was attempted. The sample deposited at 30 pA shows no peaks in the region typically associated with carbon in agreement with the very low amount of C observed in the EDX analysis. The broad Raman signal observed for FIBID-Co_2Si samples was deconvoluted in 2 contributions using Gaussian fit functions. The major contribution at approximately

1470 cm^{-1} to 1490 cm^{-1} could be assigned to predominantly sp³ carbon, also known as tetrahedral amorphous ta-C.[316] However, Raman spectroscopy of carbon materials is highly complex and a definitive description of the bonding situation would require a systematic investigation. Nevertheless, similar carbon species have been reported for ion beam modified carbon films[321] or amorphous carbon formed by other techniques.[322]

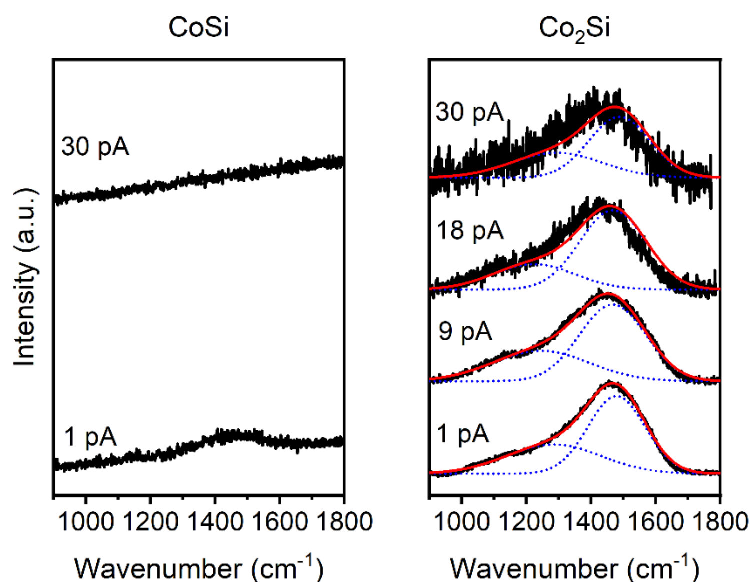

Figure 46: Raman spectra of the carbon region for FIBID-CoSi and FIBID-Co_2Si material deposited at 30 kV and varying currents. The Co_2Si have been normalized to the peak maximum (background subtracted). The red curve shows the fit to the data using two Gaussian curves (blue)

For both precursors, the volume-based growth rates were determined from AFM measurements of material deposited on SiO_2. Insets in Figure 47 show representative cross-sections of samples deposited at varying currents using an acceleration voltage of 30 kV. SiO_2 was chosen as substrate material due to its very low sputtering rate, thus having the least interference with the material deposition. However, very similar growth rates were measured for samples deposited on Cu substrates (Figure 48(a)). In the case of FIBID-CoSi, growth rates of 6.6×10^{-1} µm³/nC to 4×10^{-2} µm³/nC, decreasing with increasing current, were observed. With lower growth rates sputtering will be more pronounced and thus the significant co-sputtering of silicon could be explained. Additionally, the low growth rates, together with the high sputter yield of Au, explain the observed embedding of the material in the gold substrates. Co_2Si, on the other hand, has a very high deposition efficiency with values of 1.7 µm³/nC to 0.5 µm³/nC. These growth rates are approximately 2 orders of magnitude larger than those reported for electron beam deposition, similar effects have been reported for other precursors.[131] The higher growth rate of FIBID-Co_2Si when compared to FIBID-CoSi will also contribute to the significantly lower Ga incorporation as well as the retention of the predefined Co:Si ratio.

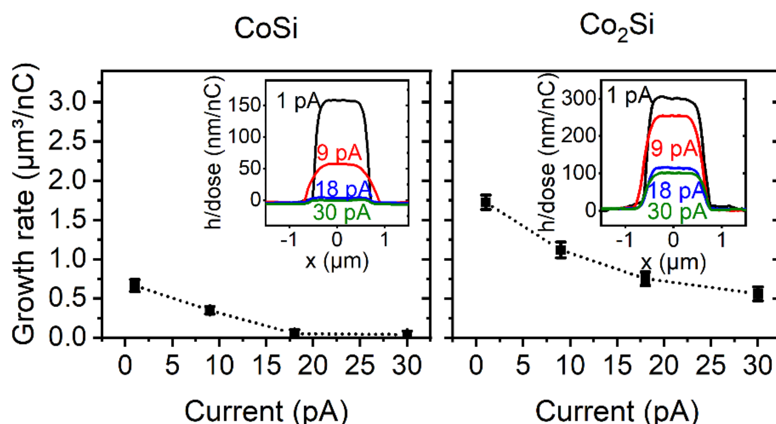

Figure 47: Volume based growth rates for FIBID deposits of CoSi and Co_2Si at varying currents and an acceleration voltage of 30 kV. Further deposition parameters include, 20 nm × 20 nm pitch, 1 µs dwell time, typical size 1.0 µm × 5.0 µm. SiO_2 (300 nm) on Si was used as substrate due to its low sputtering rate.

When comparing the growth rate of FIBID-Co_2Si samples with different lateral dimensions (1.0 µm × 5.0 µm and 1.4 µm × 1.4 µm) deposited on SiO_2 and Cu respectively, very similar growth rates were observed (Figure 48(a)). Deposits grow very fast in both cases, thus significant embedding of the samples in the substrate material should be negligible. The slightly higher deposition rate observed for the smaller samples could therefore be related to edge effects playing a more pronounced role. When edges are irradiated by electron or ion beams more secondary particles will be able to exit the substrate material and thus contribute to decomposition. In combination with additional scattering effects this causes a broadening of deposits beyond the actually defined pattern in FEBID.[185, 287] For ion beams similar effects will be observed as well. With the relative amount of side wall to volume being larger for smaller samples an increase in growth rate could be expected and could explain the trends shown in Figure 48(a).

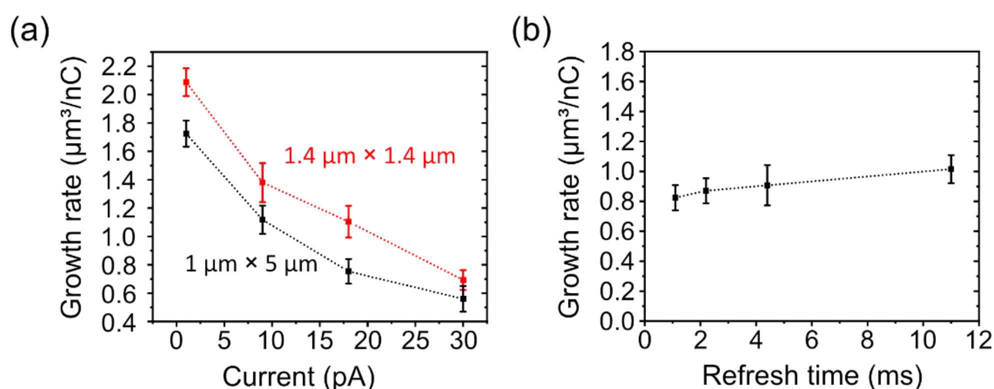

Figure 48 (a) Comparison of growth rate of samples deposited on Cu (1.4 µm × 1.4 µm) and SiO_2 (1.0 µm × 5.0 µm). (b) Effect of refresh time on growth rate for samples of 1.0 µm × 5.0 µm deposited on SiO_2 with a current of 18 pA and an acceleration voltage of 30 kV. Reprinted with permission from Ref. 323. Copyright 2022 American Chemical Society.

In addition, the effect of refresh time on growth rate has been studied for samples deposited with 30 kV/18 pA, and lateral dimensions of 1.0 µm × 5.0 µm. With increased refresh time more time for precursor replenishment is available and a significant increase in growth rate would be expected for pronounced precursor limited growth. The slight increase observed here, indicates that precursor replenishment is not the limiting factor of the deposition rate for this sample geometry and this set of deposition parameters. However, increasing the current or decreasing the refresh time could shift the growth regime towards a more precursor limited growth.

4.2.2.3.2 Electronic characterization

Room temperature resistivity measurements have been carried out directly in the SEM chamber after deposition of the material. I-V curves were recorded in two-probe configuration and the exact geometries were determined by AFM allowing for the calculation of resistivity values. The material was typically deposited across two gold electrodes located on a SiO_2 (300 nm) coated Si substrate. The typical device dimensions were 1.0 µm × 5.0 µm with heights of 50-200 nm and 100-250 nm for CoSi and Co_2Si respectively. Figure 49 shows the resulting resistivity values for both precursors. However, microstructural investigations presented below revealed a porous material for FIBID-Co_2Si and a similar microstructure could be expected for FIBID-CoSi. As a consequence the reported values will overestimate the volume of the deposits since the degree of porosity cannot be assessed easily. General trends are visible nevertheless and can be discussed.

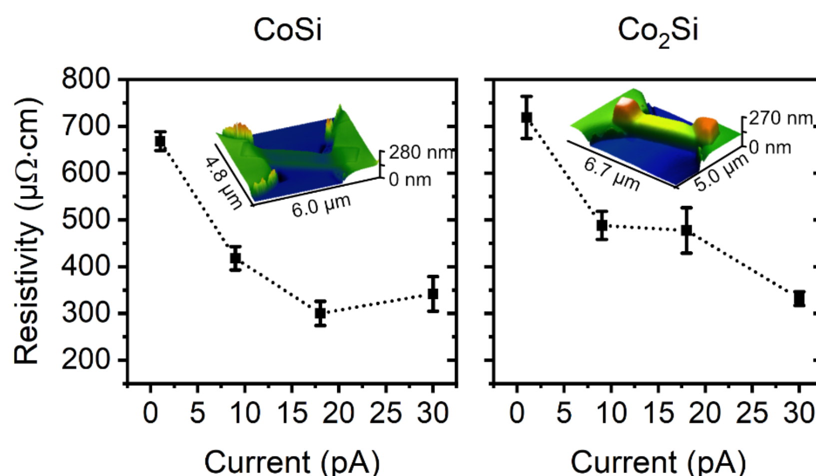

Figure 49: Room temperature two-probe resistivities in dependence of beam current for FIBID-CoSi and FIBID-Co_2Si. The acceleration voltage was set to 30 kV. The insets show AFM images of representative devices used. Both were deposited using 30 kV and 18 pA. The inset in the CoSi data shows the problematic incorporation of the deposit in the Au electrodes.

FIBID deposits of CoSi showed resistivities in the range of 670 µΩ·cm to 300 µΩ·cm, decreasing with increasing current. The resistivity value for the highest current is in good agreement with values reported for CoSi nanowires (287 µΩ·cm to 27 µΩ·cm).[324] The initial decrease is potentially related to the drastic increase in Ga incorporated in the deposit (approx. 30 at%). As a result percolation of Ga may become possible forming a conductive path and dominating the electronic behavior of the sample. Similar effects have been reported for $MeCpPtMe_3$ and $W(CO)_6$ based FIBID deposits, showing a decrease in resistivity by multiple orders of magnitude with increasing amount of Ga.[137] Alternatively, microstructural effects could play a role. Similar to the deposition on Au substrates, significant embedding of the deposit into the Au electrodes is observed (inset Figure 53). For FIBID-Co_2Si very similar room temperature resistivities are measured ranging from 720 µΩ·cm to 330 µΩ·cm. With increasing deposition current the resistivities decrease, however no significant changes in composition are observed according to EDX analysis. Thus the observed changes could be either related to a denser material or microstructural changes and larger grains, similar to effects often reported for FEBID deposits.[102] Overall, both materials show resistivity values two orders of magnitude lower than those reported for the respective FEBID deposits. Moreover, the resistivity values reported are merely 3 to 1.5 times that of Co_2Si single crystals (192 µΩ·cm) in good agreement with the high purity of the deposits.[325]

Temperature dependent electrical transport measurements have been investigated in a temperature range of 2 K to 300 K using devices in four-probe geometry prepared with 18 pA and 30 kV. Lead and contact-resistances have been found to be negligible (approx. 1-2 %) for FIBID-Co_2Si and FIBID-CoSi material at room temperature. When comparing the temperature dependent conductance normalized at 285 K (Figure 50) for FEBID and FIBID deposits, very different behaviors are observed. For both FEBID deposits the temperature dependent normalized conductance shows a behavior typically reported for granular metals (discussed in more detail above), while both FIBID deposits show only slight variations with temperature. For the FIBID-CoSi deposit an initial decrease in normalized conductivity until about 90 K (Figure 50(a), blue curve) is observed, slightly increasing again at lower temperatures. This behavior could indicate a material close to the transition between metallic and quasi-metallic behavior as the temperature coefficient of the conductance changes sign from negative to positive at the transition point.[326] However, the large amount of gallium, in conjunction with the selective loss of silicon complicates the discussion. The FIBID-Co_2Si sample, on the other hand, shows a slight increase with decreasing temperature (Figure 50(b), blue curve). A very similar behavior was reported for films of Co_2Si nanoparticles.[327] Various factors can play a role in this case. If the size of Co_2Si nanoparticles is in the range of the bulk mean-free path of electrons, scattering at cluster surfaces, as well as, contact points will have significant

contribution to the overall resistivity of the system.[327] Additionally, the interesting magnetic properties of Co_2Si have to be considered. Bulk Co_2Si is very close to the border between exchange-enhanced Pauli paramagnetism and very weak itinerant ferromagnetism.[327] Due to the material almost satisfying the Stoner criterion it is very close to ferromagnetism and existing magnetic moments can easily cause a spin polarization.[327] For Co_2Si nanoparticles this leads to strongly spin-polarized surface atoms, subsequently causing ferromagnetic behavior of the clusters already at room temperature. Bulk Co_2Si on the other hand becomes ferromagnetic only below 10 K.[327]

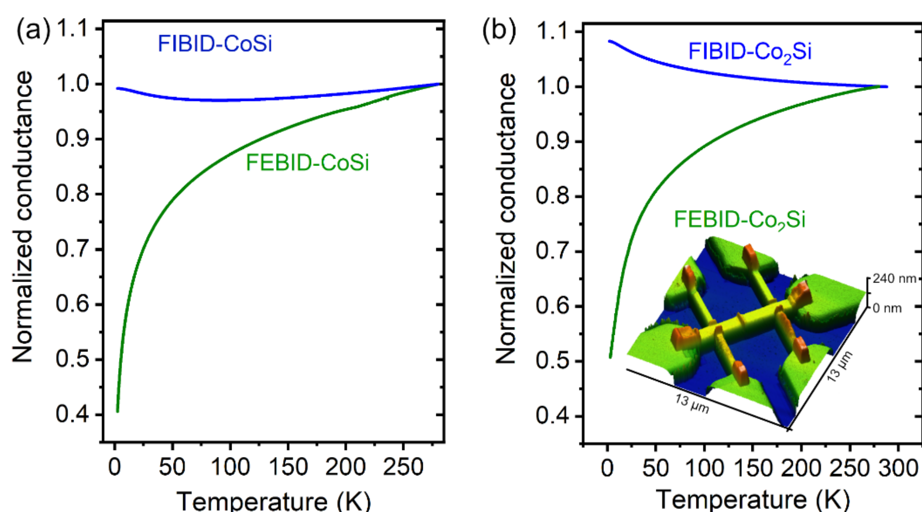

Figure 50: Temperature dependent conductance for (a) Co_2Si and (b) CoSi deposited by FEBID and FIBID normalized at 285 K. FEBID and FIBID deposits show very distinct behavior revealing significant differences of the material derived by both techniques. The inset shows a typical 6-probe device used for these measurements as well as magneto-resistance and Hall effect. (b) Reprinted with permission from Ref. 323. Copyright 2022 American Chemical Society

As discussed above FEBID materials deposited with both precursors show negative magnetoresistance with a saturation of -1.0 % for FEBID-CoSi and a saturation of -0.6 % for FEBID-Co_2Si at saturation fields of approximately 1.5 T. Contrary, both FIBID materials show positive MR (Figure 51), more pronounced for FIBID-Co_2Si. This is rather unusual since nanostructured CoSi and Co_2Si have both been reported to show ferromagnetic behavior and thus a negative MR would be expected.[283, 327]

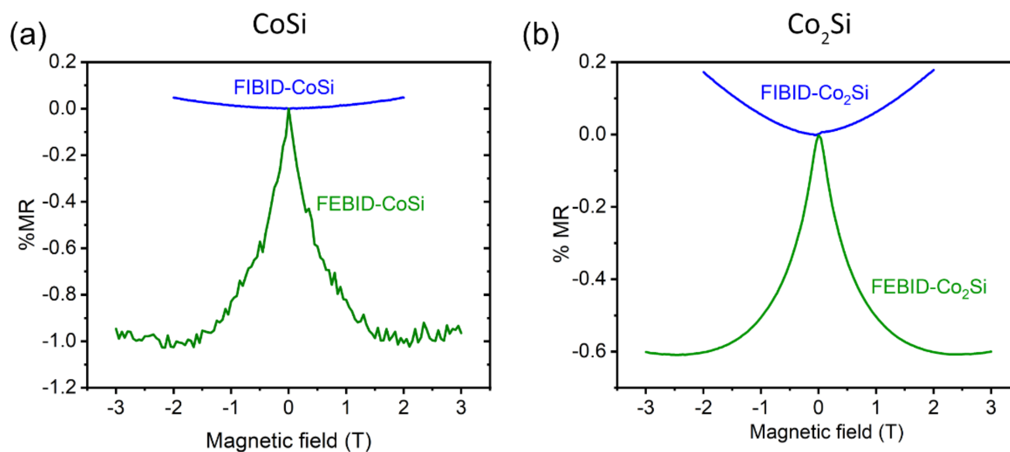

Figure 51: Magneto-resistance for samples deposited with FEBID and FIBID respectively. (a) using $H_3SiCo(CO)_4$ as and (b) using $H_2Si(Co(CO)_4)_2$ as precursor. (b) Reprinted with permission from Ref. 323. Copyright 2022 American Chemical Society.

Magneto-transport measurements at different temperatures of a FIBID-CoSi sample show a linear increase of Hall voltage with the magnetic field (Figure 52) and show no hysteresis, typical for diamagnetic materials. At low temperatures a slight asymmetry is observed, potentially related to the sample preparation. A possible error source could be asymmetries in the sample geometry due to drift during sample preparation causing thickness modulation or bad contact of the electrodes. The exact cause of this behavior, however, was not investigated. Additionally, the diamagnetic behavior is in contrast to single-crystalline CoSi nanowires for which a ferromagnetic behavior has been observed.[328] The differences potentially are related to different microstructures as well as the large amount of Ga incorporated in the samples ($CoSi_{0.36}C_{0.15}O_{0.09}Ga_{0.72}$).

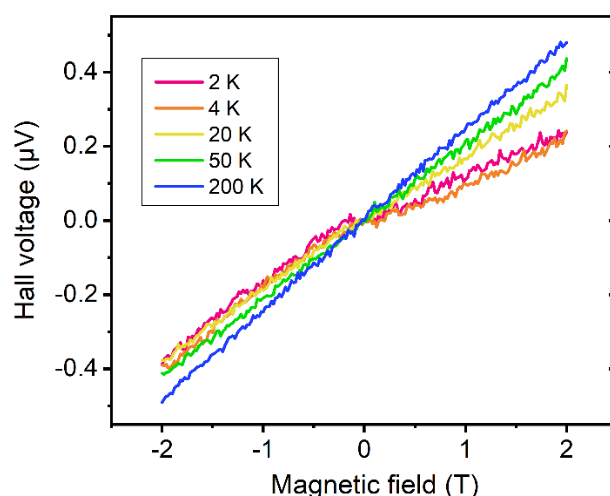

Figure 52: Magneto-transport measurements for FIBID-CoSi showing a linear increase in Hall voltage.

In order to investigate the differences in electronic conduction behavior for FEBID-Co_2Si and FIBID-Co_2Si further, magneto-transport measurements have been performed on material deposited at 5 kV/6.3 nA and 30 kV/18 pA respectively. A comparison of both materials is provided in the following. CoSi deposits have not been investigated in such detail because of the undesirable behavior of the precursor for FIBID deposits.

Magneto-transport measurements of FEBID-Co_2Si, illustrated by the Hall voltage $V_H(H)$ recorded at 2 K, reveal that the FEBID-Co_2Si material behaves superparamagnetic for fields between ± 2 T as (Figure 53(a)). This would indicate the presence of very small magnetic domains and is in agreement with the microstructural characterization discussed below, showing small (1-2 nm) separated clusters of Co rich material. Similar superparamagnetic behavior was recorded for $Co_2(CO)_8$ derived material deposited with FEBID.[329-330]

In contrast, ferromagnetic behavior is observed for FIBID-Co_2Si samples. A hysteresis with a coercive field H_c of 6 mT and a remanence M_r/M_s of 0.11 is recorded at 2 K (inset Figure 53(a)). The small remanence suggests a superposition of ferromagnetic and superparamagnetic contributions. Hysteretic behavior was observed up to a temperature of 150 K with similar coercivities and decreasing remanence. In contrast, ferromagnetic behavior up to room temperature was observed for sputtered Co_2Si nanoparticles.[327] Additionally, higher coercive fields of 230 mT at 3 K, decreasing with increasing temperature, were reported.[327] The variation between FIBID-Co_2Si and the sputtered sample could be caused by a secondary phase or compositional variations caused by Si oxidation.

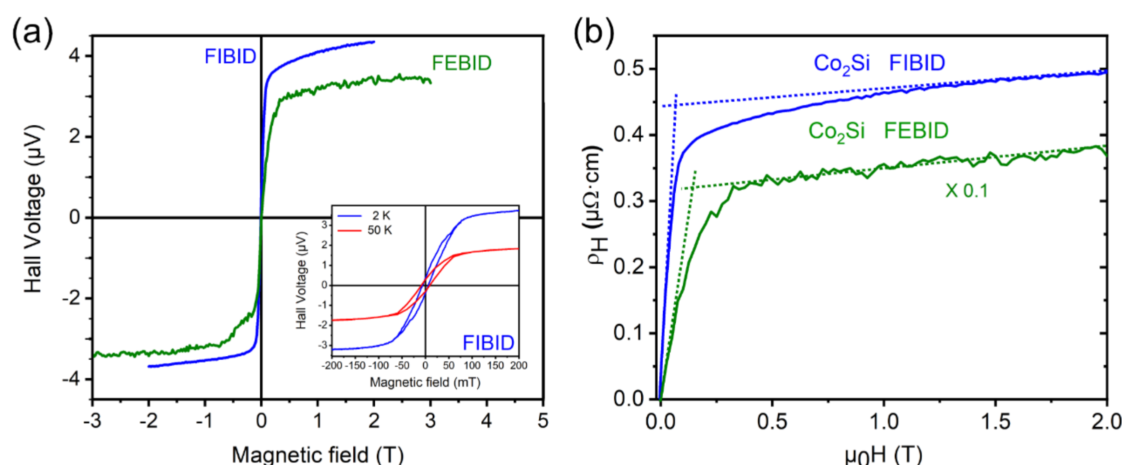

Figure 53: (a) Hall voltage measurements for FIBID-Co_2Si and FEBID-Co_2Si. The FEBID derived material shows superparamagnetic behavior. For FIBID-Co_2Si a hysteresis (shown in the inset) emerges, indicating ferromagnetic behavior. (b) Hall resistivities of the two Co_2Si materials used for the calculation of charge carrier density. Reprinted with permission from Ref. 323. Copyright 2022 American Chemical Society.

The Hall resistivity ρ_H calculated by Eq. (11) with V_H being the Hall voltage, I the applied current, and t the thickness of the sample, is plotted for the FEBID and FIBID Co_2Si samples in Figure 53(b).

$$\rho_h = V_H t / I \qquad \text{Eq. (11)}$$

The Hall resistivity is given by the sum of ordinary σ_{OR} and anomalous σ_{AN} Hall effect:

$$\rho_H = \rho_{OR} + \rho_{AN} = (R_0 \times \mu_0 \times M) + (R_S \times \mu_0 \times M) \qquad \text{Eq. (12)}$$

With R_0 and R_S being the ordinary and anomalous Hall coefficients and M the magnetization of the sample in field direction, assuming a demagnetizing factor N of approximately 1. The ordinary Hall coefficient R_0 corresponds to the slope of the Hall resistivity measurements at high fields. R_0 is related to the charge carrier density n and the elemental charge e by:

$$R_0 = \frac{1}{n \times e} \qquad \text{Eq. (13)}$$

The positive slope found in both measurements is associated with a hole dominated transport, which is in agreement with crystalline Co_2Si thin films.[331] Ordinary Hall coefficients of 0.118 μΩ cm/T and 0.027 μΩ cm/T are found for the FEBID and FIBID material respectively. Using these values, the charge carrier density can be calculated from Eq. (13). For FEBID-Co_2Si this equates to a charge carrier density of 5.3×10^{21} cm^{-3} while higher values of 2.3×10^{22} cm^{-3} are found in FIBID-Co_2Si. These values are larger than the charge carrier densities of about 2×10^{21} cm^{-3} reported for polycrystalline Co_2Si.[327, 331] Additionally, the saturation magnetization M_S can be determined by the intersection between the slopes at low and high fields and amounts to 145 mT for FEBID and 65 mT for FIBID. Both values are smaller than the approximately 350 mT reported for single-crystalline Co_2Si nanowires.[278]

4.2.2.4 Microstructural investigations of $H_2Si(Co(CO)_4)_2$ derived material for FEBID and FIBID

Microstructural investigations of both FEBID-Co_2Si and FIBID-Co_2Si deposits have been performed to better understand the drastic differences observed in electronic and magnetic transport measurements. $H_3SiCo(CO)_4$ derived deposits have not been investigated since their low growth rate limits their application, especially in FIBID as discussed above.

4.2.2.4.1 Microstructural investigations of FEBID-Co_2Si

TEM lamellas have been prepared for FEBID-Co_2Si material deposited at 5 kV and 6.3 nA. In the HAADF image in Figure 54(a), a dense material is revealed. Distinct features are not visible due to the high contrast associated with the Au metal substrate layer to the right. The brightfield (BF) image provides more information and reveals a dense material with small features of approximately 1 nm to 2 nm in size. In the corresponding EDX elemental maps, no macroscopic compositional fluctuation or aggregation is observed, which is in agreement with the EDX line scan (Figure 54(b)). This indicates a homogeneous growth process with no changes of composition or microstructure with deposition duration.

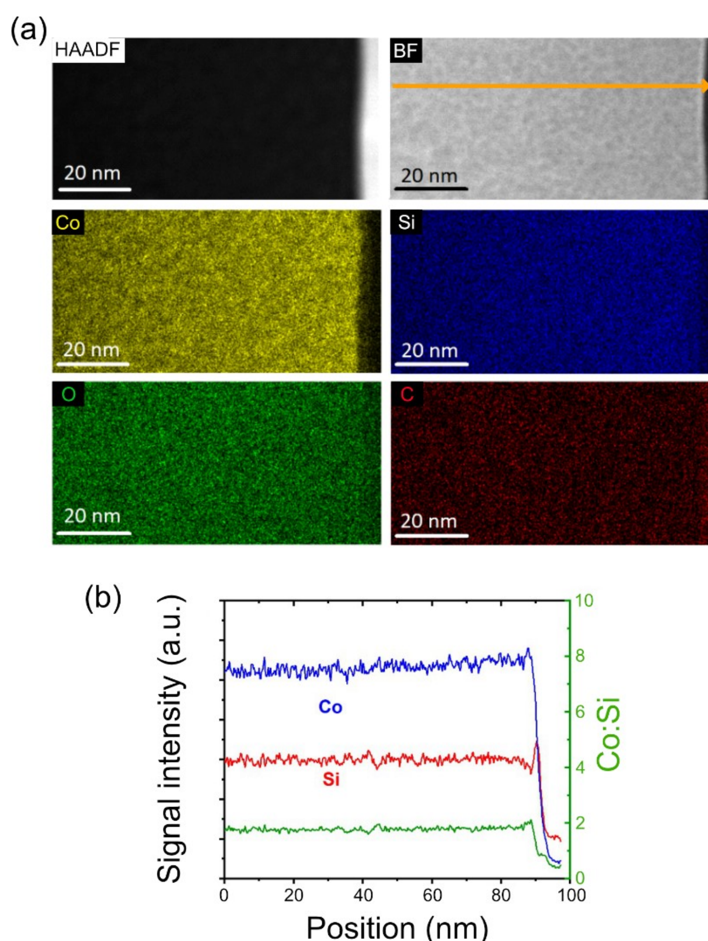

Figure 54: (a) HAADF image of a FEBID-Co_2Si deposit prepared at 5 kV, 6.3 nA on Au. The corresponding bright field (BF) image of the same sample reveals small particles evenly distributed in a matrix. Related STEM-EDX elemental maps for Co, Si, O, and C show a mostly homogeneous distribution of the elements within the sample. (b) Signal intensity of an EDX scan along the orange line shown in the BF image. Reprinted with permission from Ref. 323. Copyright 2022 American Chemical Society.

More details are observed in the high-resolution images shown in Figure 55. The high-resolution HAADF image shows Z-contrast variations which can be ascribed to clusters of 1 nm to 2 nm in size. The EDX elemental maps associated with the HAADF image reveal partial

phase-separation of Co-rich cluster. Lighter elements such as oxygen are enriched in the regions between these clusters. Silicon is mostly distributed homogeneously within the sample, even though a slight enrichment in oxygen-rich areas can be observed. This would be in agreement with the high oxygen affinity of silicon.

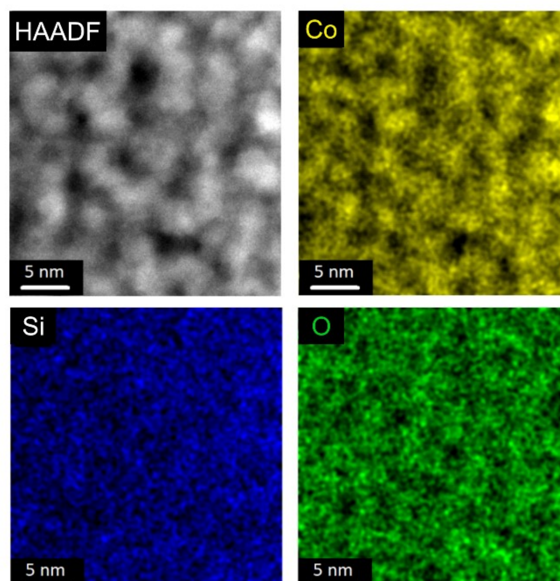

Figure 55: High-resolution HAADF image of a FEBID-Co_2Si deposit prepared at 5 kV and 6.3 nA showing brightness contrast and particle formation of approx. 1-2 nm in size. The corresponding STEM-EDX elemental maps for Co, Si and O show the formation of Co-rich clusters within an oxygen containing matrix. Si is mostly distributed homogeneously in the sample. Reprinted with permission from Ref. 323. Copyright 2022 American Chemical Society.

The phase contrast observed in the high resolution brightfield image (Figure 56(a)) also shows particles of approximately 1 nm to 2 nm in size. Due to the small sizes of the particles no crystalline phase could be determined from the FFT of the bright field image (Figure 56(b)) as well as nanobeam electron diffraction (Figure 56(c)).

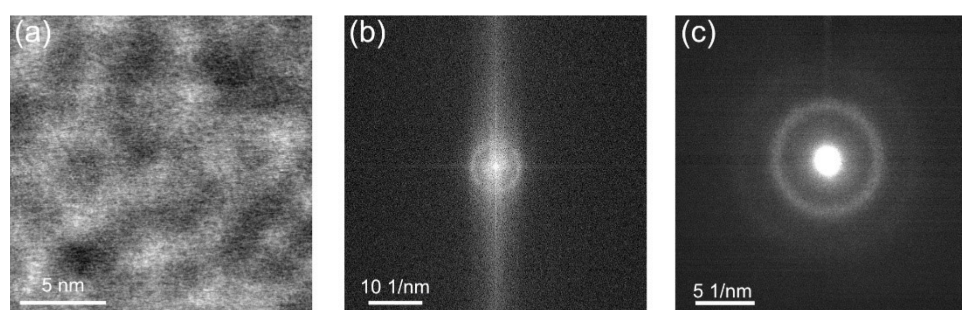

Figure 56: (a) High resolution bright field image showing clusters of 1-2 nm as revealed by phase contrast and (b) corresponding fast Fourier transform image. (c) Nanobeam diffraction image. No distinct phase could be identified. The sample was prepared at 5 kV and 6.3 nA. Reprinted with permission from Ref. 323. Copyright 2022 American Chemical Society.

4.2.2.4.2 Microstructure of FIBID-Co_2Si

Microstructural investigations were performed on a FIBID-Co_2Si sample deposited at 18 pA and 30 kV. The HAADF TEM cross-section image in Figure 57(a) reveals an, initially unexpected, highly porous structure with pore features approximately 10 nm in size. Interestingly, the pore formation was observed independent of substrate material (Cu, Au and SiO_2) and beam current. Additionally, granular PtC_x deposited by FEBID to protect the sample during the lamella preparation can be seen on the left as well as the polycrystalline Cu substrate to the right.

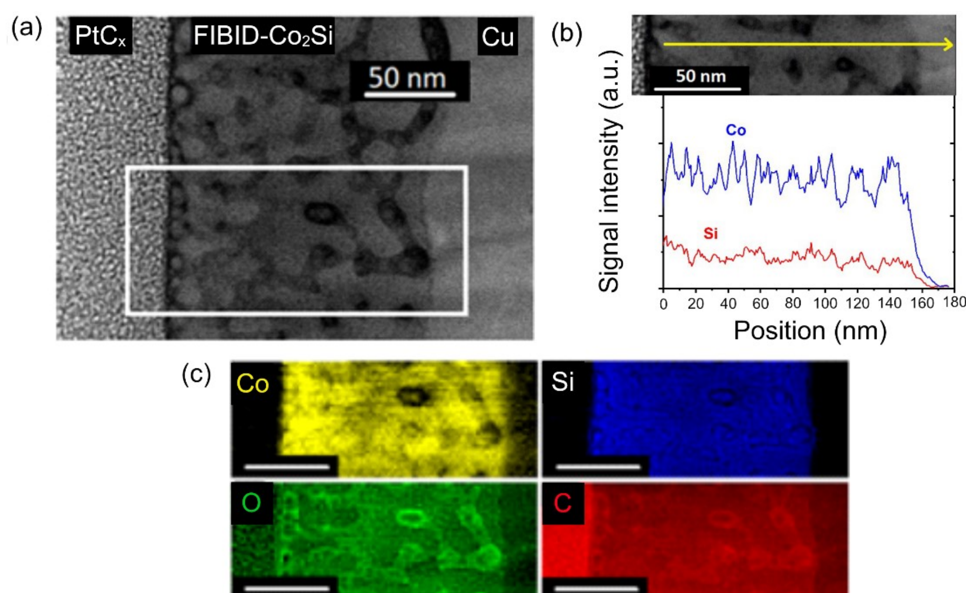

Figure 57: (a) HAADF image of a FIBID-Co_2Si deposit prepared at 30 kV and 18 pA on Cu (right) and FEBID-PtC_x cover layer (left) on top for protection during TEM lamella preparation. (b) EDX line scan along the line shown in the TEM inset. (c) STEM-EELS maps for Co_L, Si_L, O_K and C_K showing the elemental distribution in the region marked by a box in (a), all scall bars represent 50 nm. Reprinted with permission from Ref. 323. Copyright 2022 American Chemical Society.

The porous nature of the deposit and the associated variation in thickness makes EDX characterization very challenging, as demonstrated in the EDX line scan in Figure 57(b). Therefore, STEM-EELS maps for Co, Si, O, and C are provided in Figure 57(c) illustrating the spatial distribution. Cobalt and silicon are well spread within the sample showing no clustering. Areas corresponding to darker regions in the HAADF image contain less of both elements, indicated by lower signal intensities, as would be expected for pores. Oxygen and carbon elemental maps reveal a concentration of both elements at the pore edges with signal intensities inverse to the aforementioned Si and Co. In high-resolution imaging, the same features are reproduced and additional smaller features are revealed (Figure 58). The HAADF image shows darker spots of 1 nm to 2 nm in size distributed evenly between the larger pores. It can, however, not be distinguished between inclusions of lighter elements or a decrease of material thickness due to the formation of smaller bubbles. The HAADF image is reproduced

in the high-resolution EDX map of Co (Figure 58 b) Similar to the low-resolution EELS maps an enrichment of oxygen in the pore areas is visible (Figure 58(d)). Additionally, slightly more signal intensity of Si is observed in the pore regions (Figure 58(c)). This could be expected due to the high oxophilicity of silicon causing a preferential oxidation of Si rather than Co. A clear phase-separation however is not visible. The carbon mapping (Figure 58(e)) does not provide additional information. Ga is distributed evenly (Figure 58(f)), reproducing the overall microstructure, and no accumulation or cluster formation is observed.

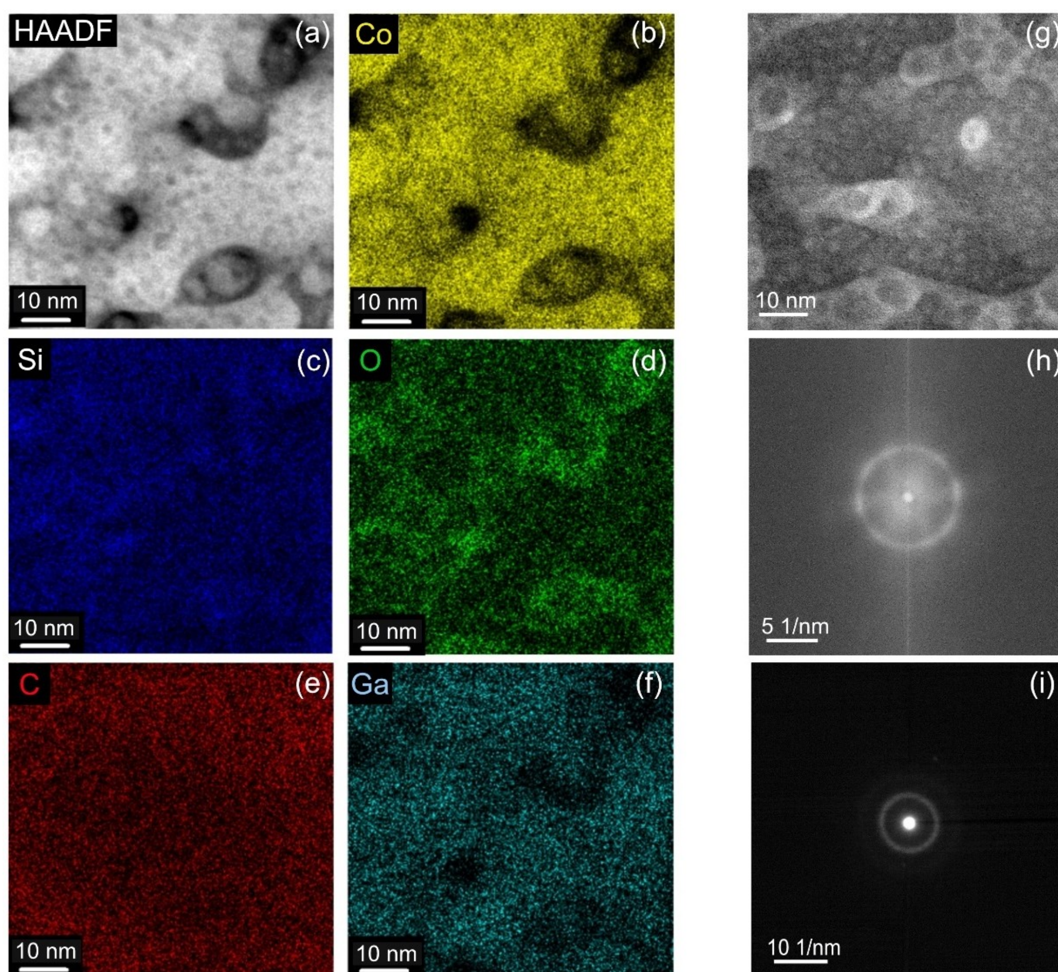

Figure 58: (a) High-resolution HAADF image of a FIBID-Co_2Si sample deposited at 30 kV, 18 pA. (b)-(f) Corresponding STEM-EDX mappings for the elements Co_L, Si_L, O_K, C_K and Ga_K. (g) High-resolution bright field image of a FIBID-Co_2Si sample. Based on the corresponding FFT (h) or the nanobeam diffraction image (i) no distinct crystal phase can be identified. The sample was prepared at 30 kV and 18 pA. Adapted with permission from Ref. 323. Copyright 2022 American Chemical Society.

The high resolution brightfield image (Figure 58(g)) does not provide any additional information. Moreover, no distinct crystal phase can be assigned based on FFT of the BF image (Figure 58(h)) or nanobeam diffraction (Figure 58(i)).

As already mentioned above, pore formation is not limited to a specific set of deposition parameters. Figure 59 shows cross sections of samples deposited at 30 kV and varying ion beam currents. The substrate in this case is SiO_2 typically used for the electronic characteriaztion of the deposits. In Figure 59(a), a complete cross section of material deposited at 30 kV and 1 pA is shown. A clear trend of reduced porosity is observed when the current is increased from 1 pA to 30 pA (Figure 59(b)-(d)). Keeping this in mind, the resistivity values discussed in the upcomming section have to be considered as lower limits, since free volume is not taken into account in AFM measurements and will not contribute to the conductivity of the samples.

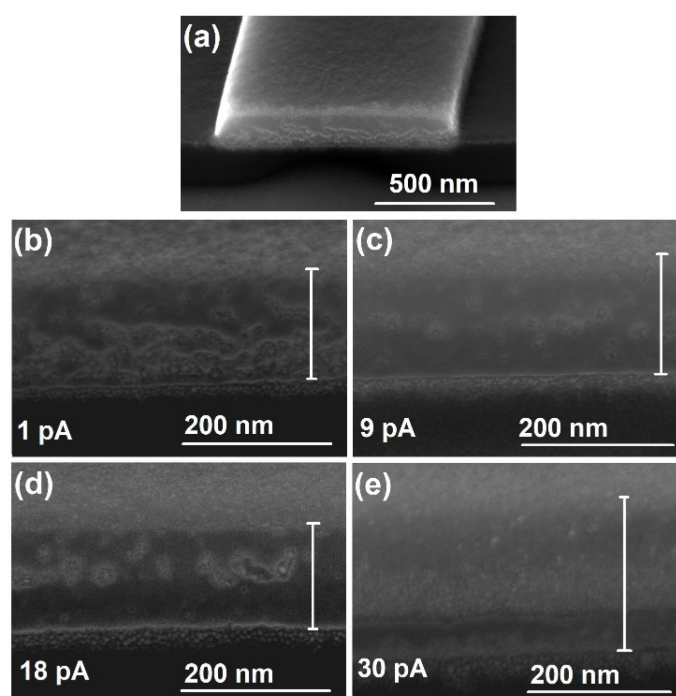

Figure 59: (a) SEM cross section of a FIBID-Co_2Si deposit showing significant porosity. (b)-(e) shows cross section images in higher resolution demonstrating the effect of beam current on porosity. A tendency of decreasing porosity with increasing beam current is observed. All samples were deposited with 30 kV acceleration voltage. The vertical bars demonstrate the thickness of the deposits. Reprinted with permission from Ref. 323. Copyright 2022 American Chemical Society

4.2.2.5 Proposed decomposition paths FEBID vs FIBID for $H_2Si(Co(CO)_4)_2$

Based on the TEM/STEM and cross section SEM images a more detailed discussion of the underlying mechanism responsible for the pore formation is possible. The microstructural details allow to propose a decomposition path deviating between FEBID and FIBID (Figure 60). Initially adsorbed precursor molecules are decomposed by a combination of reactions involving secondary electrons (FEBID and FIBID) as well as ion impact (FIBID). As a consequence, most CO and H ligands are liberated and a surface bound intermediate ($Co_2SiC_xO_y(CO)_z$), containing decomposed as well as intact CO ligands, is formed. The exact stoichiometry of this intermediate will differ, depending on the decomposition method and deposition parameters. In the case of FIBID consecutive deposition leads to an ongoing ion impact and implantation process. As a consequence, additional energy is deposited into the sample by impinging ions. The penetration depth of Ga^+ ions at 30 kV is very shallow, approximately 50 nm (Figure 8), when compared to electrons and thus much more energy is deposited in a very small volume. This provides enough energy for the liberation of intact CO ligands as well as the rearrangement of the local microstructure. The energy transfer can be either considered as momentum transfer, or, more simply, as very localized thermal effects. The combination of intra-deposit release of gaseous CO, together with the momentum transfer of the Ga-ions providing energy for solid diffusion, could be responsible for the formation of pores or voids inside the material. The gaseous carbon monoxide will stay trapped in the material's pores and subsequent interactions with SE will cause its decomposition. The resulting carbon will be deposited at the pore walls and the atomic oxygen will readily oxidize the Co_2Si material, thus also accumulating at the pore walls.[48] With increasing deposition current the initially formed surface bound intermediate will contain less intact CO ligands. Therefore, less CO can be liberated by subsequent irradiation and samples deposited at higher currents will show less pronounced pore formation, explaining the trend observed in Figure 59(b)-(e). Additionally, the relatively smooth surfaces of the FIBID deposits (for example Figure 59(a)) can be explained by this mechanism. When growing deposits, new material is continuously added on top of the sample while previously deposited layers experience curing due to the penetration depth of the ion beam. As a consequence microstructural changes are only observed in layers closer to the substrate surface while the top layers remain relatively unaltered and pristine.

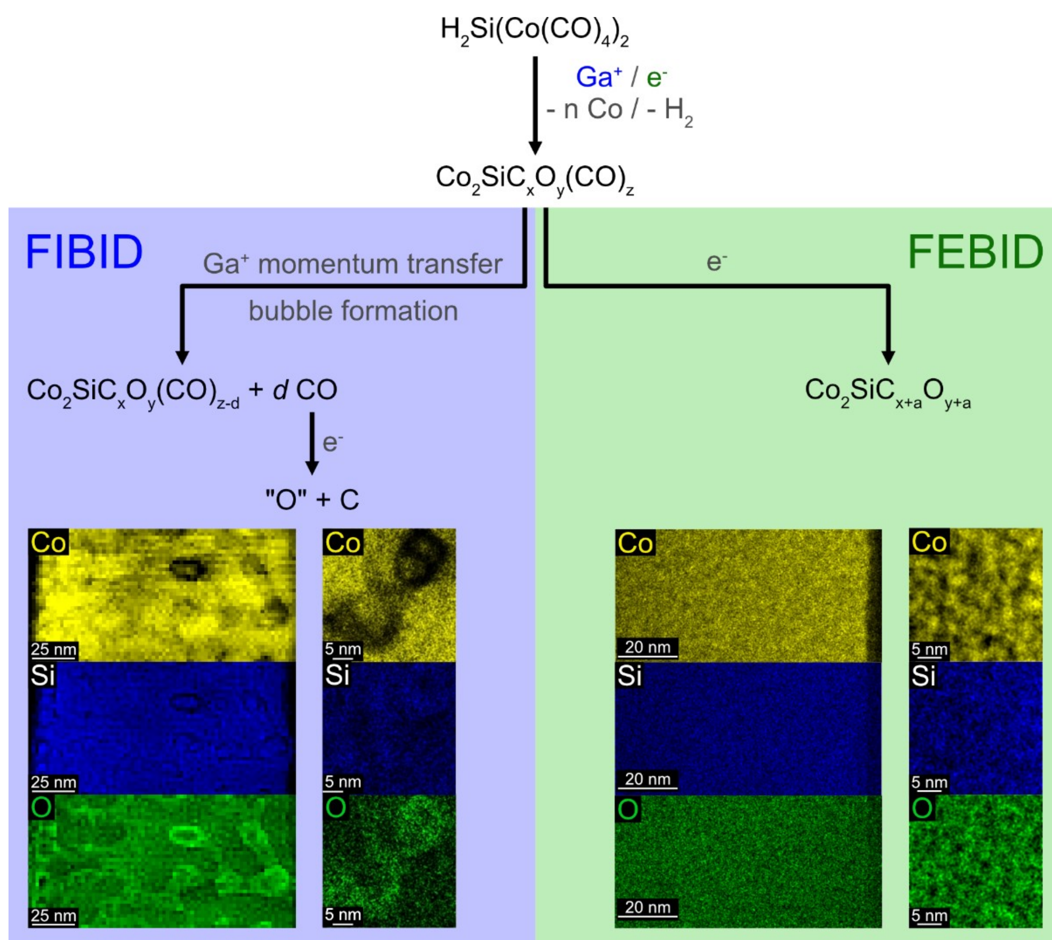

Figure 60: Proposed reaction sequence responsible for bubble formation in the FIBID material by liberation of CO from initially partially fragmented intermediate.

In contrast, the dense FEBID deposit, discussed above, will also contain intact carbonyl ligands ($Co_2SiC_xO_y(CO)_z$). However, the CO will not be liberated intact but will be fragmented directly by continuous electron irradiation. Additionally, the energy of the impinging electrons is distributed in a much larger volume (typical penetration depth of 400 nm at 5 kV acceleration voltage, Figure 8). Therefore, electron-induced CO cleavage will also occur but the resulting species will have much smaller diffusion lengths and the material will be affected much more localized.

5 Summary and Conclusion

In the first part of this work FEBID and CVD experiments with the transition metal carbonyls $V(CO)_6$ and $Mn_2(CO)_{10}$ are presented. These two precursors complement the existing data on transition metal carbonyls used as FEBID precursors. In general, the compositions derived by FEBID and CVD are similar for both $V(CO)_6$ and $Mn_2(CO)_{10}$. CVD deposits derived from $V(CO)_6$ indicate the formation of a vanadium (oxy)carbide material with a V:C ratio of approximately 1.1 to 1.3. Slightly lower V:C ratios, 0.6 to 0.9, have been observed in FEBID indicating a more pronounced ligand incorporation in the deposit. Microstructural characterizations of a FEBID deposit revealed small, crystalline grains dispersed in an amorphous matrix. The crystalline phase was identified as cubic $VC_{1-x}O_x$ in agreement with the crystalline phase observed for CVD thin films. Additionally, the TEM investigations showed surface oxidation of the deposits. These surface oxides are most likely formed post growth as consequence of electron stimulated reactions with residual water during EDX measurements or imaging. Resistivities of 0.8×10^3 µΩ·cm to 1.2×10^3 µΩ·cm have been found for FEBID deposits, decreasing with increasing deposition current. In agreement with TEM investigations, temperature dependent electrical transport measurements showed a behavior typically observed for granular metals on the metallic side of the metal-insulator transition.

Both CVD and FEBID experiments using $Mn_2(CO)_{10}$ did result in similar Mn contents of approximately 40 at%. FEBID deposits of $Mn_2(CO)_{10}$ did show insulating behavior with room temperature resistivities in the range of 5×10^{10} µΩ·cm to 1.5×10^9 µΩ·cm. A reduction of resistivity by approximately one order of magnitude could be achieved by post-growth electron beam irradiation. Temperature dependent conductivity measurements revealed insulating behavior for as grown, as well as, cured samples, with a peculiar phase transition being observed at about 15 K for both materials.

The second part of this work covers the application of three new single-source precursors for the deposition of material with defined stoichiometry using focused beam induced deposition and CVD. The precursors investigated were: $H_3SiMn(CO)_5$, $H_3SiCo(CO)_4$, and $H_2Si(Co(CO)_4)_2$. The compositions as well as the metal silicon ratios obtained for each deposition method are presented in Table 2.

Table 2: Comparison of metal/metalloid contents and average M:Si ratio obtained for all hetero-bimetallic precursors used in this study. M designates Mn or Co respectively. Results for FIBID do include Ga. All values for FEBID and FIBID deposits are for material deposited at 5 kV and 30 kV respectively. Values for CVD of $H_3SiMn(CO)_5$ have been corrected for post growth oxidation assuming a C:O ratio of 1:1.

Precursor	**CVD**		**FEBID**		**FIBID**	
	M + Si (at%)	**M:Si (-)**	**M + Si (at%)**	**M:Si (-)**	**M + Ga +Si (at%)**	**M:Si (-)**
$H_3SiMn(CO)_5$	74-84	1.6:1	45-50	2.4:1-2.5:1	-	-
			40-55[197]	2:1-4:1[197]		
$H_3SiCo(CO)_4$	80	1.2:1-1.3:1	58-62	0.9:1–1.2:1	83-90	1.5:1-2.8:1
$H_2Si(Co(CO)_4)_2$	72-82	2.2:1	55-60	2.0:1–2.2:1	76-89	1.9:1-2.2:1

Thin films deposited in CVD experiments did show similar metal/metalloid contents of approximately 80 at% for all three precursors. For CVD-Co_2Si deposits the values have been corrected for post growth oxidation assuming a C:O ratio of 1:1 discussed in more detail in chapter 4.2.1.1. Additionally, selective silicon loss was observed in all cases, most pronounced for samples deposited with $H_3SiMn(CO)_5$, with about every third silicon being removed during deposition. Contrary, the loss of only 10 % to 20 % of silicon was observed for thin films deposited with both Co-Si precursors. However, the exact reason for the silicon loss has not been investigated and could be related to thermally induced secondary reactions or side reactions with residual water. Nevertheless, the diffractogram showed the formation of the expected silicide phases in all three cases.

In FEBID lower metal/metalloid contents are observed for all precursors when compared to CVD. For deposits derived from $H_3SiMn(CO)_5$ metal contents of 45 at% to 50 at% were obtained, in good agreement with literature.[197] Additionally, pronounced silicon loss resulting in Mn:Si ratios of approximately 2.5:1 was observed indicating a highly efficient, formation of volatile silicon containing fragments. In an attempt to potentially retain these fragments or to suppress the reaction causing their formation FEBID experiments at substrate temperatures down to 250 K were performed, however no changes in Mn:Si ratio were observed.

Contrary, both $H_3SiCo(CO)_4$ and $H_2Si(Co(CO)_4)_2$ can be considered suitable single-source precursors for FEBID. In both cases metal/metalloid contents of 55 at% to 62 at% are observed with very good retention of the predefined Co:Si ratio. Variations in deposition parameters only

had minor impact on the overall composition. Noteworthy is also the high growth rate of the Co_2Si precursor when compared to FEBID-CoSi as well as FEBID-MnSi. Similar resistivity values, in the range of 4.8×10^4 µΩ·cm to 0.5×10^4 µΩ·cm, have been observed for FEBID-CoSi and FEBID-Co_2Si materials, in both cases decreasing with increasing deposition current. Post growth electron treatment not only resulted in a decrease in resistivity but also caused a change in magnetoresistance. Temperature dependent resistivity measurements showed behavior typically expected for granular metals for both, as-deposited and cured, FEBID-CoSi and FEBID-Co_2Si samples. Only as-grown FEBID-CoSi was found to be on the insulating side of the metal-insulator transition, while all other samples showed quasi-metallic behavior.

$H_3SiCo(CO)_4$ proved to be not well suited for FIBID experiments, contrary to what was observed for FEBID. The slow growth rate already observed during FEBID deposition caused a significant co-sputtering of silicon as well as the incorporation of large amounts of Ga in the deposits. The overall composition of the material can be described as $CoSi_{0.36}C_{0.15}O_{0.09}Ga_{0.72}$ corresponding to a metal/metalloid content of 90 at%. On the contrary, FIBID-Co_2Si deposits did show a very good retention of the predefined Co:Si ratio, low Ga incorporation, and total metal/metalloid contents of up to 90 at%. Drastically lower room temperature resistivities of 720 µΩ·cm to 300 µΩ·cm were observed for FIBID-CoSi and FIBID-Co_2Si when compared to their respective FEBID deposits. Additionally, the temperature dependent conductivity behavior was significantly different, showing an increase with decreasing temperature for both FIBID samples. Magneto-transport investigations showed ferromagnetic behavior for FIBID-Co_2Si while diamagnetic behavior was observed for FIBID-CoSi.

Microstructural investigations were carried out in order to better understand the differences in physical properties of $H_2Si(Co(CO)_4)_2$ derived FEBID and FIBID deposits. TEM studies of the FEBID-Co_2Si sample revealed a nanogranular material with cobalt rich grains. The small size of the grains however did not allow for a phase identification. In contradiction porous deposits were observed for FIBID. Based on the microstructural differences observed for the two charged particle beam induced deposition methods altered fragmentation channels are proposed, which would have to be validated by further experiments.

6 General Materials and Methods

6.1 Precursor synthesis

General

Sodium, mercury, $Mn_2(CO)_{10}$, $Co_2(CO)_8$, VCl_3, $(N(C_2H_5)_4)Br$, $H_3Si(C_6H_5)$, iodine, $LiAlH_4$, H_2SiI_2 methylnaphthalene, phosphoric acid, phosphorous pentoxide, acetone, tetrahydrofuane (THF), pentane, dimethylether and diethylether were purchased from Sigma-Aldrich. 1,2,3,4-tetrahydronaphthalene was purchased from ABCR. Diethylether, pentane, THF and 1,2,3,4-tetrahydronaphthalene were dried over sodium and degassed by three freeze-pump-thaw cycles. Condensed dimethylether was dried over $LiAlH_4$ before use. All reactions and handling of the precursors require inert gas/Schlenk techniques to prevent oxidation or hydrolysis.

$V(CO)_6$

Vanadium carbonyl was prepared similar to a reported procedure.[285] Initially, $(N(C_2H_5)_4)(V(CO)_6)$ is formed which then is converted to $V(CO)_6$. In a first step, a solution of $VCl_3(THF)_3$ was formed by refluxing 10.0 g VCl_3 (64 mmol) in 380 mL THF for 8 h at 339 K under argon. Simultaneously, a solution of lithium methylnapththalenide in THF was prepared by slowly adding 54.6 g (384 mmol) methylnaphthalene to a suspension of 1.8 g Li (256 mmol) in 180 mL THF over the course of 30 min and stirring at room temperature for 8 h. The $VCl_3(THF)_3$ solution was cooled to room temperature and added to the child solution of lithium methylnaphthalenide (approximately 213 K) over the course of 30 min, always maintaining the temperature below 223 K. The obtained dark brown solution subsequently was stirred for 12 h and allowed to slowly warm to about 263 K. Afterwards, the argon atmosphere was exchanged to pure CO (*Caution: CO is a highly poisonous gas and should be handled with care!*) and vigorously stirred for 24 h at room temperature while replacing the consumed CO. The CO atmosphere was exchanged with argon. Subsequently the black solution was filtered and the grey residue was washed with 20 mL THF. The volume of the filtrate was reduced to about 50 mL and 500 mL pentane were added to precipitate the crude lithium salt. The dark brown tar was washed several times with copious amounts of pentane to remove methylnaphthalene. The residue was dried in vacuo, redissolved in 300 mL acetone and added to a solution of 16.1 g $(N(C_2H_5)_4)Br$ (77 mmol) in 200 mL ethanol from which the crude $(N(C_2H_5)_4)(V(CO)_6)$ was precipitated by reducing the volume to approximately 50 mL and adding 600 mL of water. The crude product was isolated by filtration as brown solid. After redissolving in 300 mL THF the pure product was isolated as yellow solid by reducing the volume to about 30 mL and adding 20 mL of diethylether. After drying in dynamic vacuum typically 10.0 g (29 mmol, 45 %) yellow solid were obtained.

$V(CO)_6$ was formed in a second step. Typically, 5.0 g of $(N(C_2H_5)_4)(V(CO)_6)$ (14 mmol) were added to 40 mL phosphoric acid (dried by the addition of about 5.0 g of phosphorous pentoxide) leading to the formation of vanadium carbonyl hydride which readily decomposes to $V(CO)_6$ and H_2. The crude product was collected by sublimation in a specially designed Schlenk tube with the stopcock attached at about ¼ of the height. To ensure a complete removal of water phosphorous pentoxide was added to the crude product. The final product was obtained by resublimation, keeping the crude product at 298 K and the collecting trap at 77 K (at approx. 1×10^{-3} mbar using a modified Stock apparatus). $V(CO)_6$ was obtained as dark blue crystals in a yield of 2.7 g (12 mmol, 86 %).

Vanadium carbonyl is sensitive to photodegradation and oxidation but can be stored for several weeks at subdued light and 253 K under argon or in evacuated stainless-steel containers.

H_3SiI

For the preparation of iodosilane, initially anhydrous HI was prepared from 60.0 g of iodine with 250 mL of 1,2,3,4-tetrahydronapthalene at approximately 480 K. The HI was collected at 180 K using an ethanol cooling bath and recondensed on 20 mL $H_3Si(C_6H_5)$. The reaction mixture was vigorously stirred for 16 h at 231 K to 235 K. Excess HI was removed by slowly warming the reaction mixture to room temperature disposing of it by bubbling through an aqueous KOH solution. Subsequently the product was purified by triple distillation at atmospheric pressures under inert gas using a Vigreux column at 45 °C. Pure H_3SiI was obtained as colorless liquid with a yield of 13.0 g (82 mmol, 51 %).

NMR was used for characterization: ^{1}H-NMR (300 MHz, C_6D_6, 298 K, TMS): 3.04 ppm (s; 3H; $^1J(^1H, ^{29}Si)$ = 241 Hz; **H_3**SiI); ^{29}Si-NMR (79 MHz, C_6D_6, 298 K, TMS): -83.69 ppm (q; 1Si; $^1J(^1H, ^{29}Si)$ = 241 Hz; H_3**Si**I).

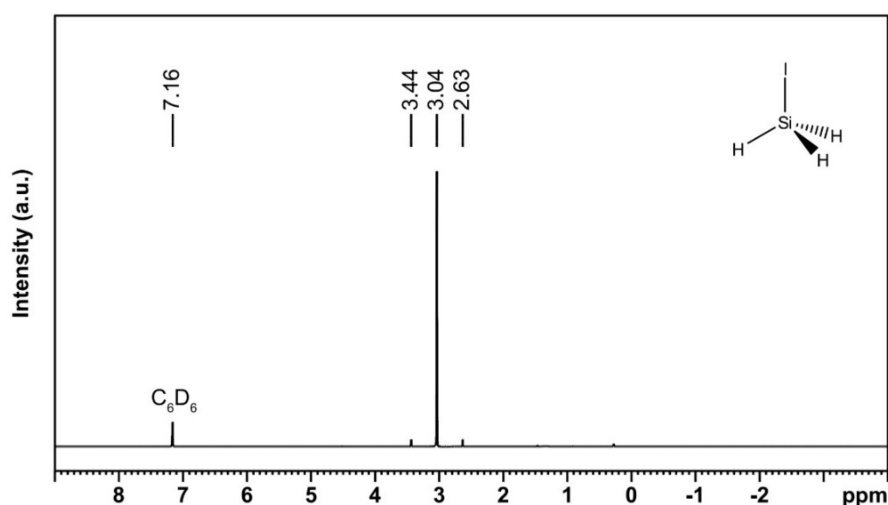

Figure 61: ^{1}H-NMR spectrum of H_3SiI (C_6D_6, 300 MHz).

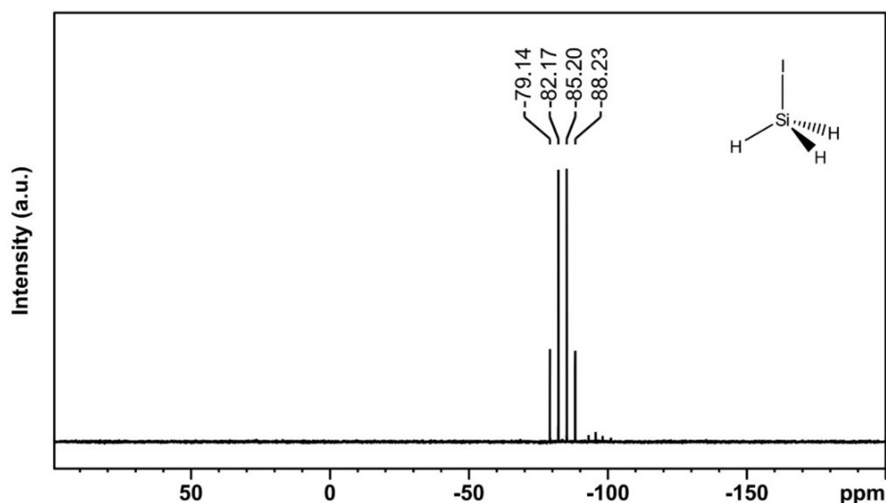

Figure 62: ^{29}Si-NMR spectrum of H_3SiI (C_6D_6, 79 MHz).

$NaMn(CO)_5$

Typically, 4.0 g $Mn_2(CO)_{10}$ (10 mmol) were reduced by 5 % sodium (22 mmol) amalgam in diethylether at room temperature under vigorous stirring. After 2 h the green $NaMn(CO)_5$ ether complex was extracted with 500 mL of diethylether and dried under dynamic vacuum. $NaMn(CO)_5$ was obtained as greenish, fine powder in a yield of 2.7 g (12 mmol, 60 %) and used without further purification.

$NaCo(CO)_4$

Typically, 4.3 g $Co_2(CO)_8$ (13 mmol) was reduced by 5 % sodium (30 mmol) amalgam in diethylether at room temperature under vigorous stirring. $NaCo(CO)_4$ was extracted as red solution after 2 h with 500 mL of diethylether and dried under dynamic vacuum. $NaCo(CO)_4$ was obtained as reddish, fine powder with a yield of 3.1 g (16 mmol, 63 %).

$H_3SiMn(CO)_5$

$H_3SiMn(CO)_5$ was prepared by salt elimination from H_3SiI and $Na(Co(CO)_4)$ similar to a published procedure.[307] 2.7 g of $NaMn(CO)_5$ (12 mmol) were dispersed in approx. 15 mL dimethylether at 193 K using an ethanol cooling bath. Subsequently, 1.8 g H_3SiI (11 mmol) were added and the mixture was warmed to about 243 K and stirred for 3 h. The solvent was then removed under reduced pressure at temperatures in the range of 200-233 K. Afterwards, the crude product was collected by sublimation keeping the reaction vessel at 253-273 K and the cold trap at 77 K. In order to ensure a complete removal of solvent the sublimation was repeated two times. $H_3SiMn(CO)_5$ was obtained as colorless solid melting at 298 K with a yield of 1.2 g (5 mmol, 46 %).

NMR was used for characterization: ^{1}H-NMR (500 MHz, C_6D_6, 298 K, TMS): 3.64 ppm (t; 3H; $^{1}J(^{1}H, ^{29}Si)$ = 195 Hz; **H_3**SiMn(CO)$_5$); ^{29}Si-NMR (99 MHz, C_6D_6, 298 K, TMS): -57.24 ppm (q; 1Si; $^{1}J(^{1}H, ^{29}Si)$ = 195 Hz; H_3**Si**Mn(CO)$_5$).

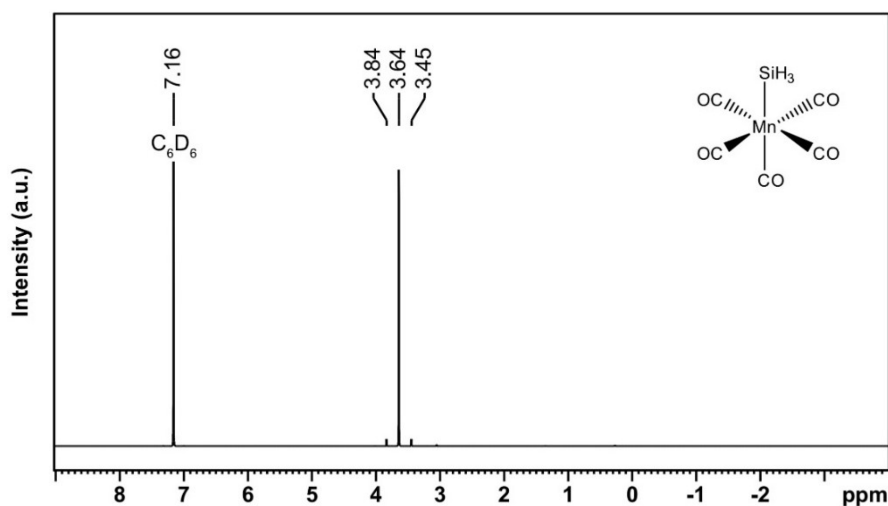

Figure 63: ^{1}H-NMR spectrum of $H_3SiMn(CO)_5$ (C_6D_6, 500 MHz).

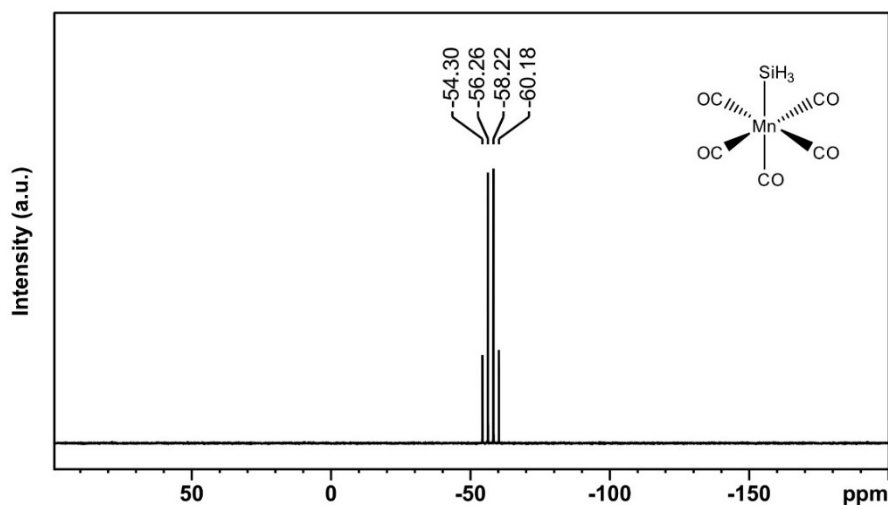

Figure 64: ^{29}Si-NMR spectrum of $H_3SiMn(CO)_5$ (C_6D_6, 99 MHz).

$H_3SiCo(CO)_4$

Analogous to $H_3SiMn(CO)_5$ the precursor was prepared by a salt elimination reaction similar to a literature procedure.[309] Typically 3.0 g (16 mmol; not considering potential residual ether) of $NaCo(CO)_4$ were disperse in approx. 15 mL of dimethylether at 193 K using an ethanol cooling bath. 2.4 g H_3SiI (15 mmol) was added and the mixture was stirred at approx. 243 K for 3 h. The solvent was removed under reduced pressure at temperatures of 200-233 K. The crude product was collected by resublimation using evaporation temperatures of 233 K while

keeping the cold trap at 77 K. To ensure the complete removal of solvents sublimation was repeated two times. $H_3SiCo(CO)_4$ was obtained as slightly yellow, clear liquid in a yield of 1.2 g (6 mmol, 38 %) .

NMR was used for characterization: ^{1}H-NMR (300 MHz, C_6D_6, 298 K, TMS): 3.84 ppm (t; 3H; $^1J(^1H, ^{29}Si)$ = 212 Hz; $\mathbf{H_3}SiCo(CO)_4$); ^{29}Si-NMR (99 MHz, C_6D_6, 298 K, TMS): -47.20 ppm (q; 1Si; $^1J(^1H, ^{29}Si)$ = 212 Hz; $H_3\mathbf{Si}Co(CO)_4$).

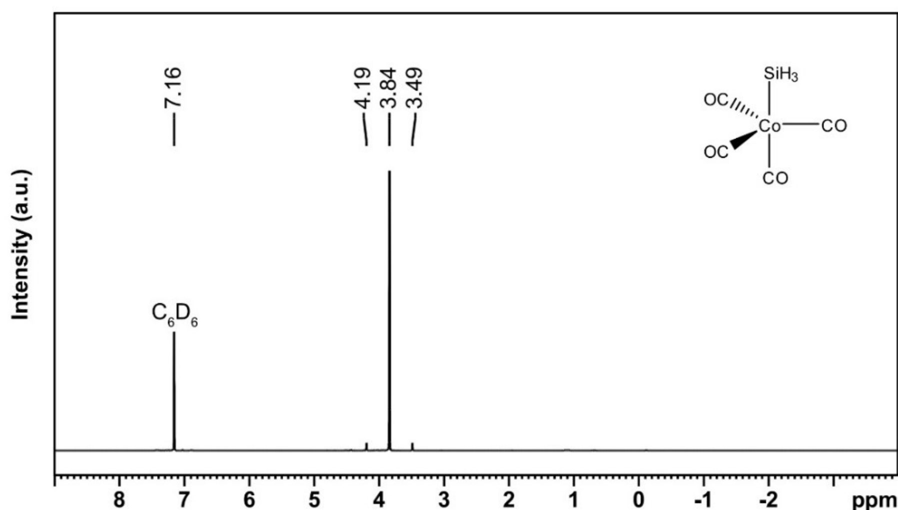

Figure 65: ^{1}H-NMR spectrum of $H_3SiCo(CO)_4$ (C_6D_6, 300 MHz).

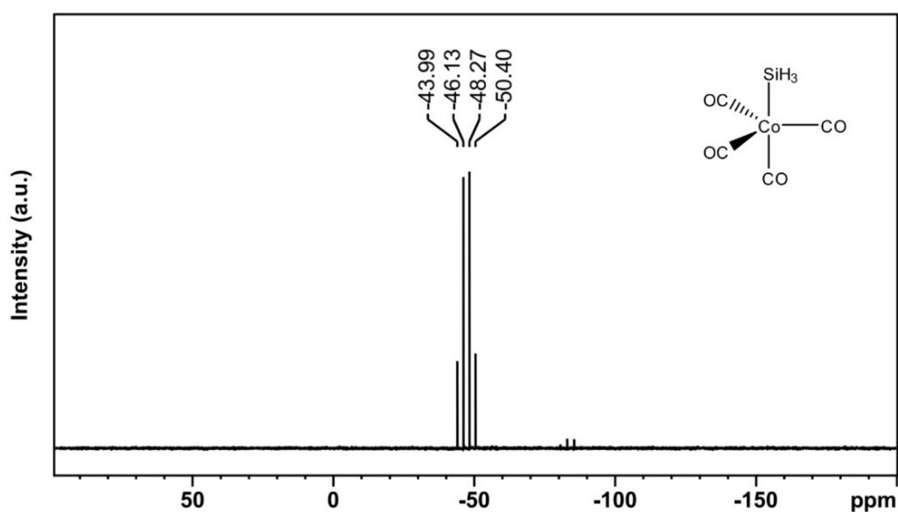

Figure 66: ^{29}Si-NMR spectrum of $H_3SiCo(CO)_4$ (C_6D_6, 99 MHz).

$H_2Si(Co(CO)_4)_2$

$H_2Si(Co(CO)_4)_2$ was prepared similar to $H_3Si(CO)_4$ using a salt elimination method and replacing H_3SiI with H_2SiI_2.[309] Typically 3.0 g (15.8 mmol; not considering potential residual

ether) of $NaCo(CO)_4$ were disperse in approx. 15 mL of dimethylether at 193 K. 2.36 g H_2SiI_2 (8 mmol) were added and the mixture was stirred at approx. 243 K for 3 h using an ethanol cooling bath. The solvent was removed under reduced pressure at temperatures of 200-233 K. The crude product was collected by resublimation using evaporation temperatures of 298 K while keeping the cold trap at 77 K. To ensure the complete removal of solvents sublimation was repeated two times. $H_2Si(Co(CO)_4)_2$ was obtained as slightly yellow, clear liquid melting at approx. 288 K in a yield of 2.5 g (7 mmol, 81 %).

NMR was used for characterization: ^{1}H-NMR (500 MHz, C_6D_6, 298 K, TMS): 4.88 ppm (t; 2H; $^1J(^1H, ^{29}Si)$ = 206 Hz; **H_2**$Si(Co(CO)_4)_2$); ^{29}Si-NMR(99 MHz, C_6D_6, 298 K, TMS): 8.96 ppm (t; 1Si; $^1J(^1H, ^{29}Si)$ = 206 Hz; H_2**Si**$(Co(CO)_4)_2$)).

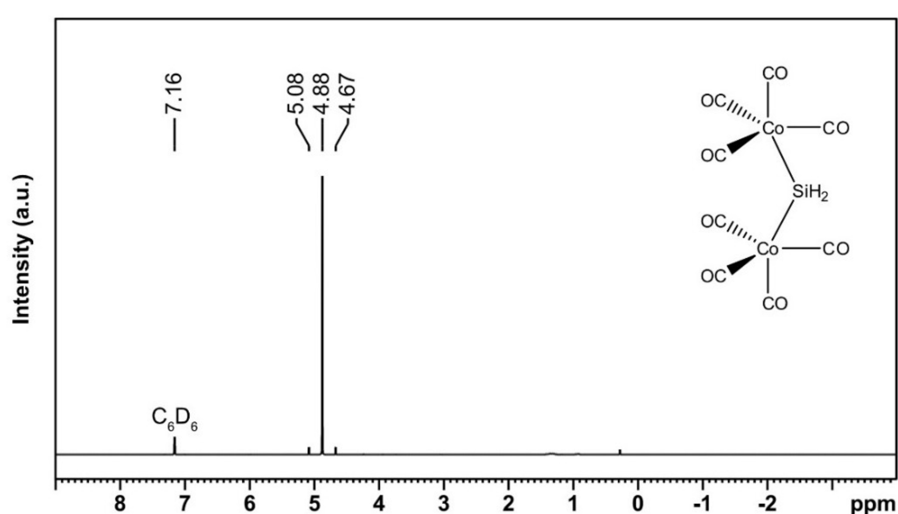

Figure 67: ^{1}H-NMR spectrum of $H_2Si(Co(CO)_4)_2$ (C_6D_6, 500 MHz).

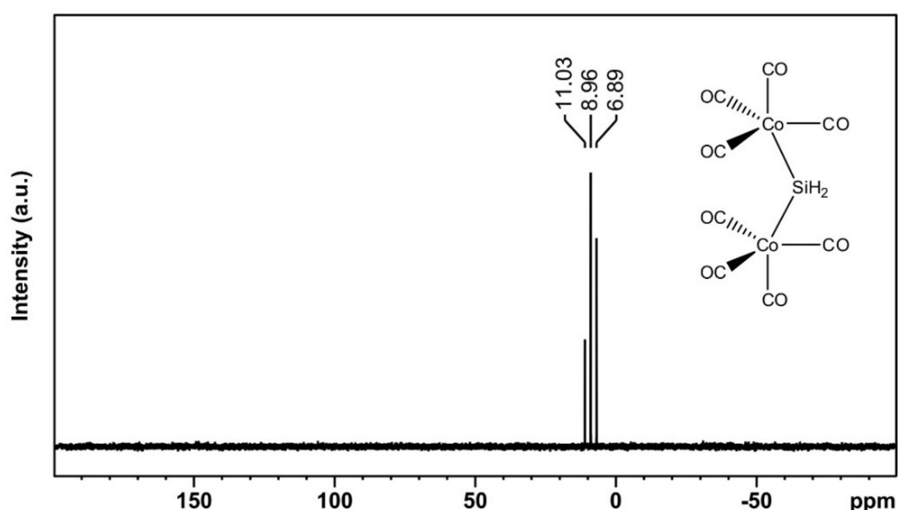

Figure 68: ^{29}Si-NMR spectrum of $H_2Si(Co(CO)_4)_2$ (C_6D_6, 99 MHz).

6.2 CVD Process

CVD has been carried out in a home-built cold-wall reactor using high frequency inductive heating of a graphite susceptor (Figure 69).[332] The desired substrates were attached to a wedge-shaped susceptor using silver paste ensuring good thermal contact. The temperature was controlled by a thermocouple inserted into the graphite susceptor. Prior to use the apparatus was dried under vacuum at 373 K ensuring a removal of adsorbed water. For deposition, typically 50 mg of precursor were used and introduced into the chamber by applying a dynamic vacuum (approximately 10^{-6} mbar). Approximately 50 mg of precursor were typically used and growth was carried out for 60-120 min. The investigated temperature region has been limited to 473 to 773 K.

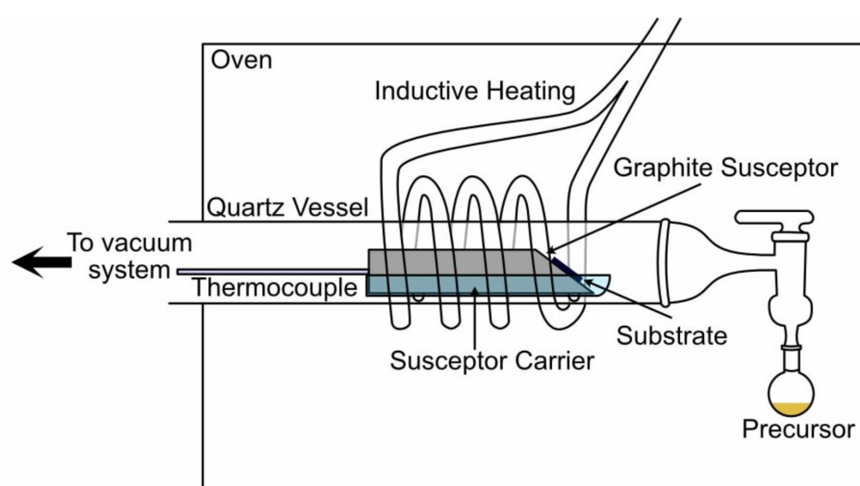

Figure 69: Schematic of the low-pressure cold-wall CVD reactor used in this work. Adapted from ref [332].

6.3 FEBID and FIBID Process

FEBID and FIBID were performed using a dual beam SEM/FIB (FEI, Nova600 NanoLab) with a Schottky electron emitter and a Ga ion source. The precursor molecules were injected using a custom-built GIS equipped with a capillary with an inner diameter of 500 µm. For both processes, the capillary was positioned 100 µm laterally and vertically from the intended deposition spot. For FEBID the capillary-substrate angle was 15°. For FIBID capillary-substrate angles of 35° were used. Substrates used in this work were either (i) (0001) sapphire single crystals coated with 100 nm to 250 nm Au with an 8 nm Cr adhesion layer; (ii) (0001) sapphire single crystals coated with approximately 150 nm Cu or (iii) p-doped (100) Si with a 300 nm SiO_2 coating from. SiO_2/Si substrates were obtained from CrysTec GmbH all other substrates were obtained from Crystal GmbH.

Typically, air plasma cleaning for 30 min was performed after mounting the sample to reduce the hydrocarbon level in the chamber. Prior to deposition the system typically was pumped for 48 h and the residual water was reduced by using a Meissner trap for 4 h. Using this procedure background pressures of typically below 4.2×10^{-7} mbar were achieved reliably. The temperature of the precursor container was adjusted using an ethanol cooling bath according to the vapor pressure of the precursor. The total pressure during deposition was typically kept below 2×10^{-6} mbar for all precursors used and the exact value was regulated by a needle valve. All precursors were stored at 243 K or below when not in use to prevent thermal degradation.

FEBID process parameters such as electron beam current and voltage were varied to study the influence on the deposits' properties. Pitch (20 nm × 20 nm), dwell time (1 µs) and scanning strategy (serpentine) were kept constant for all samples. For FIBID ion beam current and voltage were varied to investigate the influence on the material properties. Pitch (30 nm × 30 nm), dwell time (0.2 µs) and scanning strategy (serpentine) were kept constant for all samples. Sample sizes did vary and are specified in the respective chapters.

6.4 Analysis

6.4.1 NMR

NMR spectra were recorded on a Bruker AV-500, a Bruker Ascend 400 and a Bruker Avance DPX 250 at room temperature. The chemical shifts were referenced to $SiMe_4$. Deuterated solvents were purchased from Eurisotop and stored over sodium wire or 4 Å molecular sieves.

6.4.2 Transport measurements

Au microelectrodes were prepared by standard ultraviolet contact photolithography and sputtering of 8 nm Cr adhesion layer and 75 nm Au for the microelectrodes on SiO_2(200-300 nm)/p-type substrates (CrysTec GmbH). Two-probe I-V curves were recorded inside the SEM after FEBID and FIBID. Temperature dependent electronic and magnetic measurements were performed in a variable-temperature insert mounted in a ^{4}He cryostat equipped with a 12 T superconducting solenoid in a temperature range of 2-300 K. Standard measurements at room temperature were performed using a Keithly source meter 2400 and an Agilent 34420A nanovoltmeter. For magnetotransport measurements the magnetic field was applied perpendicular to the sample surface.

6.4.3 Compositional and microstructural analysis

Compositional analysis was carried out by EDX. The beam energy was adapted according to the samples investigated. However, typically lowest beam energies possible were used to

reduce the contribution from the substrate material. Generally, the deposits were thick enough to avoid significant contributions from the substrate. The composition of the samples was quantified using a standard-less procedure, thus only an estimate of the actual composition is provided. However, general trends can be discussed regardless as all samples were characterized using the same system. Additionally, a slight overestimation of carbon due to deposition of carbon from residual gases is possible but control measurements on the bare substrate material did not show any significant parasitic carbon deposition under the conditions used. For V-containing samples derived from $V(CO)_6$ quantification of oxygen was not possible due to an overlap of V_L (0.511 keV) and $O_{K\alpha}$ (0.523 keV). As a consequence, the V_L peak was used and set into relation with the C_K signal to provide information on the general trends. The overlap of both signals makes it very challenging for automated quantification software and would require newest detector hardware and simulation software packages to be solved.

TEM lamellae for cross-sectional analysis were prepared by standard FIB milling using Ga^+ ions. To protect samples during the milling steps they were covered in FEBID-PtC_x and subsequently FIBID-PtC_x using $MeCpPtMe_3$ as precursor, in a FIB/SEM Dual Beam Microscope FEI NOVA 200. Initial milling and lift out have been carried out at 30 kV while 5 kV were used for the final milling. The lamellae were mounted on an Omniprobe copper-based lift-out grid and transferred to the TEM. TEM investigations were carried out using a FEI TITIAN^3 G2 operated at 300 kV in scanning mode. Compositional analysis was performed with a Gatan Quantum imaging filter for EELS as well as a high-sensitivity four-quadrant SDD (Super-X) detector for EDX. For data acquisition and analysis Gatan Microscopy suite (version 3.4) and Thermo Scientific Velox (version 3.0) were used.

6.4.4 X-Ray Diffraction

Thin films deposited by CVD were characterized using a Bruker D8 Discovery (Billerica, MA, USA) in Bragg-Bretano geometry. All measurements were recorded using Cu $K\alpha$ radiation. Data analysis was performed using Match! Software (crystal impact, Bonn, Germany).

6.4.5 AFM

Exact topographies of deposited samples were acquired by AFM operated in tapping mode (nanosurf, easyscan2). Cantilevers shaped like a pyramid, with a tip radius of less than 7 nm have been used (Nanosensors PPP-NCLR).

7 Appendix

7.1 List of references

1. Takagishi, K.; Umezu, S., *Development of the Improving Process for the 3D Printed Structure*. Sci. Rep. **2017,** *7*, 39852.
2. Gibson, I.; Rosen, D.; Stucker, B., *Additive Manufacturing Technologies*. Springer International Publishing : Imprint: Springer, 2021.
3. Alimi, O. A.; Meijboom, R., *Current and Future Trends of Additive Manufacturing for Chemistry Applications: a Review*. J. Mater. Sci. **2021,** *56*, 16824-16850.
4. Hirt, L.; Reiser, A.; Spolenak, R.; Zambelli, T., *Additive Manufacturing of Metal Structures at the Micrometer Scale*. Adv. Mater. **2017,** *29*, 1604211.
5. van Dorp, W. F., *Sub-10 nm Writing: Focused Electron Beam-Induced Deposition in Perspective*. Appl. Phys. A **2014,** *117*, 1615-1622.
6. van Dorp, W. F.; van Someren, B.; Hagen, C. W.; Kruit, P.; Crozier, P. A., *Approaching the Resolution Limit of Nanometer-Scale Electron Beam-Induced Deposition*. Nano Lett. **2005,** *5*, 1303-1307.
7. Winkler, R.; Fowlkes, J. D.; Rack, P. D.; Plank, H., *3D Nanoprinting via Focused Electron Beams*. J. Appl. Phys. **2019,** *125*, 210901.
8. Fernández-Pacheco, A.; Skoric, L.; De Teresa, J. M.; Pablo-Navarro, J.; Huth, M.; Dobrovolskiy, O. V., *Writing 3D Nanomagnets Using Focused Electron Beams*. Materials **2020,** *13*, 3774.
9. Utke, I.; Michler, J.; Winkler, R.; Plank, H., *Mechanical Properties of 3D Nanostructures Obtained by Focused Electron/Ion Beam-Induced Deposition: A Review*. Micromachines **2020,** *11*, 397.
10. Weirich, P. M.; Schwalb, C. H.; Winhold, M.; Huth, M., *Superconductivity in the System* $Mo_xC_yGa_zO_\delta$ *Prepared by Focused Ion Beam Induced Deposition*. J. Appl. Phys. **2014,** *115*.
11. Porrati, F.; Barth, S.; Sachser, R.; Dobrovolskiy, O. V.; Seybert, A.; Frangakis, A. S.; Huth, M., *Crystalline Niobium Carbide Superconducting Nanowires Prepared by Focused Ion Beam Direct Writing*. ACS Nano **2019,** *13*, 6287-6296.
12. Dobrovolskiy, O. V.; Kompaniiets, M.; Sachser, R.; Porrati, F.; Gspan, C.; Plank, H.; Huth, M., *Tunable Magnetism on the Lateral Mesoscale by Post-Processing of Co/Pt Heterostructures*. Beilstein J. Nanotechnol. **2015,** *6*, 1082-1090.
13. Sanz-Hernández, D.; Hierro-Rodriguez, A.; Donnelly, C.; Pablo-Navarro, J.; Sorrentino, A.; Pereiro, E.; Magén, C.; McVitie, S.; de Teresa, J. M.; Ferrer, S.; Fischer, P.; Fernández-Pacheco, A., *Artificial Double-Helix for Geometrical Control of Magnetic Chirality*. ACS Nano **2020,** *14*, 8084-8092.
14. Winkler, R.; Schmidt, F. P.; Haselinann, U.; Fowlkes, J. D.; Lewis, B. B.; Kothleitner, G.; Rack, P. D.; Plank, H., *Direct-Write 3D Nanoprinting of Plasmonic Structures*. ACS Appl. Mater. Interfaces **2017,** *9*, 8233-8240.
15. Esposito, M.; Tasco, V.; Todisco, F.; Cuscunà, M.; Benedetti, A.; Scuderi, M.; Nicotra, G.; Passaseo, A., *Programmable Extreme Chirality in the Visible by Helix-Shaped Metamaterial Platform*. Nano Lett. **2016,** *16*, 5823-5828.
16. Blagg, K.; Allen, P.; Lu, T.-M.; Lilly, M. P.; Singh, M., *Focused Ion Beam Deposited Carbon-Platinum Nanowires for Cryogenic Resistive Thermometry*. Carbon **2020,** *169*, 482-487.
17. Sattelkow, J.; Fröch, J. E.; Winkler, R.; Hummel, S.; Schwalb, C.; Plank, H., *Three-Dimensional Nanothermistors for Thermal Probing*. ACS Appl. Mater. Interfaces **2019,** *11*, 22655-22667.
18. Moczała, M.; Kwoka, K.; Piasecki, T.; Kunicki, P.; Sierakowski, A.; Gotszalk, T., *Fabrication and Characterization of Micromechanical Bridges with Strain Sensors Deposited Using Focused Electron Beam Induced Technology*. Microelectron. Eng. **2017,** *176*, 111-115.

19. Kolb, F.; Schmoltner, K.; Huth, M.; Hohenau, A.; Krenn, J.; Klug, A.; List, E. J. W.; Plank, H., *Variable Tunneling Barriers in FEBID Based PtC Metal-Matrix Nanocomposites as a Transducing Element for Humidity Sensing*. Nanotechnology **2013,** *24*, 305501.
20. Keller, L.; Al Mamoori, M. K. I.; Pieper, J.; Gspan, C.; Stockem, I.; Schröder, C.; Barth, S.; Winkler, R.; Plank, H.; Pohlit, M.; Müller, J.; Huth, M., *Direct-Write of Free-Form Building Blocks for Artificial Magnetic 3D Lattices*. Sci. Rep. **2018,** *8*, 6160.
21. Utke, I.; Hoffmann, P.; Melngailis, J., *Gas-Assisted Focused Electron Beam and Ion Beam Processing and Fabrication*. J. Vac. Sci. Technol., B: Microelectron. Nanometer Struct.--Process., Meas., Phenom. **2008,** *26*, 1197-1276.
22. van Dorp, W. F.; Hagen, C. W., *A Critical Literature Review of Focused Electron Beam Induced Deposition*. J. Appl. Phys. **2008,** *104*, 42.
23. Barth, S.; Huth, M.; Jungwirth, F., *Precursors for Direct-Write Nanofabrication with Electrons*. J. Mater. Chem. C **2020,** *8*, 15884-15919.
24. Böhler, E.; Warneke, J.; Swiderek, P., *Control of Chemical Reactions and Synthesis by Low-Energy Electrons*. Chem. Soc. Rev. **2013,** *42*, 9219-9231.
25. Franz, G., *Low Pressure Plasmas and Microstructuring Technology*. Springer-Verlag Berlin and Heidelberg GmbH & Co. KG, 2008.
26. Utke, I. R. P. M. S., *Nanofabrication Using Focused Ion and Electron Beams: Principles and Applications (Nanomanufacturing Series)*. Oxford University Press, 2011.
27. Arumainayagam, C. R.; Lee, H.-L.; Nelson, R. B.; Haines, D. R.; Gunawardane, R. P., *Low-Energy Electron-Induced Reactions in Condensed Matter*. Surf. Sci. Rep. **2010,** *65*, 1-44.
28. Thorman, R. M.; Kumar, T. P. R.; Fairbrother, D. H.; Ingolfsson, O., *The Role of Low-Energy Electrons in Focused Electron Beam Induced Deposition: Four Case Studies of Representative Precursors*. Beilstein J. Nanotechnol. **2015,** *6*, 1904-1926.
29. Ingolfsson, O., *Low-Energy Electrons : Fundamentals and Applications*. **2019**.
30. Thorman, R. M. Surface Reactions of Low Energy Electrons and Ions with Organometallic Precursors for Charged Particle Deposition Processes. Johns Hopkins University 2020.
31. Allan, M.; Lacko, M.; Papp, P.; Matejčík, Š.; Zlatar, M.; Fabrikant, I. I.; Kočišek, J.; Fedor, J., *Dissociative Electron Attachment and Electronic Excitation in* $Fe(CO)_5$. PCCP **2018,** *20*, 11692-11701.
32. Melngailis, J., *Focused Ion Beam Technology and Applications*. J. Vac. Sci. Technol., B: Microelectron. Process. Phenom. **1987,** *5*, 469-495.
33. Zlatar, M.; Allan, M.; Fedor, J., *Excited States of* $Pt(PF_3)_4$ *and Their Role in Focused Electron Beam Nanofabrication*. Journal of Physical Chemistry C **2016,** *120*, 10667-10674.
34. Wnorowski, K.; Stano, M.; Matias, C.; Denifl, S.; Barszczewska, W.; Matejčík, Š., *Low-Energy Electron Interactions with Tungsten Hexacarbonyl –* $W(CO)_6$. Rapid Commun. Mass Spectrom. **2012,** *26*, 2093-2098.
35. Neustetter, M.; Mauracher, A.; Limão-Vieira, P.; Denifl, S., *Complete Ligand Loss in Electron Ionization of the Weakly Bound Organometallic Tungsten Hexacarbonyl Dimer*. PCCP **2016,** *18*, 9893-9896.
36. Neustetter, M.; Jabbour Al Maalouf, E.; Limão-Vieira, P.; Denifl, S., *Fragmentation Pathways of Tungsten Hexacarbonyl Clusters upon Electron Ionization*. J. Chem. Phys. **2016,** *145*, 054301.
37. Lengyel, J.; Papp, P.; Matejčík, Š.; Kočišek, J.; Fárník, M.; Fedor, J., *Suppression of Low-Energy Dissociative Electron Attachment in* $Fe(CO)_5$ *upon Clustering*. Beilstein J. Nanotechnol. **2017,** *8*, 2200-2207.
38. Yu, J.-C.; Abdel-Rahman, M. K.; Fairbrother, D. H.; McElwee-White, L., *Charged Particle-Induced Surface Reactions of Organometallic Complexes as a Guide to Precursor Design for Electron- and Ion-Induced Deposition of Nanostructures*. ACS Appl. Mater. Interfaces **2021**.
39. Rosenberg, S. G.; Barclay, M.; Fairbrother, D. H., *Electron Induced Reactions of Surface Adsorbed Tungsten Hexacarbonyl* ($W(CO)_6$). PCCP **2013,** *15*, 4002-4015.
40. Thorman, R. M.; Unlu, I.; Johnson, K.; Bjornsson, R.; McElwee-White, L.; Fairbrother, D. H.; Ingolfsson, O., *Low Energy Electron-Induced Decomposition of* (η^5-

Cp)Fe(CO)$_2$Mn(CO)$_5$, A Potential Bimetallic Precursor for Focused Electron Beam Induced Deposition of Alloy Structures. PCCP **2018,** *20*, 5644-5656.
41. Rohdenburg, M.; Martinović, P.; Ahlenhoff, K.; Koch, S.; Emmrich, D.; Gölzhäuser, A.; Swiderek, P., *Cisplatin as a Potential Platinum Focused Electron Beam Induced Deposition Precursor: NH$_3$ Ligands Enhance the Electron-Induced Removal of Chlorine*. J. Phys. Chem. C **2019,** *123*, 21774-21787.
42. Kumar, R. T. P.; Unlu, I.; Barth, S.; Ingólfsson, O.; Fairbrother, D. H., *Electron Induced Surface Reactions of HFeCo$_3$(CO)$_{12}$, a Bimetallic Precursor for Focused Electron Beam Induced Deposition (FEBID)*. J. Phys. Chem. C **2018,** *122*, 2648-2660.
43. Rosenberg, S. G.; Barclay, M.; Fairbrother, D. H., *Electron Induced Surface Reactions of Organometallic Metal(hfac)$_2$ Precursors and Deposit Purification*. ACS Appl. Mater. Interfaces **2014,** *6*, 8590-8601.
44. Spencer, J. A.; Wu, Y. C.; McElwee-White, L.; Fairbrother, D. H., *Electron Induced Surface Reactions of cis-Pt(CO)$_2$Cl$_2$: A Route to Focused Electron Beam Induced Deposition of Pure Pt Nanostructures*. J. Am. Chem. Soc. **2016,** *138*, 9172-9182.
45. Thorman, R. M.; Brannaka, J. A.; McElwee-White, L.; Ingolfsson, O., *Low Energy Electron-Induced Decomposition of (η^3-C$_3$H$_5$)Ru(CO)$_3$Br, A Potential Focused Electron Beam Induced Deposition Precursor with a Heteroleptic Ligand Set*. PCCP **2017,** *19*, 13264-13271.
46. Ramsier, R. D.; Henderson, M. A.; Yates, J. T., *Electron Induced Decomposition of Ni(CO)$_4$ Adsorbed on Ag(111)*. Surf. Sci. **1991,** *257*, 9-21.
47. Henderson, M. A.; Ramsier, R. D.; Yates, J. T., *Low-Energy Electron Induced Decomposition of Fe(CO)$_5$ adsorbed on Ag(111)*. Surf. Sci. **1991,** *259*, 173-182.
48. Bilgilisoy, E.; Thorman, R. M.; Barclay, M. S.; Marbach, H.; Fairbrother, D. H., *Low Energy Electron- and Ion-Induced Surface Reactions of Fe(CO)$_5$ Thin Films*. J. Phys. Chem. C **2021,** *125*, 17749-17760.
49. Kumar, R. T. P.; Weirich, P.; Hrachowina, L.; Hanefeld, M.; Bjornsson, R.; Hrodmarsson, H. R.; Barth, S.; Fairbrother, D. H.; Huth, M.; Ingólfsson, O., *Electron Interactions with the Heteronuclear Carbonyl Precursor H$_2$FeRu$_3$(CO)$_{13}$ and Comparison with HFeCo$_3$(CO)$_{12}$: From Fundamental Gas Phase and Surface Science Studies to Focused Electron Beam Induced Deposition*. Beilstein J. Nanotechnol. **2018,** *9*, 555-579.
50. Rosenberg, S. G.; Barclay, M.; Fairbrother, D. H., *Electron Beam Induced Reactions of Adsorbed Cobalt Tricarbonyl Nitrosyl (Co(CO)$_3$NO) Molecules*. J. Phys. Chem. C **2013,** *117*, 16053-16064.
51. Spencer, J. A.; Brannaka, J. A.; Barclay, M.; McElwee-White, L.; Fairbrother, D. H., *Electron-Induced Surface Reactions of η^3-Allyl Ruthenium Tricarbonyl Bromide [(η^3-C$_3$H$_5$)Ru(CO)$_3$Br]: Contrasting the Behavior of Different Ligands*. J. Phys. Chem. C **2015,** *119*, 15349-15359.
52. Unlu, I.; Spencer, J. A.; Johnson, K. R.; Thorman, R. M.; Ingólfsson, O.; McElwee-White, L.; Fairbrother, D. H., *Electron Induced Surface Reactions of (η^5-C$_5$H$_5$)Fe(CO)$_2$Mn(CO)$_5$, A Potential Heterobimetallic Precursor for Focused Electron Beam Induced Deposition (FEBID)*. PCCP **2018,** *20*, 7862-7874.
53. Spencer, J. A.; Rosenberg, S. G.; Barclay, M.; Wu, Y.-C.; McElwee-White, L.; Howard Fairbrother, D., *Understanding the Electron-Stimulated Surface Reactions of Organometallic Complexes to Enable Design of Precursors for Electron Beam-Induced Deposition*. Appl. Phys. A **2014,** *117*, 1631-1644.
54. Sápi, A.; Rajkumar, T.; Kiss, J.; Kukovecz, Á.; Kónya, Z.; Somorjai, G. A., *Metallic Nanoparticles in Heterogeneous Catalysis*. Catal. Lett. **2021,** *151*, 2153-2175.
55. Myers, A. K.; Schoofs, G. R.; Benziger, J. B., *Comparison of Benzene Adsorption on Nickel(111) and Nickel(100)*. J. Phys. Chem. **1987,** *91*, 2230-2232.
56. Reimer, L., *Scanning Electron Microscopy : Physics of Image Formation and Microanalysis*. 2010.
57. Seiler, H., *Secondary Electron Emission in the Scanning Electron Microscope*. J. Appl. Phys. **1983,** *54*, R1-R18.
58. Lin, Y.; Joy, D. C., *A new Examination of Secondary Electron Yield Data*. Surf. Interface Anal. **2005,** *37*, 895-900.

59. Huth, M.; Porrati, F.; Barth, S., *Living up to Its Potential—Direct-Write Naofabrication with Focused Electron Beams*. J. Appl. Phys. **2021,** *130*, 170901.
60. Fowlkes, J. D.; Randolph, S. J.; Rack, P. D., *Growth and Simulation of High-Aspect Ratio Nanopillars by Primary and secondary Electron-Induced Deposition*. J. Vac. Sci. Technol., B: Microelectron. Nanometer Struct.--Process., Meas., Phenom. **2005,** *23*, 2825-2832.
61. Kunz, R. R.; Allen, T. E.; Mayer, T. M., *Selective Area Deposition of Metals using Low - Energy Electron Beams*. J. Vac. Sci. Technol., B: Microelectron. Process. Phenom. **1987,** *5*, 1427-1431.
62. Toth, M.; Lobo, C.; Friedli, V.; Szkudlarek, A.; Utke, I., *Continuum Models of Focused Electron Beam Induced Processing*. Beilstein J. Nanotechnol. **2015,** *6*, 1518-1540.
63. Huth, M.; Porrati, F.; Dobrovolskiy, O. V., *Focused Electron Beam Induced Deposition Meets Materials Science*. Microelectron. Eng. **2018,** *185-186*, 9-28.
64. Huth, M.; Porrati, F.; Gruszka, P.; Barth, S., *Temperature-Dependent Growth Characteristics of Nb- and CoFe-Based Nanostructures by Direct-Write Using Focused Electron Beam-Induced Deposition*. Micromachines **2020,** *11*.
65. Engmann, S.; Stano, M.; Matejčík, Š.; Ingólfsson, O., *Gas Phase Low Energy Electron Induced Decomposition of the Focused Electron Beam Induced Deposition (FEBID) Precursor Trimethyl (methylcyclopentadienyl) platinum(iv) ($MeCpPtMe_3$)*. PCCP **2012,** *14*, 14611-14618.
66. Cullen, J.; Bahm, A.; Lobo, C. J.; Ford, M. J.; Toth, M., *Localized Probing of Gas Molecule Adsorption Energies and Desorption Attempt Frequencies*. J. Phys. Chem. C **2015,** *119*, 15948-15953.
67. Cullen, J.; Lobo, C. J.; Ford, M. J.; Toth, M., *Electron-Beam-Induced Deposition as a Technique for Analysis of Precursor Molecule Diffusion Barriers and Prefactors*. ACS Appl. Mater. Interfaces **2015,** *7*, 21408-21415.
68. Szkudlarek, A.; Szmyt, W.; Kapusta, C.; Utke, I., *Lateral Resolution in Focused Electron Beam-Induced Deposition: Scaling Laws for Pulsed and Static Exposure*. Appl. Phys. A **2014,** *117*, 1715-1726.
69. Szkudlarek, A.; Gabureac, M.; Utke, I., *Effects of Adsorbate Surface Diffusion in Focused Electron-Beam-Induced-Deposition*. ECS Transactions **2013,** *50*, 495-498.
70. Winkler, R.; Fowlkes, J.; Szkudlarek, A.; Utke, I.; Rack, P. D.; Plank, H., *The Nanoscale Implications of a Molecular Gas Beam during Electron Beam Induced Deposition*. ACS Appl. Mater. Interfaces **2014,** *6*, 2987-2995.
71. Winkler, R.; Geier, B.; Plank, H., *Spatial Chemistry Evolution During Focused Electron Beam-Induced Deposition: Origins and Workarounds*. Appl. Phys. A **2014,** *117*, 1675-1688.
72. Bruch, L. W., *Theory of Physisorption Interactions*. Surf. Sci. **1983,** *125*, 194-217.
73. Ehrichs, E. E.; Smith, W. F.; de Lozanne, A. L., *Four-Probe Resistance Measurements of Nickel Wires Written with a Scanning Tunneling Microscope/Scanning Electron Microscope System*. Ultramicroscopy **1992,** *42-44*, 1438-1442.
74. Lukasczyk, T.; Schirmer, M.; Steinrück, H.-P.; Marbach, H., *Electron-Beam-Induced Deposition in Ultrahigh Vacuum: Lithographic Fabrication of Clean Iron Nanostructures*. Small **2008,** *4*, 841-846.
75. Mulders, J. J. L.; Belova, L. M.; Riazanova, A., *Electron Beam Induced Deposition at Elevated Temperatures: Compositional Changes and Purity Improvement*. Nanotechnology **2010,** *22*, 055302.
76. Córdoba, R.; Sharma, N.; Kölling, S.; Koenraad, P. M.; Koopmans, B., *High-Purity 3D Nano-Objects Grown by Focused-Electron-Beam Induced Deposition*. Nanotechnology **2016,** *27*, 355301.
77. Botman, A.; Mulders, J. J. L.; Hagen, C. W., *Creating Pure Nanostructures from Electron-Beam-Induced Deposition using Purification Techniques: a Technology Perspective*. Nanotechnology **2009,** *20*, 372001.
78. Landheer, K.; Rosenberg, S. G.; Bernau, L.; Swiderek, P.; Utke, I.; Hagen, C. W.; Fairbrother, D. H., *Low-Energy Electron-Induced Decomposition and Reactions of Adsorbed Tetrakis(trifluorophosphine)platinum [$Pt(PF_3)_4$]*. J. Phys. Chem. C **2011,** *115*, 17452-17463.

79. Barry, J. D.; Ervin, M.; Molstad, J.; Wickenden, A.; Brintlinger, T.; Hoffman, P.; Meingailis, J., *Electron Beam Induced Deposition of Low Resistivity Platinum from $Pt(PF_3)_4$*. J. Vac. Sci. Technol., B: Microelectron. Nanometer Struct.--Process., Meas., Phenom. **2006,** *24*, 3165-3168.
80. Fernández-Pacheco, A.; De Teresa, J. M.; Córdoba, R.; Ibarra, M. R., *Magnetotransport Properties of High-Quality Cobalt Nanowires Grown by Focused-Electron-Beam-Induced Deposition*. J. Phys. D: Appl. Phys. **2009,** *42*, 055005.
81. Su, D., *Electron Beam Induced Changes in Transition Metal Oxides*. Analytical and Bioanalytical Chemistry **2002,** *374*, 732-735.
82. Sengupta, S.; Li, C.; Baumier, C.; Kasumov, A.; Gueron, S.; Bouchiat, H.; Fortuna, F., *Superconducting Nanowires by Electron-Beam-Induced Deposition*. Appl. Phys. Lett. **2015,** *106*, 5.
83. Roberts, N. A.; Gonzalez, C. M.; Fowlkes, J. D.; Rack, P. D., *Enhanced By-Product Desorption via Laser Assisted Electron Beam Induced Deposition of $W(CO)_6$ with Improved Conductivity and Resolution*. Nanotechnology **2013,** *24*, 415301.
84. Henry, M. R.; Kim, S.; Fedorov, A. G., *High Purity Tungsten Nanostructures via Focused Electron Beam Induced Deposition with Carrier Gas Assisted Supersonic Jet Delivery of Organometallic Precursors*. J. Phys. Chem. C **2016,** *120*, 10584-10590.
85. Kim, S.; Henry, M.; Moon, Y. H.; Fedorov, A. G., *Multimode Jetting Unlocks a Trade-Off between Nanostructure Morphology and Composition in Focused Electron Beam Induced Deposition*. Mater. Today Commun. **2019,** *21*, 100645.
86. Folch, A.; Servat, J.; Esteve, J.; Tejada, J.; Seco, M., *HigVacuum Versus "Environmental" Electron Beam Deposition*. J. Vac. Sci. Technol., B: Microelectron. Nanometer Struct.--Process., Meas., Phenom. **1996,** *14*, 2609-2614.
87. Belić, D.; Shawrav, M. M.; Gavagnin, M.; Stöger-Pollach, M.; Wanzenboeck, H. D.; Bertagnolli, E., *Direct-Write Deposition and Focused-Electron-Beam-Induced Purification of Gold Nanostructures*. ACS Appl. Mater. Interfaces **2015,** *7*, 2467-2479.
88. Koops, H. W. P.; Schössler, C.; Kaya, A.; Weber, M., *Conductive Dots, Wires, and Supertips for Field Electron Emitters Produced by Electron-Beam Induced Deposition on Samples having Increased Temperature*. J. Vac. Sci. Technol., B: Microelectron. Nanometer Struct.--Process., Meas., Phenom. **1996,** *14*, 4105-4109.
89. Shawrav, M. M.; Taus, P.; Wanzenboeck, H. D.; Schinnerl, M.; Stoger-Pollach, M.; Schwarz, S.; Steiger-Thirsfeld, A.; Bertagnolli, E., *Highly Conductive and Pure Gold Nanostructures Grown by Electron Beam Induced Deposition*. Sci. Rep. **2016,** *6*.
90. Thompson, L. R.; Rocca, J. J.; Emery, K.; Boyer, P. K.; Collins, G. J., *Electron Beam Assisted Chemical Vapor Deposition of SiO_2*. Appl. Phys. Lett. **1983,** *43*, 777-779.
91. Perentes, A.; Hoffmann, P.; Munnik, F., *Focused Electron Beam Induced Deposition of DUV Transparent SiO_2*. SPIE, 2007; Vol. 6533.
92. Makise, K.; Mitsuishi, K.; Shimojo, M.; Shinozaki, B., *Microstructural Analysis and Transport Properties of MoO and MoC Nanostructures Prepared by Focused Electron Beam-Induced Deposition*. Sci. Rep. **2014,** *4*, 5740.
93. Shimojo, M.; Takeguchi, M.; Furuya, K., *Formation of Crystalline Iron Oxide Nanostructures by Electron Beam-Induced Deposition at Toom Temperature*. Nanotechnology **2006,** *17*, 3637-3640.
94. Lewis, B. B.; Stanford, M. G.; Fowlkes, J. D.; Lester, K.; Plank, H.; Rack, P. D., *Electron-Stimulated Purification of Platinum Nanostructures Grown via Focused Electron Beam Induced Deposition*. Beilstein J. Nanotechnol. **2015,** *6*, 907-918.
95. Sachser, R.; Reith, H.; Huzel, D.; Winhold, M.; Huth, M., *Catalytic Purification of Directly Written Nanostructured Pt Microelectrodes*. ACS Appl. Mater. Interfaces **2014,** *6*, 15868-15874.
96. Geier, B.; Gspan, C.; Winkler, R.; Schmied, R.; Fowlkes, J. D.; Fitzek, H.; Rauch, S.; Rattenberger, J.; Rack, P. D.; Plank, H., *Rapid and Highly Compact Purification for Focused Electron Beam Induced Deposits: A Low Temperature Approach Using Electron Stimulated H_2O Reactions*. J. Phys. Chem. C **2014,** *118*, 14009-14016.

97. Langford, R. M.; Ozkaya, D.; Sheridan, J.; Chater, R., *Effects of Water Vapour on Electron and Ion Beam Deposited Platinum*. Microsc. Microanal. **2004,** *10*, 1122-1123.
98. Rohdenburg, M.; Winkler, R.; Kuhness, D.; Plank, H.; Swiderek, P., *Water-Assisted Process for Purification of Ruthenium Nanomaterial Fabricated by Electron Beam Induced Deposition*. ACS Appl. Nano Mater. **2020,** *3*, 8352-8364.
99. Botman, A.; Hesselberth, M.; Mulders, J. J. L., *Improving the Conductivity of Platinum-Containing Nano-Structures Created by Electron-Beam-Induced Deposition*. Microelectron. Eng. **2008,** *85*, 1139-1142.
100. Puydinger dos Santos, M. V.; Velo, M. F.; Domingos, R. D.; Zhang, Y.; Maeder, X.; Guerra-Nuñez, C.; Best, J. P.; Béron, F.; Pirota, K. R.; Moshkalev, S.; Diniz, J. A.; Utke, I., *Annealing-Based Electrical Tuning of Cobalt–Carbon Deposits Grown by Focused-Electron-Beam-Induced Deposition*. ACS Appl. Mater. Interfaces **2016,** *8*, 32496-32503.
101. Ervin, M. H.; Chang, D.; Nichols, B.; Wickenden, A.; Barry, J.; Melngailis, J., *Annealing of Electron Beam Induced Deposits of Platinum from* $Pt(PF_3)_4$. J. Vac. Sci. Technol., B: Microelectron. Nanometer Struct.--Process., Meas., Phenom. **2007,** *25*, 2250-2254.
102. Porrati, F.; Sachser, R.; Schwalb, C. H.; Frangakis, A. S.; Huth, M., *Tuning the Electrical Conductivity of Pt-Containing Granular Metals by Postgrowth Electron Irradiation*. J. Appl. Phys. **2011,** *109*, 063715.
103. Plank, H.; Kothleitner, G.; Hofer, F.; Michelitsch, S. G.; Gspan, C.; Hohenau, A.; Krenn, J., *Optimization of Postgrowth Electron-Beam Curing for Focused Electron-Beam-Induced Pt Deposits*. J. Vac. Sci. Technol. B **2011,** *29*, 051801.
104. Huth, M.; Porrati, F.; Schwalb, C.; Winhold, M.; Sachser, R.; Dukic, M.; Adams, J.; Fantner, G., *Focused Electron Beam Induced Deposition: A Perspective*. Beilstein J. Nanotechnol. **2012,** *3*, 597-619.
105. Li, P.; Chen, S. Y.; Dai, H. F.; Yang, Z. M.; Chen, Z. Q.; Wang, Y. S.; Chen, Y. Q.; Peng, W. Q.; Shan, W. B.; Duan, H. G., *Recent Advances in Focused Ion Beam Nanofabrication for Nanostructures and Devices: Fundamentals and Applications*. Nanoscale **2021,** *13*, 1529-1565.
106. Goldstein, J. I.; Newbury, D. E.; Michael, J. R.; Ritchie, N. W. M.; Scott, J. H. J.; Joy, D. C., Focused Ion Beam Applications in the SEM Laboratory. In *Scanning Electron Microscopy and X-Ray Microanalysis*, Goldstein, J. I.; Newbury, D. E.; Michael, J. R.; Ritchie, N. W. M.; Scott, J. H. J.; Joy, D. C., Eds. Springer New York: New York, NY, 2018; pp 517-528.
107. Kim, C.-S.; Ahn, S.-H.; Jang, D.-Y., *Review: Developments in Micro/Nanoscale Fabrication by Focused Ion Beams*. Vacuum **2012,** *86*, 1014-1035.
108. Bischoff, L.; Mazarov, P.; Bruchhaus, L.; Gierak, J., *Liquid Metal Alloy Ion Sources—An Alternative for Focussed Ion Beam Technology*. Appl. Phys. Rev. **2016,** *3*, 021101.
109. Swanson, L. W., *Liquid Metal Ion Sources: Mechanism and Applications*. Nucl. Instrum. Methods Phys. Res. **1983,** *218*, 347-353.
110. Ward, B. W.; Notte, J. A.; Economou, N. P., *Helium Ion Microscope: A New Tool for Nanoscale Microscopy and Metrology*. J. Vac. Sci. Technol., B: Microelectron. Nanometer Struct.--Process., Meas., Phenom. **2006,** *24*, 2871-2874.
111. Wu, H.; Stern, L. A.; Xia, D.; Ferranti, D.; Thompson, B.; Klein, K. L.; Gonzalez, C. M.; Rack, P. D., *Focused Helium Ion Beam Deposited Low Resistivity Cobalt Metal Lines with 10 nm Resolution: Implications for Advanced Circuit Editing*. J. Mater. Sci.: Mater. Electron. **2014,** *25*, 587-595.
112. Cordoba, R.; Ibarra, A.; Mailly, D.; Guillamon, I.; Suderow, H.; De Teresa, J. M., *3D Superconducting Hollow Nanowires with Tailored Diameters Grown by Focused* He^+ *Beam Direct Writing*. Beilstein J. Nanotechnol. **2020,** *11*, 1198-1206.
113. Goldstein, J. I.; Newbury, D. E.; Michael, J. R.; Ritchie, N. W. M.; Scott, J. H. J.; Joy, D. C., Ion Beam Microscopy. In *Scanning Electron Microscopy and X-Ray Microanalysis*, Goldstein, J. I.; Newbury, D. E.; Michael, J. R.; Ritchie, N. W. M.; Scott, J. H. J.; Joy, D. C., Eds. Springer New York: New York, NY, 2018; pp 529-539.
114. Indrajith, S.; Rousseau, P.; Huber, B. A.; Nicolafrancesco, C.; Domaracka, A.; Grygoryeva, K.; Nag, P.; Sedmidubská, B.; Fedor, J.; Kočišek, J., *Decomposition of Iron*

Pentacarbonyl Induced by Singly and Multiply Charged Ions and Implications for Focused Ion Beam-Induced Deposition. J. Phys. Chem. C **2019,** *123*, 10639-10645.
115. Thorman, R. M.; Matsuda, S. J.; McElwee-White, L.; Fairbrother, D. H., *Identifying and Rationalizing the Differing Surface Reactions of Low-Energy Electrons and Ions with an Organometallic Precursor*. The Journal of Physical Chemistry Letters **2020**, 2006-2013.
116. Bilgilisoy, E.; Thorman, R. M.; Yu, J.-C.; Dunn, T. B.; Marbach, H.; McElwee-White, L.; Fairbrother, D. H., *Surface Reactions of Low-Energy Argon Ions with Organometallic Precursors*. J. Phys. Chem. C **2020,** *124*, 24795-24808.
117. Giannuzzi, L. A. S. F. A., *Introduction to Focused Ion Beams*. Springer Science+Business Media, Inc., 2005.
118. Sigmund, P., *Mechanisms and Theory of Physical Sputtering by Particle Impact*. Nucl. Instrum. Methods Phys. Res., Sect. B **1987,** *27*, 1-20.
119. Dubner, A. D.; Wagner, A.; Melngailis, J.; Thompson, C. V., *The role of the Ion-Solid Interaction in Ion-Beam-Induced Deposition of Gold*. J. Appl. Phys. **1991,** *70*, 665-673.
120. Alkemade, P. F. A.; Chen, P.; Veldhoven, E. v.; Maas, D., *Model for Nanopillar Growth by Focused Helium Ion-Beam-Induced Deposition*. J. Vac. Sci. Technol. B **2010,** *28*, C6F22-C6F25.
121. Smith, D. A.; Joy, D. C.; Rack, P. D., *Monte Carlo Simulation of Focused Helium Ion Beam Induced Deposition*. Nanotechnology **2010,** *21*, 175302.
122. Volkert, C. A.; Minor, A. M., *Focused Ion Beam Microscopy and Micromachining*. MRS Bull. **2007,** *32*, 389-399.
123. Sakurai, M.; Nagano, S.; Joachim, C., *Local Heat Generated by a Focused He^+ Ion Beam*. Nanotechnology **2020,** *31*, 345708.
124. Myers, M. T.; Sencer, B. H.; Shao, L., *Multi-scale Modeling of Localized Heating Caused by Ion Bombardment*. Nucl. Instrum. Methods Phys. Res., Sect. B **2012,** *272*, 165-168.
125. Alkemade, P. F. A.; Miro, H., *Focused Helium-Ion-Beam-Induced Deposition*. Appl. Phys. A **2014,** *117*, 1727-1747.
126. Sanford, C. A.; Stern, L.; Barriss, L.; Farkas, L.; DiManna, M.; Mello, R.; Maas, D. J.; Alkemade, P. F. A., *Beam Induced Deposition of Platinum Using a Helium Ion Microscope*. J. Vac. Sci. Technol., B: Microelectron. Nanometer Struct.--Process., Meas., Phenom. **2009,** *27*, 2660-2667.
127. Allen, F. I., *Branched High Aspect Ratio Nanostructures Fabricated by Focused Helium Ion Beam Induced Deposition of an Insulator*. Micromachines **2021,** *12*, 232.
128. Belianinov, A.; Burch, M. J.; Ievlev, A.; Kim, S.; Stanford, M. G.; Mahady, K.; Lewis, B. B.; Fowlkes, J. D.; Rack, P. D.; Ovchinnikova, O. S., *Direct Write of 3D Nanoscale Mesh Objects with Platinum Precursor via Focused Helium Ion Beam Induced Deposition*. Micromachines **2020,** *11*.
129. Salvador-Porroche, A.; Sangiao, S.; Philipp, P.; Cea, P.; Teresa, J. M. D., *Optimization of Pt-C Deposits by Cryo-FIBID: Substantial Growth Rate Increase and Quasi-Metallic Behaviour*. Nanomaterials **2020,** *10*, 1906.
130. Porrati, F.; Jungwirth, F.; Barth, S.; Gazzadi, G. C.; Frabboni, S.; Dobrovolskiy, O. V.; Huth, M., *Highly-Packed Proximity-Coupled DC-Josephson Junction Arrays by a Direct-Write Approach*. Adv. Funct. Mater. **2022,** *5*, 2203889.
131. De Teresa, J. M.; Córdoba, R.; Fernández-Pacheco, A.; Montero, O.; Strichovanec, P.; Ibarra, M. R., *Origin of the Difference in the Resistivity of As-Grown Focused-Ion- and Focused-Electron-Beam-Induced Pt Nanodeposits*. J. Nanomater. **2009,** *2009*, 936863.
132. Hill, R.; Notte, J. A.; Scipioni, L., Scanning Helium Ion Microscopy. In *Advances in Imaging and Electron Physics*, Hawkes, P. W., Ed. Elsevier: 2012; Vol. 170, pp 65-148.
133. Gazzadi, G. C.; Mulders, J. J. L.; Trompenaars, P.; Ghirri, A.; Rota, A.; Affronte, M.; Frabboni, S., *Characterization of a New Cobalt Precursor for Focused Beam Deposition of Magnetic Nanostructures*. Microelectron. Eng. **2011,** *88*, 1955-1958.
134. Sanz-Martin, C.; Magen, C.; De Teresa, J. M., *High Volume-Per-Dose and Low Resistivity of Cobalt Nanowires Grown by Ga^+ Focused Ion Beam Induced Deposition*. Nanomaterials **2019,** *9*.

135. Chakraborti, H.; Joshi, B. P.; Barman, C. K.; Jain, A. K.; Pal, B.; Barik, B. C.; Maiti, T.; Schott, R.; Wieck, A. D.; Prasad, M. J. N. V.; Dhar, S.; Pal, H. K.; Alam, A.; Gupta, K. D., *Formation of Tungsten Carbide by Focused Ion Beam Process: A Route to High Magnetic Field Resilient Patterned Superconducting Nanostructures*. Appl. Phys. Lett. **2022,** *120*, 132601.
136. Salvador-Porroche, A.; Sangiao, S.; Magen, C.; Barrado, M.; Philipp, P.; Belotcerkovtceva, D.; Kamalakar, M. V.; Cea, P.; De Teresa, J. M., *Highly-Efficient Growth of Cobalt Nanostructures Using Focused Ion Beam Induced Deposition Under Cryogenic Conditions: Application to Electrical Contacts on Graphene, Magnetism and Hard Masking*. Nanoscale Adv. **2021,** *3*, 5656-5662.
137. Faraby, H.; DiBattista, M.; Bandaru, P. R., *Percolation of Gallium Dominates the Electrical Resistance of Focused Ion Beam Deposited Metals*. Appl. Phys. Lett. **2014,** *104*, 173107.
138. Faraby, H.; DiBattista, M.; Bandaru, P. R., *Reduced Electrical Impedance of SiO_2, Deposited through Focused Ion Beam Based Systems, due to Impurity Percolation*. J. Appl. Phys. **2014,** *116*, 204301.
139. Shorubalko, I.; Pillatsch, L.; Utke, I., Direct–Write Milling and Deposition with Noble Gases. In *Helium Ion Microscopy*, Hlawacek, G.; Gölzhäuser, A., Eds. Springer International Publishing: Cham, 2016; pp 355-393.
140. Ziegler, J. F.; Ziegler, M. D.; Biersack, J. P., *SRIM – The Stopping and Tange of Ions in Matter*. Nucl. Instrum. Methods Phys. Res., Sect. B **2010,** *268*, 1818-1823.
141. Drouin, D.; Couture, A. R.; Joly, D.; Tastet, X.; Aimez, V.; Gauvin, R., *CASINO V2.42—A Fast and Easy-to-use Modeling Tool for Scanning Electron Microscopy and Microanalysis Users*. Scanning **2007,** *29*, 92-101.
142. Mond, L.; Langer, C.; Quincke, F., *Action of Carbon Monoxide on Nickel*. J. Chem. Soc., Trans. **1890,** *57*, 749-753.
143. Choy, K. L., *Chemical Vapour Deposition of Coatings*. Prog. Mater Sci. **2003,** *48*, 57-170.
144. Barth, S.; Jimenez-Diaz, R.; Samà, J.; Daniel Prades, J.; Gracia, I.; Santander, J.; Cane, C.; Romano-Rodriguez, A., *Localized Growth and in Situ Integration of Nanowires for Device Applications*. Chem. Commun. **2012,** *48*, 4734-4736.
145. Hrachowina, L.; Domènech-Gil, G.; Pardo, A.; Seifner, M. S.; Gràcia, I.; Cané, C.; Romano-Rodríguez, A.; Barth, S., *Site-Specific Growth and in Situ Integration of Different Nanowire Material Networks on a Single Chip: Toward a Nanowire-Based Electronic Nose for Gas Detection*. ACS Sensors **2018,** *3*, 727-734.
146. Fauteux, C.; Pegna, J., *Radial Characterization of 3D-LCVD Carbon Fibers by Raman Spectroscopy*. Appl. Phys. A **2004,** *78*, 883-888.
147. Li, Y.; Ruan, W.; Wang, Z., *Localized Synthesis of Carbon Nanotube Films on Suspended Microstructures by Laser-Assisted Chemical Vapor Deposition*. IEEE Transactions on Nanotechnology **2013,** *12*, 352-360.
148. Utke, I.; Swiderek, P.; Höflich, K.; Madajska, K.; Jurczyk, J.; Martinović, P.; Szymańska, I. B., *Coordination and Organometallic Precursors of Group 10 and 11: Focused Electron Beam Induced Deposition of Metals and Insight Gained from Chemical Vapour Deposition, Atomic Layer Deposition, and Fundamental Surface and Gas Phase Studies*. Coord. Chem. Rev. **2022**, 213851.
149. Orús, P.; Córdoba, R.; De Teresa, J. M., *Focused Ion Beam Induced Processing*. In *Nanofabrication*, IOP Publishing: 2020; pp 5-1-5-58.
150. Sato, T.; Mitsui, M.; Yamanaka, J.; Nakagawa, K.; Aoki, Y.; Sato, S.; Miyata, C., *Formation of Microcrystalline Silicon and SiN_x Films by Electron-Beam-Induced-Chemical Vapor Deposition at Ultra Low Temperature*. Thin Solid Films **2006,** *508*, 61-64.
151. Ketharanathan, S.; Sharma, R.; Crozier, P. A.; Drucker, J., *Electron Beam Induced Deposition of Pure, Nanoscale Ge*. J. Vac. Sci. Technol., B: Microelectron. Nanometer Struct.--Process., Meas., Phenom. **2006,** *24*, 678-681.

152. Perentes, A.; Hoffmann, P., *Focused Electron Beam Induced Deposition of Si-Based Materials From SiO_xC_y to Stoichiometric SiO_2: Chemical Compositions, Chemical-Etch Rates, and Deep Ultraviolet Optical Transmissions*. Chem. Vap. Deposition **2007,** *13*, 176-184.
153. Funsten, H. O.; Boring, J. W.; Johnson, R. E.; Brown, W. L., *Low-Temperature Beam-Induced Deposition of Thin Tin Films*. J. Appl. Phys. **1992,** *71*, 1475-1484.
154. Weirich, P. M.; Schwalb, C. H.; Winhold, M.; Huth, M., *Superconductivity in the System $Mo_xC_yGa_zO_\delta$ Prepared by Focused Ion Beam Induced Deposition*. J. Appl. Phys. **2014,** *115*, 174315.
155. Winhold, M.; Weirich, P. M.; Schwalb, C. H.; Huth, M., *Superconductivity and Metallic Behavior in $Pb_xC_yO_\delta$ Structures Prepared by Focused Electron Beam Induced Deposition*. Appl. Phys. Lett. **2014,** *105*, 162603.
156. Elbadawi, C.; Toth, M.; Lobo, C. J., *Pure Platinum Nanostructures Grown by Electron Beam Induced Deposition*. ACS Appl. Mater. Interfaces **2013,** *5*, 9372-9376.
157. Wang, S.; Sun, Y. M.; Wang, Q.; White, J. M., *Electron-Beam Induced Initial Growth of Platinum Films using $Pt(PF_3)_4$*. J. Vac. Sci. Technol., B: Microelectron. Nanometer Struct.--Process., Meas., Phenom. **2004,** *22*, 1803-1806.
158. O'Regan, C.; Lee, A.; Holmes, J. D.; Petkov, N.; Trompenaars, P.; Mulders, H., *Electrical Properties of Platinum Interconnects Deposited by Electron Beam Induced Deposition of the Carbon-Free Precursor, $Pt(PF_3)_4$*. J. Vac. Sci. Technol. B **2013,** *31*, 021807.
159. Perentes, A.; Sinicco, G.; Boero, G.; Dwir, B.; Hoffmann, P., *Focused Electron Beam Induced Deposition of Nickel*. J. Vac. Sci. Technol., B: Microelectron. Nanometer Struct.--Process., Meas., Phenom. **2007,** *25*, 2228-2232.
160. Shimojo, M.; Bysakh, S.; Mitsuishi, K.; Tanaka, M.; Song, M.; Furuya, K., *Selective Growth and Characterization of Nanostructures with Transmission Electron Microscopes*. Appl. Surf. Sci. **2005,** *241*, 56-60.
161. Macaulay, J. M.; Allen, R. M.; Brown, L. M.; Berger, S. D., *Nanofabrication Using Inorganic Resists*. Microelectron. Eng. **1989,** *9*, 557-560.
162. Christy, R. W., *Conducting Thin Films Formed by Electron Bombardment of Substrate*. J. Appl. Phys. **1962,** *33*, 1884-1888.
163. Kim, S. H.; Somorjai, G. A., *Stereospecific Ziegler−Natta Model Catalysts Produced by Electron Beam-Induced Deposition of $TiCl_4$: Deposition Kinetics, Film Structure, and Surface Structure*. J. Phys. Chem. B **2002,** *106*, 1386-1391.
164. Bell, D. A.; Falconer, J. L.; Lü, Z.; McConica, C. M., *Electron Beam-Induced Deposition of Tungsten*. J. Vac. Sci. Technol., B: Microelectron. Nanometer Struct.--Process., Meas., Phenom. **1994,** *12*, 2976-2979.
165. Welipitiya, D.; Green, A.; Woods, J. P.; Dowben, P. A.; Robertson, B. W.; Byun, D.; Zhang, J., *Ultraviolet and Electron Radiation Induced Fragmentation of Adsorbed Ferrocene*. J. Appl. Phys. **1996,** *79*, 8730-8734.
166. Svensson, K.; Bedson, T. R.; Palmer, R. E., *Dissociation and Desorption of Ferrocene on Graphite by Low Energy Electron Impact*. Surf. Sci. **2000,** *451*, 250-254.
167. Casey, C. P.; O'Connor, J. M.; Haller, K. J., *Interconversions of η^5-C_5H_5, η^1-C_5H_5, and ionic "η^0"-C_5H_5 Rhenium Compounds - X-Ray Crystal Structure of $[Re(NO)(CH_3)PMe_3)_4]^+[C_5H_5]^-$*. J. Am. Chem. Soc. **1985,** *107*, 1241-1246.
168. Matsui, S.; Mori, K., *New Selective Deposition Technology by Electron-Beam Induced Surface Reaction*. J. Vac. Sci. Technol., B: Microelectron. Process. Phenom. **1986,** *4*, 299-304.
169. Kopyra, J.; Maciejewska, P.; Maljković, J., *Dissociative Electron Attachment to Coordination Complexes of Chromium: Chromium(0) Hexacarbonyl and Benzene-Chromium(0) Tricarbonyl*. Beilstein J. Nanotechnol. **2017,** *8*, 2257-2263.
170. Khvostenko, V. I.; Nekrasov, Y. S.; Furley, I. I.; Vasyukova, N. I.; Tolstikov, G. A., *Mass Spectrometry of π-Complexes of Transition Metals: XXV. Dissociative Electron Capture by Molecule π-Arenechromium Tricarbonyl Complexes*. J. Organomet. Chem. **1981,** *212*, 369-372.
171. Ramsier, R. D.; Yates, J. T., *Thermal and Electron-Induced Behavior of d_6-Benzene-Chromium-Tricarbonyl Adsorbed on Ag(111)*. Surf. Sci. **1993,** *289*, 39-46.

172. Jurczyk, J.; Brewer, C. R.; Hawkins, O. M.; Polyakov, M. N.; Kapusta, C.; McElwee-White, L.; Utke, I., *Focused Electron Beam-Induced Deposition and Post-Growth Purification Using the Heteroleptic Ru Complex (η^3-C_3H_5)Ru(CO)$_3$Br*. ACS Appl. Mater. Interfaces **2019,** *11*, 28164-28171.
173. Miyazoe, H.; Utke, I.; Kikuchi, H.; Kiriu, S.; Friedli, V.; Michler, J.; Terashima, K., *Improving the Metallic Content of Focused Electron Beam-Induced Deposits by a Scanning Electron Microscope Integrated Hydrogen-Argon Microplasma Generator*. J. Vac. Sci. Technol. B **2010,** *28*, 744-750.
174. Luisier, A.; Utke, I.; Bret, T.; Cicoira, F.; Hauert, R.; Rhee, S.-W.; Doppelt, P.; Hoffmann, P., *Comparative Study of Cu-Precursors for 3D Focused Electron Beam Induced Deposition*. J. Electrochem. Soc. **2004,** *151*, C590-C593.
175. Hoflich, K.; Jurczyk, J.; Zhang, Y. C.; dos Santos, M. V. P.; Gotz, M.; Guerra-Nunez, C.; Best, J. P.; Kapusta, C.; Utke, I., *Direct Electron Beam Writing of Silver-Based Nanostructures*. ACS Appl. Mater. Interfaces **2017,** *9*, 24071-24077.
176. Lacko, M.; Papp, P.; Szymańska, I. B.; Szłyk, E.; Matejčík, Š., *Electron Interaction with Copper(II) Carboxylate Compounds*. Beilstein J. Nanotechnol. **2018,** *9*, 384-398.
177. Fahlman, B. D.; Barron, A. R., *Substituent Effects on the Volatility of Metal β-Diketonates*. Adv. Mater. Opt. Electron. **2000,** *10*, 223-232.
178. Szkudlarek, A.; Rodrigues Vaz, A.; Zhang, Y.; Rudkowski, A.; Kapusta, C.; Erni, R.; Moshkalev, S.; Utke, I., *Formation of Pure Cu Nanocrystals Upon Post-Growth Annealing of Cu–C Material Obtained from Focused Electron Beam Induced Deposition: Comparison of Different Methods*. Beilstein J. Nanotechnol. **2015,** *6*, 1508-1517.
179. Mansilla, C.; Zondag, Y.; Mulders, J. J. L.; Trompenaars, P. H. F., *Comparison of Pd Electron Beam Induced Deposition using Two Precursors and an Oxygen Purification Strategy*. Nanotechnology **2017,** *28*.
180. Spoddig, D.; Schindler, K.; Rödiger, P.; Barzola-Quiquia, J.; Fritsch, K.; Mulders, H.; Esquinazi, P., *Transport Properties and Growth Parameters of PdC and WC Nanowires Prepared in a Dual-Beam Microscope*. Nanotechnology **2007,** *18*, 495202.
181. Berger, L.; Jurczyk, J.; Madajska, K.; Edwards, T. E. J.; Szymańska, I.; Hoffmann, P.; Utke, I., *High-Purity Copper Structures from a Perfluorinated Copper Carboxylate Using Focused Electron Beam Induced Deposition and Post-Purification*. ACS Appl. Electron. Mater. **2020,** *2*, 1989-1996.
182. Höflich, K.; Jurczyk, J. M.; Madajska, K.; Götz, M.; Berger, L.; Guerra-Nuñez, C.; Haverkamp, C.; Szymanska, I.; Utke, I., *Towards the Third Dimension in Direct Electron Beam Writing of Silver*. Beilstein J. Nanotechnol. **2018,** *9*, 842-849.
183. Martinović, P.; Rohdenburg, M.; Butrymowicz, A.; Sarigül, S.; Huth, P.; Denecke, R.; Szymańska, I. B.; Swiderek, P., *Electron-Induced Decomposition of Different Silver(I) Complexes: Implications for the Design of Precursors for Focused Electron Beam Induced Deposition*. Nanomaterials **2022,** *12*, 1687.
184. Jurczyk, J.; Pillatsch, L.; Berger, L.; Priebe, A.; Madajska, K.; Kapusta, C.; Szymańska, I. B.; Michler, J.; Utke, I., *In Situ Time-of-Flight Mass Spectrometry of Ionic Fragments Induced by Focused Electron Beam Irradiation: Investigation of Electron Driven Surface Chemistry inside an SEM under High Vacuum*. Nanomaterials **2022,** *12*, 2710.
185. Weitzer, A.; Huth, M.; Kothleitner, G.; Plank, H., *Expanding FEBID-Based 3D-Nanoprinting toward Closed High-Fidelity Nanoarchitectures*. ACS Appl. Electron. Mater. **2022,** *4*, 744-754.
186. Plank, H.; Gspan, C.; Dienstleder, M.; Kothleitner, G.; Hofer, F., *The Influence of Beam Defocus on Volume Growth Rates for Electron Beam Induced Platinum Deposition*. Nanotechnology **2008,** *19*, 485302.
187. Botman, A.; Mulders, J. J. L.; Weemaes, R.; Mentink, S., *Purification of Platinum and Gold Structures after Electron-Beam-Induced Deposition*. Nanotechnology **2006,** *17*, 3779-3785.
188. Schwalb, C. H.; Grimm, C.; Baranowski, M.; Sachser, R.; Porrati, F.; Reith, H.; Das, P.; Müller, J.; Völklein, F.; Kaya, A.; Huth, M., *A Tunable Strain Sensor Using Nanogranular Metals*. Sensors **2010,** *10*, 9847-9856.

189. Sachser, R.; Porrati, F.; Schwalb, C. H.; Huth, M., *Universal Conductance Correction in a Tunable Strongly Coupled Nanogranular Metal*. Phys. Rev. Lett. **2011,** *107*, 206803.
190. Langford, R. M.; Wang, T. X.; Ozkaya, D., *Reducing the Resistivity of Electron and Ion Beam Assisted Deposited Pt*. Microelectron. Eng. **2007,** *84*, 784-788.
191. Warneke, Z.; Rohdenburg, M.; Warneke, J.; Kopyra, J.; Swiderek, P., *Electron-Driven and Thermal Chemistry During Water-Assisted Purification of Platinum Nanomaterials Generated by Electron Beam Induced Deposition*. Beilstein J. Nanotechnol. **2018,** *9*, 77-90.
192. Hernandez-Ramirez, F.; Tarancon, A.; Casals, O.; Pellicer, E.; Rodriguez, J.; Romano-Rodriguez, A.; Morante, J. R.; Barth, S.; Mathur, S., *Electrical Properties of Individual Tin Oxide Nanowires Contacted to Platinum Electrodes*. Phys. Rev. B **2007,** *76*, 085429.
193. Burnett, T. L.; Kelley, R.; Winiarski, B.; Contreras, L.; Daly, M.; Gholinia, A.; Burke, M. G.; Withers, P. J., *Large Volume Serial Section Tomography by Xe Plasma FIB Dual Beam Microscopy*. Ultramicroscopy **2016,** *161*, 119-129.
194. Nanda, G.; Veldhoven, E. v.; Maas, D.; Sadeghian, H.; Alkemade, P. F. A., *Helium Ion Beam Induced Growth of Hammerhead AFM Probes*. J. Vac. Sci. Technol. B **2015,** *33*, 06F503.
195. Fernández-Pacheco, A.; De Teresa, J. M.; Córdoba, R.; Ibarra, M. R., *Metal-Insulator Transition in Pt-C Nanowires Grown by Focused-Ion-Beam-Induced Deposition*. Phys. Rev. B **2009,** *79*, 174204.
196. Porrati, F.; Pohlit, M.; Muller, J.; Barth, S.; Biegger, F.; Gspan, C.; Plank, H.; Huth, M., *Direct Writing of CoFe Alloy Nanostructures by Focused Electron Beam Induced Deposition from a Heteronuclear Precursor*. Nanotechnology **2015,** *26*.
197. Porrati, F.; Barth, S.; Sachser, R.; Jungwirth, F.; Eltsov, M.; Frangakis, A. S.; Huth, M., *Binary Mn–Si Nanostructures Prepared by Focused Electron Beam Induced Deposition from the Precursor $SiH_3Mn(CO)_5$*. J. Phys. D: Appl. Phys. **2018,** *51*, 455301.
198. Jungwirth, F.; Porrati, F.; Schuck, A. G.; Huth, M.; Barth, S., *Direct Writing of Cobalt Silicide Nanostructures Using Single-Source Precursors*. ACS Appl. Mater. Interfaces **2021,** *13*, 48252-48259.
199. Gavagnin, M.; Wanzenboeck, H. D.; Belic, D.; Shawrav, M. M.; Persson, A.; Gunnarsson, K.; Svedlindh, P.; Bertagnolli, E., *Magnetic Force Microscopy Study of Shape Engineered FEBID Iron Nanostructures*. Phys. Status Solidi A **2014,** *211*, 368-374.
200. Utke, I.; Friedli, V.; Michler, J.; Bret, T.; Multone, X.; Hoffmann, P., *Density Determination of Focused-Electron-Beam-Induced Deposits with Simple Cantilever-based Method*. Appl. Phys. Lett. **2006,** *88*, 031906.
201. Rodríguez, L. A.; Deen, L.; Córdoba, R.; Magén, C.; Snoeck, E.; Koopmans, B.; De Teresa, J. M., *Influence of the Shape and Surface Oxidation in the Magnetization Reversal of Thin Iron Nanowires Grown by Focused Electron Beam Induced Deposition*. Beilstein J. Nanotechnol. **2015,** *6*, 1319-1331.
202. Sadki, E. S.; Ooi, S.; Hirata, K., *Focused-Ion-Beam-Induced Deposition of Superconducting Nanowires*. Appl. Phys. Lett. **2004,** *85*, 6206-6208.
203. Córdoba, R.; Orús, P.; Jelić, Ž. L.; Sesé, J.; Ibarra, M. R.; Guillamón, I.; Vieira, S.; Palacios, J. J.; Suderow, H.; Milosević, M. V.; De Teresa, J. M., *Long-Range Vortex Transfer in Superconducting Nanowires*. Sci. Rep. **2019,** *9*, 12386.
204. Liu, X.; Ellis, J. E.; Mesaros, E. F.; Pearson, A. J.; Schoffers, E.; Hall, J. M.; Hoyne, J. H.; Shapley, J. R.; Fauré, M.; Saccavini, C.; Lavigne, G.; Chi, Y.; Liu, C.-S.; Lai, Y.-H.; Carty, A. J.; Serp, P.; Hernandez, M.; Kalck, P.; Richard, B.; Hernandez-Gruel, M. A. F.; Pérez-Torrente, J. J.; Ciriano, M. A.; Oro, L. A., Transition Metal Carbonyl Compounds. In *Inorg. Synth.*, 2004; pp 96-132.
205. Shufler, S. L.; Sternberg, H. W.; Friedel, R. A., *Infrared Spectrum and Structure of Chromium Hexacarbonyl, $Cr(CO)_6$*. J. Am. Chem. Soc. **1956,** *78*, 2687-2688.
206. Huth, M.; Gruszka, P., *unpublished results*
207. Haas, H.; Sheline, R. K., *Analysis of the Infrared Spectra of Metal Carbonyls*. J. Chem. Phys. **1967,** *47*, 2996-3021.

208. Weber, M.; Koops, H. W. P.; Rudolph, M.; Kretz, J.; Schmidt, G., *New Compound Quantum Dot Materials Produced by Electron-Beam Induced Deposition*. J. Vac. Sci. Technol., B: Microelectron. Nanometer Struct.--Process., Meas., Phenom. **1995,** *13*, 1364-1368.
209. Shih, P.-Y.; Cipriani, M.; Hermanns, C. F.; Oster, J.; Edinger, K.; Gölzhäuser, A.; Ingólfsson, O., *Low-Energy Electron Interaction and Focused Electron Beam-Induced Deposition of Molybdenum Hexacarbonyl ($Mo(CO)_6$)*. Beilstein J. Nanotechnol. **2022,** *13*, 182-191.
210. Sheline, R. K., *The Infrared Spectrum and Structure of Tungsten Carbonyl*. J. Am. Chem. Soc. **1950,** *72*, 5761-5762.
211. Gavagnin, M.; Wanzenboeck, H. D.; Belić, D.; Bertagnolli, E., *Synthesis of Individually Tuned Nanomagnets for Nanomagnet Logic by Direct Write Focused Electron Beam Induced Deposition*. ACS Nano **2013,** *7*, 777-784.
212. Adams, D. M.; Taylor, I. D., *Solid-State Metal Carbonyls. Part 3.—An infrared study of $Fe_2(CO)_9$, tri-μ-carbonyl(hexacarbonyl)di-iron(0)*. J. Chem. Soc., Faraday Trans. 2 **1982,** *78*, 1551-1559.
213. Bor, G., *Infrared Spectroscopic Studies on Metal Carbonyl Compounds- Assignment of the Totally Symmetric C-O Stretching Bands of the Metal Carbonyls, with Special Respect to the Spectra of Tetracobalt-Dodekacarbonyl and Dicobalt-Octacarbonyl*. Spectrochim. Acta **1963,** *19*, 1209-1224.
214. Utke, I.; Bret, T.; Laub, D.; Buffat, P.; Scandella, L.; Hoffmann, P., *Thermal Effects During Focused Electron Beam Induced Deposition of Nanocomposite Magnetic-Cobalt-Containing Tips*. Microelectron. Eng. **2004,** *73-74*, 553-558.
215. Nikulina, E.; Idigoras, O.; Vavassori, P.; Chuvilin, A.; Berger, A., *Magneto-Optical Magnetometry of Individual 30 nm Cobalt Nanowires Grown by Electron Beam Induced Deposition*. Appl. Phys. Lett. **2012,** *100*, 142401.
216. Andreoni, W.; Varma, C. M., *Binding and Dissociation of CO on Transition-Metal Surfaces*. Phys. Rev. B **1981,** *23*, 437-444.
217. Broden, G.; Rhodin, T. N.; Brucker, C.; Benbow, R.; Hurych, Z., *Synchrotron Radiation Study of Chemisorptive Bonding of CO on Transition Metals — Polarization Effect on Ir(100)*. Surf. Sci. **1976,** *59*, 593-611.
218. Fielicke, A.; Gruene, P.; Meijer, G.; Rayner, D. M., *The Adsorption of CO on Transition Metal Clusters: A Case Study of Cluster Surface Chemistry*. Surf. Sci. **2009,** *603*, 1427-1433.
219. Sung, S. S.; Hoffmann, R., *How Carbon Monoxide Bonds to Metal Surfaces*. J. Am. Chem. Soc. **1985,** *107*, 578-584.
220. Elschenbroich, C., *Organometallchemie*. 2008.
221. Lacko, M.; Papp, P.; Wnorowski, K.; Matejčík, Š., *Electron-Induced Ionization and Dissociative Ionization of Iron Pentacarbonyl Molecules*. Eur. Phys. J. D **2015,** *69*, 84.
222. Wnorowski, K.; Stano, M.; Barszczewska, W.; Jówko, A.; Matejčík, Š., *Electron Ionization of $W(CO)_6$: Appearance Energies*. Int. J. Mass spectrom. **2012,** *314*, 42-48.
223. Belova, L. M.; Dahlberg, E. D.; Riazanova, A.; Mulders, J. J. L.; Christophersen, C.; Eckert, J., *Rapid Electron Beam Assisted Patterning of Pure Cobalt at Elevated Temperatures via Seeded Growth*. Nanotechnology **2011,** *22*, 145305.
224. Greiner, D.; Lauche, J.; Heinemann, M. D.; Hinrichs, V.; Stange, H.; Navirian, H. A.; Kalus, C.; Schlatmann, R.; Kaufmann, C. A. In *Influence of Residual Gas Composition and Background Pressure in a Multi-Stage Co-Evaporation Chamber on the Quality of Cu(In, Ga)Se_2 Thin Films and their Device Performance*, 2016 IEEE 43rd Photovoltaic Specialists Conference (PVSC), 5-10 June 2016; 2016; pp 1151-1156.
225. Valdrè, U.; Robinson, E. A.; Pashley, D. W.; Stowell, M. J.; Law, T. J., *An Ultra-High Vacuum Electron Microscope Specimen Chamber for Vapour Deposition Studies*. J. Phys. E: Sci. Instrum. **1970,** *3*, 501-506.
226. Lavrijsen, R.; Córdoba, R.; Schoenaker, F. J.; Ellis, T. H.; Barcones, B.; Kohlhepp, J. T.; Swagten, H. J. M.; Koopmans, B.; De Teresa, J. M.; Magén, C.; Ibarra, M. R.; Trompenaars, P.; Mulders, J. J. L., *Fe:O:C Grown by Focused-Electron-Beam-Induced Deposition: Magnetic and Electric Properties*. Nanotechnology **2010,** *22*, 025302.

227. Israelachvili, J. N.; Pashley, R. M., *Molecular Layering of Water at Surfaces and Origin of Repulsive Hydration Forces*. Nature **1983,** *306*, 249-250.
228. Antognozzi, M.; Humphris, A. D. L.; Miles, M. J., *Observation of Molecular Layering in a Confined Water Film and Study of the Layers Viscoelastic Properties*. Appl. Phys. Lett. **2001,** *78*, 300-302.
229. Park, J. H.; Aluru, N. R., *Diffusion of Water Submonolayers on Hydrophilic Surfaces*. Appl. Phys. Lett. **2008,** *93*, 253104.
230. Winhold, M.; Schwalb, C. H.; Porrati, F.; Sachser, R.; Frangakis, A. S.; Kämpken, B.; Terfort, A.; Auner, N.; Huth, M., *Binary Pt–Si Nanostructures Prepared by Focused Electron-Beam-Induced Deposition*. ACS Nano **2011,** *5*, 9675-9681.
231. Porrati, F.; Begun, E.; Winhold, M.; Schwalb, C. H.; Sachser, R.; Frangakis, A. S.; Huth, M., *Room Temperature $L1_0$ Phase Transformation in Binary CoPt Nanostructures Prepared by Focused-Electron-Beam-Induced Deposition*. Nanotechnology **2012,** *23*, 185702.
232. Porrati, F.; Kämpken, B.; Terfort, A.; Huth, M., *Fabrication and Electrical Transport Properties of Binary Co-Si Nanostructures Prepared by Focused Electron Beam-Induced Deposition*. J. Appl. Phys. **2013,** *113*, 053707.
233. Kakefuda, Y.; Yamashita, Y.; Mukai, K.; Yoshinobu, J., *Fabrication and Analysis of Buried Iron Silicide Microstructures Using a Focused Low Energy Electron Beam*. Surf. Sci. **2007,** *601*, 5108-5111.
234. Al Mamoori, M.; Keller, L.; Pieper, J.; Barth, S.; Winkler, R.; Plank, H.; Müller, J.; Huth, M., *Magnetic Characterization of Direct-Write Free-Form Building Blocks for Artificial Magnetic 3D Lattices*. Materials **2018,** *11*, 289.
235. Kumar, R. T. P.; Bjornsson, R.; Barth, S.; Ingólfsson, O., *Formation and Decay of Negative Ion States up to 11 eV Above the Ionization Energy of the Nanofabrication Precursor $HFeCo_3(CO)_{12}$*. Chem. Sci. **2017,** *8*, 5949-5952.
236. Rowntree, P.; Dugal, P. C.; Hunting, D.; Sanche, L., *Electron Stimulated Desorption of H_2 from Chemisorbed Molecular Monolayers*. J. Phys. Chem. **1996,** *100*, 4546-4550.
237. Wnuk, J. D.; Gorham, J. M.; Rosenberg, S. G.; van Dorp, W. F.; Madey, T. E.; Hagen, C. W.; Fairbrother, D. H., *Electron Induced Surface Reactions of the Organometallic Precursor Trimethyl(methylcyclopentadienyl)platinum(IV)*. J. Phys. Chem. C **2009,** *113*, 2487-2496.
238. Luo, Y.-R., *Comprehensive Handbook of Chemical Bond Energies*. Taylor & Francis, 2007.
239. Moltved, K. A.; Kepp, K. P., *The Chemical Bond between Transition Metals and Oxygen: Electronegativity, d-Orbital Effects, and Oxophilicity as Descriptors of Metal–Oxygen Interactions*. J. Phys. Chem. C **2019,** *123*, 18432-18444.
240. Burroughs, J. A.; Hanley, L., *Molecular Ion Modification of a Hexanethiolate Self-Assembled Monolayer during Surface-Induced Dissociation*. Anal. Chem. **1994,** *66*, 3644-3650.
241. Pelleg, J., *Mechanical Properties of Silicon Based Compounds: Silicides*. SPRINGER NATURE, 2020.
242. Murarka, S. P., *Refractory Silicides for Integrated Circuits*. Journal of Vacuum Science and Technology **1980,** *17*, 775-792.
243. Murarka, S. P., *Silicide Thin Films and their Applications in Microelectronics*. Intermetallics **1995,** *3*, 173-186.
244. Goldfarb, I.; Cesura, F.; Dascalu, M., *Magnetic Binary Silicide Nanostructures*. Adv. Mater. **2018,** *30*, 1800004.
245. Cabanski, W. A.; Schulz, M. J., *Electronic and IR-Optical Properties of Silicide/Silicon Interfaces*. Infrared Phys. **1991,** *32*, 29-44.
246. Kieffer, R.; Benesovsky, F., *Hartmetalle*. Springer-Verlag, 1963.
247. Chen, X.; Liang, C., *Transition metal Silicides: Fundamentals, Preparation and Catalytic Applications*. Catal. Sci. Technol. **2019,** *9*, 4785-4820.
248. Chi, D. Z., *Semiconducting beta-Phase $FeSi_2$ for Light Emitting Diode Applications: Recent Developments, Challenges, and Solutions*. Thin Solid Films **2013,** *537*, 1-22.
249. Szypryt, P.; Meeker, S. R.; Coiffard, G.; Fruitwala, N.; Bumble, B.; Ulbricht, G.; Walter, A. B.; Daal, M.; Bockstiegel, C.; Collura, G.; Zobrist, N.; Lipartito, I.; Mazin, B. A., *Large-Format*

Platinum Silicide Microwave Kinetic Inductance Detectors for Optical to Near-IR Sstronomy. Opt. Express **2017,** *25*, 25894-25909.
250. Baker, H., *ASM handbook.* ASM International, 1997; Vol. 3.
251. Gokhale, A. B.; Abbaschian, G. J., *The Cr−Ge (Chromium-Germanium) System*. Bulletin of Alloy Phase Diagrams **1986,** *7*, 477-485.
252. Okamoto, H., *Si-Y (Silicon-Yttrium)*. J. Phase Equilib. Diffus. **2011,** *32*, 475.
253. Okamoto, H., *Mo-Si (Molybdenum-Silicon)*. J. Phase Equilib. Diffus. **2011,** *32*, 176-176.
254. Guo, Z.; Yuan, W.; Sun, Y.; Cai, Z.; Qiao, Z., *Thermodynamic Assessment of the Si-Ta and Si-W Systems*. J. Phase Equilib. Diffus. **2009,** *30*, 564.
255. Okamoto, H., *Ru−Si (Ruthenium-Silicon)*. J. Phase Equilib. Diffus. **2006,** *27*, 203-203.
256. Schellenberg, L.; Jorda, J. L.; Muller, J., *The Rhodium-Silicon Phase Diagram*. Journal of the Less Common Metals **1985,** *109*, 261-274.
257. Okamoto, H., *Ir-Si (Iridium-Silicon)*. J. Phase Equilib. Diffus. **2007,** *28*, 495-495.
258. Okamoto, H., *Cu-Si (Copper-Silicon)*. J. Phase Equilib. Diffus. **2012,** *33*, 415-416.
259. Gokhale, A. B.; Abbaschian, R., *The Mn-Si (Manganese-Silicon) System*. J. Phase Equilib. **1990,** *11*, 468-480.
260. Karpinskii, O.; Evseev, B., *Izv. Akad. Nauk SSSR*. Neorg. Mater. **1969,** *5*, 525.
261. Schwomma, O.; Preisinger, A.; Nowotny, H.; Wittmann, A., *Die Kristallstruktur von $Mn_{11}Si_{19}$ und deren Zusammenhang mit Disilicid-Typen*. Monatsh. Chem. **1964,** *95*, 1527-1537.
262. Knott, H. W.; Mueller, M. H.; Heaton, L., *The Crystal Structure of $Mn_{15}Si_{26}$*. Acta Crystallogr. **1967,** *23*, 549-555.
263. Zwilling, G.; Nowotny, H., *Zur Struktur der Defekt-Mangansilicide Kristallstruktur von $Mn_{27}Si_{47}$*. Monatsh. Chemie **1973,** *104*, 668-675.
264. Fredrickson, D. C.; Lee, S.; Hoffmann, R.; Lin, J., *The Nowotny Chimney Ladder Phases: Following the cpseudo Clue toward an Explanation of the 14 Electron Rule*. Inorg. Chem. **2004,** *43*, 6151-6158.
265. Higgins, J. M.; Schmitt, A. L.; Guzei, I. A.; Jin, S., *Higher Manganese Silicide Nanowires of Nowotny Chimney Ladder Phase*. J. Am. Chem. Soc. **2008,** *130*, 16086-16094.
266. Allam, A.; Nunes, C. A.; Zalesak, J.; Record, M.-C., *On the Stability of the Higher Manganese Silicides*. J. Alloys Compd. **2012,** *512*, 278-281.
267. Allam, A.; Boulet, P.; Nunes, C. A.; Record, M.-C., *Investigation of New Routes for the Synthesis of Mn_4Si_7*. Metall. Mater. Trans. A **2013,** *44*, 1645-1650.
268. Higgins, J. M.; Ding, R.; DeGrave, J. P.; Jin, S., *Signature of Helimagnetic Ordering in Single-Crystal MnSi Nanowires*. Nano Lett. **2010,** *10*, 1605-1610.
269. Mühlbauer, S.; Binz, B.; Jonietz, F.; Pfleiderer, C.; Rosch, A.; Neubauer, A.; Georgii, R.; Böni, P., *Skyrmion Lattice in a Chiral Magnet*. Science **2009,** *323*, 915-919.
270. Fert, A.; Cros, V.; Sampaio, J., *Skyrmions on the Track*. Nat. Nanotechnol. **2013,** *8*, 152-156.
271. Pokhrel, A.; Degregorio, Z. P.; Higgins, J. M.; Girard, S. N.; Jin, S., *Vapor Phase Conversion Synthesis of Higher Manganese Silicide ($MnSi_{1.75}$) Nanowire Arrays for Thermoelectric Applications*. Chem. Mater. **2013,** *25*, 632-638.
272. Pathak, R.; Balasubramanian, B.; Sellmyer, D. J.; Skomski, R.; Kashyap, A., *Magnetocrystalline Anisotropy of Co_3Si (001) Films from First Principles*. AIP Advances **2019,** *9*, 035128.
273. Ishida, K.; Nishizawa, T.; Schlesinger, M. E., *The Co-Si (Cobalt-Silicon) System*. J. Phase Equilib. **1991,** *12*, 578-586.
274. Balasubramanian, B.; Manchanda, P.; Skomski, R.; Mukherjee, P.; Das, B.; George, T. A.; Hadjipanayis, G. C.; Sellmyer, D. J., *Unusual Spin Correlations in a Nanomagnet*. Appl. Phys. Lett. **2015,** *106*, 242401.
275. Balasubramanian, B.; Manchanda, P.; Skomski, R.; Mukherjee, P.; Valloppilly, S. R.; Das, B.; Hadjipanayis, G. C.; Sellmyer, D. J., *High-Coercivity Magnetism in Nanostructures with Strong Easy-Plane Anisotropy*. Appl. Phys. Lett. **2016,** *108*, 152406.
276. Frolov, A. A.; Krentsis, R. P.; Sidorenko, F. A.; Gel'd, P. V., *Some Physical Properties of Co_2Si and Ni_2Si in the 10–350 K temperature range*. Russ. Phys. J. **1972,** *15*, 418-420.

277. Bormio-Nunes, C.; Nunes, C. A.; Coelho, A. A.; Faria, M. I. S. T.; Suzuki, P. A.; Coelho, G. C., *Magnetization Studies of Binary and Ternary Co-Rich Phases of the Co–Si–B System*. J. Alloys Compd. **2010,** *508*, 5-8.
278. Seo, K.; Lee, S.; Yoon, H.; In, J.; Varadwaj, K. S. K.; Jo, Y.; Jung, M.-H.; Kim, J.; Kim, B., *Composition-Tuned ConSi Nanowires: Location-Selective Simultaneous Growth along Temperature Gradient*. ACS Nano **2009,** *3*, 1145-1150.
279. Qu, Y.; Bai, J.; Liao, L.; Cheng, R.; Lin, Y.-C.; Huang, Y.; Guo, T.; Duan, X., *Synthesis and Electric Properties of Cicobalt Silicide Nanobelts*. Chem. Commun. **2011,** *47*, 1255-1257.
280. Petrova, A. E.; Krasnorussky, V. N.; Shikov, A. A.; Yuhasz, W. M.; Lograsso, T. A.; Lashley, J. C.; Stishov, S. M., *Elastic, Thermodynamic, and Electronic Properties of MnSi, FeSi, and CoSi*. Phys. Rev. B **2010,** *82*, 155124.
281. Fitz, C.; Goldbach, M.; Dupont, A.; Schmidbauer, S., *Silicides as Contact Material for DRAM Applications*. Microelectron. Eng. **2005,** *82*, 460-466.
282. Wu, H.; Kratzer, P.; Scheffler, M., *First-Principles Study of Thin Magnetic Transition-Metal Silicide Films on Si(001)*. Phys. Rev. B **2005,** *72*, 144425.
283. Seo, K.; Varadwaj, K. S. K.; Mohanty, P.; Lee, S.; Jo, Y.; Jung, M.-H.; Kim, J.; Kim, B., *Magnetic Properties of Single-Crystalline CoSi Nanowires*. Nano Lett. **2007,** *7*, 1240-1245.
284. Rabie, M. A.; Mirza, S.; Hu, Y.; Haddara, Y. M., *Cobalt Germanide Contacts: Growth Reaction, Phase Formation Models, and Electrical Properties*. J. Mater. Sci.: Mater. Electron. **2019,** *30*, 10031-10063.
285. Liu, X.; Ellis, J. E.; Mesaros, E. F.; Pearson, A. J.; Schoffers, E.; Hall, J. M.; Hoyne, J. H.; Shapley, J. R.; Fauré, M.; Saccavini, C.; Lavigne, G.; Chi, Y.; Liu, C.-S.; Lai, Y.-H.; Carty, A. J.; Serp, P.; Hernandez, M.; Kalck, P.; Richard, B.; Hernandez-Gruel, M. A. F.; Pérez-Torrente, J. J.; Ciriano, M. A.; Oro, L. A., *Transition Metal Carbonyl Compounds Shapley/Inorganic Syntheses V. 34*. **2004**, 96-132.
286. Jungwirth, F.; Knez, D.; Porrati, F.; Schuck, A. G.; Huth, M.; Plank, H.; Barth, S., *Vanadium and Manganese Carbonyls as Precursors in Electron-Induced and Thermal Deposition Processes*. Nanomaterials **2022,** *12*, 1110.
287. Schmied, R.; Fowlkes, J. D.; Winkler, R.; Rack, P. D.; Plank, H., *Fundamental Edge Broadening Effects During Focused Electron Beam Induced Nanosynthesis*. Beilstein J Nanotechnol **2015,** *6*, 462-71.
288. Porrati, F.; Sachser, R.; Huth, M., *The Transient Electrical Conductivity of W-based Electron-Beam-Induced Deposits During Growth, Irradiation and Exposure to Air*. Nanotechnology **2009,** *20*, 195301.
289. Huth, M.; Klingenberger, D.; Grimm, C.; Porrati, F.; Sachser, R., *Conductance Regimes of W-based Granular Metals Prepared by Electron Beam Induced Deposition*. New J. Phys. **2009,** *11*, 033032.
290. Winters, R. E.; Kiser, R. W., *Mass Spectrometric Studies of Chromium, Molybdenum, and Tungsten Hexacarbonyls*. Inorg. Chem. **1965,** *4*, 157-161.
291. Kislov, N. A.; Khodos, I. I.; Ivanov, E. D.; Barthel, J., *Electron-Beam-Induced Fabrication of Metal-Containing Nanostructures*. Scanning **1996,** *18*, 114-118.
292. Bidinosti, D. R.; McIntyre, N. S., *Electron-Impact Study of Some Binary Metal Carbonyls*. Can. J. Chem. **1967,** *45*, 641-648.
293. Devthade, V.; Lee, S., *Synthesis of Vanadium Dioxide Thin Films and Nanostructures*. J. Appl. Phys. **2020,** *128*, 231101.
294. Qin, X.; Sun, H.; Zaera, F., *Thermal Chemistry of* $Mn_2(CO)_{10}$ *During Deposition of Thin Manganese Films on Silicon Oxide and on Copper Surfaces*. J. Vac. Sci. Technol. A **2012,** *30*, 01A112.
295. Wiberg, N.; Fischer, G.; Holleman, A. F.; Wiberg, E., *Lehrbuch der Anorganischen Chemie*. 2008.
296. Córdoba, R.; Fernández-Pacheco, R.; Fernández-Pacheco, A.; Gloter, A.; Magén, C.; Stéphan, O.; Ibarra, M. R.; De Teresa, J. M., *Nanoscale Chemical and Structural Study of Co-based FEBID Structures by STEM-EELS and HRTEM*. Nanoscale Res. Lett. **2011,** *6*, 592.
297. Ghosh, S. K., *Diversity in the Family of Manganese Oxides at the Nanoscale: From Fundamentals to Applications*. ACS Omega **2020,** *5*, 25493-25504.

298. Brézin, E.; Zinn-Justin, J., *Finite Size Effects in Phase Transitions*. Nucl. Phys. B **1985,** *257*, 867-893.
299. Scheuer, V.; Koops, H.; Tschudi, T., *Electron Beam Decomposition of Carbonyls on Silicon*. Microelectron. Eng. **1986,** *5*, 423-430.
300. Douard, A.; Maury, F., *Chromium-Based Coatings by Atmospheric Chemical Vapor Deposition at low Temperature from $Cr(CO)_6$*. Surf. Coat. Technol. **2005,** *200*, 1407-1412.
301. GESHEVA, K., A.; ABROSIMOVA, V.; BESHKOV, G., D., *CVD Carbonyl Thin Films of Tungsten and Molybdenum and their Silicides - A Good Alternative to CVD Fluoride Tungsten Technology*. J. Phys. IV France **1991,** *02*, C2-865-C2-871.
302. Lai, K. K.; Lamb, H. H., *Tungsten Chemical Vapor Deposition Using Tungsten Hexacarbonyl: Microstructure of As-deposited and Annealed Films*. Thin Solid Films **2000,** *370*, 114-121.
303. Kaplan, R.; Bottka, N., *Epitaxial Growth of Fe on GaAs by Metalorganic Chemical Vapor Deposition in Ultrahigh Vacuum*. Appl. Phys. Lett. **1982,** *41*, 972-974.
304. Walsh, P. J.; Bottka, N., *Growth of Fe and $FeAs_2$ Films on GaAs by Organo-Metal Chemical Vapor Deposition Using Pentacarbonyl Iron and Arsine*. J. Electrochem. Soc. **1984,** *131*, 444-446.
305. Dormans, G. J. M.; Meekes, G. J. B. M.; Staring, E. G. J., *OMCVD of Cobalt and Cobalt Silicide*. J. Cryst. Growth **1991,** *114*, 364-372.
306. Gross, M. E.; Schnoes Kranz, K.; Brasen, D.; Luftman, H., *Organometallic Chemical Vapor Deposition of Cobalt and Formation of Cobalt Disilicide*. J. Vac. Sci. Technol., B: Microelectron. Process. Phenom. **1988,** *6*, 1548-1552.
307. Aylett, B. J.; Campbell, J. M., *Silicon–Transition Metal Compounds. Part II. Preparation and Properties of Silylpentacarbonylmanganese*. J. Chem. Soc. A **1969**, 1916-1920.
308. Aylett, B. J.; Colquhoun, H. M., *Chemical Vapour Deposition of Transition-Metal Silicides by Pyrolysis of Silyl Transition-Metal Carbonyl Compounds*. J. Chem. Soc., Dalton Trans. **1977**, 2058-2061.
309. Aylett, B. J.; Campbell, J. M., *Silicon–Transition-Metal Compounds. Part I. Silyltetracarbonylcobalt and Related Compounds*. J. Chem. Soc. A **1969**, 1910-1916.
310. Weaver, L.; Simard-Normandin, M.; Naem, A.; Clark, A., *The Use of Tem and Raman Spectroscopy to Determine the Absorption Coefficient and Silicidation Sequence of Cobalt Silicide*. MRS Online Proceedings Library **1992,** *260*, 287-291.
311. Liu, F. M.; Ye, J. H.; Ren, B.; Yang, Z. L.; Liao, Y. Y.; See, A.; Chan, L.; Tian, Z. Q., *Raman Spectroscopic Studies of the Formation Processes of Cobalt Silicide Thin Films*. Thin Solid Films **2005,** *471*, 257-263.
312. Zhao, J.; Ballast, L. K.; Hossain, T. Z.; Trostel, R. E.; Bridgman, W. C., *Effect of Rapid Thermal Annealing Temperature on the Formation of CoSi Studied by X-Ray Photoelectron Spectroscopy and Micro-Raman Spectroscopy*. J. Vac. Sci. Technol. A **2000,** *18*, 1690-1693.
313. Bret, T.; Mauron, S.; Utke, I.; Hoffmann, P., *Characterization of Focused Electron Beam Induced Carbon Deposits from Organic Precursors*. Microelectron. Eng. **2005,** *78-79*, 300-306.
314. Tuinstra, F.; Koenig, J. L., *Raman Spectrum of Graphite*. J. Chem. Phys. **1970,** *53*, 1126-1130.
315. Ferrari, A. C.; Robertson, J., *Interpretation of Raman Spectra of Disordered and Amorphous Carbon*. Phys. Rev. B **2000,** *61*, 14095-14107.
316. Chu, P. K.; Li, L., *Characterization of Amorphous and Nanocrystalline Carbon Films*. Mater. Chem. Phys. **2006,** *96*, 253-277.
317. Puydinger dos Santos, M. V.; Barth, S.; Béron, F.; Pirota, K. R.; Pinto, A. L.; Sinnecker, J. P.; Moshkalev, S.; Diniz, J. A.; Utke, I., *Magnetoelectrical Transport Improvements of Postgrowth Annealed Iron–Cobalt Nanocomposites: A Possible Route for Future Room-Temperature Spintronics*. ACS Appl. Nano Mater. **2018,** *1*, 3364-3374.
318. Möbius, A., *Comment on "Critical behavior of the Zero-Temperature Conductivity in Compensated Silicon, Si:(P,B)"*. Phys. Rev. B **1989,** *40*, 4194-4195.
319. Hattink, B. J.; García del Muro, M.; Konstantinović, Z.; Batlle, X.; Labarta, A.; Varela, M., *Tunneling Magnetoresistance in Co-ZrO_2 Granular Thin Films*. Phys. Rev. B **2006,** *73*, 045418.

320. Trummer, C.; Winkler, R.; Plank, H.; Kothleitner, G.; Haberfehlner, G., *Analyzing the Nanogranularity of Focused-Electron-Beam-Induced-Deposited Materials by Electron Tomography*. ACS Appl. Nano Mater. **2019,** *2*, 5356-5359.
321. Stanishevsky, A.; Khriachtchev, L., *Modification of Hydrogen-Free Amorphous Carbon Films by Focused-Ion-Beam Milling*. J. Appl. Phys. **1999,** *86*, 7052-7058.
322. Xu, L.; Li, S.; Wu, Z.; Li, H.; Yan, D.; Zhang, C.; Zhang, P.; Yan, P.; Li, X., *Growth and Field Emission Properties of Nanotip Arrays of Amorphous Carbon with Embedded Hexagonal Diamond Nanoparticles*. Appl. Phys. A **2011,** *103*, 59-65.
323. Jungwirth, F.; Porrati, F.; Knez, D.; Sistani, M.; Plank, H.; Huth, M.; Barth, S., *Focused Ion Beam vs Focused Electron Beam Deposition of Cobalt Silicide Nanostructures Using Single-Source Precursors: Implications for Nanoelectronic Gates, Interconnects, and Spintronics*. ACS Appl. Nano Mater. **2022**.
324. Tsai, C.-I.; Yeh, P.-H.; Wang, C.-Y.; Wu, H.-W.; Chen, U.-S.; Lu, M.-Y.; Wu, W.-W.; Chen, L.-J.; Wang, Z.-L., *Cobalt Silicide Nanostructures: Synthesis, Electron Transport, and Field Emission Properties*. Cryst. Growth Des. **2009,** *9*, 4514-4518.
325. Adambaev, K.; Yusupov, A.; Yakubov, K., *Formation of Manganese Silicide Films on Silicon*. Inorg. Mater. **2003,** *39*, 942-946.
326. Porrati, F.; Sachser, R.; Gazzadi, G. C.; Frabboni, S.; Terfort, A.; Huth, M., *Alloy Multilayers and Ternary Nanostructures by Direct-Write Approach*. Nanotechnology **2017,** *28*, 415302.
327. Balasubramanian, B.; George, T. A.; Manchanda, P.; Pahari, R.; Ullah, A.; Skomski, R.; Sellmyer, D. J., *Magnetic and Electron Transport properties of Co_2Si nanomagnets*. Phys. Rev. Mater. **2021,** *5*, 024402.
328. Schmitt, A. L.; Zhu, L.; Schmeiβer, D.; Himpsel, F. J.; Jin, S., *Metallic Single-Crystal CoSi Nanowires via Chemical Vapor Deposition of Single-Source Precursor*. J. Phys. Chem. B **2006,** *110*, 18142-18146.
329. Gabureac, M.; Bernau, L.; Utke, I.; Boero, G., *Granular Co–C Nano-Hall Sensors by Fpcused-Beam-Induced Deposition*. Nanotechnology **2010,** *21*, 115503.
330. Boero, G.; Utke, I.; Bret, T.; Quack, N.; Todorova, M.; Mouaziz, S.; Kejik, P.; Brugger, J.; Popovic, R. S.; Hoffmann, P., *Submicrometer Hall Devices Fabricated by Focused Electron-Beam-Induced Deposition*. Appl. Phys. Lett. **2005,** *86*, 042503.
331. Lien, C. D.; Finetti, M.; Nicolet, M. A.; Lau, S. S., *Electrical Properties of Thin Co_2Si, CoSi, and $CoSi_2$ Layers Grown on Evaporated Silicon*. J. Electron. Mater. **1984,** *13*, 95-105.
332. Mathur, S.; Barth, S.; Shen, H., *Chemical Vapor Growth of $NiGa_2O_4$ Films: Advantages and Limitations of a Single Molecular Source*. Chem. Vap. Deposition **2005,** *11*, 11-16.

7.2 List of figures and tables

Figure 1: Examples of different FEBID deposits:(a) Square deposit of V:C:O deposited from $V(CO)_6$, (b) tilted view of a bar deposited from $V(CO)_6$ between two gold electrodes for two point conductivity measurements, (c) freestanding PtC nano-cage. Reprinted with permission from Ref. 14. Copyright 2017 American Chemical Society. (d) 3D $FeCo_3$ wire-array. Adapted from Ref. 20 by Keller, *et.al.*, licensed under CC BY 4.0 (https://creativecommons.org/licenses/by/4.0/). Published 2018 by Springer Nature. (e) 3D PtC tetrapod acting as thermal nanoprobe deposited across two gold electrodes, (f) side view of the tetrapod, (g) top-view of the tetrapod. Adapted with permission from Ref 17. Copyright 2019 American Chemical Society 2

Figure 2: Schematic representation of (a) gas phase single collision experiments and (b) surface science experiments. Reproduced from Ref. 23 with permission from the Royal Society of Chemistry 3

Figure 3: Schematic representation of electron energy distribution emitted from a metallic surface upon electron irradiation with an electron beam of energy E_0. Electrons below 50 eV are defined as secondary electrons (SE) while electrons exceeding 50 eV are called backscattered electrons (BSE). Additionally, Auger electron (AE) peaks and signals corresponding to plasmon losses are visible. Redrawn following Reimer.[56] 9

Figure 4: Schematic representation of the FEBID process. 10

Figure 5: (a) Shapes observed for a Gaussion electron beam dependent on the different growth regimes, based on.[68] (b) Development of growth rate as a function of electron supply (current). With increasing current, a transition from electron limited growth to precursor limited growth is observed. 12

Figure 6: Schematic representation of the FEBID process. Adapted from Ref. 23 with permission from the Royal Society of Chemistry. 14

Figure 7: Schematic representation of the FIBID process. 21

Figure 8: Comparison of penetration depth for electrons and ions at typical acceleration voltages used in FIBID and FEBID. The substrate material is silicon. While Ga^+ ions are already stopped within approximately 50 nm He^+ ions of the same energy will penetrate much deeper into the substrate. Both electron and ion trajectories were calculated using Monte Carlo simulations. Ion trajectories were calculated using SRIM,[140] electron trajectories were calculated using CASINO.[141] 22

Figure 9: Schematic representation of the CVD process. 23

Figure 10: Overview of different ligand classes and their potential for providing metallic deposits. Arrow colors range from green (almost ideal) to red (bad) indicating the suitability for obtaining pure metallic deposits. Adapted from Ref. 23 with permission from the Royal Society of Chemistry. 28

Figure 11: List of all known homometallic, homoleptic transition metal carbonyls. Carbonyls already investigated for FEBID/FIBID are marked in bold and have a green background. The orange background denotes carbonyls not yet used. * indicates precursors that have been investigated in this work. Exact composition and sources are provided in Table 1. 29

Figure 12: Correlation of abstracted CO groups with the corresponding metal content illustrating the extreme requirements for “pure” metallic deposits. Values were calculated for generic $M(CO)_x$ x = 4, 5, 6 with equal amounts of C and O in the deposit. Reprinted from Ref. 23 with permission from the Royal Society of Chemistry. 32

Figure 13: Periodic table of transition metal silicides, adapted from Kieffer and Benesovsky,[246] with revised and updated data.[250-258] 38

Figure 14: Binary phase diagram of Mn-Si. Reprinted by permission from Springer Nature Customer Service Centre GmbH: Springer Nature, Journal of Phase Equilibria[259], Copyright 1990. 39

Figure 15: Binary phase diagram of Co-Si. Reprinted by permission from Springer Nature Customer Service Centre GmbH: Springer Nature, Journal of Phase Equilibria[273], Copyright 1991. 42

Figure 16. (a) V:C ratio and representative EDX spectra determined for the CVD films at different temperatures. (b) SEM image of a homogeneous CVD film deposited at 573 K on Si (911). (c) XRD patterns recorded at room temperature for films grown at T_S = 473–573 K showing oriented growth. With increased deposition rate less oriented films are obtained facilitating the phase identification. Adapted from Ref. 286 by Jungwirth, *et.al.*, licensed under CC BY 4.0 (https://creativecommons.org/licenses/by/4.0/). Published 2022 by MDPI...............46

Figure 17: Dependence of V:C ratio for the variation of different deposition parameters as well as representative EDX spectra. Variation in current was carried out at 5 kV, the beam parameters for pressure variation are 5 kV and 1.6 nA. Further deposition parameters include deposition area of 1.4 µm × 1.4 µm, pitch of 20 nm × 20 nm and a dwell time of 1 µs. Sapphire single crystals with 200 nm Au and 8 nm Cr as adhesion layer were used as substrates. EDX spectra were recorded at 11 kV acceleration voltage. 48

Figure 18: (a) Volume-based growth rates determined for V-based FEBID material in dependence on beam current at constant voltage of 5 kV. The inset shows corresponding, representative height profiles normalized to the dose at different currents. (b) Volume-based growth rates in dependence on deposition voltage. The inset shows an AFM image of a sample deposited at 5 kV and 1.6 nA. Further deposition parameters include deposition area of 1.4 µm × 1.4 µm, pitch of 20 nm × 20 nm and a dwell time of 1 µs. Sapphire single crystals with 200 nm Au and 8 nm Cr as adhesion layer were used as substrates. 49

Figure 19: TEM investigation of a sample deposited at 5 kV, 6.3 nA. (a) high resolution brightfield image of the V-based FEBID material with diffraction/phase contrast suggesting particles of 2-5 nm. (b) High angle annular dark field image (HAADF) of the lamella showing the ~200 nm thick deposit with the gold substrate layer (bright). (c) Fast Fourier transform (FFT) of image (a) showing distinct rings indicating a poly-crystalline nature which is further supported by the (d) nanobeam electron diffraction both of which provide information on the crystalline fraction of the FEBID material. (e) Rotational brightness profile of (c) and (d) allowing the assignment of a crystalline phase such as VC or VO, which can be described as generalized solid-solution of type $VC_{1-x}O_x$. Reprinted from ref. 286 by Jungwirth, *et.al.*, licensed under CC BY 4.0 (https://creativecommons.org/licenses/by/4.0/). Published 2022 by MDPI...............50

Figure 20: (a) EDX spectra recorded in the SEM as well as TEM. F observed in the TEM sample is a residue of the lamella preparation. (b) EELS line scan of the region indicated by the orange square. For the bulk material a constant V:C is observed. (b) Reprinted from ref. 286 by Jungwirth, *et.al.*, licensed under CC BY 4.0 (https://creativecommons.org/licenses/by/4.0/). Published 2022 by MDPI...............51

Figure 21: (a) Resistivity measured in two-probe configuration for material deposited at 5 kV and varying current. The inset shows an AFM image of a typical device geometry. (b) Effect of post growth electron beam irradiation on samples deposited at 5 kV and 1.6 nA and 6.3 nA respectively. (c) Temperature dependence of the conductance normalized to the conductance at 285 K for deposits prepared at 5 kV and beam currents of 6.3 nA and 1.6 nA. The inset shows again the geometry of a typical four-probe device as measured by AFM. (c) Reprinted from ref. 286 by Jungwirth, *et.al.*, licensed under CC BY 4.0 (https://creativecommons.org/licenses/by/4.0/). Published 2022 by MDPI...............53

Figure 22: (a) EDX analysis of CVD grown thin films at different temperatures, as well as ratios of Mn:O and C:O. (b) SEM image of a representative film grown at 673 K showing a highly porous nanostructure. 55

Figure 23: (a) Compositional analysis of the deposits via EDX as well as elemental ratios for varying current and voltage. For the variation of current the voltage was set to 5 kV. (b) Influence of Meissner trap usage on the composition of samples deposited at 5 kV and 1.6 nA. Further deposition parameters: sample size 1.4 µm × 1.4 µm, 20 nm × 20 nm pitch and a dwell time of 1 µs was used. Sapphire single crystals with 200 nm Au and 8 nm Cr as adhesion layer were used as substrates. 56

Figure 24: Volume based growth-rate determined by AFM. The insert shows representative height profiles for each current normalized to the total dose. Parameters used for the deposition were 5 kV, 0.4 nA to 6.3 nA, 20 nm × 20 nm pitch, 1 µs dwell time, typically 1.0 µm × 5.0 µm deposit size.................................57

Figure 25: (a) Two-probe resistivity measurements of samples deposited with 5 kV and varying current; the geometry of the samples has been determined by AFM. (b) Change in resistivity during post growth curing of a sample deposited at 5 kV and 6.3 nA using the same beam parameters and a dose of 1350 nC/µm². (c) Temperature dependence of normalized resistance normalized at 285 K for samples deposited with 6.3 nA and 5 kV. The cured sample was irradiated with 6.3 nA and 5 kV for a dose of 1000 µC/µm². Adapted from ref. 286 by Jungwirth, *et.al.*, licensed under CC BY 4.0 (https://creativecommons.org/licenses/by/4.0/). Published 2022 by MDPI. 58

Figure 26: Slice of the periodic table showing homoleptic homometallic transition metal carbonyls described in FEBID literature[49, 73-76, 82, 92, 199, 201, 209, 211, 215] with their associated metal contents. The values for $Cr(CO)_6$ are unpublished results by P. Gruszka and M. Huth. *Precursors discussed in this work, ⁺SAED shows only pure Re, but no compositional analysis was performed[291], ‡ no compositional analysis provided[299] 59

Figure 27: Comparison of maximum metal contents obtained in CVD with those obtained in FEBID. FEBID[49, 73-76, 82, 92, 199, 201, 209, 211, 215] and CVD[142, 300-306] compositions have been deduced from literature. The FEBID values for $Cr(CO)_6$ are unpublished results by P. Gruszka and M. Huth. 60

Figure 28: (a) EDX analysis of the thin films as well as elemental ratio of Mn:Si and C:O. (b) Representative SEM image of a film grown at 673 K showing a network of interconnected nanowires. (c) Diffractogram of thin films deposited at 573 K and 673 K. 62

Figure 29: (a) Compositional analysis of deposits at varying current and 5 kV acceleration voltage. (b) Composition of samples deposited at varying deposition voltage. Further deposition parameters: sample size 1.4 µm × 1.4 µm, 20 nm × 20 nm pitch and a dwell time of 1 µs was used. Sapphire single crystals with 200 nm Au and 8 nm Cr as adhesion layer were used as substrates. 63

Figure 30: Composition of samples deposited at different substrate temperatures and beam currents using a constant acceleration voltage of 5 kV. Further deposition parameters: sample size 1.4 µm × 1.4 µm, 20 nm × 20 nm pitch, dwell time of 1 µs. Sapphire single crystals with 200 nm Au and 8 nm Cr as adhesion layer were used as substrates...64

Figure 31: Volume based growth rates for samples deposited at room temperature with varying currents and an acceleration voltage of 5 kV. The inset shows representative cross sections normalized to the supplied electron dose. Further deposition parameters: sample size 1.4 µm × 1.4 µm, 20 nm × 20 nm pitch, dwell time 1 µs. Sapphire single crystals with 200 nm Au and 8 nm Cr as adhesion layer were used as substrates. 65

Figure 32: EDX analysis of thin films deposited at different temperatures for both (a) CVD-CoSi and (b) CVD-Co_2Si. SEM image of a representative CVD-CoSi (b) and CVD-Co_2Si (c) thin film deposited at 773 K. (d), (e) XRD patterns recorded at room temperature for thin films deposited at 573 K – 773 K for CVD-CoSi and CVD-Co_2Si respectively. 67

Figure 33: Raman spectra of thin films deposited at 773 K for both CVD-CoSi and CVD-Co_2Si normalized to the respective maximum intensity. (a) Low energy region of the spectrum showing peaks corresponding to a CoSi- and Co_2Si-phase respectively. (b) Carbon region of the Raman spectra (background subtracted). The red curve shows the fit to the data using two Gaussian curves (blue). 69

Figure 34: Compositional analysis of CoSi and Co_2Si FEBID deposits for varying current with a fixed acceleration voltage of 5 kV. The sample size was 1.4 µm × 1.4 µm, further deposition parameters were: 20 nm × 20 nm pitch and 1 µs dwell time. Sapphire single crystal substrates with 200 nm Au and 8 nm Cr as adhesion layer were used. 70

Figure 35: (a) Compositional variation of FEBID CoSi and Co_2Si deposits with varying deposition pressure and acceleration voltage. Deposition pressure was varied for 5 kV and 1.6 nA. (b) Influence of changes in acceleration voltage on the composition of FEBID-CoSi and FEBID-Co_2Si. For (a) and (b) deposit size was 1.4 µm × 1.4 µm, 20 nm × 20 nm pitch and a dwell time of 1 µs was used. Sapphire single crystals with 200 nm Au and 8 nm Cr as adhesion layer were used as substrates...71

Figure 36: (a) Raman spectra of the carbon region for FEBID-CoSi and FEBID-Co_2Si normalized to their respective maximum (background subtracted). The red curve shows the fit to the data using two Gaussian curves (blue). (b) Corresponding Intensity ratios I_D/I_G and position of the G band maximum in dependence of the deposition current. All samples have been deposited with 5 kV and varying current of 98 pA to 6.3 nA. 73

Figure 37: Volume-based growth rates of FEBID CoSi and Co_2Si deposits for varying currents with a constant acceleration voltage of 5 kV. Insets show line scans of representative deposits at varying currents with height normalized to dose for better comparability. Parameters used for the deposition were 5 kV, 98 pA to 6.3 nA, 20 nm × 20 nm pitch, 1 µs dwell time, and a deposit size of 1.4 µm × 1.4 µm. 74

Figure 38: Volume-based growth rate of FEBID deposits of CoSi and Co_2Si in dependence of deposition pressure. The insets show line scans at the respective pressures normalized to the total dose. Parameters used for the deposition were 5 kV, 98 pA to 6.3 nA, 20 nm × 20 nm pitch, 1 µs dwell time, and typically sample size 1.4 µm × 1.4 µm. 75

Figure 39: Comparison of room temperature resistivity measured in two-probe configuration for FEBID-CoSi and FEBID-Co_2Si. The samples were deposited at 5 kV and the beam currents were varied from 0.4 nA to 6.3 nA. The insets show AFM images of representative devices used for the measurement. Adapted with permission from Ref. 198. Copyright 2021 American Chemical Society. 75

Figure 40: (a) Effect of post-growth electron beam irradiation of CoSi and Co_2Si samples deposited at 5 kV and 6.3 nA and irradiated with the same beam parameters. Irradiation was performed for a total dose of 1200 nC/µm². (b) Comparison of different beam currents for post growth irradiation of FEBID-Co_2Si deposits. The resistivity decrease appears to be dependent on electron dose but not beam current. (b) Adapted with permission from Ref. 198. Copyright 2021 American Chemical Society. 77

Figure 41: Temperature dependence of conductivity normalized at 285 K for FEBID samples of CoSi and Co_2Si deposited with 5 kV and 6.3 nA. Cured samples were irradiated with 5 kV and 6.3 nA for a total dose of 1200 nC/µm². The inset shows the AFM image of a typical deposit used in these studies. Adapted with permission from Ref. 198. Copyright 2021 American Chemical Society. 78

Figure 42: Magnetoresistance measurement of as-grown and beam cured FEBID material. Samples were deposited at 5 kV and 6.3 nA, post growth curing was performed using the same beam parameters and a total dose of 1200 nC/µm². Adapted with permission from Ref. 198. Copyright 2021 American Chemical Society. 79

Figure 43: (a) AFM image and line scans of FIBID-CoSi having been deposited on a Au substrate showing the problematic embedding of the sample in the substrate material. Beam parameters: 30 kV, 9 pA, 0.2 µs dwell time, and 30 nm × 30 nm pitch. (b) Comparison of composition in dependence of beam current for Au and Cu as substrate material. (c) AFM image and corresponding line scans of a FIBID-CoSi deposit on Cu. Parameters and duration were the same as in (a). 80

Figure 44: Comparison of composition for FEBID and FIBID deposits of CoSi and Co_2Si at varying currents using 5 kV and 30 kV as acceleration voltage respectively. Additionally, the Co:Si elemental ratio is plotted showing the retention of the initial ratio in all cases but FIBID-CoSi. 81

Figure 45: Comparison of composition for FIBID deposits of CoSi and Co_2Si at varying voltages with a current corresponding to 30 pA. The high current was chosen to facilitate focusing for 15 kV. Additionally, the Co:Si elemental ratio is plotted. 82

Figure 46: Raman spectra of the carbon region for FIBID-CoSi and FIBID-Co_2Si material deposited at 30 kV and varying currents. The Co_2Si have been normalized to the peak maximum (background subtracted). The red curve shows the fit to the data using two Gaussian curves (blue) 83

Figure 47: Volume based growth rates for FIBID deposits of CoSi and Co_2Si at varying currents and an acceleration voltage of 30 kV. Further deposition parameters include, 20 nm × 20 nm pitch, 1 µs dwell time, typical size 1.0 µm × 5.0 µm. SiO_2 (300 nm) on Si was used as substrate due to its low sputtering rate. 84

Figure 48 (a) Comparison of growth rate of samples deposited on Cu (1.4 µm × 1.4 µm) and SiO_2 (1.0 µm × 5.0 µm). (b) Effect of refresh time on growth rate for samples of 1.0 µm × 5.0 µm deposited on SiO_2 with a current of 18 pA and an acceleration voltage of 30 kV. Reprinted with permission from Ref. 323. Copyright 2022 American Chemical Society. 84

Figure 49: Room temperature two-probe resistivities in dependence of beam current for FIBID-CoSi and FIBID-Co_2Si. The acceleration voltage was set to 30 kV. The insets show AFM images of representative devices used. Both were deposited using 30 kV and 18 pA. The inset in the CoSi data shows the problematic incorporation of the deposit in the Au electrodes....85

Figure 50: Temperature dependent conductance for (a) Co_2Si and (b) CoSi deposited by FEBID and FIBID normalized at 285 K. FEBID and FIBID deposits show very distinct behavior revealing significant differences of the material derived by both techniques. The inset shows a typical 6-probe device used for these measurements as well as magneto-resistance and Hall effect. (b) Reprinted with permission from Ref. 323. Copyright 2022 American Chemical Society....87

Figure 51: Magneto-resistance for samples deposited with FEBID and FIBID respectively. (a) using $H_3SiCo(CO)_4$ as and (b) using $H_2Si(Co(CO)_4)_2$ as precursor. (b) Reprinted with permission from Ref. 323. Copyright 2022 American Chemical Society....88

Figure 52: Magneto-transport measurements for FIBID-CoSi showing a linear increase in Hall voltage....88

Figure 53: (a) Hall voltage measurements for FIBID-Co_2Si and FEBID-Co_2Si. The FEBID derived material shows superparamagnetic behavior. For FIBID-Co_2Si a hysteresis (shown in the inset) emerges, indicating ferromagnetic behavior. (b) Hall resistivities of the two Co_2Si materials used for the calculation of charge carrier density. Reprinted with permission from Ref. 323. Copyright 2022 American Chemical Society. 89

Figure 54: (a) HAADF image of a FEBID-Co_2Si deposit prepared at 5 kV, 6.3 nA on Au. The corresponding bright field (BF) image of the same sample reveals small particles evenly distributed in a matrix. Related STEM-EDX elemental maps for Co, Si, O, and C show a mostly homogeneous distribution of the elements within the sample. (b) Signal intensity of an EDX scan along the orange line shown in the BF image. Reprinted with permission from Ref. 323. Copyright 2022 American Chemical Society. 91

Figure 55: High-resolution HAADF image of a FEBID-Co_2Si deposit prepared at 5 kV and 6.3 nA showing brightness contrast and particle formation of approx. 1-2 nm in size. The corresponding STEM-EDX elemental maps for Co, Si and O show the formation of Co-rich clusters within an oxygen containing matrix. Si is mostly distributed homogeneously in the sample. Reprinted with permission from Ref. 323. Copyright 2022 American Chemical Society. 92

Figure 56: (a) High resolution bright field image showing clusters of 1-2 nm as revealed by phase contrast and (b) corresponding fast Fourier transform image. (c) Nanobeam diffraction image. No distinct phase could be identified. The sample was prepared at 5 kV and 6.3 nA. Reprinted with permission from Ref. 323. Copyright 2022 American Chemical Society. 92

Figure 57: (a) HAADF image of a FIBID-Co_2Si deposit prepared at 30 kV and 18 pA on Cu (right) and FEBID-PtC_x cover layer (left) on top for protection during TEM lamella preparation. (b) EDX line scan along the line shown in the TEM inset. (c) STEM-EELS maps for Co_L, Si_L, O_K and C_K showing the elemental distribution in the region marked by a box in (a), all scall bars represent 50 nm. Reprinted with permission from Ref. 323. Copyright 2022 American Chemical Society. 93

Figure 58: (a) High-resolution HAADF image of a FIBID-Co_2Si sample deposited at 30 kV, 18 pA. (b)-(f) Corresponding STEM-EDX mappings for the elements Co_L, Si_L, O_K, C_K and Ga_K. (g) High-resolution bright field image of a FIBID-Co_2Si sample. Based on the corresponding FFT (h) or the nanobeam diffraction image (i) no distinct crystal phase can be identified. The sample was prepared at 30 kV and 18 pA. Adapted with permission from Ref. 323. Copyright 2022 American Chemical Society. 94

Figure 59: (a) SEM cross section of a FIBID-Co_2Si deposit showing significant porosity. (b)-(e) shows cross section images in higher resolution demonstrating the effect of beam current on porosity. A tendency of decreasing porosity with increasing beam current is observed. All samples were deposited with 30 kV acceleration voltage. The vertical bars demonstrate the thickness of the deposits. Reprinted with permission from Ref. 323. Copyright 2022 American Chemical Society...........95

Figure 60: Proposed reaction sequence responsible for bubble formation in the FIBID material by liberation of CO from initially partially fragmented intermediate............97

Figure 61: ^{1}H-NMR spectrum of H_3SiI (C_6D_6, 300 MHz). 102

Figure 62: ^{29}Si-NMR spectrum of H_3SiI (C_6D_6, 79 MHz). 103

Figure 63: ^{1}H-NMR spectrum of $H_3SiMn(CO)_5$ (C_6D_6, 500 MHz). 104

Figure 64: ^{29}Si-NMR spectrum of $H_3SiMn(CO)_5$ (C_6D_6, 99 MHz). 104

Figure 65: ^{1}H-NMR spectrum of $H_3SiCo(CO)_4$ (C_6D_6, 300 MHz). 105

Figure 66: ^{29}Si-NMR spectrum of $H_3SiCo(CO)_4$ (C_6D_6, 99 MHz). 105

Figure 67: ^{1}H-NMR spectrum of $H_2Si(Co(CO)_4)_2$ (C_6D_6, 500 MHz). 106

Figure 68: ^{29}Si-NMR spectrum of $H_2Si(Co(CO)_4)_2$ (C_6D_6, 99 MHz). 106

Figure 69: Schematic of the low-pressure cold-wall CVD reactor used in this work. Adapted from ref [332]. 107

Table 1: Comparison of metal carbonyl IR-data and amount of metal obtained in FEBID and FIBID. The metal content given for FIBID is the sum of the respective metal and Ga except: † indicates noble gas FIB (Ar^+ or He^+) where no additional Ga is incorporated. Values for $V(CO)_6$ and $Mn_2(CO)_{10}$, marked by *, are taken from this work and will be discussed in detail in chapter 4.1. 30

Table 2: Comparison of metal/metalloid contents and average M:Si ratio obtained for all hetero-bimetallic precursors used in this study. M designates Mn or Co respectively. Results for FIBID do include Ga. All values for FEBID and FIBID deposits are for material deposited at 5 kV and 30 kV respectively. Values for CVD of $H_3SiMn(CO)_5$ have been corrected for post growth oxidation assuming a C:O ratio of 1:1. 99